



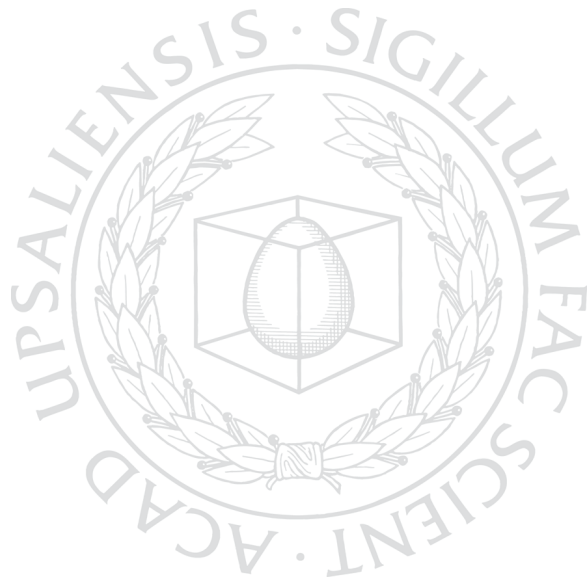
UPPSALA
UNIVERSITET

*Digital Comprehensive Summaries of Uppsala Dissertations
from the Faculty of Science and Technology 593*

Turbulence-Assisted Planetary Growth

*Hydrodynamical Simulations of Accretion Disks and
Planet Formation*

WLADIMIR LYRA



ACTA
UNIVERSITATIS
UPSALIENSIS
UPPSALA
2009

ISSN 1651-6214
ISBN 978-91-554-7395-2
urn:nbn:se:uu:diva-9537

Dissertation presented at Uppsala University to be publicly examined in Polhemsalem, Ångströmlaboratoriet, Lägerhyddsvägen 1, Uppsala, Thursday, February 26, 2009 at 14:00 for the degree of Doctor of Philosophy. The examination will be conducted in English.

Abstract

Lyra, W. 2009. Turbulence-Assisted Planetary Growth. Hydrodynamical Simulations of Accretion Disks and Planet Formation. Acta Universitatis Upsaliensis. *Digital Comprehensive Summaries of Uppsala Dissertations from the Faculty of Science and Technology* 593. viii, 102 pp. Uppsala. ISBN 978-91-554-7395-2.

The current paradigm in planet formation theory is developed around a hierarchical growth of solid bodies, from interstellar dust grains to rocky planetary cores. A particularly difficult phase in the process is the growth from meter-size boulders to planetary embryos of the size of our Moon or Mars. Objects of this size are expected to drift extremely rapid in a protoplanetary disk, so that they would generally fall into the central star well before larger bodies can form.

In this thesis, we used numerical simulations to find a physical mechanism that may retain solids in some parts of protoplanetary disks long enough to allow for the formation of planetary embryos. We found that such accumulation can happen at the borders of so-called dead zones. These dead zones would be regions where the coupling to the ambient magnetic field is weaker and the turbulence is less strong, or maybe even absent in some cases. We show by hydrodynamical simulations that material accumulating between the turbulent active and dead regions would be trapped into vortices to effectively form planetary embryos of Moon to Mars mass.

We also show that in disks that already formed a giant planet, solid matter accumulates on the edges of the gap the planet carves, as well as at the stable Lagrangian points. The concentration is strong enough for the solids to clump together and form smaller, rocky planets like Earth. Outside our solar system, some gas giant planets have been detected in the habitable zone of their stars. Their wakes may harbour rocky, Earth-size worlds.

Keywords: accretion, accretion disks, hydrodynamics, instabilities, methods: numerical, solar system: formation, planets and satellites: formation, magnetohydrodynamics (MHD), turbulence, diffusion, stars: planetary systems: formation

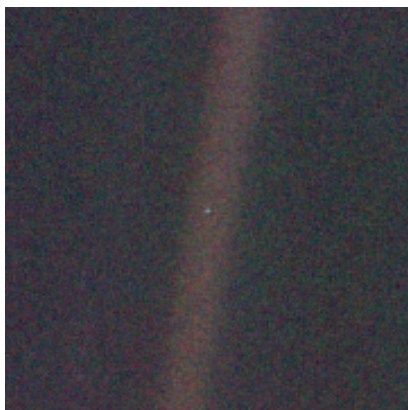
Wladimir Lyra, Department of Physics and Astronomy, Lägerhyddsvägen 1, Box 516, Uppsala University, SE-751 20 Uppsala, Sweden

© Wladimir Lyra 2009

ISSN 1651-6214

ISBN 978-91-554-7395-2

urn:nbn:se:uu:diva-9537 (<http://urn.kb.se/resolve?urn=urn:nbn:se:uu:diva-9537>)



Look again at that dot. That's here. That's home. That's us. On it everyone you love, everyone you know, everyone you ever heard of, every human being who ever was, lived out their lives. The aggregate of our joy and suffering, thousands of confident religions, ideologies, and economic doctrines, every hunter and forager, every hero and coward, every creator and destroyer of civilization, every king and peasant, every young couple in love, every mother and father, hopeful child, inventor and explorer, every teacher of morals, every corrupt politician, every "superstar," every "supreme leader," every saint and sinner in the history of our species lived there - on a mote of dust suspended in a sunbeam.

The Earth is a very small stage in a vast cosmic arena. Think of the rivers of blood spilled by all those generals and emperors so that, in glory and triumph, they could become the momentary masters of a fraction of a dot. Think of the endless cruelties visited by the inhabitants of one corner of this pixel on the scarcely distinguishable inhabitants of some other corner, how frequent their misunderstandings, how eager they are to kill one another, how fervent their hatreds.

Our posturings, our imagined self-importance, the delusion that we have some privileged position in the Universe, are challenged by this point of pale light. Our planet is a lonely speck in the great enveloping cosmic dark. In our obscurity, in all this vastness, there is no hint that help will come from elsewhere to save us from ourselves.

The Earth is the only world known so far to harbor life. There is nowhere else, at least in the near future, to which our species could migrate. Visit, yes. Settle, not yet. Like it or not, for the moment the Earth is where we make our stand.

It has been said that astronomy is a humbling and character-building experience. There is perhaps no better demonstration of the folly of human conceits than this distant image of our tiny world.

Carl Sagan (1934-1996)
Pale Blue Dot

The *Pale Blue Dot* photograph, reproduced on the previous page, was taken by the spacecraft *Voyager 1*, on February 14, 1990, from its vantage point approximately 40 AU (6 billion km) away from the Earth, and 32° above the ecliptic. The Earth takes up less than a single pixel.

List of Papers

This thesis is based on the following papers, which are referred to in the text by their Roman numerals.

- I **Lyra, W.**, Johansen, A., Klahr, H., & Piskunov, N. (2008)
Global magnetohydrodynamical models of turbulence in protoplanetary disks. I. A cylindrical potential on a Cartesian grid and transport of solids
Astronomy & Astrophysics, 479, 883
- II **Lyra, W.**, Johansen, A., Klahr, H., & Piskunov, N. (2008)
Embryos grown in the dead zone. Assembling the first protoplanetary cores in low mass self-gravitating circumstellar disks of gas and solids
Astronomy & Astrophysics, 491L, 41
- III **Lyra, W.**, Johansen, A., Zsom, A., Klahr, H., & Piskunov, N. (2009)
Planet formation bursts at the borders of the dead zone in 2D numerical simulations of circumstellar disks
Astronomy & Astrophysics, in progress (arXiv0901.1638)
- IV **Lyra, W.**, Johansen, A., Klahr, H., & Piskunov, N. (2009)
Standing on the shoulders of giants: Trojan Earths and vortex trapping in low mass self-gravitating protoplanetary disks of gas and solids
Astronomy & Astrophysics, in press (arXiv0810.3192)

Reprints were made with permission from the publishers.

Papers not included in the thesis.

- V **Lyra, W.**, & Porto de Mello, G. F. (2005)
Fine structure of the chromospheric activity in Solar-type stars -
The H α line
Astronomy & Astrophysics, 431, 329
- VI Pinotti, R., Arany-Prado, L., **Lyra, W.**, & Porto de Mello, G. F.
(2005)
A link between the semimajor axis of extrasolar gas giant planets
and stellar metallicity
Monthly Notices of the Royal Astronomical Society, 364, 29
- VII Moitinho, A., Vázquez, R. A., Carraro, G., Baume, G., Giorgi, E.
E., & **Lyra, W.** (2006)
Spiral structure of the third galactic quadrant and the solution to
the Canis Major debate
Monthly Notices of the Royal Astronomical Society, 368L, 77
- VIII **Lyra, W.**, Moitinho, A., van der Bliek, N. S., & Alves, J. (2006)
On the difference between nuclear and contraction ages
Astronomy & Astrophysics, 453, 101
- IX de Val-Borro, M., Edgar, R. G., Artymowicz, P., Ciecielag, P.,
Cresswell, P., D'Angelo, G., Delgado-Donate, E. J., Dirksen,
G., Fromang, S., Gawryszczak, A., Klahr, H., Kley, W., **Lyra,**
W., Masset, F., Mellema, G., Nelson, R. P., Paardekooper, S.-J.,
Peplinski, A., Pierens, A., Plewa, T., Rice, K., Schäfer, C., &
Speith, R. (2006)
A comparative study of disc-planet interaction
Monthly Notices of the Royal Astronomical Society, 370, 529
- X Porto de Mello, G. F., **Lyra, W.**, & Keller, G. R. (2008)
The Alpha Centauri binary system. Atmospheric parameters
and element abundances
Astronomy & Astrophysics, 488, 653
- XI Liljeström, A. J., Korpi, M. J., Käpylä, P. J., Brandenburg, A., &
Lyra, W. (2009)
Turbulent stresses as a function of shear rate in a local disk
model
Astronomische Nachrichten, in press (arXiv0811.2341)

Contents

1	Introduction	9
2	Dynamical Equations	15
2.1	Viscous disk solution	16
2.1.1	Steady state viscous evolution	18
2.2	The need for turbulence	19
3	Aerodynamics of solid bodies	21
3.1	Dimensionless numbers	22
3.2	Epstein drag	23
3.3	Stokes drag	24
3.4	General case	26
3.5	Radial drift of solids in gaseous disks	27
3.5.1	Pressure trapping	29
3.6	Gravitational Instability of the layer of solids	29
4	Magnetic Turbulence in Accretion Disks	31
4.1	The Magneto-Rotational Instability	32
4.1.1	From turbulent stresses to laminar alpha viscosity	33
4.1.2	Dispersion relation	35
4.2	The MRI in global models	36
4.2.1	Solids trapped in turbulence	37
4.3	Origin of the field	38
5	The magnetically dead zone and the Rossby wave instability	41
5.1	The nature of resistivity	41
5.2	Suppression of the MRI	43
5.2.1	The dead zone	44
5.3	Accretion onto and through the dead zone	46
5.4	The Rossby wave instability	46
5.5	Vortices	49
5.5.1	Vortices as particle traps	50
5.5.2	Vortex stability	50
6	Subordinate planet formation	53
6.1	Planet-Disk interaction	54
6.1.1	The carved gap	56
6.2	Lagrangian points	58
6.2.1	The Jacobi constant	59
6.3	PENCIL's results	60
7	Ongoing and future work	65

7.1	The RWI in three dimensions	65
7.2	Radiation	67
7.3	Gas accretion onto giant planets	68
8	Contribution to Included Papers	71
9	Summary in Swedish	73
10	Acknowledgements	77
	Appendix A	79
	A.1 High-frequency filters	79
	A.1.1 Conservative Hyperdissipation	79
	A.1.2 Hyperviscosity	82
	A.1.3 Anisotropic hyperdissipation	84
	Appendix B	85
	B.1 Poisson solver	85
	B.1.1 Potential of flattened disks	86
	Appendix C	89
	C.1 <i>N</i> -body solver	89
	C.1.1 Conservation of the Jacobi constant	90
	C.1.2 A many-body test	91
	Appendix D	95
	D.1 Useful numbers and relations	95
	Bibliography	97

1. Introduction

The worlds come into being as follows: many bodies of all sorts and shapes move from the infinite into a great void; they come together there and produce a single whirl, in which, colliding with one another and revolving in all manner of ways, they begin to separate like to like.

Leucippus (480-420? B.C.)

Stars shine due to the production of energy by nuclear reactions occurring in their center. However, there is yet another source of energy in astrophysical objects: the release of gravitational binding energy, a process known as *accretion*.

Indeed, before the recognition that the Sun is powered by nuclear reactions and that the Earth keeps its warm interior due to radioactive decay of heavy nuclides, accretion was pointed out by Helmholtz (1854) and Lord Kelvin (Thomson, 1862) as the only possible source of their energy: the Sun was continuously shrinking and the Earth was still radiating away the heat from accretion. It led, of course, to too short timescales, with the Sun and the Earth being as young as a few tens of millions of years. Geologists, however, knew of rocks that were considerably older than that, and biologist Charles Darwin certainly needed much longer timescales to explain the origin of the species. Unfortunately, rock dating was no match for Kelvin's lengthy calculations, backed up not only by the known physics of the time, but also by his immense influence and prestige. Only with the advent of nuclear physics and the realization of the superb amounts of energy the atomic nucleus stored, could accretion be dismissed as the main energy source for the Sun and the Earth, and the question be settled - in favor of the geologists and evolutionary biologists¹.

There are classes of objects, however, for which accretion *is* the dominant source of energy. Indeed, accretion onto a central object is believed to power some of the most energetic phenomena in the Universe. We

¹Kelvin actually argued *against* evolution through natural selection, based on the youth of the Earth and the Sun (Thomson 1862, 1897). We can invert the argument to illustrate the power of Darwinian evolution theory: it can be said that it *predicted* that stars should be powered by some other mechanism.

can estimate, for instance, the energy release of a particle of mass m falling in the gravitational potential well of a black hole. The gravitational potential energy difference from infinity to the last stable orbit $R_{\text{ls}} = 3R_c$ (where $R_c = 2GM/c^2$ is the Schwarzschild radius, beyond which light cannot escape) is

$$E_p = \frac{GMm}{R_{\text{ls}}} = \frac{1}{6}mc^2, \quad (1.1)$$

i.e., an appreciable fraction of its rest energy. Half of it stays as kinetic energy in the accretion disk. The other half, approximately 9% of the rest energy, is radiated away. The standard theory of black hole accretion (Lynden-Bell 1969, Lynden-Bell & Pringle 1974) shows by simple order of magnitude estimates that a black hole of $10^8 - 10^9$ solar masses, accreting at a rate of $1 M_{\odot} \text{yr}^{-1}$ will radiate copious amounts of energy at the rate of $10^{47} L_{\odot}$, thus explaining why quasars are seen all the way across the Universe.

Yet, although a theory of nuclear fusion is firmly established to explain stellar luminosities, our current understanding of accretion processes is just marginal. This is because the physics of accretion is, in some respects, considerably more complicated than the already extreme physics occurring in stellar cores. It involves, for instance, non-linear advection - that renders most mathematical techniques useless - and *turbulence*, for which not even a consistent physical theory exists. Legend tells that distinguished physicist Werner Heisenberg found this combination to be such a difficult subject that after completing his doctoral thesis *Über Stabilität und Turbulenz von Flüssigkeitsströmen* (On the Stability and Turbulence of Fluid Flow; Heisenberg 1924), he sought refuge in quantum mechanics.

The problem of accretion is intimately related to the field of planet formation and extrasolar planets, one of the most fascinating topics of contemporary astronomy. Early mathematical considerations by Laplace (1796) applied Newton's theory of universal gravitation and laws of motion to a slowly rotating spherical cloud, implying that it should collapse under its own weight. Due to conservation of angular momentum, the gas settles into a flat disk orbiting the condensing proto-sun in the center. In this solar nebula, planets are taking shape. Nevertheless, it was later realized that the correct picture is far from that trivial. As interstellar clouds are huge in size, even the slightest rotation means far too much angular momentum. Even a formed disk stores in its innermost astronomical unit two orders of magnitude more angular momentum than a star can accommodate before achieving break-up velocities. In order to accrete, the gas must somehow get rid of its angular momentum. Even more difficult is to

explain the leap of 14 orders of magnitude in size from micron-sized interstellar dust grains to giant planet Jupiter.

The modern paradigm requires the presence of turbulence in the disk in order to provide both the anomalous viscosity necessary for star formation and the trapping of solids needed to quickly congregate the dust into progressively larger bodies. The turbulence is brought about by the magneto-rotational instability (MRI; Chandrashekar 1961, Balbus & Hawley 1991, Balbus & Hawley 1998), whereby the combination of a weak (subthermal) magnetic field and the shear present in the Keplerian rotation of the gas de-stabilizes the flow. The concurrent processes that lead to planet formation, once believed to be a progress of deterministic steps, must instead take place in this turbulent environment. Starting with micron-sized dust grains, coagulation models (Brauer et al. 2007) predict growth to centimeter (pebbles) and meter size (boulders) by electromagnetic hit-and-stick mechanisms (mostly van der Waals forces). However, growth beyond this size is halted, for two reasons. First, collisions between boulders lead to destruction rather than growth (Benz 2000). Second, because of the balance between pressure, rotation and gravity, the gas orbits the star slightly slower than an independent body at the same distance would. Consequently, pebbles and boulders tend to outpace the gas. The resulting headwind drains their angular momentum, leading them into spiral trajectories towards the star, in timescales as short as a hundred years at 1AU (Weidenschilling 1977a). Avoiding this ill fate of the building blocks of planets stands as one of the major unsolved problems in the theory of planet formation.

A distinct possibility to solve these problems is gravitational instability of the layer of solids (Safronov 1969; Lyttleton 1972; Goldreich & Ward 1973; Youdin & Shu 2002). When the dust aggregates had grown to centimeter and meter size, the gas drag is reduced and the solids are pushed to the midplane of the disk due to the stellar gravity. Although such bodies do not have enough mass to attract each other individually, the sedimentation increases the solids-to-gas ratio by orders of magnitude when compared to the interstellar value of 10^{-2} . It was then hypothesized (Safronov 1969) that due to the high densities of this midplane layer, the solids could collectively achieve critical number density and undergo direct gravitational collapse. Such a scenario has the advantage of occurring on very rapid timescales, thus avoiding the radial drift barrier.

This picture was nonetheless shown to be simplistic, in the view that even low levels of turbulence in the disk preclude the midplane layer of solids from achieving densities high enough to trigger the gravitational instability (Weidenschilling 1980). Even in the absence of self-sustained turbulence such as the one generated by the MRI, the

solids themselves can generate turbulence due to the backreaction of the drag force onto the gas. Such turbulence can be brought about by Kelvin-Helmholtz instabilities due to the vertical shear the dense layer of solids induces on the gas (Weidenschilling 1980; Weidenschilling & Cuzzi 1993; Sekiya 1998; Johansen et al. 2006), or by streaming instabilities induced by the radial migration of solids particles (Youdin & Goodman 2005; Paardekooper 2006; Youdin & Johansen 2007; Johansen & Youdin 2007). In the turbulent motion, the solids are stirred up by the gas, forming a vertically extended layer where the stellar gravity is balanced by turbulent diffusion (Dubrulle et al. 1995; Garaud & Lin 2004).

But if turbulence precludes direct gravitational collapse through sedimentation, it was also shown that it allows for it in an indirect way. As solid particles concentrate in high pressure regions (Haghighipour & Boss 2003), the solids-to-gas ratio can be enhanced in the transient turbulent gas pressure maxima, potentially reaching values high enough to trigger gravitational collapse. Numerical calculations by Johansen et al. (2007) show that this is indeed the case, with the particles trapped in the pressure maxima generated by the MRI collapsing into dwarf planets when the gravitational interaction between particles is considered. They also show that the MRI is not necessarily needed, since the weak turbulence brought about by the streaming instability itself can lead to enough clumping under certain conditions.

Such models, however, ignored the possibility of fragmentation of particles upon collisions. As the turbulence enhances the velocity dispersion of solids, destructive collisions become more likely. Moreover, upon destruction, the smaller fragments are tightly coupled to the gas and therefore dragged away from the midplane (Johansen et al. 2008), reducing the effective amount of solid material available for collapse.

The fragmentation problem would be less severe in areas where random velocities are reduced. Anticyclonic vortices similar to Jupiter's Great Red Spot (Cassini 1666, Schwabe 1831, Marcus 1988) have long been believed to favour planet formation since they enhance the local shear and induce a net force on solid particles towards their centers (Barge & Sommeria 1995). Klahr & Bodenheimer (2006) further argue that anticyclonic vortices may potentially be less turbulent than the ambient gas, which in turn would lead to velocity dispersions that are low enough to prevent fragmentation of the boulders upon collisions.

The formation of vortices in disk is a direct consequence of the presence of long-lived axisymmetric pressure maxima. Such maxima launch inertial waves (Rossby waves in planetary atmospheres being a close analog) that upon breaking, coalesce into regions of large anti-cyclonic vorticity (Lovelace et al. 1999, Li et al. 2000, Li et al. 2001). Such favorable pressure maxima can occur in the following

scenario. The magneto-rotational instability, as the name suggests, depends on the coupling between the gas and the magnetic field, which in turn just occurs in the presence of sufficient ionization. In the inner disk this condition is met, since high temperatures provide enough free electrons through collisional ionization of alkali metals. In the outer regions the gas is cold but the gas density is low enough for cosmic rays to penetrate all the way to the disk's midplane and provide ionization throughout. In an intermediate region, however, the gas is too cold and too dense to be ionized either way. The result is that, when threaded by a weak magnetic field, the disk displays MRI-active regions in the ionized layers, and a MRI-dead zone in the neutral parts around the midplane (Gammie 1996, Miller & Stone 2000; Oishi et al. 2007). Matter flows towards the star due to the high turbulent viscosity of the MRI-active layers, but upon hitting the border of the dead zone, it reaches a region of slow accretion and the flow stalls. Nevertheless, as the flow proceeds unabridgedly from the outer active regions, a surface density maximum forms, which launches the inertial waves and triggers the formation of vortices (Varnière & Tagger 2006, Inaba & Barge 2006).

As we see, the words of Leucippus quoted in the opening of this introduction are not exactly without foundation within the modern theory of planet formation. Substitute "many bodies of all sorts and shapes" by *gas and dust*, then "single whirl" by *protoplanetary disk* and finally "revolving in all manner of ways" by *turbulence* (here broadly defined to include long-lived vortices), and it could have figured in the introduction of a paper in the latest issue of *Astronomy & Astrophysics*. This attests not to clairvidence of the ancient Greeks, but to the antiquity of the question that we try to answer in this thesis: *How did the Earth come to be?* Virtually every society in recorded history tried at some point to answer this question. Given the huge sample space, some of the educated guesses of the time are bound to contain some truth.

In this project, I aimed at providing an answer to this ancient question by constructing state-of-the-art global simulations of turbulent protoplanetary disks that could be used to explore the implications of this scenario for planet formation. The gas disk is modelled in a fixed grid in Cartesian, cylindrical or spherical coordinates, while the solids are treated as numerical particles. In paper I we built MRI-unstable global models of protoplanetary disks, confirming the predictions of local models that meter-size particles concentrate enough in the transient pressure maxima of the turbulence. In paper II we built on the vortex-producing dead zone model of Varnière & Tagger (2006) by including interacting centimeter and meter sized particles to their 2D model, showing that

the particle accumulation inside the vortices is so efficient that it leads to gravitational collapse of the cluster of particles. As a result, a planet formation burst ensues in the disk, leading to the formation of 300 gravitationally bound planetary embryos, 20 of them being more massive than Mars. Their mass spectrum follows a power law of index -2.3 ± 0.2 . In paper III we addressed, among other issues, the fragmentation problem by calculating the collisional velocity history of the particles that compose the embryos, finding that the vast majority of them never experienced a collision with another particle at relative speeds faster than 1 m s^{-1} . This result lends further support to the long-held idea that anti-cyclonic vortices provide a superbly favorable environment for planet formation.

We also went on to show, in paper IV, that the same mechanism occurs in disks with giant planets, where vortices are also excited (de Val-Borro et al. 2007). The gravitational collapse of the solids, in this case, leads to the formation of Super-Earths, that could well be the cores of a second generation of giant planets. An interesting by-product of this work was the realization that collapse of solids into Earth mass planets also occurs at the stable Lagrangian points of the orbit of a giant planet. This raises the possibility that some of the gas giant extra-solar planets discovered so far may have Trojan Earth-mass companions, which in turn allows for the addition of solar-type stars with giant planets in Earth-like orbits to the list of potentially habitable stellar systems.

The simulations were performed with the PENCIL CODE. The code, including improvements done for the Thesis work, is publicly available under a GNU open source license and can be downloaded at <http://www.nordita.org/software/pencil-code/>

In the following chapters we provide what intends to be a pedagogical review of the underlying physics of the simulations used to obtain the results presented in the papers. In chapter 2 we introduce the model equations and outline the main results of the standard theory of viscous accretion disks, which constitute a starting point for more advanced models. This is followed by a review of the aerodynamics of embedded solid bodies, in chapter 3. In chapter 4 we introduce the basic physics of the magneto-rotational instability. Chapter 5 deals with departure from ideal MHD, introducing resistive effects and the emergence of dead zones in disks, the Rossby wave instability, and vortex formation. In chapter 6 we review the results of planet-disk interaction and explore the consequences for a second event of planet formation. Chapter 7 provides a brief outline of ongoing works and future projects I intend to pursue. Numerical issues relevant to this work are discussed in the appendices.

2. Dynamical Equations

*When I meet God, I am going to ask him two questions:
Why relativity? Why turbulence?
I really believe he will have an answer for the first.*

Werner Heisenberg

The equations we solve will be quoted through the Thesis. The gas follows the equations of magnetohydrodynamics (MHD)

$$\frac{D\rho_g}{Dt} = -\rho_g \nabla \cdot \mathbf{u} \quad (2.1)$$

$$\frac{DS}{Dt} = \frac{1}{\rho_g T} \left[\nabla \cdot (K \nabla T) + \eta \mu_0 \mathbf{J}^2 + 2\nu \rho_g \mathbf{S}^2 \right] \quad (2.2)$$

$$\frac{D\mathbf{u}}{Dt} = -\nabla \Phi - \rho_g^{-1} \left[\nabla p + \mathbf{J} \times \mathbf{B} + \rho_p f_d + \nabla \cdot (2\nu \rho_g \mathbf{S}) \right] \quad (2.3)$$

$$\frac{\partial \mathbf{A}}{\partial t} = \mathbf{u} \times \mathbf{B} - \eta \mu_0 \mathbf{J} \quad (2.4)$$

$$p = \rho_g c_s^2 / \gamma \quad (2.5)$$

$$\Phi = \Phi_{\text{sg}} - \sum_i^N \frac{GM_i}{|\mathbf{r} - \mathbf{r}_i|} \quad (2.6)$$

$$\nabla^2 \Phi_{\text{sg}} = 4\pi G (\rho_g + \rho_p). \quad (2.7)$$

In the above equations, the operator

$$\frac{D}{Dt} = \frac{\partial}{\partial t} + \mathbf{u} \cdot \nabla \quad (2.8)$$

represents the advective derivative. The quantities ρ_g and \mathbf{u} are the density and velocity of the gas, T is the temperature, c_s is the sound speed, p is the pressure, and $S = c_v [\ln T - (\gamma - 1) \ln \rho]$ its specific entropy, where γ is the adiabatic index and c_v the specific heat capacity at constant volume. ν is the kinematic viscosity, K is the heat conductivity, \mathbf{S} is the rate-of-strain tensor, \mathbf{A} is the magnetic vector potential,

$\mathbf{B} = \nabla \times \mathbf{A}$ is the magnetic field, η is the resistivity, μ_0 is the magnetic permmissivity, $\mathbf{J} = \mu_0^{-1} \nabla \times \mathbf{B}$ is the volume current density, G is the gravitational constant, Φ is the gravitational potential, M is the mass of each of the N massive bodies (the Sun and the planets, for instance).

The quantity $\rho_p = n_p m_\bullet$ stand for the bulk density of solids, where m_\bullet is the mass of an individual particle and n_p their number density. The solids follow the Lagrangian equations

$$\frac{d\mathbf{v}_p}{dt} = -\nabla\Phi + \mathbf{f}_d \quad (2.9)$$

$$\frac{d\mathbf{x}_p}{dt} = \mathbf{v}_p \quad (2.10)$$

$$\mathbf{f}_d = -\frac{1}{\tau_s} (\mathbf{v}_p - \mathbf{u}) \quad (2.11)$$

where \mathbf{x}_p and \mathbf{v}_p are the position and velocity of each particle. Solids and gas exchange momentum through the drag force \mathbf{f}_d . The quantity τ_s is the stopping time, representing the timescale on which the solids couple to the gas, explained in detail on the next chapter.

In Eq. (2.2)-(2.4) we write the usual heat conductivity, viscosity and resistivity terms, but in practice we employ higher order versions of these dissipation terms, to maximize the inertial range of the simulations. In addition, we also add explicit diffusion (also high-order) to the continuity equation, since this equation has no dissipation term to stabilize high frequency modes. These terms are described in Appendix A. The Poisson solver for Eq. (2.7) is detailed in Appendix B.

Throughout this work, we write cylindrical coordinates as (s, ϕ, z) and spherical coordinates as (r, ϕ, θ) , where θ is the polar angle, ϕ the azimuthal angle, and z is the direction perpendicular to the midplane of the disk. In 2D situations, where $s=r$, we use the more common r designation.

2.1 Viscous disk solution

The equilibrium of an unmagnetized accretion disk orbiting a central mass is found directly from the momentum equation. In cylindrical coordinates and under the conditions of azimuthal symmetry ($\partial/\partial\phi=0$), and initial centrifugal balance $u_r(t_0)=0$, they read

$$\ddot{s} - s\dot{\phi}^2 = -\frac{1}{\rho} \frac{\partial p}{\partial s} - \frac{GM}{r^3} s \quad (2.12)$$

$$s\ddot{\phi} = -\nu \left(s \frac{\partial^2 \dot{\phi}}{\partial s^2} + 3 \frac{\partial \dot{\phi}}{\partial s} \right) \quad (2.13)$$

$$\ddot{z} = -\frac{1}{\rho} \frac{\partial p}{\partial z} - \frac{GM}{r^3} z \quad (2.14)$$

where we ignored the particles' backreaction terms, which only become important when $\rho_p \gtrsim \rho_g$. The self-gravity terms were also ignored since the disk is assumed of low mass.

Equation (2.12) gives the condition for initial centrifugal balance ($\ddot{s}=0$)

$$\Omega^2 = \Omega_K^2 + \frac{1}{s\rho} \frac{\partial p}{\partial s} \quad (2.15)$$

where we substituted $\Omega_K = GM/r^3$ for the Keplerian angular frequency and $\Omega = \dot{\phi}$ for the true, pressure-corrected, sub-Keplerian, angular frequency.

Equation (2.13) reflects the fact that viscosity is continuously depriving the disk of angular momentum and making it accrete onto the central star. Although, as the viscosity ν is small, this effect takes many orbits to settle into a steady inflow.

The third equation gives the condition for vertical hydrostatic equilibrium ($\ddot{z}=0$)

$$\frac{1}{\rho} \frac{\partial p}{\partial z} = -\Omega_K^2 z \quad (2.16)$$

which, if the sound speed does not depend on z , is readily integrated to yield the density stratification

$$\rho(r, z) = \rho(r) e^{-\gamma z^2 / 2H^2} \quad (2.17)$$

where $H=c_s/\Omega_K$ is the pressure scale height. As the dependency of the sound speed with radius (we usually use $c_s \propto r^{-1/2}$) is less steep than the dependency of Ω_K with radius ($\propto r^{-3/2}$), H is invariably an increasing function of distance, so protoplanetary disks are flared. It follows that the disk's aspect ratio is

$$h \equiv \frac{H}{r} = \frac{c_s}{u_K}, \quad (2.18)$$

and since the Keplerian flow is very supersonic, the above equation implies $h \ll 1$, so the disk is geometrically thin.

Equation (2.17) is valid near the midplane, since we assumed that Ω_K did not depend on z , which is not strictly valid. The expression is similar considering the full dependency of Ω_K on z

$$\rho(r, z) = \rho(r) e^{-\gamma z^2 / [H^2(1 + \sin\theta)]} \quad (2.19)$$

and Eq. (2.17) is recovered near the midplane where θ , the polar angle, is $\approx \pi/2$. A similar expression, also yielding Eq. (2.17) at $\theta \approx \pi/2$ is found if the sound speed is also allowed to depend on z .

2.1.1 Steady state viscous evolution

Under the viscous force, a small radial velocity will ensue in the flow and the equilibrium solution will turn into an non-static but steady state, with non-zero mass accretion rate

$$\dot{m}(s) = \oint_{\mathcal{A}} \rho_g \mathbf{u} \cdot \hat{\mathbf{n}} dA \quad (2.20)$$

$$= -2\pi s \int \rho_g(s, z) u_s(s, z) dz. \quad (2.21)$$

where we assume the surface \mathcal{A} to be a cylinder at a radial distance s from the origin, with $\hat{\mathbf{n}} = \hat{\mathbf{s}}$. If u_s does not depend on z , then

$$\dot{m}(r) = -2\pi r \Sigma_g u_r, \quad (2.22)$$

where $\Sigma_g = \int \rho_g dz$ is the surface density and we use r instead of s since in 2D the two quantities are equal. Steady state solutions exist if \dot{m} does not depend on radius (so that matter does not pile up anywhere in the disk).

The steady-state radial velocity can be found from the axisymmetric and vertically integrated continuity and angular momentum equations, which read

$$\frac{\partial \Sigma}{\partial t} + \frac{1}{r} \frac{\partial}{\partial r} (r \Sigma u_r) = 0 \quad (2.23)$$

$$\frac{\partial}{\partial t} (\Sigma r^2 \Omega) + \frac{1}{r} \frac{\partial}{\partial r} (\Sigma r^3 \Omega u_r) = \frac{1}{r} \frac{\partial}{\partial r} \left(\nu \Sigma r^3 \frac{d\Omega}{dr} \right) \quad (2.24)$$

For a steady state disk, the time derivatives are zero, so we have

$$r\Sigma u_r = c_1 \quad (2.25)$$

$$\Sigma r^3 \Omega u_r - \nu \Sigma r^3 \frac{d\Omega}{dr} = c_2 \quad (2.26)$$

where c_1 and c_2 are constants of integration. It is readily seen from Eq. (2.22) that $c_1 = -\dot{m}/2\pi$, so the mass accretion rate is constant. The constant c_2 is evaluated by noticing that at the surface of the star (r_*), the accreting gas is dragged into rigid rotation, so $d\Omega/dr=0$ at $r=r_*$. We thus have

$$c_2 = c_1 r_*^2 \Omega(r_*) = c_1 (GM r_*)^{1/2} \quad (2.27)$$

we substitute this back into Eq. (2.26). Noticing that $\Omega \approx \Omega_K$ and $d\Omega_K/dr = -3\Omega_K/2r$, we find

$$\nu \Sigma = \frac{\dot{m}}{3\pi} \left[1 - \left(\frac{r_*}{r} \right)^{1/2} \right] \quad (2.28)$$

which throughout the disk, where ($r \gg r_*$), reduces to

$$\dot{m} = 3\pi\nu\Sigma \quad (2.29)$$

The viscous inflow velocity u_r is found by substituting Eq. (2.29) into Eq. (2.22)

$$u_r = -\frac{3\nu}{2r} \quad (2.30)$$

2.2 The need for turbulence

Equation (2.29) allows for a direct comparison with observations. Observations of T-Tauri disks reveal mass accretion rates of the order of $\approx 10^{-8} M_\odot \text{ yr}^{-1}$ (e.g., Sicilia-Aguilar et al. 2004). Using this value for \dot{m} and the typical densities of the minimum mass solar nebula at $\sim 1\text{AU}$, 10^3 g cm^3 (Weidenschilling 1977b), the viscosity needed is

$$\nu \approx \frac{\dot{m}}{10\Sigma} \approx 10^{14} \text{ cm}^2 \text{ s}^{-1}. \quad (2.31)$$

The immediate source of viscosity one can think of is the natural, microscopic, molecular viscosity. We can estimate it from dimensional

analysis. Viscosity has dimension of $\text{cm}^2 \text{ s}^{-1}$, so we can estimate it (e.g., Spitzer 1962), in terms of a typical length l and velocity v . For molecular viscosity, these are the mean free path of the medium and the thermal velocity. The mean free path λ is a function of the number density of molecules and of their collisional cross section σ_{coll}

$$\lambda = \frac{1}{n\sigma_{\text{coll}}}. \quad (2.32)$$

For the inner regions of a protoplanetary disk, $n \approx 10^{14} \text{cm}^{-3}$ and the cross section of molecular hydrogen is $\sigma_{\text{coll}} = 2 \times 10^{-15} \text{cm}^2$, so $\lambda \approx 10 \text{cm}$. The typical sound speed is of the order of 1 km s^{-1} , so that $v \approx 10^7 \text{ cm}^2 \text{ s}^{-1}$.

This is *seven orders of magnitude* lower than required. Other physical mechanism, that acts as an *effective* viscosity, must be invoked to explain accretion.

Turbulence has long been known to provide viscosity due to the interaction of the turbulent eddies. Such “eddy viscosity” comes naturally from the equation of motion when we consider turbulence by splitting the quantities ψ into mean $\bar{\psi}$ and perturbation $\delta\psi$ (i.e., $\psi = \bar{\psi} + \delta\psi$). Then writing the (incompressible) Euler equation

$$\rho \partial_t u_i = \rho F_i - \partial_j (p \delta_{ij} + \rho u_i u_j) \quad (2.33)$$

in terms of the mean quantities, we obtain

$$\rho \partial_t \bar{u}_i = \rho \bar{F}_i - \partial_j (\bar{p} \delta_{ij} + \rho \bar{u}_i \bar{u}_j + \rho \overline{\delta u_i \delta u_j}). \quad (2.34)$$

Equation. (2.34) was first obtained by Reynolds (1895) and is therefore called *Reynolds equation*. We see that all perturbations average out except for the term $\rho \overline{\delta u_i \delta u_j}$. Comparing Eq. (2.34) with the Navier-Stokes equation (Eq. (2.3)), we see that this term, the *Reynolds stress*, behaves exactly like the rate-of-strain tensor and therefore transports angular momentum. We will return to this point in chapter 4.

3. Aerodynamics of solid bodies

Leave no stone unturned!

Euripides commands the solar nebula
Heraclidae, circa 428 B.C.

Solid particles and gas interchange momentum due to interactions that happen at the surface of the solid body. The many processes that can occur are generally described by the collective name of “drag” or “friction”. Due to the details involved, a general description of drag forces derived from first principles is not available, since simplifications are often needed to arrive at linear equations suitable for analytical manipulation. Nevertheless, great insight can be obtained from limiting cases. Consider a solid body of cross section σ travelling through a fluid medium of uniform density ρ with velocity Δv . In a time interval dt , it sweeps a volume $dV = \sigma|\Delta v|dt$. In the reference frame of the particle, the gas molecules are travelling ballistically with velocity $-\Delta v$. If all their momentum is transferred to the particle, the force is

$$F_d = \frac{dp}{dt} = \rho dV \frac{dv}{dt} = -\rho\sigma|\Delta v|\Delta v. \quad (3.1)$$

In aerodynamics it is usual to define a factor C_D that takes into account the deviations from this idealized picture

$$F_d = -0.5\sigma C_D \rho |\Delta v| \Delta v. \quad (3.2)$$

The factor 0.5 comes in because it is common to define the drag force in terms of kinetic energy instead of momentum. Considering spheres of radius a , their cross section is πa^2 . The acceleration f_d that appears in the equation of motion is found upon dividing F_d by the mass of the

particle $4/3\pi a_\bullet^3 \rho_\bullet$, where ρ_\bullet is its internal density

$$f_d = - \left(\frac{3\rho C_D |\Delta v|}{8a_\bullet \rho_\bullet} \right) \Delta v. \quad (3.3)$$

The quantity in parenthesis has dimension of time⁻¹ and therefore represents the timescale within which the particle couples to the gas flow

$$\tau_s = \frac{8a_\bullet \rho_\bullet}{3\rho C_D |\Delta v|}. \quad (3.4)$$

The drag then can be cast in the compact form

$$f_d = - \frac{1}{\tau_s} \Delta v \quad (3.5)$$

and we just need to know the coefficient C_D to obtain the friction force.

3.1 Dimensionless numbers

One can judge from the approximations used in obtaining Eq. (3.1) which quantities are important in the determination of C_D . We neglected the thermal velocity dispersion of the particles, simply equating their velocities to Δv . This approximation corresponds to very supersonic motion, and we therefore expect the Mach number of the relative flow

$$\text{Ma} = \frac{|\Delta v|}{c_s} \quad (3.6)$$

to play a role at lower relative speeds. Equation (3.1) also assumed that the gas molecules collide with the particle's surface at ballistic trajectories. This supposes that the mean free path λ of the gas is much larger than the particle's dimensions. It will thus break when this assumption is relaxed, and we can expect C_D to depend on the Knudsen number of the flow past the particle

$$\text{Kn} = \frac{\lambda}{2a_\bullet}. \quad (3.7)$$

The regime of low Knudsen numbers is usually referred to as Stokes drag, while the regime of high Knudsen numbers is usually called Epstein drag (Epstein 1924). Both regimes show dependencies on the Mach number. A third dimensionless number is also important. In the Stokes regime when the Knudsen number is low, intermolecular collisions in the gas are frequent and molecular viscosity becomes rel-

evant. Thus, regimes of low and high Reynolds numbers should exist for Stokes drag. However, one can write the Reynolds number in terms of the Knudsen and Mach numbers

$$\text{Re} = \frac{2a_\bullet \rho |\Delta v|}{\mu} = 3 \sqrt{\frac{\pi}{8}} \frac{\text{Ma}}{\text{Kn}} \quad (3.8)$$

such that only two of these three dimensionless numbers need be treated as independent quantities.

3.2 Epstein drag

For supersonic free molecular flow, the case considered in Eq. (3.1), the coefficient is obviously $C_D^{(\text{Kn} \gg 1, \text{Ma} \gg 1)} = 2$. We will substitute the superscript “Kn $\gg 1$ ” by “Eps” hereafter. For very subsonic motion, the thermal velocities of the molecules are much greater than the drift velocity of the particles. The number n of molecules per unit volume colliding with the particles within an interval of speeds between v and $v + dv$ follows the Maxwell-Boltzmann distribution

$$n(v) d^3 u = n (\beta / \sqrt{\pi})^3 \exp \{-\beta^2 u^2\} d^3 u \quad (3.9)$$

where $u = |\Delta v|$ is the speed of the impinging molecules seen from the reference frame of the subsonic particle and $\beta = \sqrt{m_{\text{H}_2} / 2k_B T_g}$. In this equation, m_{H_2} is the mass of molecular hydrogen, k_B stands for the Boltzmann constant and T_g is the gas temperature. Upon integration, the rate of momentum transfer from the impinging molecules to the surface of a spherical particle is (Epstein 1924)

$$F_d^{\text{Eps}, \text{Ma} \ll 1} = -\frac{4\pi}{3} \rho v_{\text{th}} a_\bullet^2 \Delta v, \quad (3.10)$$

where $v_{\text{th}} = 2/\sqrt{\pi}\beta$ is the mean thermal speed. Substituting β yields

$$F_d^{\text{Eps}, \text{Ma} \ll 1} = -\frac{\sqrt{128\pi}}{3} \rho a_\bullet^2 c_s \Delta v, \quad (3.11)$$

where we already substituted $c_s = \sqrt{k_B T_g / m_{\text{H}_2}}$ for the isothermal sound speed. The coefficient C_D in this regime is therefore

$$C_D^{\text{Eps}, \text{Ma} \ll 1} = \frac{16\sqrt{2/\pi}}{3\text{Ma}} \quad (3.12)$$

The general coefficient for arbitrary Mach numbers was calculated by Baines et al. (1965)

$$C_D^{\text{Eps}} = \frac{2W^2 + 1}{W^3\sqrt{\pi}} e^{-W^2} + \frac{4W^4 + 4W^2 - 1}{2W^4} \text{erf}(W) + \frac{2\sqrt{\pi}(1 - \epsilon)}{3W} \sqrt{\frac{T_p}{T_g}} \quad (3.13)$$

where $W = |\Delta v|\beta = \text{Ma}/\sqrt{2}$, T_p is the temperature of the particle, erf denotes the Gauss error function

$$\text{erf}(x) = \frac{2}{\sqrt{\pi}} \int_0^x e^{-t^2} dt,$$

and ϵ is a factor that determines the importance of specular (mirror-like) to diffusive reflection of the gas molecules that hit the particle's surface (see e.g., Skorov & Rickman 1999). In practice, as this general coefficient is too cumbersome to implement numerically, a simple interpolation (Kwok 1975) is often used to connect the two regimes.

$$C_D^{\text{Eps}} \approx 2 \left(1 + \frac{128}{9\pi\text{Ma}^2} \right)^{1/2} \quad (3.14)$$

Figure 3.1a illustrates the behaviour of the interpolation compared to the exact solution for the case of pure specular reflection ($\epsilon=1$). The maximum deviation from the approximation of Kwok (1975) is at the percent level ($\approx 1.5\%$), meeting maximum deviation at $\text{Ma} \approx 2$.

3.3 Stokes drag

When the particle radius exceeds the mean free path of the particle, the approximation of ballistic collisions ceases to apply and the frequent intermolecular collisions lead to the emergence of viscous behaviour. It is a well known result that ideal fluids exert no drag (d'Alembert's paradox, e.g., Choudhuri 1998, §4.7). When the kinematic viscosity μ is considered, the Stokes drag law on a large ($\text{Kn} \ll 1$) sphere is recovered

$$F_d^{(\text{Kn} \ll 1, \text{Re} \ll 1)} = 6\pi\mu a \Delta v \quad (3.15)$$

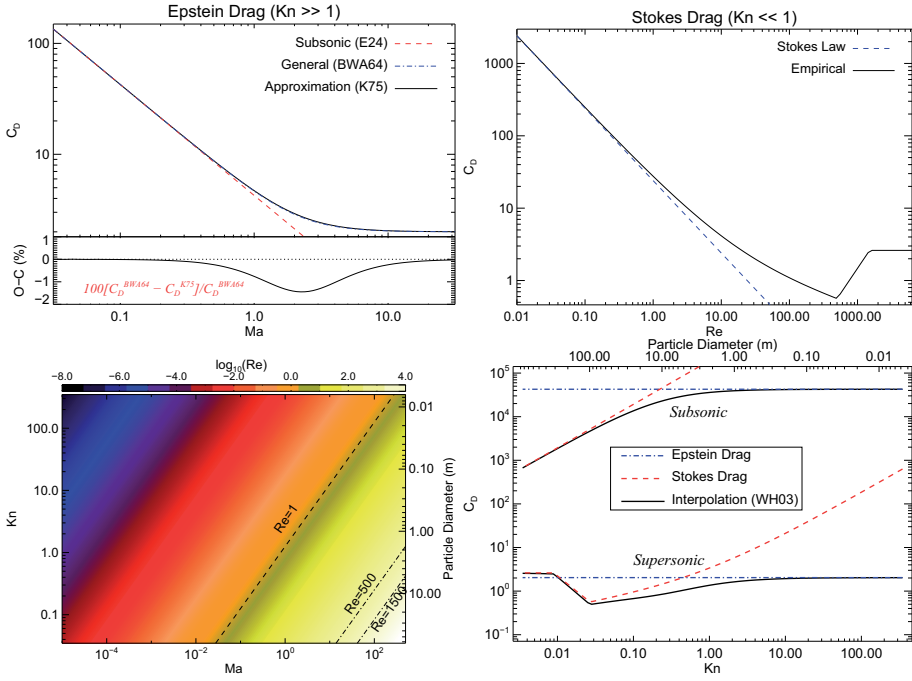


Figure 3.1: Upper panels. The dependence of the drag coefficients upon (a.) Mach number in the Epstein regime ($Kn \gg 1$) and (b.) the Reynolds number in the Stokes regime ($Kn \ll 1$). The subsonic Epstein law is valid until very close to the transition to supersonic. The viscous Stokes law only starts to deviate from the general case also at Reynolds numbers close to unity.

Lower panels. (c.) The corresponding Reynolds number in the plane of Mach and Knudsen numbers. We only expect deviations from the Stokes law at $Re \approx 1$. The transitions to turbulent drag only occur at very high Mach and very low Knudsen numbers (particle radii of the order of 10 meters). We do not expect them to play an important role in the models presented in this work.

(d.) The behaviour of the interpolated coefficient, for slices at subsonic and supersonic motion. The predictions of Epstein and Stokes drag are shown for comparison. For particles up to 10 centimeters, Epstein drag does not deviate much from the general (interpolated) coefficient. Pure Stokes drag starts to apply only beyond 10 meters.

a lengthy proof of which can be found in Landau & Lifshitz (1987, §20). Dividing Eq. (3.15) by the mass of the particle and expressing it in the form of Eq. (3.3), we have

$$C_D^{\text{Stk, Re} \ll 1} = \frac{12\mu}{a \cdot \rho |\Delta v|} = \frac{24}{Re} \quad (3.16)$$

where the superscript “Stk” replaced “Kn \ll 1”.

On obtaining this equation, the inertia of the fluid is neglected, so it only holds for low Reynolds numbers. Empirical corrections to the Stokes’ law were worked out (e.g., Arnold 1911, Millikan 1911, Millikan 1923), but a general case derived from first principles is much more difficult to obtain than in the case of free molecular flow. The major complication resides at the boundary layer immediately over the surface of the particle, where the velocity of the viscous fluid has to be zero. If the fluid has inertia, a sharp velocity gradient develops in the flow past the particle as the velocity goes to zero at the solid surface. At this boundary layer, the viscous term $\mu \nabla^2 v$ is important even at high Reynolds numbers (Prandtl 1905). It can be seen experimentally that in such cases, the flow past the particle develops into a turbulent wake (von Kármán 1905), with drag coefficients much larger than those predicted by Stokes law. Experiments reveal that the drag coefficient C_D at Stokes regime for different Reynolds numbers can be approximated as (Lain et al. 1999, Woitke & Helling 2003)

$$C_D^{\text{Stk}} = \begin{cases} 24\text{Re}^{-1} + 3.6\text{Re}^{-0.313} & ; \text{Re} \leq 500; \\ 9.5 \times 10^{-5} \text{Re}^{1.397} & ; 500 < \text{Re} \leq 1500; \\ 2.61 & ; \text{Re} > 1500. \end{cases} \quad (3.17)$$

Figure 3.1b shows its behaviour and the deviation of the inertia-neglecting viscous Stokes law (Eq. (3.15)). The fact that these coefficients are derived empirically instead of from first principles is disturbing at first, since the parameter space of the experiments might not bracket the values found in the solar nebula. However, we see from Fig. 3.1c that the range of Reynolds numbers where deviations from the Stokes law occur correspond to very high Mach numbers in the particle radius range we are interested in. In this regime the particle will suffer intense drag and be brought back to subsonic motion quite rapidly. Due to this high impulse, the exact formulation of the turbulent regime of low Knudsen numbers will not have major impacts on the results of the simulations. Indeed, most of the flow occurs at the regime of low Mach, low Reynolds, numbers, independently of the Knudsen number.

3.4 General case

As expressions for intermediate Knudsen numbers are not available, we use the interpolation expressions of Woitke & Helling (2003; see

also Paardekooper 2007)

$$C_D = \frac{\text{Kn}'^2 C_D^{\text{Eps}} + C_D^{\text{Stk}}}{(\text{Kn}' + 1)^2} \quad (3.18)$$

where $\text{Kn}' = 3\text{Kn}$ is the critical Knudsen number where Epstein and Stokes drag laws yield the same value for subsonic laminar motion. Figure 3.1d shows the behaviour of the interpolation. As stressed by Woitke & Helling (2003), at the critical Knudsen number, the true friction force yields smaller values than in both limiting cases.

3.5 Radial drift of solids in gaseous disks

It is seen from Eq. (2.15) that the gas orbits the star at sub-Keplerian speeds, due to the pressure gradient correction. Equation (2.15) can be written as

$$\begin{aligned} \Omega &= \Omega_K \left(1 + \frac{h^2}{\gamma} \frac{\partial \ln P}{\partial \ln r} \right)^{1/2} \\ &\approx \Omega_K (1 - \eta) \end{aligned} \quad (3.19)$$

where $\eta = -(h^2/2\gamma) \partial \ln P / \partial \ln r$ is a parameter often used to characterize the strength of the global pressure gradient (e.g., Nakagawa et al. 1986). It is positive for a negative radial pressure gradient and lies in the range $0 < \eta \ll 1$ (usually is between 0.001 and 0.1).

Solids, on the other hand, are pressureless, and orbit at Keplerian speeds. The difference is, of course, $\Delta v = v_K \eta \hat{\phi}$. That means that the solids will suffer gas drag, according to Eq. (3.5). The drag lowers the angular velocity of the particle, so that it loses centrifugal support and moves radially inwards. The radial velocity \dot{r} of this drift can be derived analytically. With vanishing gas radial velocity, the equations of motion for a particle in the midplane are

$$\ddot{r} - r\dot{\phi}^2 = -\Omega_K^2 r - \dot{r}/\tau_s \quad (3.20)$$

$$r\ddot{\phi} + 2\dot{r}\dot{\phi} = -(r\dot{\phi} - u_\phi)/\tau_s. \quad (3.21)$$

A steady or quasi-steady state solution implies $\ddot{r} \approx 0$. In addition, the gas velocity is $u_\phi = v_K(1 - \eta)$, according to Eq. (3.19). So,

$$r\dot{\phi}^2 = \Omega_K^2 r + \dot{r}/\tau_s \quad (3.22)$$

$$r\ddot{\phi} + 2\dot{r}\dot{\phi} = -r[\dot{\phi} - \Omega_K(1 - \eta)]/\tau_s. \quad (3.23)$$

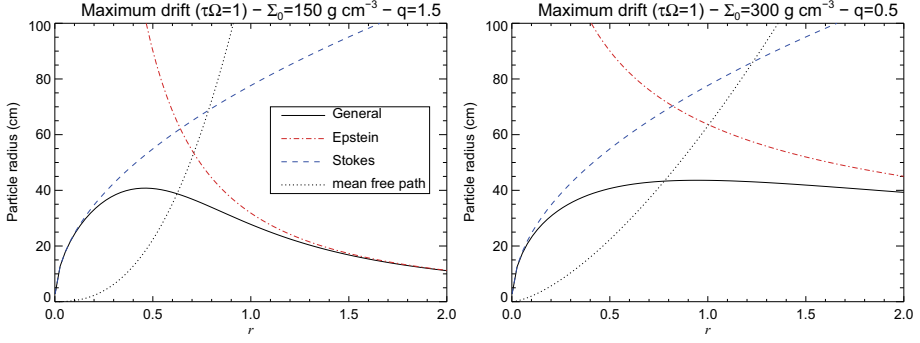


Figure 3.2: The radius of the particle subject to maximum drift ($\tau_s \Omega_K=1$) for our choice of parameters (right panel) and in the Minimum Mass Solar Nebula (Weidenschilling 1977b, left panel). $q=-\partial \ln \Sigma / \partial \ln r$ is the power law of the surface density profile. The profile is very flat compared to the ones predicted by the limiting cases of Epstein and Stokes drag, especially for our choice of parameters.

As the Keplerian motion is still dominant, we can write the particle angular velocity as $\dot{\phi} = \Omega_K + \delta\omega$, with $\Omega_K \gg \delta\omega$. It follows that

$$\dot{\phi}^2 \approx \Omega_K^2 (1 + \delta\omega/2\Omega_K),$$

as well as

$$\ddot{\phi} \approx \dot{\Omega}_K = -(3\Omega/2r)\dot{r}.$$

Plugging these two identities in Eq. (3.22)-Eq. (3.23), we have a system of equations for \dot{r} and $\delta\omega$. The first equation yields $\delta\omega = \dot{r}/(2t_s)$, where $t_s = \tau_s \Omega_K$ is the dimensionless stopping time. Plugging it into the second, the radial drift velocity is, to first order

$$\dot{r} = -\frac{2t_s \eta v_K}{(1 + t_s^2)}. \quad (3.24)$$

Equation (3.24) has a maximum at $t_s=1$, so the drift is fastest for loosely coupled particles whose stopping time τ_s is equal to the dynamical timescale Ω^{-1} . Figure 3.2 shows the size of particles of $\tau_s \Omega_K=1$ for two different disk models. The radius is normalized to 5.2 AU. The mean free path of the gas is also plotted for comparison. The particles of maximum drift have diameter of the order of 1 meter.

The timescale for the drift is $\tau_{\text{drift}} = r/|\dot{r}|$, which for $t_s=1$ amounts to $\tau_{\text{drift}} = (\eta \Omega_K)^{-1}$. For $\eta = 10^{-3}$, this timescale is

$$\tau_{\text{drift}} = 160 \left(\frac{r}{1 \text{ AU}} \right)^{3/2} \text{ yr}. \quad (3.25)$$

which leads to the disturbing realization, first seen by Weidenschilling (1977a) that once dust coagulates to this size, the particles are soon lost to the star. If planets are to form bottom-up, the jump to kilometer-size has to occur faster than this severely short timescale. Alternatively, some mechanism might occur in the disk that halts the radial drift of the meter-sized solids.

3.5.1 Pressure trapping

Equations (3.19) and (3.24) led to fast inward drift because the global pressure gradient is negative (positive η). If, however, the disk presents *local* pressure maximum, the local density peak has zero pressure gradient, constituting a point of equilibrium. It is straightforward to see that the equilibrium is stable for pressure maxima, and unstable for pressure minima. For pressure maxima, the pressure gradient is positive at radii immediately inner w.r.t. the maximum. The gas there rotates at super-Keplerian speeds and the negative η therefore turns \dot{r} positive: the particle migrates outwards, towards the pressure maximum. At the outer radii, the pressure gradient is negative, so the particle migrates inwards, also towards the pressure maximum. The opposite happens in pressure minima. As a direct result of Eq. (3.24), the particles for which the pressure trap is most efficient are those of stopping time $\tau_s \Omega_K = 1$.

Pressure maxima in disks can take a variety of forms. The next chapter deal with topics as varied as turbulence, dead zones, vortex formation and planet-disk interaction. There is however a unifying aspect behind these studies, namely, *they are ways of bringing about pressure maxima in protoplanetary disks*. If long lived, there particle-trapping structures may potentially keep the particles long enough for coagulation or gravitational instability to breach the meter-size barrier.

3.6 Gravitational Instability of the layer of solids

The Toomre criterion (Toomre 1963, Binney & Tremaine 1987) for thin gas disks states that the gas is gravitationally unstable if

$$Q \equiv \frac{c_s \kappa}{\pi G \Sigma_g} < 1 \quad (3.26)$$

where

$$\kappa^2 \equiv \frac{1}{r^3} \frac{dj^2}{dr} = 2\Omega^2 \left(2 + \frac{d \ln \Omega}{d \ln r} \right), \quad (3.27)$$

is the epicyclic frequency. In the above equation

$$j = \Omega r^2 \quad (3.28)$$

is the angular momentum per unit mass. Equation (3.26) means that a prospective collapsing mass is stabilized by shear (κ) and pressure (c_s), while destabilized, of course, by its gravity ($G\Sigma$). For the disks we model, $Q \approx 30$, so the stability of the gas is ensured. Solids, on the other hand, do not have pressure, and are more prone to gravitational instability. In the case of a pressureless turbulent fluid as the swarm of solids, the sound speed is replaced by the velocity dispersion $v_{p_{\text{rms}}}$ (Chavanis 2000)

$$\frac{v_{p_{\text{rms}}}\Omega}{\pi G\Sigma_p} < 1. \quad (3.29)$$

Once this condition is met, the gravitational potential energy overcomes the kinetic energy of the solids, and collapse ensues.

In this work we did not model coagulation. Instead, we assume that it efficiently formed centimeter and meter sized solids. We then follow the motion of these bodies and investigate possible gravitational instability inside particle trapping structures. The validity of neglecting coagulation is corroborated by the fact that in the proposed mechanism we put forth, gravitational growth is seen to occur at least one order of magnitude faster than the timescale for coagulation (≈ 1000 yr; Blum & Wurm 2008). There is, however, the possibility that the same trapping mechanism that favours gravitational instability might also speed up coagulation, growing the solids beyond the size $\tau_s\Omega_K \approx 1$ for which the particle trapping mechanism works best. Of course, this is not a drawback, since it would mean that the mechanism we present in paper II and paper III are planetesimal (instead of planet) factories. The planetesimals would then decouple from the gas and get scattered through the disk, where they could be used to form planets by the traditional gravitational focusing mechanism. A definite answer to this question has to be addressed by a simulation that includes both coagulation and gravity.

4. Magnetic Turbulence in Accretion Disks

*Big whirls have little whirls
that feed on their velocity
and little whirls have lesser whirls
and so on to viscosity*

Lewis F. Richardson
on the Kolmogorov cascade theory of isotropic turbulence.

We highlighted in Chapter 1 the need for turbulence in order to provide the necessary viscosity for accretion. Purely laminar Keplerian disks, however, cannot go turbulent. For it to occur, a particle displaced from its orbit must tend to be even further displaced, by some instability. Mathematically, the above statement means that (in the absence of pressure) the epicyclic frequency (Eq. (3.27)) must go imaginary. The condition of $\kappa^2 < 0$ only occurs for

$$\frac{d \ln \Omega}{d \ln r} \leq -2.$$

Such statement is known as the *Rayleigh criterion*. Another mechanism must come to play to trigger an instability.

Since the seventies, many possible ways to set the disk into a turbulent state were proposed, but only the magnetorotational instability seems robust and strong enough to explain the observed accretion rates in low mass disk. Gravitational turbulence may be important in the early stages of the disk, when it is still massive. We will not concern ourselves with this stage, but notice that the accretion rates then are as high or even higher than those achieved by the MRI ($\alpha=5 \times 10^{-2}$; Lodato & Rice 2005).

4.1 The Magneto-Rotational Instability

Shakura & Sunyaev (1973), in the seminal paper that set forth the principles of what became the standard theory of accretion disks, suggest that magnetic fields could lead to turbulence. The educated guess could not be more correct.

The effect of magnetic fields on flows past rotating cylinders (Couette flow) had already been studied by Velikhov (1959) and Chandrasekhar (1960, 1961). They found that it lead to an instability, but did not apply the result to an astrophysical situation. The instability was re-discovered by Steve Balbus and John Hawley (Balbus & Hawley, 1991,1992,1998; Hawley & Balbus, 1991,1992), who showed that it was operative in accretion disks, leading to the long-sought turbulence.

What triggers the instability can be intuitively understood. A magnetic field line has tension if bent. A disturbance in the field will therefore tend to restore the field to its initial position. A parcel of gas displaced of its original position will be thuged back. That is, it *resists stretching*. Another effect arises when in a differentially rotating disk. Produce a radial disturbance in the field, and two parcels initially at the same radial position will be displaced radially along with the field. However, they will be still connected by the tensed line: the magnetic field *resists shear*, trying to enforce rigid rotation.

The first is clearly a restoring force. The second is the heart of the instability. Because the field tries to enforce rigid rotation, the parcel of gas displaced inwards keeps its original velocity. For its new orbital position, it is rotating too slow and therefore loses centrifugal balance, spiraling further inwards. The parcel of gas displaced outwards likewise keeps its original velocity. It will be rotating too fast for its new radius, and therefore the centrifugal force pushes it further outwards. A little displacement leads to more displacement. The situation is unstable.

Quoting the original paper announcing the “powerful local shear instability” (Balbus & Hawley, 1991)

The Rayleigh instability criterion of a negative radial gradient in specific angular momentum is largely irrelevant to gaseous astrophysical disks if magnetic fields are present.

Instead, the combination of differential rotation in the form of a negative angular velocity radial gradient with almost any small seed field will lead to dynamical instability.

A illustration of the process is seen in fig. 4.1. This magneto-rotational instability is operative as long as stretching provided by the shear overcomes the restoring effect of the magnetic tension. It can be

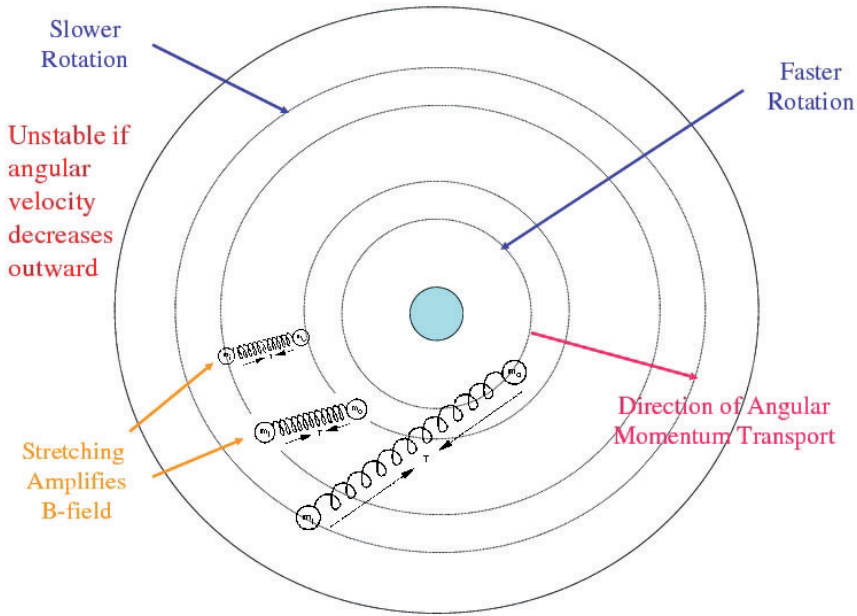


Figure 4.1: Illustration of how the magneto-rotational instability arises. A magnetic field line has tension and therefore can be thought of as a spring, connecting two gas parcels. Displace two gas parcels radially, and the field that connects them will tense, trying to enforce rigid rotation. Due to the presence of shear, the parcel now located in the inner orbit rotates too slow for its new radial position and therefore loses centrifugal support, sinking further inwards. The outer gas parcel also kept its original velocity due to the tension of field, and is rotating too fast for its new, outer, orbits. It gains centrifugal support and moves further outwards. Angular momentum is transported outwards and matter accretes.

shown that this is equal to requiring a subthermal field. This can be seen intuitively: a strong field offers too much tension. Displace the field lines and the two parcels of gas are so strongly connected that the centrifugal force cannot displace them further apart. The restoring force then takes care of leading them back to their stable positions.

4.1.1 From turbulent stresses to laminar alpha viscosity

The similarities between the properties of turbulent magnetohydrodynamic disks and those of viscous accretion disks can be seen explicitly

by writing the Navier-Stokes and the Reynolds equation in terms of angular momentum $L = s\rho u_\phi$. We do so by substituting the continuity equation in the azimuthal momentum equation, and assuming axial symmetry ($\frac{\partial}{\partial\theta} = 0$)

$$\frac{\partial L}{\partial t} + \frac{1}{s} \frac{\partial}{\partial s} (sLu_s) = \frac{1}{s} \frac{\partial}{\partial s} \left(\nu L \frac{d \ln \Omega}{d \ln s} \right) \quad (4.1)$$

$$\frac{\partial \bar{L}}{\partial t} + \frac{1}{s} \frac{\partial}{\partial s} (s\bar{L}\bar{u}_s) = -\frac{1}{s} \frac{\partial}{\partial s} \left(s^2 \overline{\rho \delta u_\phi \delta u_s} \right), \quad (4.2)$$

in which we identify the R.H.S. as the flow of momentum, i.e., the divergence of the Reynolds stress tensor.

By comparing Eq. (4.1) and Eq. (4.2), we identify

$$\nu = - \left(\frac{d \ln \Omega}{d \ln s} \right)^{-1} \frac{R^{\phi s}}{\rho \Omega} \quad (4.3)$$

Using the alpha-parametrization of Shakura & Sunyaev (1973) and recalling that $c_s = \Omega H$

$$\alpha^{(R)} = \frac{2}{3} \frac{R^{\phi s}}{\rho c_s^2}, \quad (4.4)$$

where we used $\Omega \alpha s^{-3/2}$ for a Keplerian disk. The superscript R denotes that this is a kinetic (Reynolds) alpha.

By introducing the Lorentz force in terms of the Maxwell stress in the equation of motion

$$[(\nabla \times \mathbf{B}) \times \mathbf{B}]_\phi = \frac{\partial}{\partial x_j} \left(\frac{B^2}{2} \delta_{\phi j} - B_\phi B_j \right) = \mu_0 \frac{\partial M^{\phi j}}{\partial x_j}, \quad (4.5)$$

and following the same lines, one arrives at the magnetic (Maxwell) alpha

$$\alpha^{(M)} = -\frac{2}{3} \frac{M^{\phi s}}{\rho c_s^2}. \quad (4.6)$$

We notice that the factor $2/3$ is often omitted in the literature, thus one should be careful when comparing results of different works.

4.1.2 Dispersion relation

The axisymmetric dispersion relation of the MRI for the limiting case of incompressibility can be worked out by considering waves of the form

$$\psi = \exp(k_s s + k_z z - \omega t),$$

which for the equations of motions can be solved in Fourier space to yield (Balbus & Hawley 1991)

$$\frac{k^2}{k_z^2} \omega^4 - \kappa^2 \tilde{\omega}^2 - 4\Omega^2 (\mathbf{k} \cdot \mathbf{v}_A)^2 = 0 \quad (4.7)$$

where $k^2 = k_s^2 + k_z^2$, κ is the epicyclic frequency and

$$\tilde{\omega}^2 = \omega^2 - (\mathbf{k} \cdot \mathbf{v}_A)^2 \quad (4.8)$$

Note that the field just enters the dispersion relation multiplied by the wavenumber k . Thus, even weak fields can lead to significant magnetic tension at small wavelengths. It is therefore useful to define a wavenumber parameter

$$q = \mathbf{k} \cdot \mathbf{v}_A / \Omega \quad (4.9)$$

Using this substitution and solving the quadratic equation for $\tilde{\omega}^2 / \Omega^2$, we find

$$\frac{\omega^2}{\Omega^2} = q^2 \left[1 - \frac{8}{\kappa^2 / \Omega^2 + \sqrt{\kappa^4 / \Omega^4 + 16q^2}} \right], \quad (4.10)$$

which, for a Keplerian disk reduces to

$$\frac{\omega^2}{\Omega^2} = q^2 \left[1 - \frac{8}{1 + \sqrt{1 + 16q^2}} \right] \quad (4.11)$$

since $\kappa = \Omega$. The condition for instability in this approximation is therefore having the second term in the right hand side bigger than one. This is satisfied for all $q^2 < 3$. Therefore, the unstable wavenumbers of the MRI are

$$0 < \mathbf{k} \cdot \mathbf{v}_A / \Omega < \sqrt{3} \quad (4.12)$$

The maximum growth rate occurs around $q=1$. We will refer to this fastest growing wavelength as λ_{MRI}

$$\lambda_{\text{MRI}} = 2\pi v_A \Omega^{-1} \quad (4.13)$$

For λ_{MRI} , the growth rate is 0.75Ω . This corresponds to a *million-fold amplification in 3 orbits*. The magneto-rotational is a powerful instability. The non-linear evolution in the shearing sheet (Hawley & Balbus 1991) confirms this behavior.

4.2 The MRI in global models

In the papers that comprise this Thesis, we performed simulations of protoplanetary disks encompassing a large domain in radius. These models are referred to as *global disks*. The distinction is needed because some works solve the equations in the shearing sheet approximation (e.g., Goldreich and Tremaine 1978, Brandenburg et al. 1995), where the flow is solved in a tiny Cartesian box that co-rotates with the disk at a fixed distance from the central star. The shearing box has the advantages of being closer to the dissipation scale and of keeping the computational costs to a minimum as, for instance, periodic boundary conditions can be used for the azimuthal and vertical direction (whilst the radial direction resorts to shear-periodic boundary conditions). Nonetheless, they fail to convey the full perspective of the problem, that just a global disk can yield. Yet, global disk have more elevated computational costs, since many scale lengths are present in the same simulation. A local box of size $\pm H$, for instance, comprises ≈ 10 cells of the typical resolution used in global calculations.

Modelling the MRI in global disks poses extra numerical constraints when compared to shearing boxes. The field needs to be subthermal, which means weak. Due to this, the wavelengths of the turbulence are very short, and the maximum growing wavelength is usually not resolved unless the resolution is pushed to its limits. Raising the field strength is not an option, since we cannot raise to equipartition energies, lest the instability is quenched. The fiducial simulation of paper I used a constant vertical field of 20 G and resolution 0.1 AU. For the typical densities of the solar nebula ($2 \times 10^{-11} \text{gcm}^{-3}$ at 5.2 AU), the resulting λ_{MRI} is ≈ 0.05 AU, i.e., half the grid resolution. The lack of sufficient resolution affects the numerical results: while in a shearing box the turbulence saturates in about 3 orbits, a global disk takes at least 20, and sometimes even 50 or more, as the resolved unstable wavelengths are growing much slower than the fastest growing mode.

In paper I we used several combinations of fields and sound speeds in order to study the MRI in global frames. An interesting outcome of this sound speed study was the realization that the dimensionless alpha parameter does not seem to scale with temperature as one would expect. The stresses rise obeying a power law of 0.25, while the pressure, obeying ρc_s^2 , grows much faster. The result is that alpha decreases with temperature. In paper I we also studied how solids are trapped in the overdensities generated by the turbulence, which we briefly describe below.

4.2.1 Solids trapped in turbulence

As discussed before, solid particles on Keplerian orbits experience a headwind of the sub-Keplerian gas, causing the particles to migrate inwards in a laminar disk. When turbulence is introduced, transient pressure minima and maxima occur everywhere in the disk, and long lived pressure maxima act as traps where solids get heavily concentrated.

It is possible that this particle trap mechanism lead to local enhancements of the solids-to-gas ratio that are large enough to produce gravitational instabilities in the solid phase, forming gravitationally bound objects. We studied this possibility in paper I, by including particles in late stages of our turbulent models.

Such a study has already been carried out in local box models (Johansen et al. 2007) and in gravitationally unstable global disks by SPH simulations (Lodato & Rice, 2004). Fromang & Nelson (2005) performed a study with a few thousand particles in order to understand how they should get trapped in the vorticity minima generated by the MRI. However, for the paper I a large number of particles was studied in an MRI-active global disk. We usually include 10^6 particles, which allows us to trace the swarm back onto the grid as a density field without using fluid approaches. By doing this, we could also measure other effects of the turbulence on the solid phase, such as the appearance of an effective diffusion.

As discussed by Johansen & Klahr (2005), while solid particles are pulled towards the midplane by the stellar gravity, turbulent motions stir them up again. A sedimentary layer in equilibrium between turbulent diffusion and gravitational settling is formed. The thickness of this layer is therefore a measurement of the turbulent diffusion acting on the solid particles.

Under the influence of gravity, the solids settle with a profile similar to the one generated by a pressure force (Dubrulle et al. 1995)

$$\ln \rho_p = \ln \rho_p(s, z = 0) - \frac{z^2}{2H_p^2}, \quad (4.14)$$

By comparing this profile with the analytical expression for a pressureless fluid under diffusion, gas drag and vertical gravity (Johansen & Klahr, 2005)

$$\ln \rho_p = \ln \rho_p(s, z = 0) - \frac{\tau_f}{D_z^{(t)}} \int g_z dz, \quad (4.15)$$

and recalling that $g_z = -\Omega^2 z$, we have

$$D_z^{(t)} = \Omega^2 H_p^2 \tau_f \quad (4.16)$$

From Eq. (4.14), we see that the scale height of the solids is the vertical distance in which the bulk density falls by a factor $1/\sqrt{e} \approx 0.6$ relative to the value at midplane. In paper I we measured the diffusion coefficient of particles due to the turbulence, according to Eq. (??), finding diffusion coefficients of approximately same strength of the turbulent viscosity that acts on the gas phase.

In terms of the Schmidt number, i.e., the ratio of turbulent viscosity to turbulent diffusion

$$\text{Sc} = \frac{\nu^{(t)}}{D^{(t)}} \quad (4.17)$$

the particle scale height can be written as

$$H_p = H \sqrt{\frac{\alpha}{\text{Sc} t_s}} \quad (4.18)$$

where we substituted $\nu^{(t)} = \alpha \Omega H^2$. For $\text{Sc} \approx 1$, $t_s = 1$, and typical α values of 10^{-2} , Eq. (4.18) leads to a particle scale height ten times smaller than the gas scale height. This validates the use, in paper I, of cylindrical disks where the gas is not vertically stratified.

4.3 Origin of the field

Observations of circularly polarized lines in the disk of FU Ori (Donati et al. 2005), indicating fields of 1 kG in the inner regions, supports an

accretion mechanism mediated by magnetic fields. However, the origin of the field is still a matter of debate. It could be the “fossil” field of the original nebula, the stellar magnetic field, or a field generated by the MRI-driven disk dynamo itself. All these possibilities have problems.

The magnetic field of the proto-stellar magnetosphere falls too fast with radius ($1/r^3$) to be of any significance at large radii. Any external field that tries to enter the disk will reconnect at the outer boundary. The existence of a self-sustained disk dynamo remains a matter of debate. The theory predicts that in absence of resistivity, the instability will increase the coherence length of any small seed magnetic field, and grow its mean strength to a significant fraction of the equipartition value. This is because, as noted before, the field only enters the dispersion relation (Eq. (4.8)) multiplied by k , so that even weak fields generate enough tension at large wavenumbers.

Numerical simulations have had mixed success in finding supporting evidence for this behaviour. If the seed field has zero net flux, it is shown that the resulting stresses depend on numerical resolution (Pessah et al. 2007, Fromang & Papaloizou 2007), with no convergence in sight. When resistive effects are included, the effectiveness of the dynamo depend in a critical way on the value of the magnetic Prandtl number, $Pr = \nu/\eta$ (Fromang et al. 2007). For $Pr \ll 1$, as expected in accretion disks, the small scale dynamo fails.

A structured field with non-zero net flux, on the other hand, leads to a large scale dynamo with vigorous stresses, whose resulting values depend on the coherence length of the large scale field λ_{MRI} (Pessah et al. 2007). For this reason, in paper I we used imposed vertical or azimuthal initial fields to trigger the growth of the MRI, and remain agnostic in respect to their origin.

5. The magnetically dead zone and the Rossby wave instability

In this house, we OBEY the laws of thermodynamics.

Homer J. Simpson, cartoon character,
setting an example for all disk theorists.

For the MRI to operate, there are three requirements. The presence of subthermal magnetic fields, shear, and sufficient ionization to provide coupling between the gas and the magnetic field. While magnetic fields are ubiquitous and the Keplerian profile provides the shear, the third condition is not always met. As T-Tauri disks are cold and dense (≈ 100 K and 10^{-11} g cm $^{-3}$ at 5.2 AU), recombination is rapid, and the number of free electrons is therefore small. As a result, the disk is not ionized throughout, and there should exist regions where the coupling to the ambient field is too weak for the instability to operate. These regions will be “dead” to the MRI. In this chapter we briefly review some of the physics and relevant consequences of the presence a magnetically dead zone in accretion disks.

5.1 The nature of resistivity

Currents are driven by the most mobile charge carriers, the electrons. Resistivity therefore arises from impediments to the electron movement. In the case of a weakly ionized gas, the most probable collision an electron would suffer is with a neutral. The electron having speed v_e and the neutral having speed v_n , the momentum of the electron fluid is dropped by $\Delta p_e = -m_e(v_e - v_n)$ at each electron-neutral encounter. We can define an average time between collisions τ_R so that this mo-

mentum transfer amounts to a collisional drag in a form identical to Eq. (3.5)

$$f_R = -\frac{1}{\tau_R}(v_e - v_n). \quad (5.1)$$

The subscript “ R ” denotes “resistive”. Equation (5.1) is usually written in terms of an average *frequency* of collisions instead of time between collisions (Spitzer 1962, Phelps 1979, Draine 1983, Blaes & Balbus 1994). This frequency being $\nu_R = \tau_R^{-1}$, the above equation is then

$$f_R = -\nu_R(v_e - v_n). \quad (5.2)$$

The resistivity is found from its definition, the inverse of conductivity ($\eta=1/\sigma$), which in turn is defined as the proportionality factor between the current and the force per unit charge that produced it (Ohm’s law)

$$J \equiv \sigma F/e, \quad (5.3)$$

where the force F is of course $m_e f_R$, where m_e is the electron mass. The current density is defined as

$$J \equiv -n_e e v_e \quad (5.4)$$

where n_e is the electron number density. In Eq. (5.3) and Eq. (5.4), e is the electron charge. Equating both and assuming that $v_e \gg v_n$, we have

$$\eta = \frac{m_e \nu_R}{n_e e^2} \quad (5.5)$$

The term ν_R can be estimated the following way. An electron of velocity v in a time interval dt sweeps a volume $dV = \pi r_0^2 v dt$, where πr_0^2 is the electron cross section. If it collides with all the neutrals within this volume, the number of collisions is simply $N=n_n dV$, where n_n is the number density of neutrals (mostly H_2 molecules) . The frequency of collisions is thus

$$\nu_R = \frac{N}{dt} = \pi r_0^2 C_R n_n v, \quad (5.6)$$

where C_R , like the coefficient C_D in the treatment of gas drag, takes into account the deviations from this idealized picture. For thermal speeds, the situation is similar to that of subsonic Epstein drag (Eq.

(3.11)). The impinging neutrals follow a Maxwellian distribution and the integration yields (cf. Phelps 1979)

$$v_R = 10^{-15} n_n \left(\frac{128kT}{9\pi m_e} \right)^{1/2} \simeq 8.3 \times 10^{-10} n_n T^{1/2} \text{ s}^{-1}. \quad (5.7)$$

Combining it with Eq. (5.5) and substituting the electron mass and electron charge, we find the resistivity in terms of the electron fraction $x = n_e/n_n$

$$\eta \simeq 295x^{-1} T^{1/2} \text{ cm}^2 \text{ s}^{-1}. \quad (5.8)$$

5.2 Suppression of the MRI

The condition for the suppression of the MRI follows directly from the magnetic Reynolds number. Considering the induction equation, the amplification of magnetic stresses due to the MRI occurs through the electromotive term $\mathbf{u} \times \mathbf{B}$, while the resistive term $\eta \nabla \times \mathbf{B}$ yields a damping that opposes the amplification. The ratio of the two terms is the magnetic Reynolds number, of dimension $\text{Re}_M = UL/\eta$. At any length scale L the instability will be suppressed if this quantity falls below unity. The velocity associated with magnetic fields is the Alfvén velocity, and the length of interest is the scale height H , so the condition for the operation of the MRI in the presence of resistivity is

$$\text{Re}_M = \frac{v_A H}{\eta} \gtrsim 1. \quad (5.9)$$

To express this quantity in terms of non-magnetic parameters, we relate the Alfvén speed with the sound speed the following way. The Alfvén speed can be approximated via the Maxwell stress

$$M^{r\phi} \simeq \rho v_A^2,$$

which in turn, from the definition of the alpha viscosity $T^{r\phi} \equiv \alpha \rho c_s^2$, leads to

$$v_A \simeq c_s \sqrt{\alpha},$$

assuming that the Maxwell component dominates the stress tensor (i.e. $T^{r\phi} \approx M^{r\phi}$). We can therefore use the relations in Appendix D to write the magnetic Reynolds number as

$$\begin{aligned} \text{Re}_M &\simeq \frac{\alpha^{1/2} c_s H}{\eta} \\ &\simeq 2 \times 10^{13} x \alpha^{1/2} \left(\frac{r}{1 \text{ AU}} \right)^{3/2} \left(\frac{T}{500 \text{ K}} \right)^{1/2} \left(\frac{2}{\mu} \right), \end{aligned} \quad (5.10)$$

where μ is the mean molecular weight. Assuming that all terms in parenthesis (as well as $\alpha^{1/2}$) are near unity, the magnetic field will be well coupled to the gas when

$$x \gtrsim 10^{-13}, \quad (5.11)$$

give or take one order of magnitude.

5.2.1 The dead zone

The threshold value of ionization fraction $x = 10^{-13}$ seems very low, yet it is not met in many parts of the disk. We briefly mention below the main sources of ionization to define the regions that should be coupled to the magnetic field.

5.2.1.1 Collisions

Calculations by Umebayashi (1983) reveal an almost exponential increase of x with temperature, with x equalling 10^{-13} at 900 K, due mainly to collisional ionization of the alkali metals. As the other quantities vary weakly with temperature, Gammie (1996) concludes that $T > 10^3 \text{ K}$ is an acceptable approximation for the condition of coupling. This temperature corresponds to a distance of 0.5 AU for a temperature profile of $T=T_0/r$ and $T_0=100 \text{ K}$ at 5.2 AU.

5.2.1.2 Cosmic rays

Beyond the distance where the temperature drops below 1000 K, non-thermal ionization processes dominate. The main source of this ionization are cosmic rays, which impact the disk providing an ionization rate of $\zeta=10^{-17} \text{ s}^{-1}$, penetrating the disk up to a stopping depth of

$$\Sigma_{\text{CR}} \approx 96 \text{ g cm}^{-2}$$

(Umebayashi & Nakano 1981). The disk therefore shall display a layered structure, with a laminar, resistive, MRI-dead zone region around the midplane, sandwiched by MRI-active conductive layers. At greater distances where the column density drops below Σ_{CR} , throughout ionization resumes.

5.2.1.3 UV and X-rays

Glassgold et al. (1997) and Igea & Glassgold (1999) cast doubt on the effectiveness of ionization by galactic cosmic rays since they could be deflected by the stellar wind. UV and X-ray photons therefore become the main ionization source in this case. These are emitted by the protostar, at a rate of $L_X=10^{-3}L_\odot$. The penetration depth, however, is much lower than in the case of cosmic rays, with

$$\Sigma_{\text{UV}} \approx 10^{-3} \text{ g cm}^{-2}$$

and

$$\Sigma_X \approx 10 \text{ g cm}^{-2}$$

(Igea & Glassgold 1999). Ilgner & Nelson (2006) further proposed that during flares, when the X-ray luminosity is raised by 2 orders of magnitude relative to the quiescent level (and more hard X-rays are emitted), the dead zone can be completely suppressed. However, the MRI does not resume since its growth takes longer than the duration of the flare.

5.2.1.4 Radioactive decay of ^{26}Al

In the inner regions beyond the reach of cosmic rays or X-rays, there is yet another source of ionization, namely, the decay of radioactive nuclides. An exhaustive list of these processes is presented by Umebayashi & Nakano (2009). Long-lived nuclides yield an ionization rate of $1.4 \times 10^{-22} \text{ s}^{-1}$, mainly (80%) due to decay of ^{40}K . Heavy nuclides ^{232}Th , ^{235}U and ^{238}U contribute to the remaining 20%. The strongest ionizing sources among nuclides is found to be the short-lived ^{26}Al (now extinct in the solar system), with an ionization rate of $7 - 10 \times 10^{-19} \text{ s}^{-1}$. The next strongest ionizing sources among short-lived nuclides, ^{60}Fe and ^{36}Cl , are 10 times less strong than ^{26}Al . The presence of ^{26}Al in the early solar system is corroborated by studies of meteorites that indicate a large overabundance of ^{26}Mg , the daughter nuclide of ^{26}Al (MacPherson et al. 1995).

This extra source of ionization leads to some coupling in the dead zone, that therefore would show some level of activity, not being completely dead, but only quiet (some authors prefer the term “undead zone”). However, Turner and Sano (2008) show that the free electrons given out by this low ionization source would quickly recombine on the surface of μm -sized dust grains.

5.3 Accretion onto and through the dead zone

If no transport happens in the dead zone, matter can do little more than piling up there as the inflow proceeds from the active layers. However, the accumulation of matter cannot proceed indefinitely since, as matter piles up, the conditions for gravitational instability would eventually be met (Armitage et al. 2001). The gravitational turbulence that ensues (Lodato 2008) would therefore empty the dead zone as the excess matter accretes, thus re-starting the cycle.

However, local simulations show that the dead zone has some level of turbulence even in the absence of local ^{26}Al ionization. This happens because the turbulence on the active layers induce small levels of Reynolds stress in the dead zone (Fleming & Stone 2003). If the inertia of the midplane layer is not too high (Oishi et al. 2007), this forced turbulence can lead to moderate α values with non-negligible transport. Terquem (2008) shows that steady state solutions in 1D models exist in this case, as the dead zone gets denser and hotter to match the condition $\partial_r(\nu\Sigma)=0$ (Fig. 5.1). In this case, the steady state will have an α_T viscosity value in the active layers and a lower α_D in the dead zone. Várniere & Tagger (2006) studied the flow in the midplane in such conditions, with a dead zone represented by the viscosity profile

$$v = v_T - \left(\frac{v_T - v_D}{2}\right) \left[\tanh\left(\frac{r - r_1}{\Delta r}\right) - \tanh\left(\frac{r - r_2}{\Delta r}\right) \right] \quad (5.12)$$

where r_1 and r_2 are the locations of the borders of the dead zone and Δr is the width of the viscosity jump. This is the profile we used in papers II and III.

We point that, in such steady-state dead zone, there is the possibility that the some other physical process is excited before Q approaches 1, or that the 1D steady profile is unstable to some 2D or 3D instability. We show in the next section that this is indeed the case, and the dead zone is likely to be unstable to the Rossby wave instability.

5.4 The Rossby wave instability

In the absence of pressure forces, an element of the disk displaced from its orbit will execute oscillations around its stable position at the epicyclic frequency κ . In such approximation, the Rayleigh criterion suffices to determine stability. As the angular momentum $j = r^2\Omega$ in-

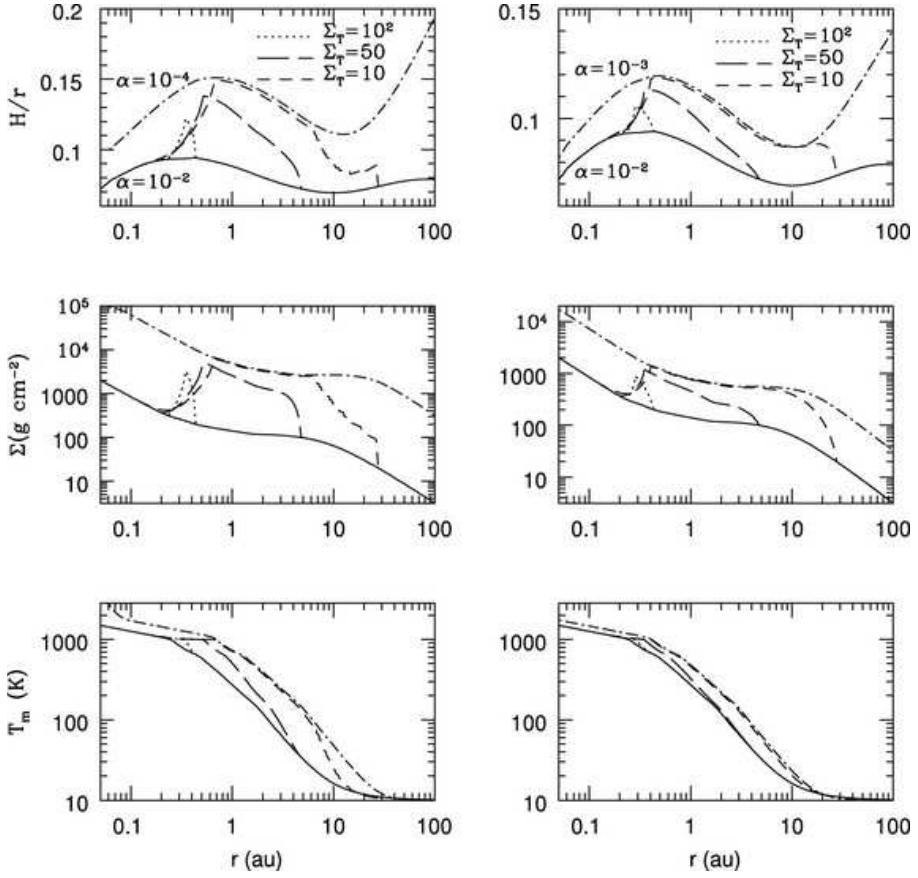


Figure 5.1: Plots of the aspect ratio, density, and midplane temperature in the steady-state dead zone model of Terquem (2008). The mass accretion rate was $\dot{m}=10^{-8} M_{\odot} \text{ yr}^{-1}$. The left hand side plots correspond to $\alpha_T = 10^{-2}$ and $\alpha_D = 10^{-4}$, whereas the right hand side plots use a dead zone alpha viscosity $\alpha_D = 10^{-3}$. The dotted, long-dashed, and short-dashed curves correspond to disk models with different penetration depths $\Sigma_T=100, 50$ and 10 g cm^{-2} , respectively. In the dead zone, the disk is thicker, more massive and hotter. The solids and dot-dashed curves correspond to standard disk models with constant $\alpha=\alpha_T$ and $\alpha=\alpha_D$. These steady-state dead zone profiles, particularly the ones with $\Sigma_T=100$ show pressure bumps that are unstable to the Rossby wave instability, and are therefore prone to develop anticyclonic vortices. Reproduced from Terquem (2008).

creases outwards, such disk is always stable. In the presence of pressure forces, this criterion is replaced by the Solberg-Høiland criterion,

$$\kappa^2 + N^2 \geq 0 \quad (5.13)$$

where

$$N^2 \equiv \frac{1}{\Sigma} \frac{dP}{dr} \left(\frac{1}{\Sigma} \frac{d\Sigma}{dr} - \frac{1}{\gamma P} \frac{dP}{dr} \right) \quad (5.14)$$

is the square of the Brunt-Väisälä frequency, the frequency of oscillation of buoyant structures. Equation (5.13) means that radial modes that are stable/unstable to shear can be destabilized/stabilized by pressure, and vice-versa.

In the context of pressure disturbances, Lovelace et al. (1999) and Li et al. (2000) find yet another instability, related not to radial, but to azimuthal perturbations. The instability exists when the following quantity has a local extremum

$$\mathcal{L}(r) \equiv \mathcal{F}(r) (P\Sigma^{-\gamma})^{2/\gamma}. \quad (5.15)$$

The quantity \mathcal{F} is defined as

$$\mathcal{F} \equiv \frac{\Sigma\Omega}{\kappa^2 - \Delta\omega^2 - c_s^2/(L_s L_p)} \quad (5.16)$$

where

$$L_s \equiv \gamma / \left[\frac{d}{dr} \ln(P\Sigma^{-\gamma}) \right] \quad (5.17)$$

$$L_p \equiv \gamma / \left[\frac{d}{dr} \ln P \right] \quad (5.18)$$

are the radial length scale of the entropy and density variations, respectively. For corotational modes ($\Delta\omega \equiv \omega - m\Omega \ll \kappa$) in a barotropic ($L_s \rightarrow \infty$) disk, the quantity \mathcal{F} reduces to $\Sigma\Omega\kappa^{-2}$, which is readily identified with (half) the inverse of vortensity ζ

$$\zeta = \omega_z / \Sigma \quad (5.19)$$

$$\begin{aligned} \omega_z &= |\nabla \times \mathbf{u}|_z \\ &= \frac{1}{r} \frac{\partial}{\partial r} (r^2 \Omega) = \frac{\kappa^2}{2\Omega}, \end{aligned} \quad (5.20)$$

which in turn led Lovelace et al. (1999) to interpret \mathcal{L} as an entropy-modified version of, or generalized, potential vorticity. An extremum in the profile of \mathcal{L} can be generated, for example, by a pressure bump somewhere in the disk. The dispersion relation of the disturbances is analogous to the dispersion relation of Rossby waves in planetary atmospheres, hence the name of the instability.

Since in planetary atmospheres the Rossby waves are known to give rise to Rossby vortices like Jupiter's Great Red Spot, Lovelace et al. (1999) speculate that the non-linear saturated state of the RWI might be the generation of vortices after the Rossby waves break and coalesce. This was indeed confirmed by Li et al. (2001) by numerical simulations.

5.5 Vortices

Vortices are equilibrium solutions to the compressible Euler equation (with barotropic equation of state), characterized as flows with closed elliptic streamlines. When dealing with vortices and vortex excitation, it is convenient to think in terms of the vorticity equation, obtained by taking the curl of the momentum equation

$$\frac{D\boldsymbol{\omega}}{Dt} = (\boldsymbol{\omega} \cdot \nabla)\mathbf{u} - \boldsymbol{\omega}(\nabla \cdot \mathbf{u}) + \frac{1}{\rho^2} \nabla\rho \times \nabla p + \nu \nabla^2 \boldsymbol{\omega}. \quad (5.21)$$

In the above equation, the first term yields stretching of the vortex lines by velocity gradients, the second arises from compression, and the third is the baroclinic term. The last term accounts for viscous dissipation. It is readily seen that for a flat 2D vortex, where $\boldsymbol{\omega} = \omega \hat{z}$ and $u_z = 0$, the first term vanishes. In the incompressible case, $\nabla \cdot \mathbf{u} = 0$ and the second term vanishes too. If the flow is barotropic, $\nabla\rho$ and ∇p are parallel and the third term also vanishes. Incompressible barotropic 2D flows thus conserve vorticity in the inviscid range.

The condition of incompressibility is not mandatory, since by mathematical construction, the velocity field of a vortex of constant vorticity $\boldsymbol{\omega} = \omega \hat{z} = \partial_x u_y - \partial_y u_x$ must satisfy

$$u_x = \epsilon \Omega_V y \quad (5.22)$$

$$u_y = -\epsilon^{-1} \Omega_V x \quad (5.23)$$

which is divergenceless. In the above equations, Ω_V is the angular frequency of the vortex in the co-rotating frame. The quantity $\epsilon \equiv a/b$ is

the aspect ratio of the vortex, where a is the semimajor-axis (in the y -direction) and b the semiminor-axis (in the x -direction) ¹.

Given an equation of state, a pressure profile can be constructed that satisfies the condition of steady state (cf. Johansen et al. 2004). For a barotropic equation of state, the “planet” solution of Goodman et al. (1987) with $\Omega_V = \epsilon\Omega\sqrt{3/(1 - \epsilon^2)}$ exactly solves the compressible Euler equations.

5.5.1 Vortices as particle traps

Inside a vortex, the flow is geostrophic, i.e., in equilibrium between pressure and Coriolis forces. Against a background Keplerian flow, cyclonic vortices (that rotate counterclockwise, opposing the local shear) are destroyed, whereas anti-cyclonic vortices are stable.

Such vortices have two properties that make them an attractive possibility for planet formation. The first, stated above, is that they are equilibrium solutions, thus persistent structures in hydrodynamic flows, as seen in the Great Red Spot of Jupiter, a remarkable high pressure vortex stable over three hundred years. The second is that under the influence of the drag force, loosely coupled particles inside an anticyclonic vortex experience a net force towards the vortex eye. While the mechanism is essentially the same mechanism responsible for the radial particle drift in a laminar disk (Chavanis 2000), the crucial difference is that whereas in a laminar disk the radial drift leads them to the inhospitable flames of the star, radial drift inside an anticyclonic vortex simply makes the particles sink towards the vortex eye. This has the convenient side effect of dramatically enhancing the solids-to-gas ratio, potentially achieving values high enough to trigger the gravitational instability.

5.5.2 Vortex stability

As seen in Eq. (5.21), a fluid element conserves vorticity in incompressible barotropic and inviscid 2D flow. Because of this constrain, 2D turbulence experiences a modification of the energy cascade, which becomes inverse (Kraichnan 1967). As a result, random eddies placed in 2D simulations cascade energy toward the largest scales of the box, thus forming progressively larger vortices (e.g., Bracco 1999, Johnson 2005).

The astrophysical literature has seen examples of works where initial vorticity was put in 3D simulations, and let to decay (Barranco &

¹In a sufficiently small patch of the disk where curvature can be ignored (i.e., the Cartesian “shearing sheet” limit, discussed in Chapter 4), x equals the radial direction and y the azimuthal.

Marcus 2005, Shen et al. 2006), concluding that vortices could not be sustained like in 2D turbulence. Shen et al. (2006) seeded a 3D box with small scale vorticity, whereas Barranco & Marcus (2005) started the simulations with a tall columnar vortex. The former sees the vorticity being dissipated all over the box. The latter observed the column going unstable, with vorticity being quenched in the midplane, but sustained above and below it.

These negative results on vortex growth and sustaining are understood as a result of the elliptic instability (Crow 1970, Gledzel et al. 1975, Kerswell 2002), by which the stretching term in Eq. (5.21), $(\boldsymbol{\omega} \cdot \nabla)\mathbf{u}$, absent in 2D, breaks down elliptical streamlines such as vortical flow. Three-dimensional barotropic simulations that perturb an equilibrium flow with noise are simply witnessing the stretching term quickly destroying the eddies. The energy then cascades towards small scales where they are dissipated.

Kerswell (2002) shows that there are ranges for the vortex's Rossby and Froude numbers where the elliptic instability is suppressed². In the presence of rigid rotation, stability exists for anticyclonic vorticity of Rossby numbers $2/3 < \text{Ro} < 2$. In the presence of stratification, vortices with Froude numbers $\text{Fr} \leq 1$ are elliptically stable. Barranco & Marcus (2005) find that vortices are destroyed in the midplane, where $\text{Fr} > 1$; and stable vortices away from the midplane, where $\text{Fr} < 1$ (see their Sect. 4.2). This is in agreement with the prediction of the elliptic instability.

The situation changes considerably when including the baroclinic term, that generates vorticity. Klahr (2004) shows that the baroclinic instability is present in accretion disks, leading to amplification of seed noise into full-fledged vortices in 2D simulations (Klahr & Bodenheimer 2003, Petersen 2007). Although 2D, this starkly contrasts with barotropic works that simply saw re-structuring of small eddies into larger ones, with vorticity conservation. The baroclinic instability also operates in 3D (Klahr, private communication). A stable anticyclonic vortex is also seen on the unstratified 3D MHD simulation of Fromang & Nelson (2005); on the stratified inviscid run of Edgar & Quillen (2008); and on the 3D RWI-unstable setup of Méheut et al. (2008).

These simulations provide evidence of the simple mechanism needed to quench the elliptic instability: a sufficiently large baroclinic term $\nabla p \times \nabla \rho$ that generates enough vorticity to counteract the negative effects of the stretching term. This possibility was not

²The Rossby number is defined as $\text{Ro} \equiv \Omega_v / \Omega$ where Ω_v is the vortex' turnover frequency and Ω the orbital frequency of the flow. The Froude number is defined as $\text{Fr} \equiv \Omega_v / N_z$, where N_z is the Brunt-Väisälä frequency for vertical buoyant modes (see Chapter 7).

touched upon on the review of Kerswell (2002), and we suggest is the main reason behind the negative results of Barranco & Marcus (2005) and Shen et al. (2006). The simulations of Shen et al. (2006) are barotropic. Without the baroclinic term, nothing opposes stretching, and it is no surprise that the vortices are destroyed. The simulations of Barranco & Marcus (2005) use a non-barotropic equation of state, but there is no large scale baroclinity since a radial entropy gradient is absent. The large scale stretching therefore vastly overcomes the small scale baroclinity and the vortical column decays.

6. Subordinate planet formation

*The King of Gods once felt the burning joy,
And sigh'd for lovely Ganymede of Troy.
Down with his masquerading wings he flies,
And bears the little Trojan to the skies;
Where now, in robes of heav'nly purple drest,
He serves the nectar at th'almighty's feast,*

Ovid predicts Trojan companions to Jovian planets
The Fable of Cyparissus (in *Metamorphoses*).

In paper II and paper III we explored the conditions for planet formation in 2D simulations of alpha disks with a dead zone. The inflow from the active layers leads to the development of surface density maxima at the edges of the dead zone that, in turn, are unstable to the Rossby wave instability. Inside the vortices that form in the saturated state, planet formation occurred, leading to the emergence of more than 300 gravitationally bound objects, 20 of which were more massive than Mars.

We now take a leap in time and assume that this collection of planetary embryos would effectively assemble into oligarchs, a small number of dominant rocky cores massive enough to undergo runaway accretion of gas in order to form giant planets such as Jupiter. Such step is predicted by N -body models starting from a number of Mars-sized bodies such as those we study in papers II and III (e.g., Kokubo et al. 2006).

In this chapter we deal with the underlying physics of paper IV, where we explored the opportunities for planet formation created by the presence of a giant planet. Such a planet gives rise to two distinct structures where a secondary burst of planet formation might ensue. These are namely, the stable Lagrangian points L4 and L5, equilibrium locations where gas is retained for at least 100 orbits; and a deep gas gap, whose borders constitute pressure jumps, propitious for the Rossby wave instability to develop new planet-forming vortices. We call this secondary burst *subordinate planet formation* since it depends

on the presence of a giant planet perturber, formed by other mechanism, to induce the favorable structures.

In this endeavour, it is worth to review the basic physics of planet-disk interaction that enables such structures. It is equally worth to introduce paper IX, a code comparison project not included in the body of this thesis. Our part in that project was to implement and run the test problem with the PENCIL CODE. The problem chosen was one that was conceptually simple and could, at the same time, highlight some of the nuances of the different codes. The problem thus chosen was the gap opening problem. In the next sections, we describe some of the analytical theory of planet-disk interaction, and the relevant results of paper IX that are pertinent to paper IV.

6.1 Planet-Disk interaction

Numerical simulations of planet disk interaction (e.g. Bryden et al. 1999, Kley 1999, Lubow et al. 1999, Artymowicz 2001) have showed that the influence of a planet in a disk appears as a distinctive one-armed spiral. Even the very first such calculation (Miki 1982), albeit done in 2D in a local box, already shows evidence of a spiral pattern in the form of high density “laces” excited by the planet. This is seen as strong shocks for high-mass planets, and slightly enhanced density regions for a low-mass (Neptune) planet.

Provided the planets are of low mass, the response they exert on the disk is linear. Ogilvie & Lubow (2002) then show that the precise shape of the spiral density perturbation launched by the planet can be calculated analytically as a superposition of the individual Fourier modes. We briefly summarize the calculation below.

In a 2D case, any linear wave can be written as a superposition of the several Fourier modes in co-sine series

$$A(r, \phi, t) = A(r) \cos(\Phi_m(r, \phi, t)) \quad (6.1)$$

where $A(r)$ is the complex amplitude and

$$\Phi_m = \int \mathbf{k} \cdot \mathbf{r} \, dr \quad (6.2)$$

$$= \int k(r) \, dr + m(\phi - \Omega_p t) \quad (6.3)$$

where k and m are the radial and azimuthal wavenumber, respectively. $\Omega_p = GM/r_p^3$ is the angular frequency of the planet, which is at the radial position r_p . The dispersion relation for such waves is

$$m^2(\Omega - \Omega_p)^2 = \kappa^2 + c_s^2 k^2, \quad (6.4)$$

where κ is the epicyclic frequency. Using this relation, a sound speed $c_s^2 = c_{s0}^2/r$, and units where $GM = r_p = \Omega_p = 1$, we find

$$\begin{aligned} k^2 &= r c_{s0}^{-2} \left(\Omega^2 (m^2 - 1) + m^2 - 2m\Omega \right) \\ &= \frac{m^2(1 + r^3) - 2mr^{3/2} - 1}{r^2 c_{s0}^2} \end{aligned} \quad (6.5)$$

since $\Omega^2 = GM/r^3$.

The above equation can be cast in the form

$$k^2 = \frac{m^2}{c_{s0}^2 r^2} (r^{2/3} - r_+^{2/3})(r^{2/3} - r_-^{2/3}) \quad (6.6)$$

where we recognize

$$r_{\pm} = \left(1 \pm \frac{1}{m} \right)^{2/3} \quad (6.7)$$

as the locations of the Lindblad resonances for mode m .

The wavefronts are calculated as lines of constant phase, defined by

$$\frac{d\phi}{dr} = -\frac{k}{m} \quad (6.8)$$

Solving for the phase ϕ and plugging it back into (6.3), the authors find that constructive interference occurs at curves $\phi = \phi(r, t)$ defined by

$$\varphi_{\text{outer}} = t - \frac{2}{3c_{s0}} \left(r^{3/2} - \frac{3}{2} \ln r - 1 \right) \quad (6.9)$$

for the outer wavefront, and

$$\varphi_{\text{inner}} = t + \frac{2}{3c_{s0}} \left(r^{3/2} - \frac{3}{2} \ln r - 1 \right) \quad (6.10)$$

for the inner wavefront.

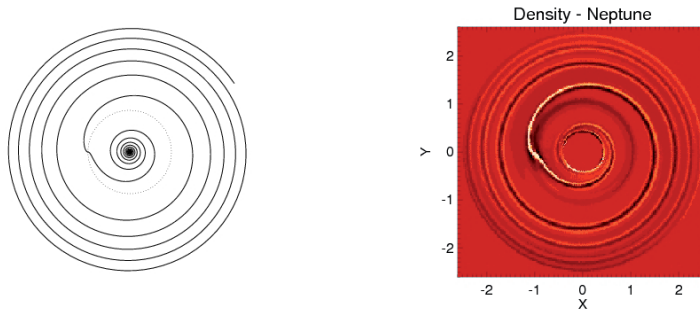


Figure 6.1: Analytical solution of the spiral wake generated by an embedded low mass planet and comparison with the numerical solution achieved with PENCIL for the case of a Neptune-mass planet.

The resulting pattern is plotted in Fig. 6.1. The flow solution attained with the PENCIL CODE for a Neptune mass planet in a laminar 2D disk shows excellent agreement.

6.1.1 The carved gap

The opening of a gap and its evolution is also a matter of concern. The gap is the most immediately recognizable structure the planet imposes on the disk, and therefore an important comparison for the several runs of Paper IX. The shape and depth of the gap was also the problem we chose to assess the role of numerical dissipation in the simulations described in Paper I, using the common setup and agreed solution of Paper IX as a model of what we should expect. It also has paramount importance in Paper IV. It is therefore interesting to describe it.

As the planet orbits inside the disk, it produces tides in the gas. The tides tend to expel material away from its vicinity, while the viscous evolution tends to smear out the sharp density gradient and fill in the gap. The steady state of the disk will be determined by the balance between the tidal and viscous torques. The rate of angular momentum transfer (torque) at a distance d from the planet's orbital radius is approximately (Lin & Papaloizou, 1979*a,b*; Lin & Papaloizou Lin, 1986; Lin & Papaloizou 1993)

$$\tau_p = 0.23q^2 \Sigma r_0^4 \Omega^2 \left(\frac{r}{d}\right)^3 \quad (6.11)$$

where this approximation applies as long as $d \geq H$, the disk's scale height.

In order to carve a gap, τ_p resulting from the tidal torque must exceed the viscous angular momentum transfer rate $\tau_v = 3\pi\Sigma\nu r_0^2\Omega$. Adopting a minimum value $d = H$, the above requirement becomes

$$q \gtrsim \frac{40\nu}{\Omega r_0^2} \quad (6.12)$$

To convert it to dimensionless quantities, we use the Shakura-Sunyaev alpha viscosity $\nu = \alpha c_s H$, leading to

$$q \gtrsim 40\alpha \left(\frac{H}{r_0}\right)^2 \quad (6.13)$$

for $H = 0.05r$, we have

$$q \gtrsim 0.1\alpha \quad (6.14)$$

With $\alpha \approx 10^{-3}$, planets with $q \gtrsim 10^{-4}$ will open gaps in disks. For a solar mass star, this critical value of q corresponds roughly to twice the mass of Neptune.

This approximation breaks down for inviscid disks, for it assumes local dissipation of the waves. Without viscosity, nothing counteracts the tides of the planet and therefore the gap width will be truncated by other mechanisms rather than viscous inflow. Without viscous torques, the planet will have full control over what happens inside its Hill radius. Conversely, it cannot influence the gas outside it. The latter statement leads to the educated guess that a deep gap can only be opened if the Hill radius of the planet is comparable to the local scale height of the disk

$$R_H = r_0 \left(\frac{M_p}{3M_\odot}\right)^{1/3} \gtrsim H \quad (6.15)$$

This can be verified mathematically. Lin & Papaloizou (1993) describe an *ansatz* for the gap opened in such a case. They assume first that the truncated disk can be described by a smooth step function

$$\Sigma = \Sigma_0 \left(\tanh\left(\frac{|r - r_0|}{H_r}\right)\right)^n \quad (6.16)$$

where H_r is the “radial scale length” of the gap and n is the index of the polytropic equation of state of the disk. They then parametrize this scale length by $H_r = (n/\beta)^{1/2}H$. This density profile leads to a modification of the epicyclic frequency (Eq. (2.15), Eq. (3.27)), and the authors

show that for κ^2 to remain real, β^2 must be less than $27/16$. This corresponds to

$$H_r \geq \left(\frac{16}{27}\right)^{1/4} n^{1/2} H \quad (6.17)$$

which is roughly H . So the planet opens a gap comparable in size with the scale height of the disk, as we intuitively suspected.

It can be shown that the maximum torque occurs when H_r becomes comparable to H , and the former must satisfy $H_r \geq r_0(q/3)^{1/3}$ so that the edge of the gap lie outside the planet's Hill radius. This reasoning leads to the conclusion that the condition for opening a gap in inviscid disks indeed is having the planet's Hill radius exceeding the scale height of the disk. In terms of q , Eq. (6.15) becomes

$$q \geq 3 \left(\frac{H}{r_0}\right)^3. \quad (6.18)$$

For flared disks of $H = 0.05s$, the above condition requires a critical q of 3.75×10^{-4} , or roughly the mass of Saturn.

This analysis also works for viscous disks provided that τ_p greatly exceeds the viscous torque τ_v .

6.2 Lagrangian points

The Lagrangian points are stationary solutions to the circular restricted three-body problem (TBP). The TBP refers to the motion of three bodies under their combined gravitational potential, a notoriously difficult problem, for which the solutions can be chaotic. The restricted TBP assumes that the mass of the third body is negligible, which simplifies the problem to finding the motion of a test particle under the influence of the other bodies, that in turn execute the fully integrable two-body problem. If in addition, the motion of the two massive bodies occur in circular orbits, the Jacobi constant is a conserved quantity for the motion of the test particle.

6.2.1 The Jacobi constant

The Jacobi constant can be calculated from the following dynamical considerations. In the inertial (sidereal) frame, the test particle is subject to the acceleration

$$\mathbf{a}_{\text{sid}} = -\frac{\mu_1}{r_1^3}\mathbf{r}_1 - \frac{\mu_2}{r_2^3}\mathbf{r}_2 \quad (6.19)$$

where $\mu_1=GM_1$ and $\mu_2=GM_2$ are the masses of the dominant bodies, and \mathbf{r}_1 and \mathbf{r}_2 are the positions of the test particle relative to these bodies. This acceleration relates to the acceleration in the synodic frame (i.e., the frame co-rotating with the secondary) by

$$\mathbf{a}_{\text{syn}} = \mathbf{a}_{\text{sid}} - \boldsymbol{\Omega} \times (\boldsymbol{\Omega} \times \mathbf{r}) - 2\boldsymbol{\Omega} \times \dot{\mathbf{r}} - \dot{\boldsymbol{\Omega}} \times \mathbf{r} \quad (6.20)$$

where $\boldsymbol{\Omega}$ is the angular velocity of the frame. For $\boldsymbol{\Omega} \equiv \text{const} = \Omega\hat{\mathbf{z}}$, it reduces to the usual expressions

$$\ddot{x} - 2\Omega y = \Omega^2 x - \mu_1 \frac{(x + \mu_2)}{r_1^3} - \mu_2 \frac{(x - \mu_1)}{r_2^3} \quad (6.21)$$

$$\ddot{y} + 2\Omega x = \Omega^2 y - \left[\frac{\mu_1}{r_1^3} + \frac{\mu_2}{r_2^3} \right] y \quad (6.22)$$

$$\ddot{z} = - \left[\frac{\mu_1}{r_1^3} + \frac{\mu_2}{r_2^3} \right] z. \quad (6.23)$$

These accelerations can be cast into the form of the gradient of a scalar

$$\ddot{x} - 2\Omega y = \frac{\partial U}{\partial x} \quad (6.24)$$

$$\ddot{y} + 2\Omega x = \frac{\partial U}{\partial y} \quad (6.25)$$

$$\ddot{z} = \frac{\partial U}{\partial z} \quad (6.26)$$

where the function U is

$$U(x, y, z) = \frac{\Omega^2}{2}(x^2 + y^2) + \frac{\mu_1}{r_1} + \frac{\mu_2}{r_2}. \quad (6.27)$$

Multiplying Eq. (6.24) by \dot{x} , Eq. (6.25) by \dot{y} , Eq. (6.26) by \dot{z} , and summing them, we get

$$\dot{x}\ddot{x} + \dot{y}\ddot{y} + \dot{z}\ddot{z} = \frac{\partial U}{\partial x}\dot{x} + \frac{\partial U}{\partial y}\dot{y} + \frac{\partial U}{\partial z}\dot{z} \equiv \frac{\partial U}{\partial t}. \quad (6.28)$$

This equation is then integrated in time, which yields

$$\dot{x}^2 + \dot{y}^2 + \dot{z}^2 + C_J = 2U \quad (6.29)$$

where C_J , the Jacobi constant, is the constant of integration. Using Eq. (6.27),

$$C_J = \frac{\Omega^2}{2}(x^2 + y^2) + 2\left(\frac{\mu_1}{r_1} + \frac{\mu_2}{r_2}\right) - v^2 \quad (6.30)$$

where $v^2 = \dot{x}^2 + \dot{y}^2 + \dot{z}^2$ is the squared velocity of the particle in the corotating frame. The value of the Jacobi constant constrains the trajectories. The motion of a test particle is possible inside surfaces bound by zero-velocity curves where $C_J=2U$. The appearance of the five Lagrangian points is readily seen from the surfaces obtained by progressively decreasing the Jacobi constant (Fig. 6.2). The figure also illustrates that the first three points are unstable, whilst L4 and L5 are stable points. We make further use of the Jacobi constant in Appendix C to assess the quality of the numerical solution of our N -body code.

6.3 PENCIL's results

In this section I show the results obtained, but not included in Paper IX. All other relevant information is in the body of that article.

Fig. 6.3 shows the state of the flow after 100 orbits for a $q = 10^{-3}$ (Jupiter mass) planets. The evolution of the gap is shown as azimuthally averaged density profiles for various orbits. The streamlines are also shown, evidencing the L4 and L5 Lagrangian points of the planets. The horseshoe orbits can also easily be spotted in the Jupiter mass case. The mass loss due to viscous inflow and the excitation of the spiral waves that reach the buffer zone is very low, being less than 3% in the timespan of the simulation. The resulting torques show agreement with the predictions of type II migration, with the outer disk out-weighting the inner, leading to a net negative torque and consequent inward migration if the planet's orbit was allowed to evolve.

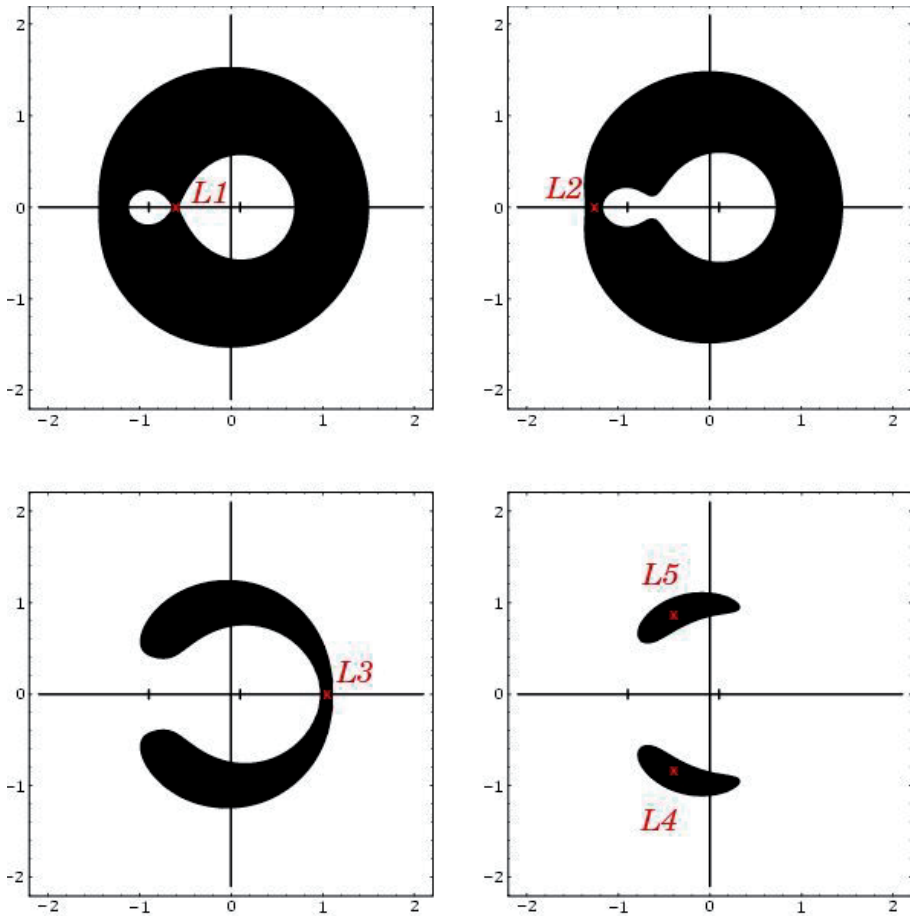


Figure 6.2: As the value of the Jacobi constant decreases, the zero velocity curves that bound the motion of a test particle in the circular restricted three body problem reveal the locations of the equilibrium Lagrangian points. The three first points lie in the line connecting the two massive bodies (marked by the vertical dashes on the horizontal axis). These points are unstable, since they are surrounded by white areas, where motion is forbidden. The points L_4 and L_5 , on the other hand, are stable. The lower plots correspond to horseshoe and tadpole orbits, respectively.

In Fig 6.4 we see PENCIL's solution as compared to other codes. Angular momentum and mass are output in the upper right and lower left panel respectively, where we see that PENCIL agrees well with the other codes. This statement is interesting if we recall that the other codes are all *conservative*, taking explicit care of mass and momentum.

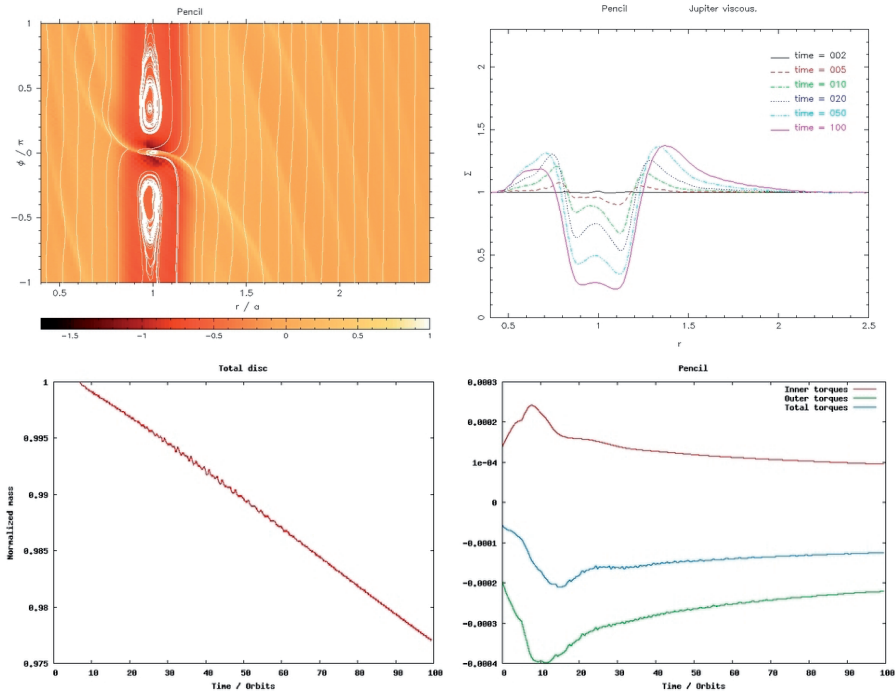


Figure 6.3: Gap opening by a Jupiter-mass planet. The upper left figure shows the state of the disk after 100 orbits, with superimposed streamlines. The Lagrangian points L4 and L5 and horseshoe orbits are clearly seen. The upper right figure shows the time-evolution of the gap. In the lower left we quantify the amount of mass loss in the box during the simulation, being less than 3%. This loss is not numerical, but due to viscous inflow and the damping of the spiral wake when it reaches the boundary. The figure in the lower right shows the averaged torque acting on the planet by the inner and outer disks. The total torque is negative, so the planet migrates inwards in type II migration.

Even more interesting is to notice that the PENCIL’s solution in this case was computed in a *Cartesian* grid. The capabilities of a Cartesian grid on modelling a cylindrical flow were further explored in Paper I.

Fig. 6.5 shows radial plots of the density profile in the azimuthal positions of the L4 and L5 points ($\phi = \pm \pi/3$) in the upper panels. The lower plots show the density profiles at $\phi = \pi$ (thus including the L3 point) and in the planet’s azimuthal location ($\phi = 0$). The agreement among the several codes is remarkable. PENCIL reveals a slightly depleted inner disk and a shallower gap compared to the other codes. This feature was explained in Paper I as effects of resolution and numerical dissipation.

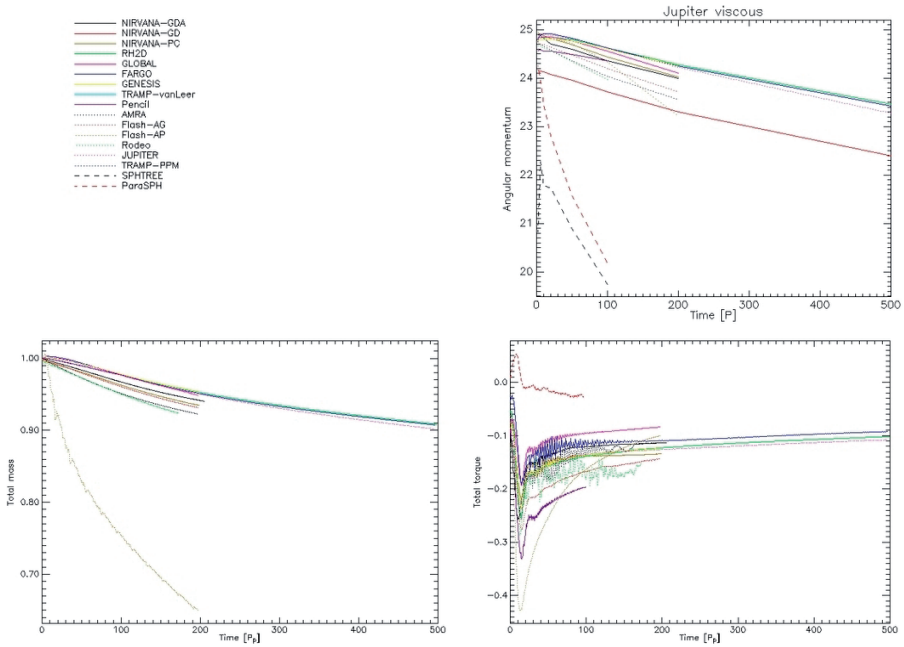


Figure 6.4: Comparison of the results of PENCIL among the other codes in respect to the evolution of mass, angular momentum and the total torques. For mass and angular momentum, PENCIL agrees well with the other codes, albeit with a different slope. The total torque, however, is the strongest among the codes (except Cartesian FLASH, which clearly differs from all others.)

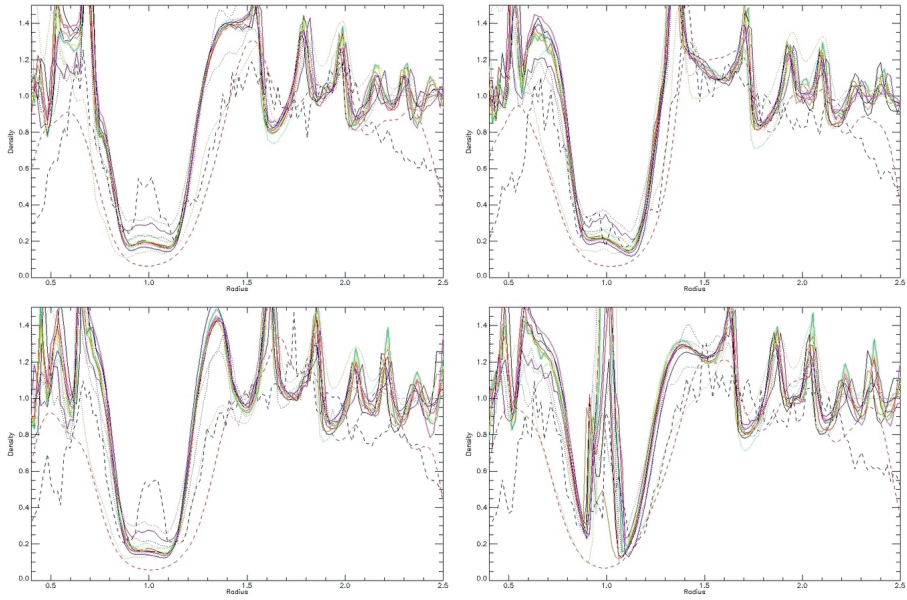


Figure 6.5: Density slices for late times of the gap opened by a Jupiter mass planet. The color and line-style coding is the same as in the previous figure. The upper panels shows radial slices at the position of the L4 (left) and L5 (right) points, respectively. The lower ones show slices at azimuthal position $\phi=\pi$ (left) and $\phi=0$ (right).

7. Ongoing and future work

(Jen:) Ok, I think I finally understand what you did in your thesis. There's this problem, right? That's really important, and all the research that's been done before doesn't quite solve it. But now your solution kinda solves it, but only under certain conditions and assumptions that may or may not apply to reality.

(Mike:) That describes every thesis ever written.

Jorge Cham's *Piled Higher and Deeper* comic strip
(www.phdcomics.com)

In this thesis, I have explored conditions for planet formation in disks with magnetorotational turbulence or vortices, as well as secondary bursts of planet formation triggered by the presence of a previously formed giant planet. In paper I the conditions were three-dimensional, but the gravity of the particles was not solved for to follow gravitational collapse. Papers II, III and IV addressed the collapse of interacting particles into planets, but in 2D disks only. Although Uriel Frisch's textbook *Turbulence* states that "doing physics in Flatland requires no apologies", and although we have good evidence that the proposed scenario also works in 3D, we believe that the 2D models presented in papers II-IV leave much room for exciting improvements. At the moment of writing, I have a number of works in progress and other, future works, that are important and that I find interesting to pursue. In this last chapter, much of an epilogue, I devote a couple of paragraphs to each of them.

7.1 The RWI in three dimensions

The Rossby wave instability as originally proposed was investigated analytically (Lovelace et al., 1999) and numerically (Li et al., 2001) in two dimensions only. It is still unclear what the conditions for its excitation would be in three dimensions, but its existence in 3D is evidenced in the simulations of Méheut et al. (2008). In 3D, the Solberg-

Høiland criteria for instability are (Rüdiger et al. 2002, and references therein)

$$\frac{1}{r^3} \frac{\partial j^2}{\partial r} - \frac{1}{c_p \rho} \nabla p \cdot \nabla S < 0 \quad (7.1)$$

$$\frac{\partial p}{\partial z} \left(\frac{\partial j^2}{\partial z} \frac{\partial S}{\partial r} - \frac{\partial j^2}{\partial r} \frac{\partial S}{\partial z} \right) < 0 \quad (7.2)$$

where c_p is the heat capacity at constant pressure and $j = \Omega r^2$ (Eq. (3.28)). The first term in Eq. (7.1) is the square of the epicyclic frequency. The dot product splits into two parcels so that we can re-write the equation as

$$\kappa^2 + N_r^2 + N_z^2 < 0 \quad (7.3)$$

where

$$N_r^2 \equiv \frac{1}{\rho} \frac{dp}{dr} \left(\frac{1}{\rho} \frac{d\rho}{dr} - \frac{1}{\gamma p} \frac{dp}{dr} \right) \quad (7.4)$$

$$N_z^2 \equiv \frac{1}{\rho} \frac{dp}{dz} \left(\frac{1}{\rho} \frac{d\rho}{dz} - \frac{1}{\gamma p} \frac{dp}{dz} \right) \quad (7.5)$$

are pieces of the Brunt-Väisälä frequency (not to be confused with vector components). Equation (7.1) states that vertical buoyancy has an additional stabilizing/destabilizing effect not present in two dimensional simulations. Equation (7.2) contains the term $\partial_z \Omega$ and determines if the disk is unstable to the strato-rotational instability (cf. Urpin & Brandenburg 1998, Yavneh et al. 2001, Rüdiger et al. 2002, Dubrulle et al. 2005, Umrhan 2006).

We modelled a 3D-disk with the same α -dead zone prescription used in paper II and paper III. We show the resulting flow in Fig. 7.1 (left panel). We confirm that the RWI is present, only taking longer to develop due to the stabilizing effect of stratification, embodied in the vertical Brunt-Väisälä frequency.

The inner edge of the dead zone breaks into eight vortices, that show no sign of merging after 30 orbits after their appearance. In contrast, 2D RWI-unstable models show 4-5 vortices that quickly merge. The discrepancy in number of vortices is probably due to a modification of the dispersion relation for the RWI in three dimensions. In 2D, the most unstable modes are those of $m=4$ and $m=5$ (Li et al., 2000), their merging due to the inverse cascade of power and direct cascade of enstrophy. In 3D, where enstrophy is not conserved, the energy cas-

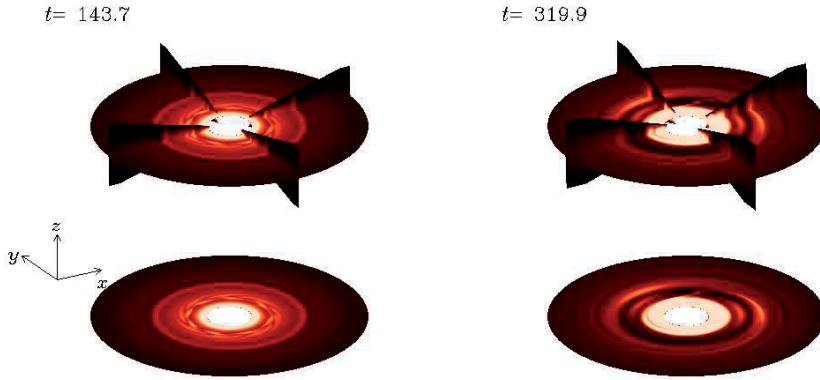


Figure 7.1: Three-dimensional Rossby wave instability launching vortices in a α dead zone model (left panel) and in a disk with an embedded planet (right panel). The stabilizing effect of stratification delays the onset of the instability, but does not quench it. Work in progress.

cade is direct, so vortex merging does not occur. On the other hand, we notice that the simulation of Meunét et al. (2008) shows only three vortices. It is not clear from the analysis they present whether this is the most unstable mode or whether some inverse cascade is present in their simulation. To study this problem self-consistently, we intend to abandon the alpha viscosity prescription, in favour of non-ideal MHD dead zone models with resistivity given by Eq. (5.8).

The RWI is also excited in disks with giant planets, as seen in Fig. 7.1 (right panel). In this simulation, two vortices are seen. A similar simulation (Edgar & Quillen 2008) also shows a low- m dominant mode, in their case $m=1$. It appears that this case is more closely related to a 2D configuration than the dead zone model, probably due to the gravity of the planet.

7.2 Radiation

The simulations done in this thesis were performed with a very simple treatment of the energy equation. For papers I and IV we did not solve it at all, using instead a locally isothermal equation of state. That means that we assumed the disk optically thin, efficiently radiating away the excess energy so no heating ever occurs. In papers II and III we did solve the energy equation, but with an adiabatic equation of state and including only pdV work. I intend to improve on that by modelling disks with a realistic treatment of radiation energy transport.

The first steps towards this goal are embodied in the undergraduate thesis of Heidar T. Thrastarson, carried out under my supervision. In that work, we relaxed the approximations of isothermality by solving the equations of hydrodynamics coupled with the detailed balance of energy e and modelling the radiative field within the box

$$\rho \frac{De}{Dt} = -p \nabla \cdot \mathbf{u} - \nabla \cdot \mathbf{F} \quad (7.6)$$

$$\mathbf{F} = \oint_{4\pi} \int_0^\infty \hat{\mathbf{n}} I_\nu d\nu d\Omega(\hat{\mathbf{n}}) \quad (7.7)$$

$$I_\nu(\hat{\mathbf{n}}) = \frac{dE_\nu}{d\nu dt d\Omega(\hat{\mathbf{n}} \cdot d\mathbf{A})} \quad (7.8)$$

$$\hat{\mathbf{n}} \cdot \nabla I_\nu = \chi_\nu (S_\nu - I_\nu) \quad (7.9)$$

where \mathbf{F} is the radiative flux, I_ν is the specific intensity, S_ν the source function, $\hat{\mathbf{n}}$ the normal unit vector, ν refers to frequency and Ω to solid angle (the last two are not to be confused with viscosity and angular frequency).

The current implementation of the equation of radiative transfer in the PENCIL CODE was slightly modified to allow for two frequency ranges: the visible range where the star radiates, and the infrared, where most of the emission of the disk itself will take place. Fig. 7.2 illustrates the temperature distribution found for a hydrostatic vertically stratified disk when subject to this radiative field. The optically thin parts heat up considerably, while the thick disk achieves equilibrium in much lower temperatures.

7.3 Gas accretion onto giant planets

The last stages of the formation of a giant planet consist of accretion of gas from the surrounding nebula (Mizuno 1980). In this process, the gravitational sphere of influence of the planet (the Hill sphere) becomes fully filled with gas, that becomes optically thick due to the high densities. Unable to radiate away the heat, the accreted gas cannot contract in order to settle onto the core. The pressure build-up prevents more gas from entering the Hill sphere, thus stalling the accretion process. The planet's final mass is ultimately determined by the ability of the accreted gas to cool and contract in order to make way for more material entering the Hill sphere. Early estimates of the timescales involved on gas accretion (Pollack et al. 1996) used the opacities of interstellar dust grains, finding that the cooling phase lasted for more than 8 million years (Myr), which is much too long to match the constraints

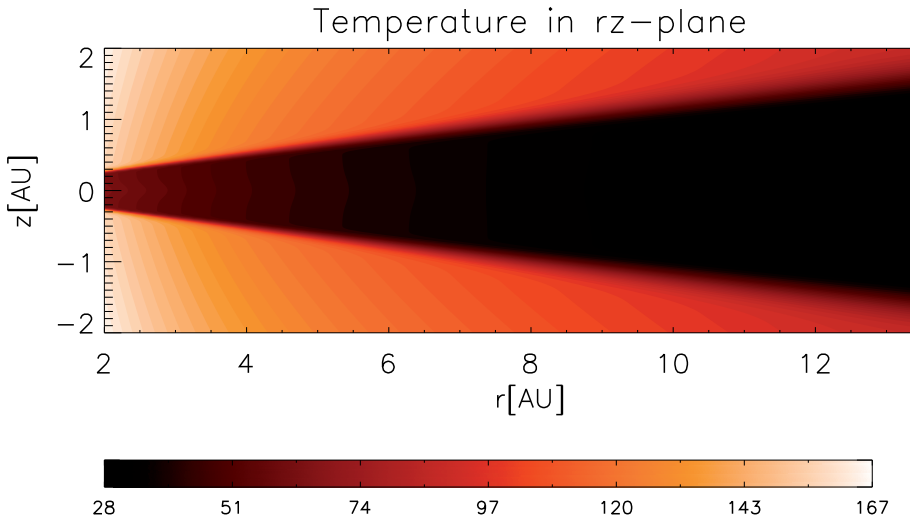


Figure 7.2: Equilibrium temperature structure for a disk irradiated from above at optical wavelengths and re-radiating in infrared. Temperature shown in K. Work in progress.

on disk lifetime posed by observations (≈ 3 Myr; Haisch et al. 2001). This early estimate was lowered to 2 Myr by Hubickyj et al. (2005), who notice that the opacities would decrease to 2% of the interstellar value if the grains settled to the bottom of the gas envelope of the protoplanet, where they are destroyed by sublimation. These models, although shedding light on the importance of accurate opacities and a detailed treatment of radiative transfer, made use of hydrostatic or quasi-static approximations. The works that modelled the hydrodynamical evolution of gas flow into the Hill sphere (Klahr & Kley 2006, Ayliffe & Bate 2008) included radiation transport through the so-called diffusion approximation (Boss 2004, Boss 2005), where the equation of radiative transfer is not actually solved, and the validity is restricted to the very optically thick media. I plan to improve on these models by explicitly solving the radiative transfer equation in a fully three-dimensional hydrodynamical model.

This simulation will be done by means of a local model, in a small Cartesian box around the forming planet, in order to finely resolve the dynamics inside the Hill sphere. Since the mass of gas that is being accreted is comparable to the mass of the rocky core (and outgrows it at later stages), the simulation will also include self-gravity. Detailed radiative transfer using the ray-tracing technique will be employed, which can treat both optically thin and thick media. Magnetic fields,

not included in any model that treated this problem so far, will be a most interesting addition.

8. Contribution to Included Papers

- I: Coded all parts of the implementation except the existing particles module. This module only had to be adapted to include the boundary conditions for embedded cylinders described in the article. Ran the simulations and wrote the paper.
- II: Adapted PENCIL 's existing Poisson solver for global boundary conditions, coded general drag force laws, ran the simulations, and wrote the paper.
- III: Coded a cylindrical grid for PENCIL, ran the simulations, and wrote the paper.
- IV: Coded a N -body module for PENCIL, ran the simulations, and wrote the paper.

9. Summary in Swedish

Planeternas turbulenta födelse

Hydrodynamiska simuleringar av ansamlingsdiskor och planetbildning

Planetbildning och extrasolära planeter är ett av astronomins mest fascinerande forskningsområden och intimt sammankopplat med forskningen om hur stjärnor bildas. Grunden inom forskningsområdet lades av den kände franske matematikern Pierre-Simon de Laplace, som i slutet av 1700-talet applicerade Newtons gravitationsteori och rörelselagar på ett långsamt roterande sfäriskt gasmoln för att på så sätt studera molnets utveckling och eventuella kollaps under påverkan av sin egen gravitation. I Laplaces modell gör rotationen i kombination med rörelsemängdsmomentets bevarande att gasen samlas i en plan skiva runt den blivande stjärnan (protostjärnan).

Fysiker har senare insett att detta är en alltför enkel modell; eftersom interstellära moln är ofantligt stora skulle minsta lilla rotation innebära att den blivande stjärnan får ett för stort rörelsemängdsmoment. En nybildad skiva skulle enligt detta scenario innehålla minst 100 gånger större rörelsemängdsmoment än vad som krävs för att spränga sönder det tänkta slutresultatet, stjärnan. För att stjärnan ska kunna "fånga in" skivans gas måste den bli av med sitt rörelsemängdsmoment på något sätt. Ett annat problem med modellen ligger i svårigheten att förstå hur mikrometerstora stoftpartiklar i skivan samlas ihop till planeter stora som Jupiter.

Den enda kända kraft som kan samla ihop material i stor skala är friktion, vilket i gaser kallas viskositet. Molekyler i gasen kolliderar, värms upp och strålar ut värme. De förlorar då rörelseenergi och börjar röra sig in mot stjärnan. Om man ersätter de små molekylerna i modellen med stora turbulenselement så har man ett recept för ansamling; turbulent viskositet. Eftersom storleken på dessa element är så mycket större än molekyler så är även friktionen större, och ansamlingen till stjärnan kan fortgå.

Turbulens i skivan uppstår på grund av en magnetisk effekt, den s.k. magneto-rotationella instabiliteten, där växelverkan mellan den differentials rotationen och magnetfältet destabiliserar det jämna gas-

flödet. De processer som därefter leder till planetbildning måste därför fungera i en turbulent och orolig miljö.

Planetbildningen startar med koagulation, där kolliderande mikrometersmå stoftpartiklar med hjälp av elektromagnetiska krafter kan bygga upp centimeterstora gruskorn och meterstora bumlingar. Vid dessa dimensioner slutar emellertid denna mekanism att fungera av två skäl. För det första är kropparnas inbördes hastigheter så stora, upp till 10 km per sekund, att kollisioner mellan två bumlingar resulterar i grus snarare än en större bumling. För det andra tenderar dessa kroppar att sjunka in mot stjärnan p.g.a. friktionen från den omgivande gasen som berövar dem rörelseenergi. Tidsskalan under vilket detta sker tycks vara så pass kort som något hundratal år. Detta fenomen har visat sig vara det mest svåröverstigliga hindret för förståelsen av planetbildning.

En möjlighet att komma förbi dessa hinder erbjuds av gravitationskraften. När stoftkornen har vuxit till centimeter- och meterstorlek, avtar gasens bromsverkan och kropparna attraheras av stjärnans gravitation mot skivans centralplan. Även om dessa kroppar är för lätta för attrahera varandra individuellt, så ökar sedimentationen stoft/gas-kvoten med flera storleksordningar. Med de höga tätheter som då uppnås kan materialet kollektivt uppnå den kritiska densiteten och genomgå en gravitationell kollaps. Detta scenario har fördelen att ha en mycket kort tidsskala och undgår därmed problemet med gasens bromsande effekt.

Denna utvecklingsväg har dock visat sig vara en överförenkling eftersom till och med ett litet mått av turbulens i skivan hindrar partiklarna från att uppnå den täthet som krävs för att trigga kollapsen. Dessutom, i avsaknad av självupprätthållande turbulens som den som orsakas av magneto-rotationella instabilitet, kan kropparna själva orsaka turbulens med sina rörelser i gasen. Gasturbulensen rör då upp de fasta partiklarna och skapar ett lager med finit tjockhet, där stjärnans gravitationella sedimenterande effekt balanseras av turbulent diffusion.

Trots att turbulens i skivan förhindrar en direkt kollaps genom sedimentation, möjliggör den ändå processen på ett indirekt sätt. Friktionen mellan gasen och de fasta partiklarna tenderar att skjuta de fasta partiklarna mot områden med högre tryck och förhöjer därmed stoft/gas-kvoten i delar av skivan, vilket ger möjlighet till gravitationell kollaps då den kritiska densiteten uppnås. Numeriska beräkningar visar att detta också sker; partiklar fångas i dessa högtryckszoner och kollapsar till dvärgplaneter under gravitationell inverkan. Turbulensen höjer dock även de fasta partiklarnas inbördes hastigheter vilket gör att sannolikheten för kollisioner, och därmed även fragmentering, ökar.

Problemet med ökad fragmentering kan undvikas om partikelackumuleringen sker i en skyddad miljö där kollisionshastigheterna är lägre. Anti-cykloniska virvelströmmar liknande Jupiters stora röda fläck har länge antagits gynna planetbildning eftersom de skapar en inåtriktad nettokraft. Virvelströmmar har också mindre intern turbulens än den omgivande gasen vilket minskar kollisionshastigheterna och förhindrar fragmentering. Sådana virvelströmmar liknar orkaner i jordatmosfären och kan bildas i områden i skivan där ansamlingsflöde bromsas. Detta sker bl.a. i den magnetiskt "döda" zonen där jonisationsgraden är så låg att materien inte kopplar till det omgivande fältet.

Jag har arbetat med globala "state-of-the-art" simuleringar av turbulenta protoplanetära skivor, vilka har använts för att utforska betydelsen av detta scenario vid bildandet av planeter. Själva skivan behandlas i modellen i en statisk struktur, medan fasta kroppar behandlas som numeriska partiklar (artikel I). I artikel II byggde vi skiv-modeller med magnetiskt döda zoner, inklusive växelverkande partiklar av centimeter- och meterstorlek. Vi visar att ansamlandet av partiklar i virvelströmmarna är så effektivt att det leder till gravitationell kollaps. Vidare visar vi att det sker ett utbrott av planetbildning i skivan, vilket i modellen resulterade i 300 gravitationellt bundna planet-embryon, varav 20 befanns vara mer massiva än Mars. I artikel III adresserade vi bland annat problemet med fragmentering genom att beräkna historiken av kollisionshastigheter hos de partiklar som utgör embryon. Resultatet visar att den övervägande majoriteten partiklar inte har utsatts för kollisioner med övriga partiklar med större hastigheter än 1 meter per sekund. Detta häpnadsväckande resultat stärker den sedan länge vidhållna teorin om att anti-cykloniska virvelströmmar är mycket fördelaktiga strukturer vid planetbildning.

I artikel IV gick vi vidare och visade att samma mekanismer även verkar i skivor med jätteplaneter. I dessa simuleringar öppnar jätteplanetern upp ett gap i skivans material, vilket ökar förekomsten av virvelströmmar. Den gravitationella kollapsen leder i det här fallet till bildandet av super-jordar, som mycket väl skulle kunna fungera som kärnor för nästa generation jätteplaneter. Som en biprodukt av detta arbete upptäckte jag också att gravitationella kollapsar till jordstorlek även sker vid de stabila Lagrange-punkterna i jätteplanetens omloppsbana. Från denna upptäckt drar vi slutsatsen att det finns en möjlighet att vissa av de gasjättar som upptäckts i andra solsystem skulle kunna ha Trojanska kompanjoner av jordstorlek och att det skulle kunna finnas jordliknande planeter även i system med jätteplaneter i jordliknande banor. Denna häpnadsväckande upptäckt blev uppmärksammas i media, och går

att läsa om i ett av de senaste numrena av den populärvetenskapliga tidningen *New Scientist*. Ytterligare en populärvetenskaplig artikel som citerar denna upptäckt kommer snart att finnas i press i den nordiska tidskriften *Illustrerad Vetenskap*.

10. Acknowledgements

I am indebted to many people that directly or indirectly contributed to the completion of this Thesis.

To my advisor Nikolai Piskunov, for giving me the opportunity to pursue pure theory. I also thank Bengt Gustafsson, for the wise insights on the sociology of Academia.

My sincere gratitude to the PENCIL CODE community, with whom I learned much of what I know today about numerical simulations. To Tobi Heinemann, with whom I got a broader understanding of the difference between “real” physics and “code” physics. To Tony Mee, for the invaluable lessons on optimization and modularity. In special to Anders Johansen, collaborator and personal friend, whose help is incalculable. To Wolfgang Dobler, a numerical wizard whose knowledge, readiness to help and ease to explain difficult concepts never ceases to amaze me. To Axel Brandenburg, a scientist like few, an inspiration to many.

To the Heidelberg planet and star formation theory group, where I always found a pleasant and stimulating environment. It’s always great to be there, among people who speak the same language. Writing the papers that comprise this thesis would have been much harder hadn’t I found such wonderful collaborators. Hubert Klahr is further thanked for hosting me and supporting me financially during the many trips there during the course of this work.

The helpfulness of the administrators of the PIA cluster in Garching can hardly be overstated. I could not have run the simulations that comprise this thesis without their support and hard work on making the cluster run smoothly.

Breaching the boundary layers from a tropical environment to a sub-polar one is a process best described as... well, *turbulent*. The silent snowfall of the Arctic is a big shift for someone who grew up in Copacabana beach. I feel very lucky to have met people whose liveliness helped smooth the flow. Andreas, Astrid, BEngt, Björn, Lars, Oleg, Paul, Sam, Susanne, Tom, Ulrike, and Sara; either at the lunch or pub table, I really enjoy our chats, and always feel we could have stayed some extra ten minutes (ok, a whole hour more in the pub case). Anna, thanks for being this extra-positive gal and a great friend. Thanks goodness our views are not always in phase, otherwise our

political discussions would be very boring. I would further like to thank Paul for being the local native English speaker, who I annoy everytime I get a language report. By the same token, I thank BEngt, Elisabet, and Sara, for the translation of the summary into proper Swedish.

I had the pleasure of meeting a number of Brazilians in Uppsala. Andrea, Becca, Fernanda, Gloria, Margit, and Monica, thanks for bringing a little bit of samba to life in Sweden. To my off-department Swedish friends, Kenny, Lisa, and Peter, you are few in quantity but awesome in quality. Living in the Flogsta corridors for over 2 years was a great social experience, where we make volatile bonds with students from all over the world. Pointless to name all, you know who you are.

And, as there is life out of Sweden, thanks to Heidar and Nila for all the fun in London. I'm definitely going back to visit you guys. Nicole, thanks for showing up in Sweden every now and then. I guess you can forgive this poor student for not going to La Serena as often as you come to Uppsala. Craig, too bad you live so far, it was great to meet you in Shanghai. I hope we cross paths again in the future. My thanks also to the Heidelberg gang, especially to Andras, Andrej, Andres, Chris, Christoph, Fritjhof, Florian, Isabel, and Niki, for the few but good times we spent together having a *glühwein* or beer at *Hauptstrasse*. Johny, thanks for the sublime indonesian food!

The completion of this Ph.D. is just the latest step in my career, not the first and certainly not the last. Concerning the latter, I take this opportunity to thank Richard Nelson, Sebastien Fromang, Willy Kley, and Mordecai Mac Low, for the kind words of encouragement during post-doc applications. On the former, I cannot forget Roberto Pimentel, my physics teacher in high-school, who triggered, noticed and nurtured my interest on the mathematical description of Nature. I am also grateful to the inspiring mentors I had during the undergraduate. Professors Encarnación Gonzalez, Gustavo Porto de Mello, Heloisa Boechat, and Lilia Arany-Prado, to you I say that Uppsala might now be my *Alma Mater*, but my home institute will always be the Federal University of Rio de Janeiro.

I was once told that one can count on one's fingers the number of people who actually feel that a victory of ours is also a victory of theirs. These are the family and half a dozen of the closest friends. It took me some time to understand the truth of these words. Family, the friends we don't choose. Friends, the family we choose. These ties are really very strong, and all the water of the Atlantic cannot possibly dilute it. I dearly miss you all. My mind was on you during the dark, long, cold winter nights when writing this thesis. I dedicate it to you.

And that's it! So long, and thanks for all the fika!

Appendix A

A.1 High-frequency filters

Being high order, PENCIL has much reduced numerical dissipation. In order to perform inviscid simulations, high-frequency filters must therefore be used to provide extra dissipation for modes approaching the Nyquist frequency. Usual Laplacian viscosity $\nu \nabla^2 \mathbf{u}$ is equivalent to a multiplication by k^2 in Fourier space, where k is the wavenumber. We use instead hyper-viscosity, which replaces the k^2 dependency by a higher power-law, k^n , $n > 2$. The idea behind it is to provide large dissipation only where it is needed, at the grid scale (high k), while minimizing it at the largest scales of the box (small k). In principle, one can use as high n as desired, but in practice we are limited by the order of the code. A multiplication by k^n is equivalent to an operator ∇^n in real space. As PENCIL is of sixth order, three ghost cells are available in each direction, thus the sixth-order derivative is the highest we can compute. The hyper-dissipation we use is therefore ∇^6 , or k^6 in Fourier space. Figure A.1 illustrates how such tool maximizes the inertial range of a simulation.

A.1.1 Conservative Hyperdissipation

It is desirable to have this high-frequency filter obeying the conservation laws. So, for density we want a mass conserving term, for velocities we want a momentum conserving term, for magnetic fields we want a term conserving magnetic flux, and for entropy we want an energy conserving term. These enter as hyperdiffusion, hyperviscosity, hyper-resistivity, and hyper heat conductivity terms in the evolution equations. To ensure conservation under transport, they must take the form of the divergence of the flux \mathcal{J} of the quantity ψ , so that Gauss theorem applies and we have

$$\frac{\partial \psi}{\partial t} + \nabla \cdot \mathcal{J} = 0 \quad (\text{A.1})$$

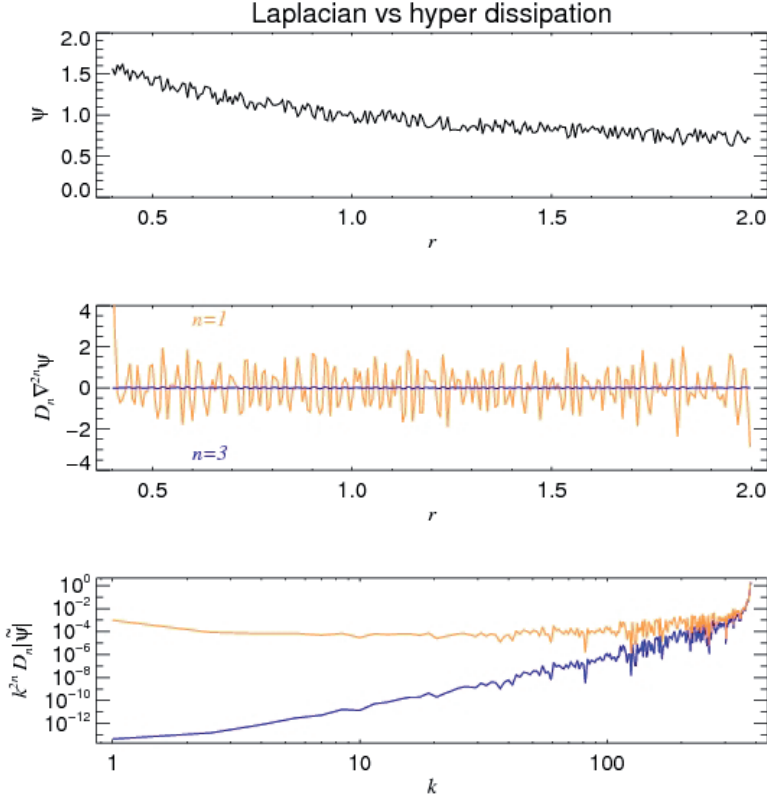


Figure A.1: Dissipation acting on a scalar field ψ , for $n=1$ (Laplacian dissipation) and $n=3$ (third-order hyperdissipation). The field is initially seeded with noise (upper panel). For $n=3$ the large scale is not affected as much as in the $n=1$ case, which is seen by the larger wiggling of the latter in the middle panel. In Fourier space (lower panel) we see that near the grid scale both formulation give strong dissipation. It also illustrates that at the large scales ($k \simeq 1$), the effect of $n=3$ is indeed negligible.

For density, the flow due to mass diffusion is usually taken as the phenomenological Fick's Law

$$\mathcal{J} = -D \nabla \rho \quad (\text{A.2})$$

i.e., proportional to the density gradient, in the opposite direction. This leads to the usual Laplacian diffusion

$$\frac{\partial \rho}{\partial t} = D \nabla^2 \rho \quad (\text{A.3})$$

under the assumption that the diffusion coefficient D is isotropic. Higher order hyperdiffusion of order $2n$ involves a generalization of Eq. (A.2), to (Haugen & Brandenburg 2004, Johansen & Klahr 2005)

$$\mathcal{J}^{(n)} = -D_n \nabla^{2n-1} \rho, \quad (\text{A.4})$$

In our case, we are interested in the case $n = 3$, so that the hyperdiffusion term is

$$\frac{\partial \rho}{\partial t} = D_3 \nabla^6 \rho. \quad (\text{A.5})$$

The hyper diffusion coefficient D_3 can be calculated from D assuming that at the Nyquist frequency the two formulations (A.3) and (A.5) yield the same quenching. Considering a wave as a Fourier series in one dimension (x), one element of the series is expressed as

$$\psi_k = A e^{i(kx + \omega t)} \quad (\text{A.6})$$

Plugging it into the second order diffusion equation (2.3) we have the dispersion condition $i\omega = -Dk^2$. The sixth order version (2.5) yields $i\omega = -D^{(3)}k^6$. Equating both we have $D^{(3)} = Dk^{-4}$. This condition should hold at the grid scale, where $k = \pi/\Delta x$, therefore

$$D^{(3)} = D \left(\frac{\Delta x}{\pi} \right)^4 \quad (\text{A.7})$$

For the magnetic potential, resistivity has the same formulation as mass diffusion

$$\frac{\partial \mathbf{A}}{\partial t} = -\eta \nabla \times \mathbf{B} = \eta \nabla^2 \mathbf{A}, \quad (\text{A.8})$$

where we used the Coulomb gauge $\nabla \cdot \mathbf{A} = 0$. The algebra is the same as above, also yielding $\eta^{(3)} = \eta (\Delta x / \pi)^4$. For entropy, the heat conduction term is

$$\frac{\partial S}{\partial t} = \frac{1}{\rho T} \nabla \cdot (K \nabla T), \quad (\text{A.9})$$

and requiring that K be constant, we substitute it by

$$\frac{\partial S}{\partial t} = \frac{K^{(3)}}{\rho T} \nabla^6 T. \quad (\text{A.10})$$

also with $K^{(3)} = K(\Delta x/\pi)^4$.

A.1.2 Hyperviscosity

Viscosity has some caveats where subtleties apply. The difference is that the momentum flux due to viscosity is not proportional to the velocity gradient, but to the rate-of-strain tensor

$$S_{ij} = \frac{1}{2} \left(\frac{\partial u_i}{\partial x_j} + \frac{\partial u_j}{\partial x_i} - \frac{1}{3} \delta_{ij} \nabla \cdot \mathbf{u} \right) \quad (\text{A.11})$$

which only allows the viscous acceleration to be reduced to the simple formulation $\nu \nabla^2 \mathbf{u}$ under the condition of incompressibility and constant dynamical viscosity $\mu = \nu \rho$. Due to this, the general expression for conservative hyperviscosity involves more terms. In some cases, it is no great overhead, but for others, simpler formulations can be applied.

A.1.2.1 Conservative case

In the general case, the viscous acceleration is

$$f_{\text{visc}} = \rho^{-1} \nabla \cdot (2\rho \nu \mathbf{S}) \quad (\text{A.12})$$

So, for the hyper-viscous force, we must replace the rate-of-strain tensor by a high order version

$$f_{\text{visc}}^{(\text{hyper})} = \rho^{-1} \nabla \cdot (2\rho \nu_n \mathbf{S}^{(n)}) \quad (\text{A.13})$$

where the n^{th} -order rate of strain tensor is (Haugen & Brandenburg 2004)

$$\mathbf{S}^{(n)} = (-\nabla^2)^{n-1} \mathbf{S}. \quad (\text{A.14})$$

For the $n = 3$ case it is

$$S_{ij}^{(3)} = \frac{1}{2} \left(\frac{\partial^5 u_j}{\partial x_i^5} + \frac{\partial^4}{\partial x_i^4} \left(\frac{\partial u_i}{\partial x_j} \right) - \frac{1}{3} \frac{\partial^4}{\partial x_i^4} (\nabla \cdot \mathbf{u}) \right) \quad (\text{A.15})$$

Plugging it into Eq. (A.13), and assuming $\mu_3 = \text{const}$

$$f_{\text{visc}}^{(\text{hyper})} = \nu_3 \left(\nabla^6 \mathbf{u} + \frac{1}{3} \nabla^4 (\nabla (\nabla \cdot \mathbf{u})) \right) \quad (\text{A.16})$$

For $\nu_3 = \text{const}$, we have to derivate the density as well

$$f_{\text{visc}}^{(\text{hyper})} = \nu_3 \left(\nabla^6 \mathbf{u} + \frac{1}{3} \nabla^4 (\nabla (\nabla \cdot \mathbf{u})) + 2\mathbf{S}^{(3)} \cdot \nabla \ln \rho \right) \quad (\text{A.17})$$

A.1.2.2 Non-conservative cases

Equations (A.16) and (A.17) explicitly conserve linear *and* angular momentum. Although desirable properties, such expressions are cumbersome and numerically expensive, due to the fourth order derivatives of $\nabla (\nabla \cdot \mathbf{u})$.

This term, however, is only important when high compressibility is present (since it depends on the divergence of \mathbf{u}). In practice we drop this term and use a simple hyper-viscosity

$$f_{\text{visc}} = \begin{cases} \nu_3 \nabla^6 \mathbf{u} & \text{if } \mu = \text{const} \\ \nu_3 (\nabla^6 \mathbf{u} + 2\mathbf{S}^{(3)} \cdot \nabla \ln \rho) & \text{if } \nu = \text{const} \end{cases} \quad (\text{A.18})$$

Notice that this can indeed be expressed as the divergence of a simple rate-of-strain tensor

$$S_{ij}^{(3)} = \frac{\partial^5 u_i}{\partial x_j^5} \quad (\text{A.19})$$

so it does conserve linear momentum. It does *not*, however, conserve *angular* momentum, since the symmetry of the rate-of-strain tensor was dropped. Thus, vorticity sinks and sources may be spuriously generated at the grid scale.

A symmetric tensor can be computed, that conserves angular momentum and can be easily implemented

$$S_{ij} = \frac{1}{2} \left(\frac{\partial^5 u_i}{\partial x_j^5} + \frac{\partial^5 u_j}{\partial x_i^5} \right) \quad (\text{A.20})$$

This tensor, however, is not traceless, and therefore accurate only for weak compressibility. It should work well if the turbulence is subsonic. In paper I we performed simulations with both Eq. (A.19) and Eq. (A.20), not finding significant differences for the turbulent problem studied. This is expected, since the spectral range in which hyper-viscosity operates is very limited: as a numerical tool, only its performance as a high-frequency filter is needed. This also supports the usage of the highest order terms only, since these are the ones that provide quenching at high k . Momentum conservation is a cheap bonus.

Angular momentum conservation is perhaps playing it too safe, at great computational expense.

A.1.3 Anisotropic hyperdissipation

As we want quenching primarily at the Nyquist frequency, hyperdissipation depends intrinsically on the resolution, according to Eq. (A.7). Because of this, *isotropic* hyperdissipation only gives equal quenching in all spatial directions if $\Delta x = \Delta y = \Delta z$, i.e., if the cells are cubic. For non-cubic cells, anisotropic dissipation is required as different directions may be better/worse sampled, thus needing less/more numerical smoothing. Such generalization is straightforward. For that, we replace Eq. (A.4) by

$$\mathcal{J} = \left(D_x \frac{\partial^5 \rho}{\partial x^5}, D_y \frac{\partial^5 \rho}{\partial y^5}, D_z \frac{\partial^5 \rho}{\partial z^5} \right), \quad (\text{A.21})$$

so that different diffusion operates in different directions. Since D_x , D_y and D_z are constants, the divergence of this vector is

$$\nabla \cdot \mathcal{J} = D_x \frac{\partial^6 \rho}{\partial x^6} + D_y \frac{\partial^6 \rho}{\partial y^6} + D_z \frac{\partial^6 \rho}{\partial z^6}. \quad (\text{A.22})$$

The formulation for resistivity and heat conductivity are strictly the same. For viscosity it also assumes the same form if we consider the simple non-conservative rate-of-strain tensor (A.19). This formulation was used for runs with enhanced resolution in z ($\Delta x = \Delta y = 2\Delta z$) in paper I.

Mathematically, these operations can be written compactly by noticing that the coefficients in Eq. (A.22) transform like diagonal tensors $\chi_{ij}^{(3)} = \chi_k^{(3)} \delta_{ijk}$, where δ_{ijk} is the unit diagonal third order tensor, $\chi^{(3)}$ is the vector containing the dissipative coefficients (diffusion, viscosity, resistivity, or heat conductivity) in x , y , and z , and summation over repeated indices applies. Therefore, for a scalar quantity ψ (density, any of the three components of the velocity or magnetic potential), we can write

$$\frac{\partial \psi}{\partial t} = -\chi_{ij}^{(3)} \partial_i \partial_j^5 \psi = -\sum_q \chi_q^{(3)} \frac{\partial^6}{\partial x_q^6} \psi. \quad (\text{A.23})$$

Appendix B

B.1 Poisson solver

The execution time of a N -body problem scales as N^2 , since all pairs of interactions have to be computed. This offers no significant overhead when few particles are being used, but in simulations with 10^6 particles, it would be pure brute force. Instead, we solve the particle's gravity by the Poisson equation (Eq. (2.7)) in which the particles are mapped onto the grid as a density field ρ_p . This is summed to the gas density ρ_g and Eq. (2.7) is then inverted in Fourier space to get the (self-)gravitational potential Φ_{sg} . This is straightforward for the case of tri-dimensional periodic boundary conditions in Cartesian coordinates. For a given wavevector $\mathbf{k} = (k_x, k_y, k_z)$, the Poisson equation

$$\frac{\partial^2 \Phi}{\partial x^2} + \frac{\partial^2 \Phi}{\partial y^2} + \frac{\partial^2 \Phi}{\partial z^2} = 4\pi G \rho \quad (\text{B.1})$$

becomes

$$\tilde{\Phi} = -\frac{4\pi G}{k^2} \tilde{\rho} \quad (\text{B.2})$$

where $k^2 = k_x^2 + k_y^2 + k_z^2$ and tilde denotes a Fourier-transformed quantity

$$\tilde{f}(\mathbf{k}) = \int_{-\infty}^{\infty} f(\mathbf{x}) e^{-i\mathbf{k}\cdot\mathbf{x}} d\mathbf{x} \quad (\text{B.3})$$

$$f(\mathbf{x}) = \frac{1}{(2\pi)^3} \int_{-\infty}^{\infty} \tilde{f}(\mathbf{k}) e^{i\mathbf{k}\cdot\mathbf{x}} d\mathbf{k} \quad (\text{B.4})$$

In the above and the following, we use $\rho = \rho_g + \rho_p$ and omit the "sg" subscript of Φ_{sg} , for clarity.

The condition of periodicity implies that the potential computed by this method will have contributions from infinite mirror-images of the grid at both sides of each axis. For x and y this is not as problematic as it sounds, because we can expand the grid by a low factor x , and solve the Fourier transforms on this expanded grid. The mirror images will then be located $2x$ away, so their impact on the motion will be diluted by

a factor $1/(4x^2)$. Using $x=2$ suffices for our applications. In the vertical direction, however, the disk is geometrically thin. The vertical mirror images would still be close to the real disk unless a huge expansion factor be used, or the order of $x=1/h$, where h is the scale height of the disk. As the scale height is usually $h=0.05$, the expanding factor should be $x=20$, which means that the resolution and computational time would become prohibitive.

B.1.1 Potential of flatenned disks

Nevertheless, for such thin disks, the situation is closer to that of a very flattened configuration

$$\frac{\partial^2 \Phi}{\partial x^2} + \frac{\partial^2 \Phi}{\partial y^2} + \frac{\partial^2 \Phi}{\partial z^2} = 4\pi G \Sigma \delta(z) \quad (\text{B.5})$$

where Σ is the vertically integrated surface density. The presence of the Dirac delta is problematic in real space, but is removed in Fourier space since $\tilde{\delta}(x - x_0) = e^{-ikx_0}$. Therefore, the transform of Eq. (B.5) reads

$$\tilde{\Phi}(k_x, k_y, k_z) = -4\pi G \tilde{\Sigma} \frac{e^{-ik_z z_0}}{k_x^2 + k_y^2 + k_z^2}. \quad (\text{B.6})$$

The denominator can be cast in the form

$$\begin{aligned} k_x^2 + k_y^2 + k_z^2 &= k^2 + k_z^2 \\ &= (k_z + i|k|) + (k_z - i|k|) \end{aligned} \quad (\text{B.7})$$

where $|k| = \sqrt{k_x^2 + k_y^2}$. In this formulation, the inverse Fourier integration (from k_z back to z)

$$\tilde{\Phi}(k_x, k_y, z) = -2G \Sigma(k_x, k_y) \int_{-\infty}^{\infty} \frac{e^{ik_z(z-z_0)}}{(k_z + i|k|)(k_z - i|k|)} dk_z \quad (\text{B.8})$$

can be done analytically via residue around the pole ik to yield the solution

$$\tilde{\Phi}(k_x, k_y, z) = -\frac{2\pi G}{|k|} \tilde{\Sigma}(k_x, k_y) e^{-|k|(z-z_0)}. \quad (\text{B.9})$$

Apart from being faster (scaling as $N \log_2 N$), this method has the obvious advantage that the combined gravity of the gas and the solids is solved simultaneously. Other methods, such as a hierarquical particle-

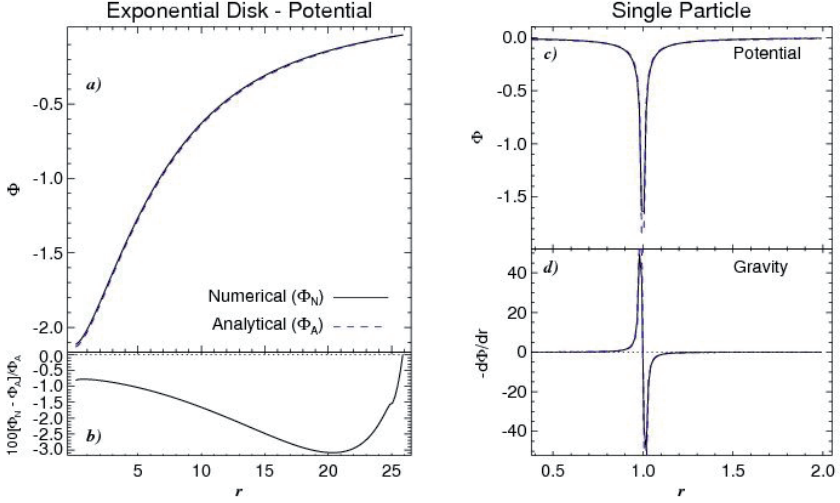


Figure B.1: *a.* The potential generated by an exponential disk computed by Eq. (B.9) is compared with the analytical expression. The accuracy (*b.*) is at the percent level.

c. The potential generated by a single particle agrees very well with its Newtonian prediction. In particular, the scheme ensures that the gravity (*d.*) is smooth and the particle does not suffer self-acceleration.

tree, would still need to solve the elliptic problem for the gas (considering that the gas gravity is of relevance).

In Fig. B.1 we show the numerical solutions for a gas distribution and for a single particle. We chose the exponential disk profile

$$\Sigma = \Sigma_0 e^{-r/r_0} \quad (\text{B.10})$$

for which the analytical solution is (Freeman 1970)

$$\Phi = -\pi G \Sigma_0 r [I_0(y)K_1(y) - I_1(y)K_0(y)] \quad (\text{B.11})$$

where $y=r/(2r_0)$ and I_n and K_n are the modified Bessel functions of first and second kind.

We see from the panels that the solution is very good. The mirror images lead to a slightly higher error at the outer disk. The error does not reach more than 3%, though. The potential generated by a single particle agrees well with its Newtonian prediction, deviating from it near the center, since we are limited by resolution and the gravity is underestimated. In particular, the solution is smooth and the particle does not experience self-acceleration.

Appendix C

C.1 N -body solver

The N -body code takes advantage of the existing Particles module of the PENCIL CODE. This module was coded by Anders Johansen and Anthony Mee with the initial intent of treating solid particles whose radius a_* is comparable to the mean free path λ of the gas (i.e., particles of Knudsen number $\text{Kn}=\lambda/2a_* \lesssim 1$), for which a fluid description is not valid. A N -body implementation based on that module only needed to include mass as extra state for the particles, solve for the N^2 gravitational pair interactions and distinguish between the N -body and the small bodies that are mapped into the grid as a ρ_p density field.

The particles of the N -body ensemble evolve due to their mutual gravity and by interacting with the gas and the swarm of small bodies. The equation of motion for particle i is

$$\frac{d\mathbf{v}_{p_i}}{dt} = \mathbf{F}_{g_i} - \sum_{j \neq i}^N \frac{GM_j}{\mathcal{R}_{ij}^2} \hat{\mathcal{R}}_{ij} \quad (\text{C.1})$$

where $\mathcal{R}_{ij} = |\mathbf{r}_{p_i} - \mathbf{r}_{p_j}|$ is the distance between particles i and j , and $\hat{\mathcal{R}}_{ij}$ is the unit vector pointing from particle j to particle i . The first term of the R.H.S. is the combined gravity of the gas and of the smaller particles onto the particle i , solved via

$$\mathbf{F}_{g_i} = -G \int_V \frac{[\rho_g(\mathbf{r}) + \rho_p(\mathbf{r})] \mathcal{R}_i}{(\mathcal{R}_i^2 + b_i^2)^{3/2}} dV, \quad (\text{C.2})$$

where the integration is carried out over the whole disk. The smoothing distance b_i is taken to be as small as possible. It is usually a fraction of the Hill radius. The stellar potential can be treated as unsoftened ($b_* = 0$) in a cylindrical grid, or if we provide an inner boundary in a Cartesian grid. For few particles (< 10), calculating the integral for every particle is practical. For larger ensembles one would prefer to solve the Poisson equation to calculate the disk's potential

$$\mathbf{F}_{gi} = -\nabla\Phi_{sg} \quad (\text{C.3})$$

$$\nabla^2\Phi_{sg} = 4\pi G(\rho_g + \rho_p). \quad (\text{C.4})$$

We note that in this formulation there is no distinction between a planet and a star except for the mass. The star evolves dynamically due to the gravity of the planets, wobbling around the center of mass of the system, which is set to the center of the grid.

The evolution of the particles is done with the same third-order Runge-Kutta time-stepping routine used for the gas. The particles define the timestep also by the Courant condition that they should not move more than one cell at a time. For pure particle runs, where the grid is absent, we adopt a fixed time-step $t_p \ll 2\pi\Omega_{\text{fp}}^{-1}$ where Ω_{fp} is the angular frequency of the fastest particle.

C.1.1 Conservation of the Jacobi constant

We test the stability of the N -body solver by monitoring the evolution of the Jacobi constant (Eq. (6.30)), a conserved quantity in the circular restricted three-body problem and thus very suitable as diagnostic of the quality of the numerical solution. We usually evolve the quantities in the inertial frame (Fig. C.1, left panel), which dismisses the addition of the extra accelerations in Eq. (6.20). Positions and velocities are transformed from the corotational to the inertial frame according to

$$\begin{aligned} \mathbf{r}_{\text{sid}} &= \mathbf{R}\mathbf{r}_{\text{syn}} \\ \mathbf{v}_{\text{sid}} &= \mathbf{v}_{\text{syn}} + \boldsymbol{\Omega} \times \mathbf{r}_{\text{syn}}, \end{aligned}$$

where $\mathbf{r}_{\text{sid}}=(\xi, \eta, z)$ are the coordinates in the inertial frame and \mathbf{R} is the rotation matrix. Equation (6.30) is thus written

$$C_J = 2\left(\frac{\mu_1}{r_1} + \frac{\mu_2}{r_2}\right) + 2\Omega(\xi\dot{\eta} - \eta\dot{\xi}) - (\dot{\xi}^2 + \dot{\eta}^2 + \dot{z}^2). \quad (\text{C.5})$$

The right hand side panel of Fig. C.1 shows the evolution of the Jacobi constant relative to its initial value in a simulation with $\mu_2=10^{-3}$, and the test particle is placed initial at position $(x, y)=(2, 0)$. The Jacobi constant is conserved up to one part in 10^5 within the timespan of 100 orbits.

We stress that the level of conservation is poor when compared to integrators designed to specifically deal with long-term N -body problems. These integrators are usually symplectic, unlike the Runge-Kutta

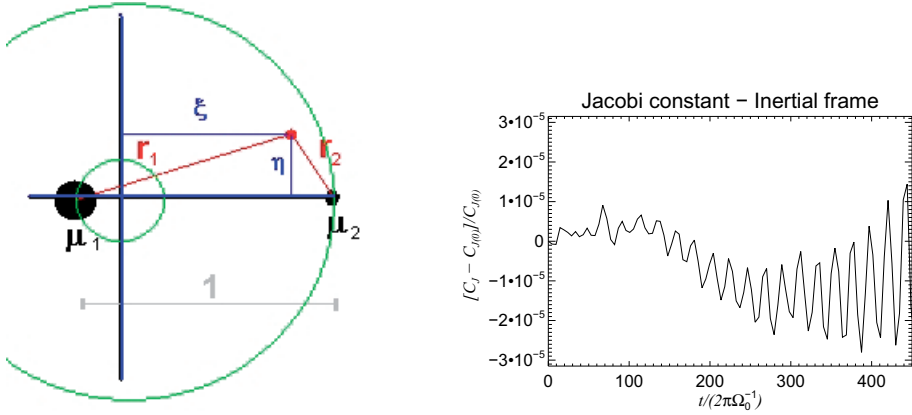


Figure C.1: Sketch of the inertial frame (left hand side), with origin at the barycenter. The masses and distances are normalized to 1. The Jacobi constant is given by Eq. (C.5). We show the degree of conservation on the image at the right hand side. For 100 orbits, the usual time we evolve the simulations, the Jacobi constant is conserved up to one part in 10^{-5} . The conservation is deemed poor when compared to dedicated N -body codes that are used for calculations of timescales of millions, billions, of years. But for hydrodynamical simulations, up to only a few thousand years, this degree of conservation is acceptable.

scheme of the PENCIL CODE. As such, PENCIL should not be used to deal with evolution over millions of years. But for the time-span we are interested on, of only thousands of years (≈ 100 orbits), this degree of conservation of the Jacobi constant can be deemed acceptable.

C.1.2 A many-body test

As a further test, we perform a simulation of the solar system in Cartesian coordinates (Fig. C.2). Nine particles, representing the Sun and the eight planets were simulated. The masses were normalized to $M_{\text{total}}=1$ and we initialize the planets aligned at their respective semi-major axes. The normalized masses and initial semimajor axes, from Mercury to Neptune, are

$$\begin{aligned}
 (\mu, a_0)_{\text{v}} &= (2 \times 10^{-7}, 0.38) & (\mu, a_0)_{\text{q}} &= (3 \times 10^{-6}, 0.72) \\
 (\mu, a_0)_{\text{p}} &= (3 \times 10^{-6}, 1.00) & (\mu, a_0)_{\text{s}} &= (3 \times 10^{-7}, 1.50) \\
 (\mu, a_0)_{\text{j}} &= (1 \times 10^{-3}, 5.20) & (\mu, a_0)_{\text{r}} &= (3 \times 10^{-4}, 10.0) \\
 (\mu, a_0)_{\text{d}} &= (4 \times 10^{-5}, 19.0) & (\mu, a_0)_{\text{n}} &= (5 \times 10^{-5}, 30.0)
 \end{aligned} \tag{C.6}$$

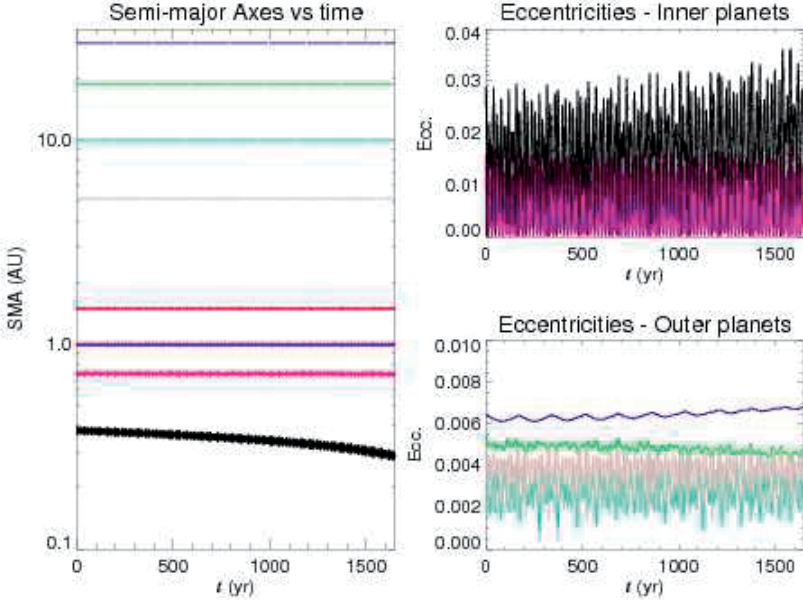


Figure C.2: Solar system simulation with the N -body solver of the PENCIL CODE. We follow the evolution of the Sun and the eight planets for $\approx 1.5 \times 10^3$ yr, with a fixed time-step of 10^{-3} yr. The time-stepping scheme is the same third order Runge-Kutta time-step scheme used for the evolution of the hydrodynamical quantities (although this simulation did not include gas). The excitation of eccentricity is a decreasing function of distance. This lead to the de-stabilisation of Mercury's orbit, whose semi-major axis decreases from 0.4 to 0.3 during the course of the simulation. All other planets have stable semi-major axes, with mild or little eccentricity pumping. We usually place the inner boundary of the hydro simulations at 1-2 AU.

The planets have their initial velocities set to the Keplerian value. The Sun, as explained, has normalized mass

$$\mu_{\odot} = 1 - \sum_{p=1}^8 \mu_p = 0.998604, \quad (\text{C.7})$$

and is initialized at a position and a velocity that keeps the center of mass at the center of the grid, at rest.

With a time-step of 10^{-3} yr, a whole Neptune orbit for the ensemble takes one minute in a single processor. We followed the evolution of the system for 10 Neptune's orbits (≈ 1652 years), during which it can be seen that all planets except Mercury keep orbiting the Sun stably,

with modest eccentricity pumping. Mercury's behavior is a result of poorer conservation of the Jacobi constant at such short distances from the star, which is also from the plot as the (numerical) eccentricity excitation is a decreasing function of semi-major axis. In contrast, we usually use an inner boundary located at 1.0-2.0 AU, which, from Fig. C.2, is seen to be stable. We conclude that the N -body solver is stable and sufficiently accurate during the usual timespan of our simulations.

As an extension of the particle's module, the N -body is fully compatible with the parallel optimization of `PENCIL`, which further speeds up the calculations. Parallelization, however, is not yet possible for pure particle runs, since it relies on splitting the grid between the processors. So far, the N -body code does not allow the sink particles to have a time-evolving mass. Such a restriction limits the study of accretion onto the planet, but we do not deal with this problem in this work.

Appendix D

D.1 Useful numbers and relations

Many readers might be familiar with Astronomy but not acquainted with the physical state of protoplanetary disks. In Table D.1, we show the nominal values of some quantities of interest that hopefully will provide a better understanding of the contents of this work.

A number of parametrizations are also of help. Below we show:

Surface density

$$\Sigma = 3 \times 10^3 \text{g cm}^{-2} \left(\frac{1\text{AU}}{r} \right)^{1.5} \quad (\text{D.1})$$

Volume density at midplane

$$\rho = 1.7 \times 10^{-9} \text{g cm}^{-3} \left(\frac{500\text{K}}{T} \right)^{1/2} \left(\frac{1\text{AU}}{r} \right)^3 \quad (\text{D.2})$$

Sound speed

$$c_s = \left(\frac{\gamma K T}{\mu m_H} \right)^{1/2} = 1.60 \text{kms}^{-1} \left(\frac{T}{500\text{K}} \right)^{1/2} \left(\frac{2}{\mu} \right)^{1/2} \quad (\text{D.3})$$

Hills Radius

$$R_H = a \left(\frac{M_p}{3M_\odot} \right)^{1/3} \quad (\text{D.4})$$

Keplerian Angular frequency

$$\Omega_K = \left(\frac{GM_\odot}{r^3} \right)^{1/2} \quad (\text{D.5})$$

Disk scale height

$$H = c_s \Omega^{-1} = 7.20 \times 10^{11} \text{cm} \left(\frac{T}{500\text{K}} \right)^{1/2} \left(\frac{r}{1\text{AU}} \right)^{3/2} \left(\frac{2}{\mu} \right)^{1/2} \quad (\text{D.6})$$

Table D.1: *Useful values and parametrizations*

Quantity	Symbol	Value
Astronomical unit	AU	1.496×10^{13} cm
Solar mass	M_{\odot}	1.99×10^{33} g
Earth mass	M_{\oplus}	5.9742×10^{27} g
Jupiter mass	$M_J, M_{\mathcal{J}}$	$0.001 M_{\odot} = 318 M_{\oplus}$
Mass accretion rate	\dot{M}	$10^{-8} M_{\odot} \text{yr}^{-1}$
Orbital velocity at 5.2 AU	u_{ϕ}	13.6 km s^{-1}
Adiabatic sound speed at 5.2 AU		775 m s^{-1}
Isothermal sound speed at 5.2 AU	c_{s0}	657 m s^{-1}
Dimensionless alpha viscosity	α	$10^{-4} - 10^{-2}$
Mean molecular weight of the gas (H_2)	μ	2
Lifetime of the disk	-	$10^6 - 10^7$ yr

Disk aspect ratio

$$h \equiv \frac{H}{r} = 0.048 \left(\frac{T}{500\text{K}} \right)^{1/2} \left(\frac{r}{1\text{AU}} \right)^{3/2} \left(\frac{2}{\mu} \right)^{1/2} \quad (\text{D.7})$$

Anomalous viscosity

$$\nu = \alpha c_s H \quad (\text{D.8})$$

Bibliography

- [1] Armitage, P. J., Livio, M., & Pringle, J. E. 2001, MNRAS, 324, 705
- [2] Arnold, H.D. 1911, Phys. Rev., 32, 233
- [3] Artymowicz P., 2001, in Penny A., Artymowicz P., Lagrange A.-M., Russel S., eds, Proc. IAU symp. 202, *Planetary Systems in the Universe: Observation, Formation and Evolution*. Astron. Soc. Pac., San Francisco, p. 13
- [4] Ayliffe, B.A., & Bate, M.R. 2008, arXiv0811.1259
- [5] Balbus, S.A., & Hawley, J.F., 1998, RvMP, 70, 1
- [6] Balbus, S.A., & Hawley, J.F., 1992, ApJ, 400, 610
- [7] Balbus, S.A., & Hawley, J.F., 1991, ApJ, 376, 214
- [8] Barranco, J.A., & Marcus, P.S. 2005, ApJ, 623, 1157
- [9] Barge, P., Sommeria, J., 1995, A&A, 295, 1
- [10] Benz, W. 2000, SSRv, 92, 279
- [11] Binney, J. & Tremaine, S. 1987, *Galactic Dynamics*, Princeton University Press
- [12] Blaes, O. M. & Balbus, S. A. 1994, ApJ, 421, 163
- [13] Blum, J. & Wurm, G. 2008, ARA&A, 46, 21
- [14] Boss, A.P. 2004, ApJ, 610, 456
- [15] Boss, A.P. 2005, ApJ, 629, 535
- [16] Bracco, A., Chavanis, P.-H., Provenzale, A., & Spiegel, E. A. 1999, Physics of Fluids, 11, 2280
- [17] Brandenburg, A, Nordlund, Å, Stein, R.F., & Torkelsson, U. 1995, ApJ, 446, 741
- [18] Brauer, F., Dullemond, C. P., Johansen, A., Henning, Th., Klahr, H., & Natta, A. 2007, A&A, 469, 1169
- [19] Bryden, G.; Chen, X.; Lin, D. N. C., Nelson, R. P., Papaloizou, J. C. B., 1999, ApJ, 514, 344

- [20] Cassini, J.D. 1666, cited in *Phil. Trans. Roy. Soc.* 1, 143, Of a permanent spot in Jupiter; by which is manifested the conversion of Jupiter about its own axis.
- [21] Chandrasekhar, S., 1960, *Proc. Nat. Acad. Sci.*, 46, 253
- [22] Chandrasekhar, S., 1961, *Hydrodynamic and Hydromagnetic Stability* (Oxford: Clarendon), 384
- [23] Chavanis, P.-H. 2000, *A&A*, 356, 1089
- [24] Choudhuri, A.R., 1998, *The Physics of Fluids and Plasmas: an Introduction for Astrophysicists*, (Cambridge University, Cambridge, England)
- [25] Crow, S.C. 1970, *AIAAJ*, 8, 2172
- [26] Donati, J.-F., Paletou, F., Bouvier, J., & Ferreira, J. 2005, *Nature*, 438, 466
- [27] Draine, B. T., Roberge, W. G., & Dalgarno, A. 1983, *ApJ*, 264, 485
- [28] Dubrulle, B., Marié, L., Normand, Ch., Richard, D., Hersant, F., & Zahn, J.-P. 2005, *A&A*, 429, 1
- [29] Dubrulle, B., Morfill, G., & Sterzik, M., 1995, 114, 237
- [30] Edgar, R. G., & Quillen, A. C. 2008, *MNRAS*, 387, 387
- [31] Epstein, P., 1924, *PhRv*, 23, 710
- [32] Fleming, T. & Stone, J. M. 2003, *ApJ*, 585, 908
- [33] Freeman, K., 1970, *ApJ*, 160, 811
- [34] Fromang, S., Papaloizou, J., Lesur, G., & Heinemann, T. 2007, *A&A*, 476, 1123
- [35] Fromang, S., & Papaloizou, J. 2007, *A&A*, 476, 1113
- [36] Fromang, S., & Nelson, R. P., 2005, *MNRAS*, 364, 81
- [37] Gammie, C. F. 1996, *ApJ*, 457, 355
- [38] Garaud, P., & Lin, D. N. C. 2004, *ApJ*, 608, 1050
- [39] Glassgold, A. E., Najita, J., & Igea, J. 1997, *ApJ*, 480, 344
- [40] Gledzer, E.B., Dolzhanskii, F.V., Obukhov, A. M., & Ponomarev, V. M. 1975, *Isv. Atmos. Ocean. Phys.*, 11, 617
- [41] Goldreich, P., & Tremaine, S. 1978, *ApJ*, 222, 850
- [42] Goldreich, P., & Ward, W. R. 1973, *ApJ*, 183, 1051
- [43] Goodman, J., Narayan, R. & Goldreich, P. 1987, *MNRAS*, 225, 695

- [44] Haghhighipour, N. & Boss, A. P. 2003, ApJ, 583, 996
- [45] Haisch, K. E., Lada, E. A., Lada, C. J., 2001, ApJ, 553, 153
- [46] Haugen, N.E.L., & Brandenburg, A., 2004, PhRvE, 70b, 6405
- [47] Hawley, J.F. & Balbus, S.A., 1991, ApJ, 376, 223
- [48] Hawley, J.F. & Balbus, S.A., 1992, ApJ,
- [49] Heisenberg, W. 1924, *Annalen der Physik*, 379, 577
- [50] Helmholtz, H. 1854, Lecture "On the interaction of natural forces," Königsberg, February 7, in *Phil. Mag.* 11 [series 4], 489-518 (1856).
- [51] Hubickyj, O., Bodenheimer, P., & Lissauer, J. J. 2005, *Icarus*, 179, 415
- [52] Igea, J. & Glassgold, A. E. 1999, ApJ, 518, 848
- [53] Ilgner, M.; Nelson, R. P. 2006, A&A, 455, 731
- [54] Inaba, S., & Barge, P. 2006, ApJ, 649, 415
- [55] Johansen, A., Brauer, F., Dullemond, C., Klahr, H., & Henning, T. 2008, A&A, 486, 597
- [56] Johansen, A., Oishi, J. S., Mac Low, M.-M., Klahr, H., Henning, Th. & Youdin, A., 2007, *Nature*, 448, 1022
- [57] Johansen, A., & Youdin, A. 2007, ApJ, 662, 627
- [58] Johansen, A., Klahr, H., & Henning, T. 2006, ApJ, 636, 1121
- [59] Johansen, A., & Klahr, H., 2005, ApJ, 634, 1353
- [60] Johansen, A., Andersen, A. C., & Brandenburg, A., 2004, A&A, 417, 361
- [61] Johnson, B.M., & Gammie, C.F. 2005, ApJ, 635, 149
- [62] Kerswell, R.R. 2002, *Annu. Rev. Fluid Mech.*, 34, 83
- [63] Klahr, H., 2004, ApJ, 606, 1070
- [64] Klahr, H., & Bodenheimer, P., 2006, ApJ, 639, 432
- [65] Klahr, H., & Bodenheimer, P., 2003, ApJ, 582, 869
- [66] Klahr, H., & Kley, W. 2006, A&A, 445, 747
- [67] Kley, W., 1999, *MNRAS*, 303, 696
- [68] Kokubo, E., Kominami, J., & Ida, S. 2006, ApJ, 642, 1131
- [69] Kraichnan, R. H. 1967, *Physics of Fluids*, 10, 1417

- [70] Kwok, S., 1975, ApJ, 198, 583
- [71] Lain, S., Bröder, D., & Sommerfeld, M. 1999, Chem. Eng. Sc., 54, 4913
- [72] Landau L.D. & Lifshitz, E.M. 1987, *Fluid Mechanics*, Pergamon Press, Oxford
- [73] Laplace P.S., 1796, *Mécanique Céleste*
- [74] Lin, D.N.C., & Papaloizou, J., 1993, *Protostars and Planets III*
- [75] Lin, D.N.C., & Papaloizou, J., 1986, ApJ, 309, 846
- [76] Lin, D.N.C., & Papaloizou, J., 1979a
- [77] Lin, D.N.C., & Papaloizou, J., 1979b
- [78] Lyttleton, R. A. 1972, MNRAS, 158, 463
- [79] Rüdiger, G., Arlt, R., & Shalybkov, D. 2002, A&A, 391, 781
- [80] Li, H., Finn, J. M., Lovelace, R. V. E., & Colgate, S. A. 2000, ApJ, 533, 1023
- [81] Li, H., Colgate, S. A., Wendroff, B., & Liska, R. 2001, ApJ, 551, 874
- [82] Lovelace, R. V. E., Li, H., Colgate, S. A., & Nelson, A. F. 1999, ApJ, 513, 805
- [83] Lodato, G. 2008, *New Astronomy Reviews*, 52, 21
- [84] Lodato, G. & Rice, W. K. M. 2005, MNRAS, 358, 1489
- [85] Lodato, G.; Rice, W. K. M., 2004, MNRAS, 351, 630
- [86] Lubow, S. H., Seibert, M., Artymowicz, P., 1999, ApJ, 526, 1001
- [87] Lynden-Bell, D., 1969, *Nature*, 223, 690
- [88] Lynden-Bell, D. & Pringle, J. E., 1974, MNRAS, 168, 603
- [89] MacPherson, G. J., Davis, A. M., & Zinner, E. K. 1995, *Meteoritics*, 30, 365
- [90] Marcus P.S., 1988, *Nature*, 331, 693
- [91] Méheut, H., Casse, F., VarniÁire, P., & Tagger, M. 2008, *Proceedings of the Annual meeting of the French Society of Astronomy and Astrophysics*, p.417, Eds.: C. Charbonnel, F. Combes and R. Samadi.
- [92] Miki, S., 1982, P.T.Ph., 67, 1053
- [93] Miller, K.A. & Stone, J.M. 2000, ApJ, 534, 398
- [94] Millikan, R. A. 1911, *Phys. Rev.*, 32, 349

- [95] Millikan, R. A. 1923, *Phys. Rev.*, 22, 1
- [96] Mizuno H., 1980, *P.T.Ph.*, 64, 2
- [97] Nakagawa Y., Sekiya M., & Hayashi C., 1986, *Icarus*, 67, 375
- [98] Oishi, J. S., Mac Low, M.-M., & Menou, K. 2007, *ApJ*, 670, 805
- [99] Ogilvie, G.I. & Lubow, S. H., 2002, *MNRAS*, 330, 950
- [100] Paardekooper, S.-J. 2007, *A&A*, 462, 355
- [101] Paardekooper S.-J. 2006, PhDT
- [102] Pessah, M. E., Chan, C.-K., & Psaltis, D. 2007, *ApJ*, 668, 51
- [103] Petersen, M. R., Stewart, G. R., Julien, Keith, 2007, *ApJ*, 658, 1252
- [104] Phelps, A. 1979, *Electron-Molecule Scattering*, Edited by Sanborn C. Brown. New York: John Wiley and Sons
- [105] Pollack, J.B, Hubickyj, O., Bodenheimer, P., Lissauer, J. J., Podolak, M., & Greenzweig, Y., 1996, *Icarus*, 124, 62
- [106] Prandtl, L. 1905, *Verhandlungen des dritten Internationalen Mathematiker-Kongresses (Heidelberg 1904)*, 484
- [107] Reynolds, O., 1895, *Phil. Trans. Roy. Soc.*, 186, 123
- [108] Safronov, V. S. 1969, *QB*, 981, 26
- [109] Sekiya, M. 1998, *Icarus*, 133, 298
- [110] Shakura, N.I., & Sunyaev, R.A., 1973, *A&A*, 24, 37
- [111] Shen, Y., Stone, J.M., & Gardiner, T.A. 2006, *ApJ*, 653, 513
- [112] Sicilia-Aguilar, A., Hartmann, L.W., Briceño, C., Muzerolle, J., & Calvet, N., 2004, *AJ*, 128, 805
- [113] Skorov, Y. V. & Rickman, H., 1999, *Planet. Space. Sci.*, 935, 949
- [114] Spitzer, L., 1962, *Physics of Fully Ionized Gases* (Wiley Interscience, New York)
- [115] Terquem C. 2008, *ApJ*, 689, 532
- [116] Thomson, W. 1862, *Macmillan's Magazine*, 5, 288
- [117] Thomson, W. 1897, *Collected Papers*, 5, 205
- [118] Toomre, A., 1963, *ApJ*, 138, 385
- [119] Turner, N. J. & Sano, T. 2008, *ApJ*, 679, 131

- [120] Umebayashi, T. 1983, P.Th.Ph., 69, 480
- [121] Umebayashi, T. & Nakano, T. 2009, ApJ, 690, 69
- [122] Umebayashi, T. & Nakano, T. 1981, PASJ, 33, 617
- [123] Umurhan, O. M. 2006, MNRAS, 365, 85
- [124] Urpin, V. & Brandenburg, A. 1998, MNRAS, 294, 399
- [125] de Val-Borro, M., Edgar, R.G., Artymowicz, P., Cieliegielag, P., Cresswell, P., D'Angelo, G., Delgado-Donate, E.J., Dirksen, G., Fromang, S., Gawryszczak, A., Klahr, H., Kley, W., Lyra, W., Masset, F., Mellema, G., Nelson, R., Paardekooper, S.-J., Peplinski, A., Pierens, A., Plewa, T., Rice, K., Schäfer, C., & Speith, R. 2006, MNRAS
- [126] de Val-Borro, M., Artymowicz, P., D'Angelo, G., & Peplinski, A., 2007, A&A, 471, 1043
- [127] Varnière, P., & Tagger, M. 2006, A&A, 446, 13
- [128] Velikhov, E. P., 1959, Soviet Phys. - JETP, 36, 1398
- [129] Youdin, A., & Goodman, J., 2005, ApJ, 620, 459
- [130] Youdin, A., & Johansen, A., 2007, ApJ, 662, 613
- [131] Weidenschilling, S. J., & Cuzzi, J. N. 1993, *Protostars and Planets III*, p1031
- [132] Weidenschilling, S.J. 1980, Icarus, 44, 172
- [133] Weidenschilling, S.J. 1977a, MNRAS, 180, 57
- [134] Weidenschilling, S.J. 1977b, Ap&SS, 51, 153
- [135] Woitke, P., & Helling, C., 2003, A&A, 399, 297
- [136] Yavneh, I., McWilliams, J. C., & Molemaker, M. 2001, Journal of Fluid Mechanics, 448, 1
- [137] Youdin, A. N., & Shu, F. H. 2002, ApJ, 580, 494

Acta Universitatis Upsaliensis

*Digital Comprehensive Summaries of Uppsala Dissertations
from the Faculty of Science and Technology 593*

Editor: The Dean of the Faculty of Science and Technology

A doctoral dissertation from the Faculty of Science and Technology, Uppsala University, is usually a summary of a number of papers. A few copies of the complete dissertation are kept at major Swedish research libraries, while the summary alone is distributed internationally through the series Digital Comprehensive Summaries of Uppsala Dissertations from the Faculty of Science and Technology. (Prior to January, 2005, the series was published under the title “Comprehensive Summaries of Uppsala Dissertations from the Faculty of Science and Technology”.)



ACTA
UNIVERSITATIS
UPSALIENSIS
UPPSALA
2009

Distribution: publications.uu.se
urn:nbn:se:uu:diva-9537

Paper I



Global magnetohydrodynamical models of turbulence in protoplanetary disks

I. A cylindrical potential on a Cartesian grid and transport of solids

W. Lyra¹, A. Johansen², H. Klahr², and N. Piskunov¹

¹ Department of Astronomy and Space Physics, Uppsala Astronomical Observatory, Box 515, 751 20 Uppsala, Sweden
e-mail: wlyra@astro.uu.se

² Max-Planck-Institut für Astronomie, Königstuhl 17, 69117 Heidelberg, Germany

Received 25 May 2007 / Accepted 6 December 2007

ABSTRACT

Aims. We present global 3D MHD simulations of disks of gas and solids, aiming at developing models that can be used to study various scenarios of planet formation and planet-disk interaction in turbulent accretion disks. A second goal is to demonstrate that Cartesian codes are comparable to cylindrical and spherical ones in handling the magnetohydrodynamics of the disk simulations while offering advantages, such as the absence of a grid singularity, for certain applications, e.g., circumbinary disks and disk-jet simulations.

Methods. We employ the PENCIL CODE, a 3D high-order finite-difference MHD code using Cartesian coordinates. We solve the equations of ideal MHD with a local isothermal equation of state. Planets and stars are treated as particles evolved with an N -body scheme. Solid boulders are treated as individual superparticles that couple to the gas through a drag force that is linear in the local relative velocity between gas and particle.

Results. We find that Cartesian grids are well-suited for accretion disk problems. The disk-in-a-box models based on Cartesian grids presented here develop and sustain MHD turbulence, in good agreement with published results achieved with cylindrical codes. Models without an inner boundary do not show the spurious build-up of magnetic pressure and Reynolds stress seen in the models with boundaries, but the global stresses and alpha viscosities are similar in the two cases. We investigate the dependence of the magnetorotational instability on disk scale height, finding evidence that the turbulence generated by the magnetorotational instability grows with thermal pressure. The turbulent stresses depend on the thermal pressure obeying a power law of 0.24 ± 0.03 , compatible with the value of 0.25 found in shearing box calculations. The ratio of Maxwell to Reynolds stresses decreases with increasing temperature, dropping from 5 to 1 when the sound speed was raised by a factor 4, maintaining the same field strength. We also study the dynamics of solid boulders in the hydromagnetic turbulence, by making use of 10^6 Lagrangian particles embedded in the Eulerian grid. The effective diffusion provided by the turbulence prevents settling of the solids in an infinitesimally thin layer, forming instead a layer of solids of finite vertical thickness. The measured scale height of this diffusion-supported layer of solids implies turbulent vertical diffusion coefficients with globally averaged Schmidt numbers of 1.0 ± 0.2 for a model with $\alpha \approx 10^{-3}$ and 0.78 ± 0.06 for a model with $\alpha \approx 10^{-1}$. That is, the vertical turbulent diffusion acting on the solids phase is comparable to the turbulent viscosity acting on the gas phase. The average bulk density of solids in the turbulent flow is quite low ($\rho_p = 6.0 \times 10^{-11} \text{ kg m}^{-3}$), but in the high pressure regions, significant overdensities are observed, where the solid-to-gas ratio reached values as great as 85, corresponding to 4 orders of magnitude higher than the initial interstellar value of 0.01.

Key words. magnetohydrodynamics (MHD) – accretion, accretion disks – instabilities – turbulence – solar system: formation – diffusion

1. Introduction

Planets have long been believed to form in disks of gas and dust around young stars (Kant 1755; Laplace 1796), interacting with their surroundings via a set of complex and highly nonlinear processes. In the core accretion scenario for giant planet formation (Mizuno 1980), dust coagulates first into km-sized icy and rocky planetesimals (Safronov 1969; Goldreich & Ward 1973; Youdin & Shu 2002) that further collide, forming progressively larger solid bodies that eventually give rise to cores of several Earth masses. If a critical mass is attained, these cores become gas giant planets by undergoing runaway accretion of gas (Pollack et al. 1996). Otherwise, just a small amount of nebular gas is retained by the core, which ends up as an ice giant.

The success of this picture in explaining the overall shape of the solar system was shaken by the discovery of the extra-solar

planets. In less than a decade, the zoo of planetary objects received exotic members such as close-in Hot Jupiters (Mayor & Queloz 1995), pulsar planets (Wolszczan & Frail 1992), highly eccentric giants (Marcy & Butler 1996), free-floating planets (Lucas & Roche 2000), and super-Earths (Rivera et al. 2005). Thus, understanding the diversity of these extra-solar planets is a crucial task in planet formation theory.

Planet-disk interaction seems to be one of the obvious candidates to account for this diversity. Planets exchange angular momentum with the disk, leading to either inward or outward migration (Ward 1981; Lin & Papaloizou 1986; Ward & Hourigan 1989; Masset et al. 2006). An understanding of the physical state of accretion disks is essential to provide a detailed picture of the effect of migration on planetary orbits.

Analytical theory must necessarily contain a number of linearizing simplifications. Therefore, numerical simulations are a

major tool to provide advances in the problem. But even then, the large computational demands of such calculations have put some restrictions and limitations in the models presented so far. Because of this, although many of the individual physical processes occurring on circumstellar environments are understood in some detail, state-of-the-art calculations on planet formation still lag behind our current understanding, containing simplifying assumptions needed to reduce the computational effort.

For example, the evolution of temperature is usually neglected in solving the dynamical equations, favoring an imposed temperature profile. Paardekooper & Mellema (2006) showed that in non-isothermal disks, the net torques acting on a forming planet can change sign due to asymmetric heating on the planet's corotation region, potentially stopping and reversing the migration of the planet. 2D and 3D models of disks with radiative transfer were presented by D'Angelo et al. (2003) and Klahr & Kley (2006), showing that a high-mass planet may carve a cold gap in the disk while retaining a thick circumplanetary cloud. But no radiative global simulation with explicit ray tracing, able to consistently treat optically thin and thick regions and the transition between them, has been presented so far.

Magnetic fields have been shown to play a major role in the structure and evolution of accretion disks. Observational efforts in the detection and analysis of protoplanetary disks show evidence that these disks accrete, with a mass accretion rate of the order $\approx 10^{-8} M_{\odot} \text{ yr}^{-1}$ (e.g., Sicilia-Aguilar et al. 2004). Such a powerful accretion cannot be explained by molecular viscosity, requiring some other mechanism to transport angular momentum outward. Balbus & Hawley (1991) pointed out the importance of the magnetorotational instability (Velikhov 1959; Chandrasekhar 1960, 1961) for accretion disks. In their important work, they show that this magnetorotational instability (MRI) is operative in sufficiently ionized Keplerian disks as long as the magnetic field is subthermal, generating a turbulence powerful enough to explain observed accretion rates in protoplanetary disks.

However, although magnetic fields are ubiquitous in the universe, protoplanetary disks are thought to be “cold” and thus not completely ionized. Cosmic rays can provide the required ionization for the MRI to operate, but they cannot penetrate all the way to the midplane of the disk (a standard value for the penetration depth is a gas column density of $\Sigma = 100 \text{ g cm}^{-2}$). The result is that in the region where giant planets are thought to form, only the surface of the disk is sufficiently ionized for the MRI to grow. Turbulence thus likely operates in a surface layer, while the midplane is neutral and laminar, constituting a so called “dead zone” (Gammie 1996; Miller & Stone 2000; Oishi et al. 2007).

As a result of the mentioned difficulties of modeling the coupled interaction between radiation, magnetic fields, dust grains, solids, neutral and ionized gas in the gravitational potential of a star and embedded planets, the numerical works in the field show a heterogeneity of methods, with most works tackling only some aspects of the problem. Particularly, numerical simulations have focused on local Cartesian shearing boxes (e.g., Hawley et al. 1995; Brandenburg et al. 1995) or global disks on cylindrical grids (e.g., Hawley 2001; Armitage et al. 2001; Nelson 2005). As the MRI is a local process, the shearing box has the advantage of capturing much of the physics of the problem while significantly reducing the computational effort and complexity – for instance (shear-) periodic boundary conditions can be used. The global disks on cylindrical grids offer the advantage of having the grid and flow geometry coinciding, but in this case, special care must be taken for the boundary conditions, as reflective boundaries make waves bounce through the computational

domain in an unphysical manner and outflow boundary conditions may lead to too much mass loss (Fromang & Nelson 2006). Fromang & Nelson (2006) have also presented the first simulation of the MRI in global disks with vertical density stratification. A comparison between their models and a stratified version of ours will be addressed in future work.

In a series of articles we aim at constructing global radiative magnetohydrodynamical simulations. In this first paper, we present the features and capabilities of the numerical scheme used by constructing cylindrical disk models of gas and solids with MHD turbulence. These models will be developed in future work to allow for stratification, radiation and a global self-consistent treatment of dead zones.

The simulations presented here are embedded in Cartesian boxes. Although it can be regarded as unpractical for simulating a flow with cylindrical symmetry, such a grid also presents some advantages. First, cylindrical grids are a strong limitation for flows that deviate from cylindrical symmetry, e.g. circumbinary disks or 3D jet simulations, mainly because it is impossible to have a flow across the center of the grid, and at $r = 0$ reflection must occur. Second, this approach has proved useful in view of computational simplicity and parallelization efficiency (e.g. Dobler et al. 2006). In particular, by having cells of constant aspect ratio, Cartesian grids have much reduced numerical dissipation when compared to grids with complex geometry (van Noort et al. 2002). Therefore, while cylindrical and spherical grids can explicitly conserve angular momentum w.r.t the origin of the coordinate system, it is of no benefit for systems that do not have the center of mass at the origin. Third, as photons travel in straight lines (in the absence of general relativistic effects), a radiative transfer scheme with ray tracing is simpler to implement in a Cartesian grid in spite of the cylindrical symmetry of the hydrodynamical flow (Freytag et al. 2002).

As a numerical solver we employ the PENCIL CODE¹, a high (6th) order finite difference code. Such a numerical tool is highly different from most other astrophysical codes in use in the literature (see de Val-Borro et al. 2006, and references therein), thus also providing an independent check of the results so far obtained in the field.

This paper is structured as follows: we discuss the model in Sect. 2, proceeding to test cases in Sect. 3. In Sect. 4 we discuss the several MHD simulations performed. In Sect. 5 the models with solids are presented, finally leading to the conclusions in Sect. 6.

2. The model

2.1. Gas dynamics

The equations solved are those of ideal MHD in an inertial reference frame with a central gravity source. The equation governing the evolution of density is the continuity equation

$$\frac{D\rho}{Dt} = -\rho \nabla \cdot \mathbf{u} + f_{\rho}(\rho), \quad (1)$$

where ρ and \mathbf{u} are the density and velocity of the gas. The operator $D/Dt = \partial/\partial t + \mathbf{u} \cdot \nabla$ represents the advective derivative.

The equation of motion is the sum of all forces acting on a parcel of gas. It reads

$$\frac{D\mathbf{u}}{Dt} = -\frac{1}{\rho} \nabla p - \nabla \Phi + \frac{\mathbf{J} \times \mathbf{B}}{\rho} + f_{\nu}(\mathbf{u}, \rho), \quad (2)$$

¹ See <http://www.nordita.dk/software/pencil-code>

where p is pressure, Φ the gravitational potential, \mathbf{B} is the magnetic field, $\mathbf{J} = \mu_0^{-1} \nabla \times \mathbf{B}$ is the volume current density, as defined by Ampère's Law, and μ_0 is the magnetic permeability of vacuum.

The evolution of the magnetic field is governed by the induction equation. The PENCIL CODE, however, works not with the magnetic field itself, but with the magnetic potential A , where $\mathbf{B} = \nabla \times A$. This automatically guarantees the solenoidality of the magnetic field, as the condition $\nabla \cdot \mathbf{B} = \nabla \cdot (\nabla \times A) = 0$ is always satisfied. The induction equation formulated for the magnetic potential reads

$$\frac{\partial A}{\partial t} = \mathbf{u} \times \mathbf{B} + f_\eta(A). \quad (3)$$

The equation of state, relating pressure and density, closes the system of equations. We use the ideal gas law

$$p = \rho c_s^2, \quad (4)$$

with a locally isothermal approximation, where the sound speed c_s is a time-independent function of the cylindrical distance s to the z -axis. We write cylindrical coordinates as (s, ϕ, z) and spherical coordinates as (r, ϕ, θ) , where θ is the polar angle and ϕ the azimuthal angle. The z direction is perpendicular to the midplane of the disk.

The gravitational potential Φ has contributions from the star and the $N - 1$ embedded planets,

$$\Phi = - \sum_i^N \frac{GM_i}{\sqrt{\mathcal{R}_i^2 + b_i^2}}, \quad (5)$$

where G is the gravitational constant, M_i is the mass of particle i and $\mathcal{R}_i = |\mathbf{r} - \mathbf{r}_{p_i}|$ is the distance of a gas parcel relative to particle i . The quantity b_i is the distance over which the gravity field of the particle i is softened to prevent singularities.

The functions $f_b(\rho)$, $f_v(\mathbf{u}, \rho)$, and $f_\eta(A)$ are explicit mass diffusion, viscosity and resistivity terms, needed to stabilize the numerical scheme. They are composed of two terms, where the first one is a conservative sixth-order dissipation. This term is described in detail in Haugen & Brandenburg (2004) as well as in Johansen & Klahr (2005) for the case of isotropic dissipation. A generalization for the anisotropic case, required for non-cubic cells, is shown in Appendix A. The second term is a localized shock-capturing dissipation, activated when large negative divergences, typical of shocks, are formed (Haugen et al. 2004). This is described in Appendix B.

2.2. Planet orbital evolution

The star and the planets are treated as an N -body ensemble, evolving due to their mutual gravitational interaction. The equation of motion for particle i is

$$\frac{d\mathbf{v}_{p_i}}{dt} = \mathbf{F}_{g_i} - \sum_{j \neq i}^N \frac{GM_j}{\mathcal{R}_{ij}^2} \hat{\mathcal{R}}_{ij} \quad (6)$$

where $\mathcal{R}_{ij} = |\mathbf{r}_{p_i} - \mathbf{r}_{p_j}|$ is the distance between particles i and j , and $\hat{\mathcal{R}}_{ij}$ is the unit vector pointing from particle j to particle i . The first term of the R.H.S. is the combined gravity of the gas onto the particle i

$$\mathbf{F}_{g_i} = -G \int_V \frac{\rho(\mathbf{r}) \mathcal{R}_i}{(\mathcal{R}_i^2 + b_i^2)^{3/2}} dV, \quad (7)$$

where the integration is carried out over the whole disk. As we are not interested in the disk's self-gravity, but rather on its gravitational effect on one specific point (or a few points in case of multiple planets), calculating the integral above is simpler and faster than using a Poisson solver to find the gravitational potential of the disk everywhere on the grid.

The smoothing distance b_i is taken to be as small as possible. It is usually a fraction of the Hill radius. For reasons described in Sect. 2.7, the stellar potential can be treated as unsoftened ($b_\star = 0$). We note that in this formulation there is no distinction between a planet and a star except for the mass. The star evolves dynamically due to the gravity of the planets, wobbling around the center of mass of the system, which is set to the center of the grid. As the disk is not massive compared to the star, we exclude the disk torques from influencing the star. For runs without planets a constant gravity profile with a star at the center of the grid is used instead of solving the equations of the N -body code.

2.3. Dynamics of solids

To model the early stages of planet formation where solids grow from cm and m sizes to kilometer-sized planetesimals we consider the dynamics of meter-sized solid boulders, also treated as individual Lagrangian particles. Each of the particles has its own position and velocity, independent of the grid, integrated by the same particle module of the PENCIL CODE that is used for the planets. The difference is that as the planets interact with the disk and with themselves by gravity, the particles interact with the disk only via a drag force that is proportional to the velocity of the particle with respect to the local gas velocity.

While in our cylindrical models there is no vertical gravity on the gas, the particles do feel this component without which no settling towards the disk midplane would occur. The evolution equation for solid particle i is therefore

$$\frac{d\mathbf{v}_i}{dt} = -\frac{1}{\tau_f}(\mathbf{v}_i - \mathbf{u}) - \frac{GM_\star}{r^3} \mathbf{r}, \quad (8)$$

where τ_f is the friction time and \mathbf{u} is the gas velocity at the position of a particle. We assume that the friction time is independent of velocity differences between gas and particles. We choose it to be $\tau = 1/\Omega_0$, which for the typical densities and temperatures in the disk (Table 1), corresponds to particle radii between 0.4 and 2.5 m, depending inversely on the orbital distance. The assumption of linearity of the drag law holds as long as the velocity difference between gas and solids is much smaller than the sound speed (Weidenschilling 1977; Paardekooper 2007; Johansen et al. 2007). The condition is met since the turbulence generated by the MRI is subsonic.

The gas velocity \mathbf{u} at the position of the particle is interpolated from the nearest 27 grid points, using a Triangular Shaped Cloud scheme, as described in Youdin & Johansen (2007).

2.4. The code

The PENCIL CODE is a non-conservative Cartesian finite-difference MHD code that uses sixth order centered spatial derivatives and a third order Runge-Kutta time-stepping scheme, being primarily designed for compressible turbulent hydromagnetic flows.

The PENCIL CODE was recently applied to a 2D global laminar disk calculation, in which the results agreed with those of polar-grid based codes (de Val-Borro et al. 2006). We extend this calculation now to three dimensions with magnetic fields, fully

Table 1. Conversion between code and physical units.

Quantity	Physical unit
Length	5.2 AU ($=7.8 \times 10^{11}$ m)
Density	2.0×10^{-8} kg m $^{-3}$
Velocity	1.31×10^4 m s $^{-1}$
Energy	1.60×10^{36} J
Pressure, stress	3.41 Pa
Time	1.89 yr ($=6.0 \times 10^7$ s)
Magnetic field	2.07×10^{-3} T
Viscosity	1.02×10^{16} m 2 s $^{-1}$
Mass	$4.73 \times 10^{-3} M_{\odot}$
Mass accretion rate	$2.51 \times 10^{-3} M_{\odot}$ yr $^{-1}$
Domain size (L_x, L_z)	2–13 AU, ± 1.3 AU
Resolution (Δx)	0.08 AU

exploiting the capabilities of the PENCIL CODE for handling the problem of numerical hydrodynamic turbulence.

2.5. Units

We adopt dimensionless units such that

$$GM = \rho_0 = \mu_0 = 1.$$

The quantity GM has dimension of length 3 time $^{-2}$, so it sets a constraint on $[x][t]$. The unit of time follows from this as being the inverse of the Keplerian angular frequency at $s = s_0 \equiv 1$

$$[t] = \sqrt{\frac{GM}{s_0^3}} = \Omega_0^{-1}, \quad (9)$$

which gives an orbital period $P = 2\pi$ at s_0 in absence of a global pressure gradient.

The unit of velocity

$$[u] = [x]/[t] = \Omega_0 s_0$$

is therefore the local Keplerian speed at s_0 . The sound speed is set accordingly, through the Mach number (see Eq. (11)). Density is measured relative to the initial density of the box $[\rho] = \rho_0$.

The unit of magnetic field follows from the Alfvén speed,

$$[B] = \Omega_0 s_0 \sqrt{\mu_0 \rho_0}.$$

It follows from this that the unit of magnetic vector potential is

$$[A] = [B][x] = \Omega_0 s_0^2 \sqrt{\mu_0 \rho_0}.$$

As the simulation is dimensionless, it scales with the choice of physical units. By assuming that s_0 is the semi-major axis of Jupiter, $a_J = 5.2$ AU, and considering the typical density of the minimum mass solar nebula at that location, $\rho_0 \approx 2 \times 10^{-8}$ kg m $^{-3}$, the physical units corresponding to the employed code units are listed in Table 1.

2.6. Initial conditions

We use a Cartesian box with a spatial range $x, y \in [-2.6, 2.6]$, and $z \in [-0.26, 0.26]$ (see Table 1 for a conversion of the units used to physical units). The number of cells is usually $N_x = N_y = 320$, $N_z = 32$. This ensures that $\Delta x = \Delta y = \Delta z$, i.e., all cells are cubes of the same size. However, for some models we double the resolution in the vertical direction in order to resolve faster growing wavelengths of the MRI. Doubling the resolution in x

and y would keep the cells cubic, but the already expensive computational costs would become unpractical without yielding any other major advantage. We therefore keep it at 320×320 and introduce anisotropic hyperdiffusivity to treat the non-cubic cells (see Appendix A).

As stated before, we use the ideal gas law approximation to evaluate the pressure. The sound speed is set as a power law

$$c_s = c_{s_0} s^{-q_{\tau}/2}. \quad (10)$$

We usually set $q_{\tau} = 1$, so that the Keplerian flow has a constant Mach number \mathcal{M}

$$\mathcal{M} = \frac{\Omega_K s}{c_s} \equiv \text{const.}, \quad (11)$$

where Ω_K is the ‘‘cylindrical’’ Keplerian angular velocity profile

$$\Omega_K^2 = \frac{GM_{\star}}{s^3}.$$

The Mach number is seen to be the inverse of the aspect ratio $h = H/r$, where $H = c_s/\Omega$ is the pressure scale height. We checked the evolution and saturated state of the turbulence for Mach numbers of 5, 10 and 20.

We also perform simulations with radially-varying \mathcal{M} where the sound speed follows a steeper power law, with $q_{\tau} = 2$.

Accretion disks exhibit a radial density gradient, but this gradient arises due to accretion itself (Shakura & Sunyaev 1973). Therefore, we initialize the midplane density at a constant value ρ_0 , in order to understand the role of the stresses in generating the density gradient.

We start our models in strict equilibrium between gravity, global (thermal and magnetic) pressure gradients and centrifugal forces,

$$\Omega^2 = \Omega_K^2 + \frac{1}{\rho} \frac{\partial}{\partial s} \left(p + \frac{B^2}{2\mu_0} \right). \quad (12)$$

2.7. Boundary conditions

In this work, we compute models with and without an inner boundary to quantify the advantages/drawbacks of such a feature in a Cartesian grid. As for the external boundary, the box limits at $x = \pm 2.6$ and $y = \pm 2.6$ do not correspond to the physical boundaries of the problem. Indeed, the dynamically evolving disk encompasses a cylinder inside of $s_{\text{ext}} = 2.5$. The frozen regions outside of this cylinder play the role of ghost rings in cylindrical codes.

After evolving the dynamical equations, we set the time derivatives of all variables to zero in the region outside $s_{\text{ext}} = 2.5$. As the variables cannot evolve outward of s_{ext} , being effectively frozen in this region, the ‘‘real’’ boundary conditions of the box (e.g., open, reflecting) do not matter if this freezing boundary condition is used.

To avoid numerical instabilities due to this abrupt jump from frozen to evolving regions, we apply a buffer zone to the derivatives of the variables, that smoothly drives the variable X to a desired value X_0 in a timescale τ , such that

$$\frac{\partial X}{\partial t} = -\frac{X - X_0}{\tau} S(s). \quad (13)$$

where $S(s)$ is the uniquely defined fifth-order step function that is 1 at the domain boundary and 0 at the interior boundary of the buffer zone while maintaining continuous second order derivatives (Dobler, private communication). Its shape is visualized

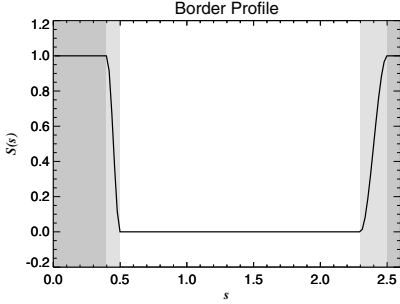


Fig. 1. Border profile of the simulations. The step function (Eq. (13)) is applied to the derivatives of the dynamical variables. The gas is free to evolve between $s = 0.5$ and $s = 2.3$, is slowed down between $[0.4, 0.5]$ and $[2.3, 2.5]$ (light-shaded areas) and is effectively frozen at $s < 0.4$ and $s > 2.5$ (dark-shaded areas).

in Fig. 1. We usually take the driving term X_0 to be the initial condition of the variable, and the driving time τ being the Keplerian period $2\pi/\Omega_K$, the dynamical timescale of the disk. The effect of this border profile is to smooth the transition between the evolving disk and the frozen regions of the grid, thus preventing large gradients and discontinuities that would otherwise arise. As the gas flow is symmetric in the vertical direction, the vertical boundary condition is set to periodic for the purpose of simplicity.

For the runs without an inner boundary, we smooth the quantities containing singularities by replacing

$$s^{-n} \Rightarrow (s^2 + b^2)^{-n/2}. \quad (14)$$

In practice, it is applied to the angular frequency Ω , the gravitational potential Φ and the sound speed c_s . We usually take $b = 0.1$, so the smoothed gravitational potential deviates from the Newtonian by less than 5% at $s_{\text{int}} = 0.4$. The physical domain thus runs from s_{int} to s_{ext} .

For runs with an inner boundary, we apply inside s_{int} the same freezing as used outside s_{ext} . The N -body particle code does not participate in the freezing, so although the star lies in a region of frozen gas, it is allowed to move.

As the gas is frozen in the inner and outer parts, the information about the flow in this region is not of interest. Therefore, we exclude these regions from the time-step calculation. As their time derivatives are set to zero at the end of the time-step, they cannot violate causality.

In principle, we could set s_{int} as close to zero as possible (by not using smoothing but retaining an inner boundary), in order to study the processes that happen in the immediate vicinity of the star, like winds, the magnetic cavity and surface accretion (von Rekowski & Piskunov 2006). However, due to the increasing Keplerian velocity in the advection and the decreasing resolution of the orbits, non-axisymmetric wave modes (particularly the $m = 4$ mode) build up in the inner disk as we try to push $s_{\text{int}} \rightarrow 0$. The density fluctuations resulting from the excitation of these modes lead to numerical instabilities.

Finally, the magnetic potential follows the same boundaries as described above. This would be a problem if we solved for the actual magnetic field, as sinks or sources of magnetic flux imply the presence of open magnetic loops (monopoles). By solving for the magnetic vector potential we do not face such problems.

The solid particles obey different boundary conditions, explained in Sect. 5.

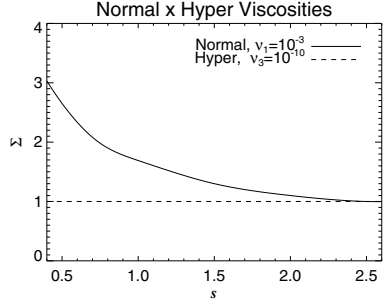


Fig. 2. The radial density profile after 100 orbits for Laplacian viscosity $\nu_1 = 10^{-3}$ is compared to the profile obtained by using sixth-order hyperviscosity ($\nu_3 = 10^{-10}$) of same strength in the small scales. In the hyperviscous case, the global flow is unaffected. Note that the frozen regions behave like infinite reservoirs of matter. The power law describing the resulting density profile for normal viscosity is very close to the $s^{-0.5}$, as expected for constant viscosity (see Pringle 1981, and references therein)

3. Influence of free parameters

In order to clarify the influence of the numerical scheme and the approximations made, a series of non-magnetic 2D models were computed, with and without planets. The grid being Cartesian, all our simulations span the whole azimuthal domain. We usually evolve the simulations up to 100 orbits at s_0 , which corresponds to ≈ 25 orbits at the outer edge of the disk and ≈ 400 orbits at its inner edge.

3.1. Viscosity

Explicit hyperviscosity and hyperdiffusion induce dissipation primarily near the grid scale, replacing the usual 2nd order Laplacian terms. A visual picture of the difference between using the two types of viscosity is seen in Fig. 2. The first model was computed with a Laplacian viscosity $\nu_1 = 10^{-3}$. The radial inflow is significant, and as the outer frozen region behaves like an infinite reservoir of matter, the total mass inside the disk keeps on rising as matter flows in from this reservoir. The radial density profile soon starts to deviate from the flat initial condition. Shown in the figure is the density profile after 100 orbits at s_0 with $\nu_1 = 10^{-3}$. When using hyperviscosity of similar strength at the grid scale, i.e., $\nu_3 = 10^{-10}$, the overall flow shows no significant deviations from the initial conditions.

The simulation shown using Laplacian viscosity was computed without an inner boundary, using a softened stellar potential with $b = 0.1$. Using the damping and freezing profile described in Sect. 2.7, the density is not allowed to deviate much from the initial condition at the boundaries. In the physically evolving part of the disk, however, a density profile of exponent $s^{-0.4}$ evolves.

3.2. Mass diffusion

To evaluate the influence of mass diffusion, we simulate a laminar disk with constant Laplacian viscosity $\nu_1 = 10^{-5}$ in the presence of a gap-opening Jupiter-mass planet. We performed runs of resolution 320×320 with hyperdiffusion coefficients ranging from $D_3 = 5 \times 10^{-11}$ to 10^{-14} . After a hundred orbits, time enough for the planet to open a deep gap, the density profiles are

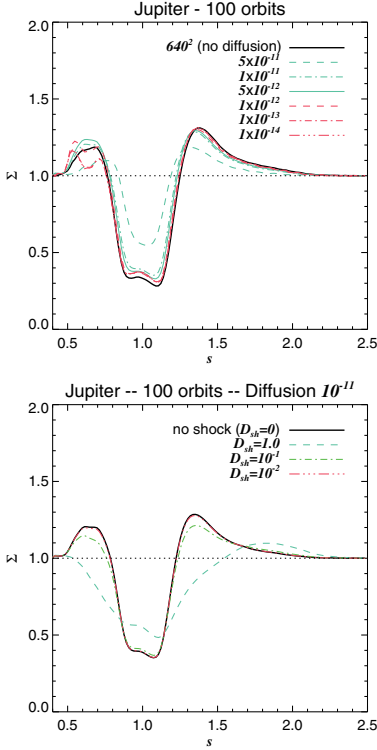


Fig. 3. *Upper panel.* The gap carved by a $1 M_J$ planet in a 2D disk reveals the influence of explicit diffusion in the calculations. The inner disk loses mass depending on the amount of diffusion. The value of $D_3 = 5 \times 10^{-12}$ seems to ensure mass conservation in the inner disk yet not distorting the shape of the gap. The solid line represents a 640×640 run without diffusion, for comparison. Resolution is 320×320 otherwise. *Lower panel.* Same but with hyperdiffusion set to $D_3 = 10^{-11}$ and varying the shock diffusion coefficient from 10^{-2} to 1.

plotted in Fig. 2a, where a run with resolution 640×640 without explicit diffusion is shown for comparison.

It is seen that $D_3 = 5 \times 10^{-11}$ constitutes too much diffusion, as the gap is significantly altered. As less diffusion is used, the shape of the gap monotonically approaches the one recovered in the higher resolution run. The walls of the gap are fairly well reproduced for lower diffusion, but its bottom is always shallower even for the lowest coefficient used ($D_3 = 10^{-14}$).

Judging from the gap alone, one could in principle use no diffusion at all, but the inner disk suffers depletion for low diffusion regimes, due to the non-conservative nature of the numerical scheme. Even the higher resolution run seems to have lost mass due to the lack of explicit diffusion.

We adopt a hyperdiffusion coefficient of $D_3 = 5 \times 10^{-12}$ as the best compromise between the need for preserving material in the inner disk and for reproducing the overall shape of the gap. Requiring Schmidt and magnetic Prandtl numbers of 1 at the grid scale, we set hyperviscosity and hyperresistivity to the same value.

3.3. Shocks

Shock viscosity and shock diffusion are needed for two reasons: (a) to stabilize the flow near the shock-generating particles in runs with planets and (b) to treat eventual supersonic motion in the turbulence (arising when the disk is exposed to a strong net vertical field), in which case shock resistivity is also included.

In Fig. 2b we show gap-opening runs with fixed hyperdiffusion coefficient D_3 but varying the shock diffusion coefficient. From the continuity equation, one can tell that the effect of shock diffusion is to slow down the time evolution of density by smearing out any large divergences. Indeed, one sees that after a hundred orbits, a shock diffusion coefficient of 1 fails to reproduce the shape of the gap as compared to the higher resolution run without shock diffusion, while 10^{-1} shows less accumulation than expected in the Lindblad resonances, also seen as compared to the higher resolution run. We therefore use shock diffusion of 10^{-2} for the turbulent runs. The flow around a high-mass planet, however, could only be stabilized with a shock viscosity of 1.

Shock resistivity is also used when the run involves the magnetic potential. The value used was not tuned in 2D runs like shock diffusion and shock viscosity. Instead, in the presence of turbulence, we simply checked what was the lowest shock resistivity coefficient that did not lead to numerical instabilities for model A (see Table 2), finding that it is of the order of unity, like the shock viscosity.

3.4. Non-turbulent runs

To verify the numerical stability of the model in the absence of physical turbulence, we perform tests for cases where the turbulence is not supposed to be present. In these runs, we monitor the evolution of the mass inflow rate \dot{M} defined as the 1D radially dependent surface integral over a surface \mathcal{A} which is a cylinder at a radial distance s from the origin

$$\dot{M}(s) = \oint_{\mathcal{A}} \rho \mathbf{u} \cdot \hat{\mathbf{n}} dA \quad (15)$$

$$= 2\pi s \int_{-L_z/2}^{L_z/2} \rho(s, z) u_s(s, z) dz. \quad (16)$$

We see that in a 2D laminar model, the mass inflow rate is constant through the radial domain once a steady flow is achieved (which simply states that mass is conserved). We thus define the mass accretion rate as the mass inflow rate across the inner boundary, $\dot{m} = \dot{M}|_{s=0.4}$, meaning that after crossing this boundary, the matter is considered lost (accreted).

We also measure the kinetic alpha parameter of turbulent viscosity, defined as

$$\alpha_R = \frac{2 R^{s\phi}}{3 \rho c_s^2},$$

where $R^{s\phi} = \overline{\rho \delta u_s \delta u_\phi}$ is the Reynolds stress; and its magnetic counterpart

$$\alpha_M = -\frac{2 M^{s\phi}}{3 \rho c_s^2},$$

where $M^{s\phi} = \mu_0^{-1} \overline{\delta B_s \delta B_\phi}$ is the Maxwell stress.

In Fig. 4 we show a 2D run where the velocities were perturbed with noise of $u_{\text{rms}} = 10^{-2}$, but the induction equation is not solved. The turbulence dies out so fast that even before ten orbits at s_0 the flow is already smooth, showing that the numerical scheme does not spuriously generate or sustain turbulence.

Table 2. Cylindrical turbulent disk models.

Run	Parameter								Results						
	s_{int}	B_0 ($\times 10^3$)	c_{s_0}	q_T	β_0	N_z	χ_{sh}	N_p	$R^{z\phi}$ ($\times 10^5$)	$-M^{z\phi}$ ($\times 10^5$)	α_R ($\times 10^3$)	α_M ($\times 10^3$)	B_{rms} ($\times 10^3$)	β_t	δ_t ($\times 10^3$)
Uniform field B_z															
A	0.4	1	0.05	1	5000	32	1	10^6	0.24 ± 0.04	1.5 ± 0.3	0.9 ± 0.2	6 ± 1	17 ± 9	13 ± 3	7 ± 1
B	0.4	1	0.10	1	20 000	32	1	...	1.0 ± 0.2	2.5 ± 0.3	0.7 ± 0.1	1.8 ± 0.2	16 ± 5	65 ± 7	...
C	0.4	1	0.20	1	80 000	32	1	...	4 ± 1	5.3 ± 0.8	0.9 ± 0.2	1.3 ± 0.2	26 ± 7	81 ± 7	...
A2	0.0	1	0.05	1	5000	32	1	...	0.20 ± 0.04	1.3 ± 0.1	0.7 ± 0.1	4.7 ± 0.3	17 ± 5	13 ± 1	...
B2	0.0	1	0.10	1	20 000	32	1	...	0.9 ± 0.2	2.6 ± 0.3	0.8 ± 0.1	2.1 ± 0.2	20 ± 11	43 ± 13	...
C2	0.0	1	0.20	1	80 000	32	1	...	5 ± 3	5 ± 1	1.2 ± 0.8	1.2 ± 0.3	22 ± 9	116 ± 19	-
Radially varying field B_z															
D	0.4	20	0.10	2	12	64	2	10^6	22 ± 2	78 ± 7	25 ± 1	87 ± 3	71 ± 9	4 ± 1	140 ± 10
E	0.4	20	0.20	2	50	64	2	...	35 ± 7	87 ± 15	13 ± 3	30 ± 5	60 ± 23	11 ± 1	...
Dw	0.4	5	0.10	2	750	64	2	...	4.1 ± 0.4	13 ± 2	5.4 ± 0.6	17 ± 2	28 ± 10	13 ± 2	...
Ew	0.4	5	0.20	2	3000	64	2	...	13 ± 4	27 ± 2	4 ± 1	8.7 ± 0.7	36 ± 11	33 ± 3	...
Uniform field B_ϕ															
F	0.0	30	0.05	1	5.5	32	2	...	0.7 ± 0.1	2.9 ± 0.4	2.5 ± 0.4	11 ± 1	12 ± 4	24 ± 2	...
G	0.0	30	0.20	1	90	32	2	...	5 ± 2	18 ± 6	0.9 ± 0.4	3.3 ± 1.4	28 ± 11	107 ± 22	...

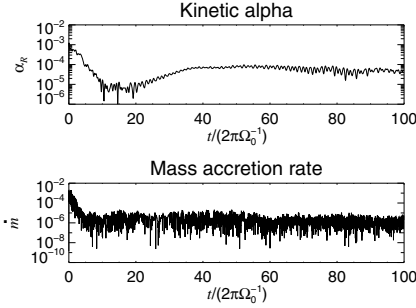


Fig. 4. Without solving the dynamical equations for the magnetic field, even initially vigorous random motions of $u_{\text{rms}} = 0.2c_{s_0}$ die out rather quickly. The plots show the time evolution of the globally averaged Reynolds stress and mass accretion rate. Time is quoted in orbits at s_0 .

A 3D cylindrical run in which we add a vertical net field of strength $B_0 = 10^{-3}$ (dimensionless), corresponding to plasma $\beta = 5000$ at s_0 , 12 500 at s_{int} and 2000 at s_{ext} (see Eq. (19)), but where the initial flow is not perturbed by noise, does not develop turbulence. We also tested if the MRI would develop in a disk seeded only with noise in both the velocity and magnetic potential ($u_{\text{rms}} = A_{\text{rms}} = 10^{-4}$). There is a short growth in magnetic energy, presumably due to reconnection of the field lines, but without a structured field to maintain the turbulence the Reynolds and Maxwell stresses quickly level down to zero as viscosity and resistivity smooth the imposed noise.

4. Cylindrical disk runs

For the main simulations in this paper we consider flat vertical profiles for the gravity field. Such an approximation is called a “cylindrical” disk and has been often used in order to study the MRI (e.g., Armitage 1998; Hawley 2001). The vertical gravity $g_z = -\Omega^2 z$ is switched off so that, physically, the star is no longer a point mass at $r = 0$, but a rod at $s = 0$ extending through the length of the z -axis. In such a setup, the pressure scale height H

has no hydrostatic meaning, being only a way to write the temperature profile of the disk. We performed simulations with non-zero net flux magnetic fields $\mathbf{B} = B_0 \hat{z}$ and $\mathbf{B} = B_0 \hat{\phi}$. Models with a radially varying vertical field proportional to $\Omega(s)$ were also computed.

For the turbulence to develop, the unstable wavelengths of the MRI must be resolved. The characteristic vertical wavelength λ_{BH} of the hydromagnetic turbulence is given by (Balbus & Hawley 1991, 1998)

$$\lambda_{\text{BH}} = 2\pi \frac{v_A}{\Omega}, \quad (17)$$

where v_A is the Alfvén speed

$$v_A = \frac{B}{\sqrt{\mu_0 \rho}}. \quad (18)$$

The turbulence will be present as long as the critical wavelength λ_c is resolved. This wavelength is $\lambda_c = \lambda_{\text{BH}}/\sqrt{3}$, whilst the most unstable wavelength of the MRI is $4\lambda_{\text{BH}}/\sqrt{15}$ (Balbus & Hawley 1991). The plasma β parameter – the ratio of thermal to magnetic pressure – can be expressed in terms of the sound and Alfvén speed, by writing the magnetic pressure $P_M = B^2/(2\mu_0)$ in terms of the Alfvén speed $P_M = B^2/(2\mu_0) = \rho v_A^2/2$, giving

$$\beta = \frac{2c_s^2}{v_A^2}. \quad (19)$$

The constant B_0 is usually set to 10^{-3} , but runs varying the field from 10^{-4} to 10^{-1} were also studied. Although the runs reported here are in the local isothermal approximation, we also varied the initial sound speed at s_0 , c_{s_0} , in order to check how the resulting turbulent viscosity depends on the global gas pressure.

The parameters of the cylindrical models presented here are specified in Table 2.

4.1. Constant vertical field – model A

The evolution of the turbulence in a fiducial run with a net vertical flux of strength $B_0 = 10^{-3}$ and temperature profile corresponding to $c_{s_0} = 0.05$ is shown in Fig. 5. The absolute value

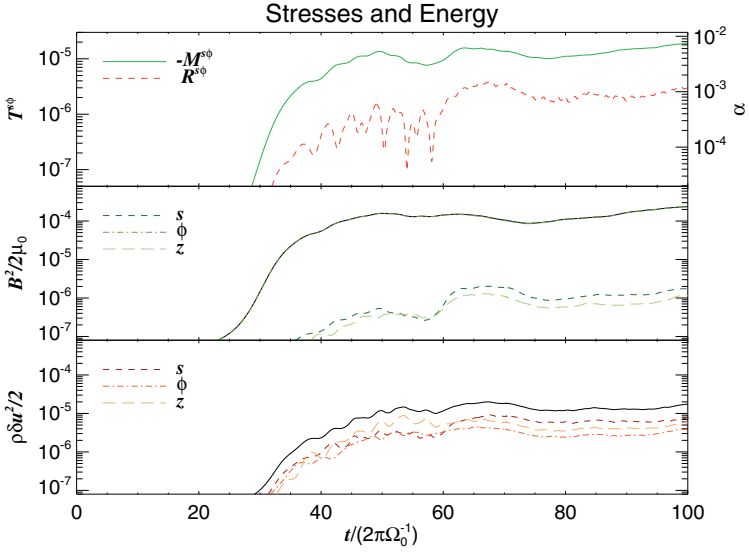


Fig. 5. Time evolution of the turbulence for model A (constant net flux vertical field $B = 10^{-3}\hat{z}$ and constant Mach number). The top panel shows the evolution of the $s\phi$ -component of the Maxwell and Reynolds stresses, while the middle and bottom panels show the evolution of magnetic and kinetic energy, respectively. The units are given in Table 1. The solid lines in the two bottom panels show the total energy. The toroidal field dominates the magnetic energy to the point that the energy in the azimuthal component can barely be distinguished from the total energy. The kinetic energy is more evenly distributed among the three dimensions, but the turbulence is not isotropic. The radial component shows 1.5 times more energy than the vertical and 2 times more than the azimuthal. Time is quoted in orbits at s_0 .

of the Maxwell stress at saturation is always larger than the Reynolds stress, but the latter fluctuates more strongly.

The minimum ratio of stresses is $-M^{s\phi}/R^{s\phi} = 3$ (at $t \approx 75$ orbits), but it reaches as much as 100 (at $t \approx 58$ orbits). After 75 orbits, the average ratio of Maxwell to Reynolds stress is around 5.

In agreement with previous shearing box simulations (Brandenburg et al. 1995; Hawley et al. 1995; Johansen & Klahr 2005), global disks (Hawley 2001; Nelson 2005) and analytical calculations (Balbus & Hawley 1991), a large scale toroidal field is seen to form, which dominates the magnetic energy, being 2 orders of magnitude stronger than the radial and vertical fields. Indeed, one can barely distinguish between the energy stored in the azimuthal field and the total magnetic energy. The kinetic energy is more evenly distributed, but it is not isotropic. The radial component accounts for 45% of the total energy, being ≈ 1.5 bigger than the vertical and twice as big as the azimuthal. The radial structure of the alpha parameter is seen in Fig. 6. The outer disk is more turbulent due to the smaller values of plasma β when compared to the inner disk.

Following the time evolution of the turbulence in the mid-plane, it is seen that different regions of the disk reach saturation at different times. The turbulence starts from the outer disk, propagating inwards. It is expected since, as Ω decreases with radius, a uniform field implies a Balbus-Hawley wavelength that increases with distance from the star. As longer wavelengths – comparable to the length of the box – are easily resolved, the outer disk goes turbulent first. It is seen that inside $s_0 = 1$ the disk did not go turbulent. In this model, the Mach number is constant, $M = 20$, with a constant field, $B = 10^{-3}$ through the whole domain, corresponding to plasma β running from 2000 at s_{ext} and 12 500 at s_{int} . The magnetic field determines the value of the critical wavelength, which ranges from $\lambda_c = 0.002$ at s_{int}

to $\lambda_c = 0.025$ at s_{ext} . As we have 32 grid points in the vertical direction, the smallest wavelength resolved with significant accuracy (8 points) by our high-order finite-difference method is $L_z/4 \approx 0.12$. From the dispersion relation of the MRI (Hawley & Balbus 1991), this unstable wavelength has a growth rate of $\approx 0.1\Omega$, much lower than the fastest growing wavelength with $\omega = (3/4)\Omega$.

We also computed models where the whole disk goes turbulent (models D and E), but we will use these weak field disk models (models A to C2, see Table 2) in the next subsection for studying the behavior of the turbulence with thermal pressure. Although dissipative and slowly growing, the weak field used in these disks has one major advantage: the turbulence grows slowly and has less spatial variability. Therefore, the damping at the frozen boundaries is more gentle than in other, rapidly growing, violently fluctuating, disks. These issues discussed above reflect the compromise between keeping the disk cold while still retaining the field subthermal and with sufficient resolution to resolve the rapidly growing unstable wavelengths.

The runs with a vertical net field of $B_0 = 10^{-4}$ or lower did not develop turbulence as the field is weaker than needed in the presence of the chosen dissipation parameters (Hawley & Balbus 1991).

4.2. Dependence on sound speed – models B and C

We investigate the dependence of the saturated state on the imposed sound speed profile. We test three different sound speeds of, $c_{s_0} = 0.05, 0.10$ and 0.20 , corresponding to runs A, B and C.

As the runs are locally isothermal, we are mainly investigating how the MRI responds to different radial pressure gradients. The cold model (A) shows a weaker turbulence at saturation

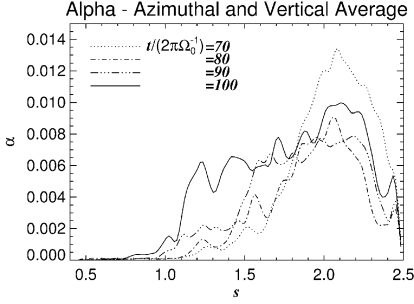


Fig. 6. Radial structure of the total alpha parameter $\alpha_R + \alpha_M$ for model A. The turbulence starts from the outer disk, where plasma β is smaller. The different curves correspond to snapshots at 70 (dotted), 80 (dot-dashed), 90 (dot-dot-dot-dashed), and 100 orbits (solid), after saturation is reached. The variability is not monotonic, but highly fluctuating.

than the hotter ones, as shown by the strength of the stresses (Figs. 7a, b) and magnetic/kinetic energies (Figs. 7c, d). The Maxwell stress is three times bigger for model C than for A, the colder version. Such behavior was reported by Sano et al. (2004), indicating a power law of exponent 0.25 for the growth of the Maxwell stress with gas pressure. Our global disk calculations agree well with this value.

The dimensionless magnetic α_M parameter, which is a measure of turbulent viscosity, decreases drastically with sound speed (Fig. 8). As seen before, the stresses actually *increase* with increasing temperature, so this decrease of α_M is due to the stresses increasing less rapidly than the temperature. Even though alpha decreases, the effective viscosity $\nu_t = \alpha c_s H$ increases. As seen in Figs. 9 and 10, a centrally concentrated density profile has developed from the initially flat configuration, a signature of mass accretion due to turbulent angular momentum transport, as also confirmed by the measured stresses. The resulting density profile in model C is smoother overall, but the overdensities seem to be similar in average.

It is clear that alpha per se is not a good measure of viscosity. Since $\nu_t = \alpha c_s^2 \Omega^{-1}$, with no reference to the Alfvén speed, the resulting alpha value of turbulent disks where the origin of the turbulence is magnetic may change with sound speed. As most of the analyses of turbulent thin accretion disks have focused on locally isothermal simulations using $c_s \approx 0.05$, such dependence of α on sound speed did not receive proper attention. Although protoplanetary disks are thin, this rise in angular momentum transport with temperature suggests that the effects of radiation will be important for high temperature regions around forming planets as well as regions where the turbulence leads to significant Joule and/or viscous heating.

4.3. Excluding the inner boundary

The correct treatment of boundaries is a major issue for numerical simulations. In global simulations of disks, outflow or frozen boundaries are usually used, both of them being more realistic than reflective, but also presenting disadvantages. Strictly speaking, a “perfect” boundary might well not exist. The best solution would be, of course, not having to use a boundary at all.

Cylindrical grids only make sense if the center of mass is at the origin of the coordinate system as only then angular momentum transport can be written in a conservative form. If the center of mass is not at the origin or there is more than one massive

object the cylindrical coordinate system artificially introduces a reflective boundary at the center. Cartesian grids, as stated before, are not hindered by this, and we can therefore study how the presence or absence of an inner boundary affects the results.

We compute a version of model A where the computational domain extends all the way to $s_{\text{int}} = 0$. Without an inner boundary, the gravitational potential, the angular frequency and the sound speed have to be smoothed according to Eq. (14) to prevent singularities. When taking global averages, we exclude the smoothed region.

The evolution of the turbulence and the globally averaged stresses at saturation are almost identical to those seen at model A. The only noticeable difference is that the highly fluctuating magnetic field observed in the inner boundary of model A (with rms amplitude ≈ 2 times seen in the rest of the disk) does not occur in this model.

In model A, the magnetic potential at the inner boundary remains frozen at the initial condition $A = 0$. As the MRI builds up the magnetic potential in the freely evolving disk, a sharp radial gradient appears at the boundaries. This sharp radial gradient in the azimuthal and vertical components of the magnetic potential translates into high values of the magnetic field. If we were solving for the magnetic field instead, a similar effect would be seen. The magnetic field would rise in the disk, but is kept frozen at the boundary, thus building up a high magnetic pressure with equally damaging effects for the simulation.

By avoiding the inner boundary altogether, such an effect does not occur. However, other problems arise as the advection on the very inner disk ($s < 0.4$) happens on tight circular trajectories that are poorly resolved in the Cartesian geometry near the center of the grid. As they behave like highly localized vortices, in most cases the explicit shock dissipation terms ensure numerical stability. But for cases with stronger turbulence (model D, Sect. 4.4), a model without an inner boundary could not be treated.

As we did for the models with an inner boundary, we check the dependency of the turbulent stresses with sound speed by computing versions of models B and C without an inner boundary. As for model A2, these models B2 and C2 behave quite similarly to models B and C, saturating at roughly the same stresses.

4.4. Radially varying field – models D and E

With the constant vertical field, it is seen that the inner disk does not go turbulent. This is due to the fact that in this rapidly advecting region, the growth of the MRI is numerically damped.

In view of this, we also compute models with a radially varying z -field

$$B = \frac{L_z \Omega(s)}{2j\pi} \sqrt{\mu_0 \rho_0} \hat{z}, \quad (20)$$

such that j Balbus-Hawley wavelengths (Eq. (17)) are resolved through the vertical extent L_z of the box at any radius. We computed a model with $j = 4$ (model D), and another version, with a weaker field (model Dw) with $j = 16$, so that unstable wavelengths are reasonably well resolved. These fields can make the whole disk go turbulent, but they grow so strong in the inner disk of model D that a more pronounced temperature profile ($q_1 = 2$) had to be used to avoid the magnetic field from going superthermal. For model D, such a setup has plasma $\beta = 20$ at s_{int} and 120 at s_{ext} . Model Dw has a field with a strength more similar to model A, and therefore would not need this fix. However, to allow a comparison with model D, we also used this steeper

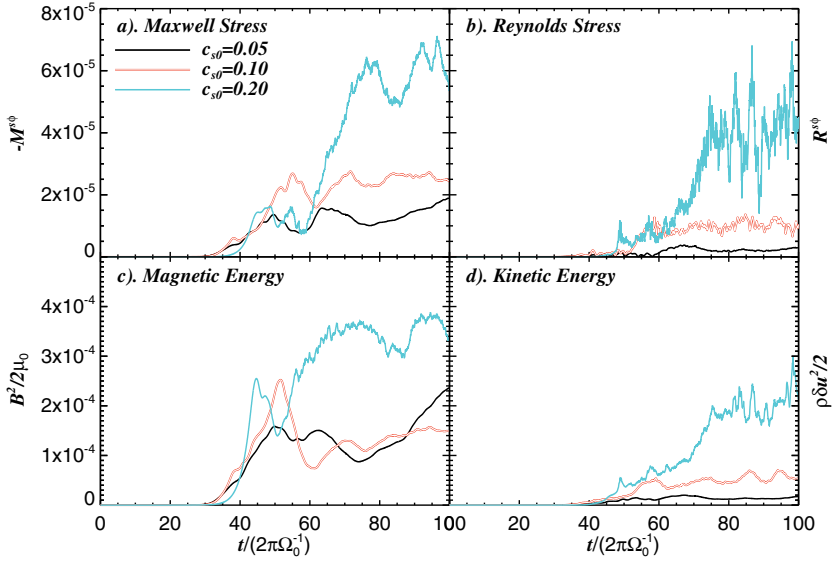


Fig. 7. Time evolution of the turbulence for different sound speed profiles. The strength of the angular momentum transport differs with sound speed. The increase in stress observed when the sound speed is raised to $c_{s0} = 0.20$ is dramatic. Time is quoted in orbits at s_0 .

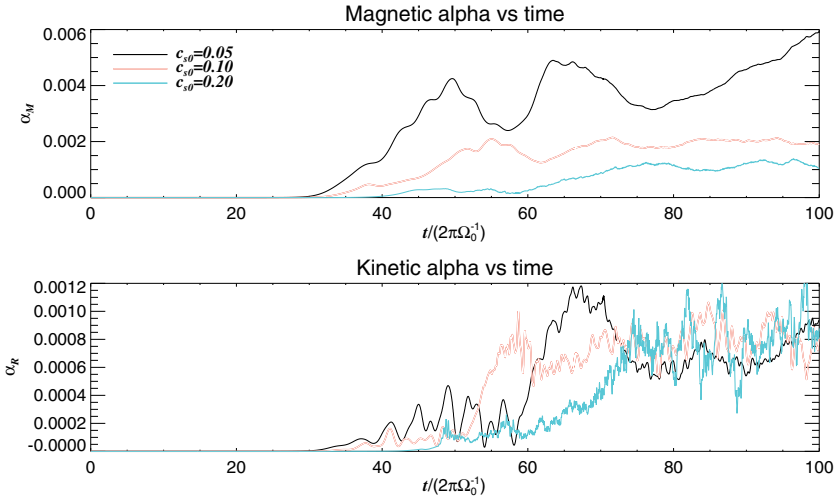


Fig. 8. Evolution of the alpha parameters for different sound speed profiles. This quantity, that measures the strength of viscosity through the parametrization $\nu_t = \alpha c_s H$, decreases with sound speed for the magnetic stresses but stays constant for hydrodynamic stresses. As seen before, the stresses actually *increase* with increasing temperature, so this decrease of the alpha parameter is due to the stresses increasing less rapidly than the pressure. Time is quoted in orbits at s_0 .

temperature gradient, thus having a plasma $\beta = 300$ at s_{int} and 1850 at s_{ext} .

As this setup has an inverse β profile compared to the models with a constant vertical field, the turbulence starts from the inner disk instead of the outer. Also, as the magnetic field is stronger, wavelengths of faster growth rate are better resolved and the turbulence saturates after a few orbits. Due to the strong stresses, we had to raise shock resistivity to 2 instead of 1 as used before.

The stresses also saturate at higher values, 0.08 for the Maxwell stress, and 0.02 for the Reynolds stress (Fig. 11) for model D. The weaker field yields a total alpha viscosity around 2×10^{-2} ($\alpha_M = 0.017$, $\alpha_R = 0.005$, see Fig. 11a and Table 2). These values are at least one order of magnitude higher than the ones obtained with a constant field. The radial structure of the alpha value, plotted in Fig. 12, reveals that the stresses follow the radial profile of $1/\beta$, being stronger in the inner disk. The

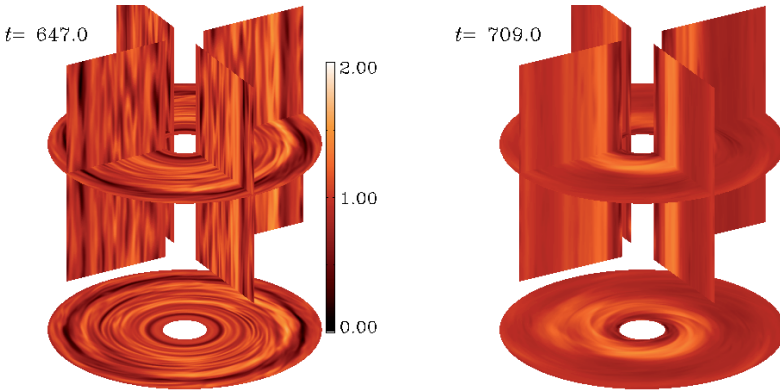


Fig. 9. Density contours at selected planes $x = 0$, $y = 0$, and $z = 0$ on saturated turbulent state for sound speed profiles of $c_{s0} = 0.05$ (model A, *left panel*) and $c_{s0} = 0.20$ (model C, *right panel*). The color code is the same for both figures. The stronger stresses for the hotter case lead to a much more effective turbulent viscosity, as seen from the steep density profile resulting from accretion. The vertical planes are stretched to show more detail than the correct aspect ratio would allow. Movies of these simulations can be found at <http://www.astro.uu.se/~wlyra/planet.html/>.

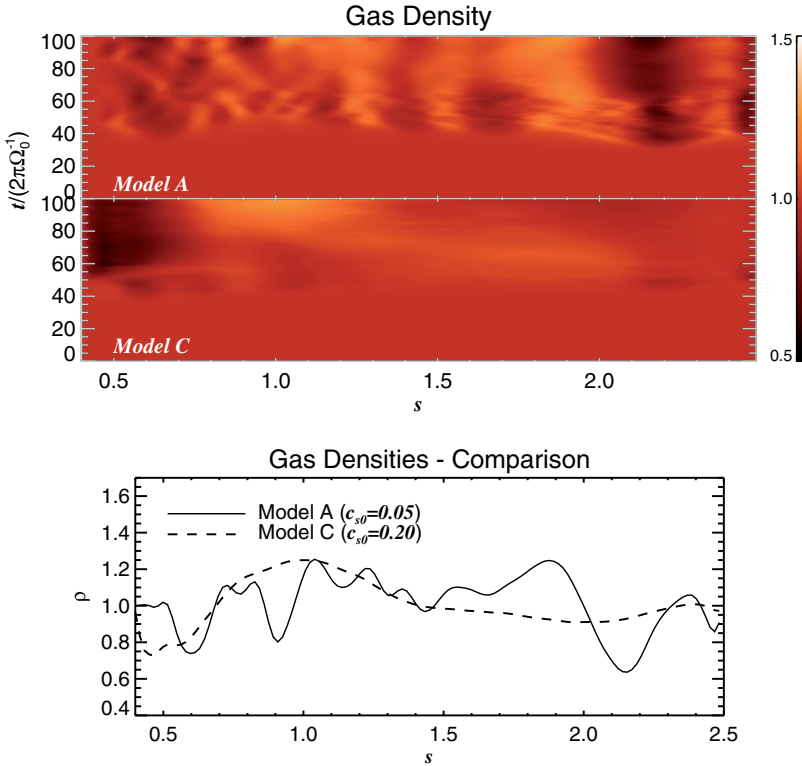


Fig. 10. Radial density profiles for models A and C. The lower panels show space-time plots of the vertically and azimuthally averaged density. Model A shows what seems to be a variability around a constant value, model C has developed a smoother radial density gradient. The lower panel shows the two density profiles at the end of the simulation.

same was seen in the simulations with a constant field, where the stresses were stronger in the more magnetic outer disk.

The stresses in this model are so high that the alpha viscosity in the saturated state is always of the order 10^{-1} , reaching ≈ 0.5 in

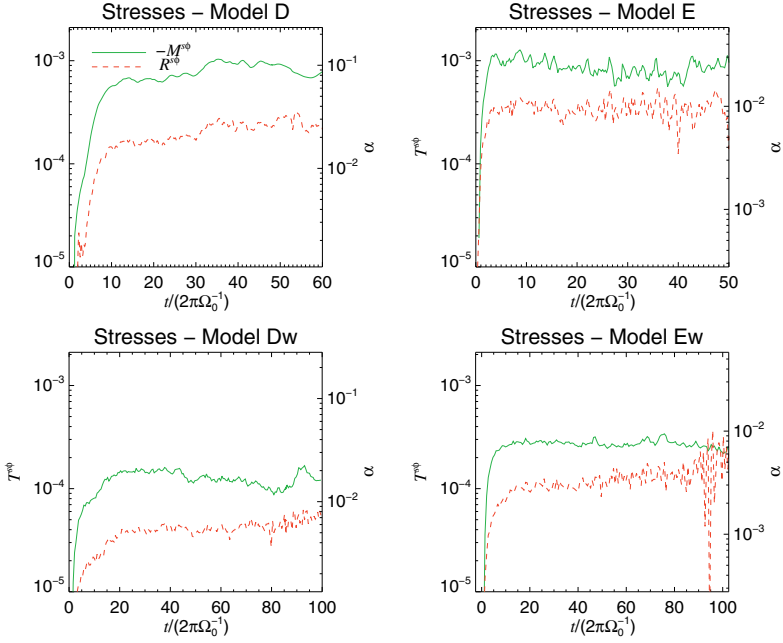


Fig. 11. Time evolution of the turbulent stresses for models D and E (*upper panels*) and Dw and Ew (*lower panels*). As compared with model A, the stresses saturate at a much earlier time. The ratio of Maxwell to Reynolds stress is around three for model D, and around two for the hotter model E, approaching one at the end of the simulation. Notice that as seen in models ABC, the stresses are bigger for the hotter model, although the alpha viscosity value is smaller. Time is quoted in orbits at s_0 .

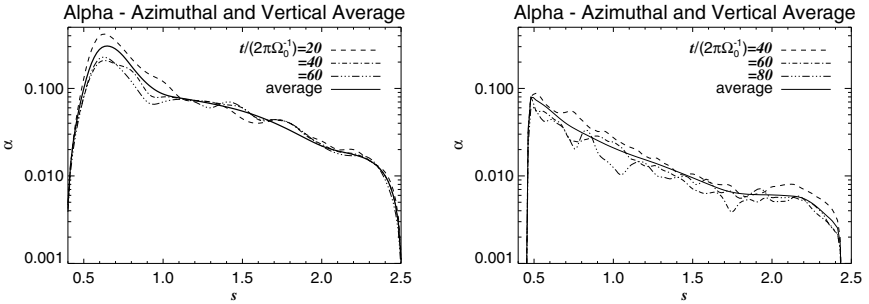


Fig. 12. Same as Fig. 6, but for models D (*left panel*) and Dw (*right panel*). The times corresponding to the snapshots are indicated in the legends, as well as the time average. The inner disk is considerably more turbulent than the outer parts.

the more magnetized inner disk (Fig. 12). That means that the inner disk approaches magnetically dominated values for plasma β as the turbulence saturates. The global average of plasma β in the saturated state is 4, although it did not reach superthermal values (<1) during the course of the simulation. Model Dw is milder, having a total alpha value of the order 10^{-2} , reaching a maximum of ≈ 0.08 in the more magnetized inner disk.

The high stresses compared to the cases with constant vertical field stem from the initially stronger magnetic field, not from a pressure effect. Indeed, in this setup, the temperature profile is steeper, but it never rises above the sound speed of model C, with $c_{s0} = 0.2$ and power law of exponent 0.5. However, we still expect the pressure effect seen on models ABC to be present. To check the behavior of this setup with the imposed temperature

profile, we compute another model (model E) with the same initial condition for the magnetic field as model D, but with a hotter temperature, with $c_{s0} = 0.2$. This setup has a plasma beta value of 80 in the inner disk and 450 in the outer. A weaker version with plasma beta value of 1200 in the inner disk and 7400 (model Ew) was also computed, for comparison with model Dw. The results (Fig. 11b) are similar to models ABC: The stresses are indeed larger than those of models D and Dw, but the alpha viscosity values are smaller. Also as seen on models ABC, the kinetic alpha did not change appreciably, but the magnetic alpha was reduced by approximately a factor of 2.

The ratio of stresses varied as well, as seen in models ABC. It is around 4 for model D, but 2 or less for model E. It is around 3 for model Dw, but less than 2 for model Ew.

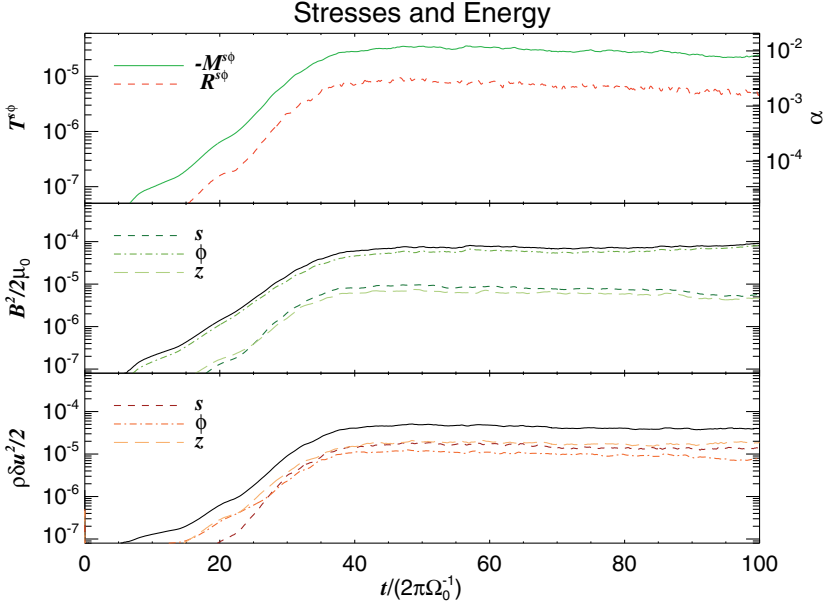


Fig. 13. Same as Fig. 5 (constant vertical field), but for model F (constant azimuthal field).

A final note on the temperature effect; we see that, like alpha, the turbulent plasma beta parameter β_t does not scale with pressure. As the rise in the turbulent magnetic energy is outpaced by the growth of the pressure, β_t increases with increasing temperature.

4.5. Constant azimuthal field – models F and G

Analytical treatment (Balbus & Hawley 1992; Ogilvie & Pringle 1996) and numerical simulations (Hawley 2000; Papaloizou & Nelson 2003) show a wealth of evidence that the MRI also exists for a purely toroidal field. In this case, waves of the form $\exp[i(m\phi - \omega t)]$, where $m = k_\phi s$ is the azimuthal wavenumber, are excited. The maximum growth rates are similar to those observed in purely vertical fields, but reached at much smaller azimuthal wavenumbers.

For an azimuthal field, the maximum growth rate occurs at the wavenumber (Balbus & Hawley 1998)

$$m_{\max}(s) = \frac{\sqrt{15} \Omega s}{2 v_A}. \quad (21)$$

Such wavelengths are now resolved in the xy plane, instead of in the vertical direction. Without the severe constraint of fitting unstable wavelengths in the tiny vertical scale height of the disk, the azimuthal field can be set at much stronger values than those used in the vertical cases. The only constraint is that we keep the field subthermal. With a temperature gradient of $q_r = 1$ and $c_{s0} = 0.05$, a constant azimuthal field of $B_0 = 3 \times 10^{-2}$ (model F) corresponds to plasma β of 12 at $s = 0.4$, 5.5 at s_0 and 2 at $s = 2.5$. The wavenumbers are $m_{\max} = 65$ at s_0 , 102 at $s = 0.4$ and 41 at the outer boundary. A hotter version, with $c_{s0} = 0.20$, yielding plasma $\beta = 220$ at $s = 0.4$, 90 at s_0 and 35 at $s = 2.5$ (model G), was also computed for comparison.

Following the time evolution of model F, we see that the turbulence actually saturates at $t = 200$ at $s = 2.0$ (≈ 11 orbits), $t = 300$ at $s = 1.5$ (≈ 30 orbits) and is still growing linearly at $s = 1.0$ at the end of the simulation at $t = 628$ (100 orbits). The global average (Fig. 13), and a space-time (s, t) inspection (Fig. 14) of the stresses reveals that after reaching saturation at $t = 250$ (40 orbits at s_0), a steady state is maintained for 20 orbits, after which the turbulence starts decaying slowly. But as a small growth is observed near the end of the simulation, it is not clear if this decay would continue to zero or if it constitutes just a unusually long fluctuation of the turbulence. Moreover, the magnetic and kinetic energies (Fig. 13) show no signs of decaying.

On the right panel of Fig. 14, we plot the total alpha viscosity parameter $\alpha_M + \alpha_R$. Curiously, it does not show the decaying effect seen on the stresses, implying that a decrease in gas pressure accompanied the decrease in Maxwell stress. Such a behavior is expected, since a negative density gradient is arising from the accretion process. Therefore, a depleted outer disk has a larger value of alpha viscosity for the same Maxwell stress.

The global average yields $R^{s\phi} = (0.7 \pm 0.1) \times 10^{-5}$, $M^{s\phi} = (2.9 \pm 0.4) \times 10^{-5}$ and total alpha viscosity $\alpha = (1.3 \pm 0.1) \times 10^{-2}$.

Model G shows Maxwell stresses that go further towards the inner disk, and Reynolds stresses that extend to inside $s = 0.4$ as seen in Fig. 14. The outer disk attains a turbulent state first, at $t = 100$ (15 orbits), and the inner disk at $t = 200$ (30 orbits). The turbulent alpha parameter peaks at 8×10^{-3} ($\alpha_M = 6 \times 10^{-3}$, $\alpha_R = 2 \times 10^{-3}$) at 30 orbits and starts a long decay until leveling after other 30 orbits at $\alpha_M = 3 \times 10^{-3}$ and $\alpha_R = 7.5 \times 10^{-4}$. The global averages are $R^{s\phi} = (5 \pm 2) \times 10^{-5}$, $M^{s\phi} = (1.8 \pm 0.6) \times 10^{-4}$ and total alpha viscosity $\alpha = (4.2 \pm 1.5) \times 10^{-3}$.

The referee, Dr. Ulf Torkelsson, pointed out to us that the non-zero tension of the constant azimuthal field,

$$\mu^{-1}(\mathbf{B} \cdot \nabla)\mathbf{B} = -\mu^{-1}B_0^2 s^{-1} \hat{s},$$

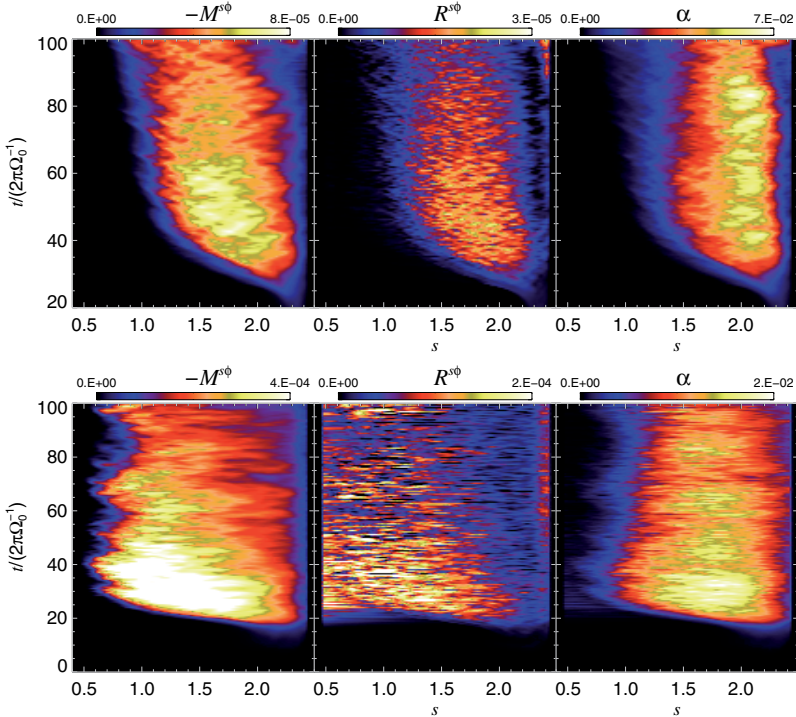


Fig. 14. Space-time diagram of the turbulent stresses and alpha viscosity for model F (*upper panels*) and model G (*lower panels*). Time is quoted in orbits at $s_0 = 1.0$. Saturation is reached at 40 orbits, but after 60 orbits the stresses seem to start a slow decay. The alpha viscosity appears constant, due to a similar decay in gas pressure in the outer disk, that starts to deplete as the resulting accretion builds a negative density gradient. Model G behaves similarly, but with higher stresses, lower alpha viscosity and being turbulent further inside.

leads to an increase in the centripetal force that is not taken into account by Eq. (12), so the models with azimuthal flux are not started in strict magnetohydrostatical equilibrium. We therefore performed a set of 2D tests to assess how this out-of-equilibrium initial condition could modify our results. First we ran a 2D disk without noise in the velocity field, so although a magnetic field is present, the spectrum of wavelengths is not excited. The departure from equilibrium launches a sound wave starting from the inner disk and propagating outwards. At time $t = 30$ (≈ 5 orbits) in model F the sound wave reaches the outer boundary and is damped by the buffer zone. After that, the oscillations slowly damp through the next orbits as the disk settles into centrifugal equilibrium between gravity, thermal pressure, and magnetic tension forces. We followed the evolution until time $t = 90$. At this time, the amplitude of the perturbation dropped to 3% of the initial density and 1% of the reference sound speed c_{s_0} .

In model G, with a sound speed 4 times faster, the sound wave reaches the outer boundary much earlier, at time $t = 12$ (about 2 orbits). By including noise we see the same results, so we conclude that in a 2D case, even though the non-vanishing magnetic tension leads to an out of equilibrium initial configuration, the discrepancy is slight and the system quickly relaxes in a timescale that is much smaller than the time the MRI takes to saturate (20 orbits).

5. Disks with solid boulders

Having presented the gaseous disk models, we now proceed to study the behavior of solid boulders inserted in these disks we have constructed. Meter-sized boulders are an important step towards kilometer-sized planetesimals. They are also interesting from a gas-dynamical point of view because they are only marginally coupled to the gas (on approximately a Keplerian shear time-scale) and can thus experience concentrations in vortices and transient gas high pressures (Barge & Sommeria 1995; Fromang & Nelson 2005; Johansen et al. 2006).

Our models are usually evolved for ≈ 75 orbits at s_0 before we add the particles, to allow for the turbulence to develop and saturate. A large number of particles (10^6) is used, which allows us to trace the swarm of particles onto the grid as a density field. The initial condition is such that the particles are concentrated in an annulus of constant bulk density ρ_p , ranging from s_{int} to s_{ext} , with a solids-to-gas ratio of 0.01, typical of the interstellar medium. Their velocity is initially the Keplerian angular velocity for their radial location.

As boundary conditions, we do not allow the particles to leave the computational domain as they drift inwards due to gas drag from the slightly sub-Keplerian gas. Instead, a particle that crosses the inner radius s_{int} will be relocated to the outer radius s_{ext} , where it will reappear at the same azimuthal location,

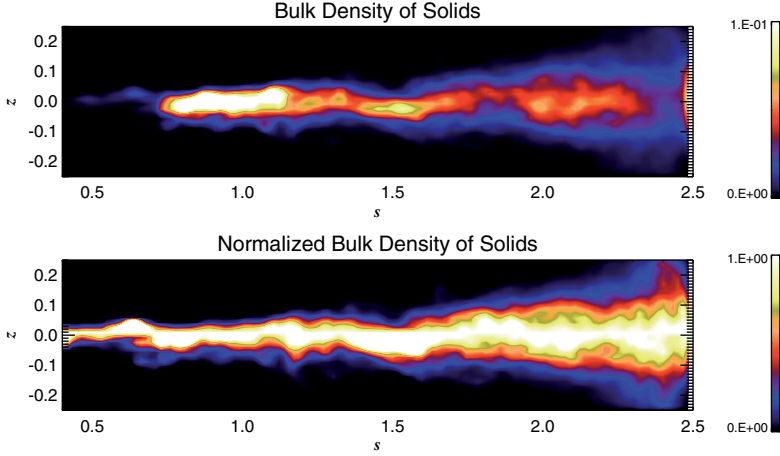


Fig. 15. Vertical slice of the bulk density of solid particles (*upper*) and the same quantity normalized by the midplane density. A midplane layer forms in equilibrium between sedimentation and turbulent diffusion. The scale height of this layer follows a linear dependence with radius.

thus mimicking periodic boundary conditions. Its velocity, however, will be reset to the Keplerian angular velocity at s_{ext} . A particle that tries to cross the outer radius will simply have its velocity reset to Keplerian without changing its radial or azimuthal location.

We include particles at the later stages of models A and D. For model A, where the inner disk does not go turbulent, it was noticed that by allowing the particles to move through all the radial range, they eventually got trapped in the several local density maxima between the concentric rings that the inner disk breaks into. As such a loss of particles is undesirable, we keep them where the turbulence is saturated by setting the inner radius of the boundary conditions for particles outwards of s_0 . In model D, where the Balbus-Hawley wavelength is resolved at all radii, such correction is not needed. We discuss the results of model D first.

5.1. Particles on model D

The particles soon fall to the disk midplane due to the vertical gravity. At the same time they get trapped in high pressure regions in the turbulent flow due to the drag force (Klahr & Lin 2001; Johansen et al. 2006). In Fig. 15 we plot a slice of the bulk density of solids profile 10 orbits after the insertion of the particles into the simulation. A pile-up of solids in the inner disk is seen to have occurred, because particles have concentrated in a pressure maximum in the gas (we discuss this further in Sect. 5.2; see also Fig. 18).

As discussed by Johansen & Klahr (2005), while solid particles are pulled towards the midplane by the stellar gravity, turbulent motions stir them up again. A sedimentary layer in equilibrium between turbulent diffusion and gravitational settling is formed. The thickness of this layer is therefore a measurement of the turbulent diffusion acting on the solid particles.

Under the influence of gravity, the solids settle with a profile similar to the one generated by a pressure force (Dubrulle et al. 1995)

$$\ln \rho_p(s, z) = \ln \rho_p(s, z = 0) - \frac{z^2}{2H_p^2}. \quad (22)$$

By comparing this profile with the analytical expression for a pressureless fluid under diffusion, gas drag and vertical gravity (Johansen & Klahr 2005)

$$\ln \rho_p = \ln \rho_p(s, z = 0) - \frac{\tau_f}{D_z^{(l)}} \int g_z dz, \quad (23)$$

and recalling that $g_z = -\Omega^2 z$, we have

$$D_z^{(l)} = \Omega^2 H_p^2 \tau_f. \quad (24)$$

From Eq. (22), we see that the scale height of the solids is the vertical distance in which the bulk density falls by a factor $1/\sqrt{e} \approx 0.6$ relative to the value at midplane. We plot in Fig. 15b the bulk density normalized by its value in the midplane. In this figure, the quantity plotted is in fact identical to the exponential term in Eq. (22). Where it reaches 0.6, the vertical distance z gives the diffusion scale height H_p .

We fit the points where the exponential term equals 0.6 with a power law $H_p = ar^n$. A linear regression in logarithm yields $a = 0.042$ and $n = 0.97$, with an rms of 0.04. This translates into a diffusion coefficient (Eq. (24)) of $D^{(l)} \approx 1.7 \times 10^{-3} \text{ s}^{-1}$. As this model has a sound speed profile $c_s = 0.1 \text{ s}^{-1}$, the diffusion coefficient in dimensionless units corresponds to $\delta^{(l)} = D^{(l)} c_s^{-2} \Omega = 0.17 \text{ s}^{-1.5}$, or 0.14 if globally averaged. The rms of 0.04 in the logarithm fit yields an uncertainty of 0.01 in this global average. As the total alpha viscosity is 0.112 ± 0.003 , the globally averaged vertical Schmidt number, i.e., the strength of viscosity when compared to vertical diffusion, is 0.78 ± 0.06 .

5.2. Particles in model A

For model A, the alpha viscosity ($\alpha \sim 10^{-3}$) is much lower than in model D ($\alpha \sim 10^{-1}$), so according to Eq. (24) and assuming that the diffusion coefficient is of the same order of the turbulent viscosity, we expect the sedimentary layer of solid particles to have a scale height of $H_p = \alpha/\Omega^2 \tau_f \approx 0.03H$. At s_{ext} , the gas scale height H equals 0.08 for $c_{s0} = 0.05$, then $H_p = 2.5 \times 10^{-3}$. With a grid resolution $\Delta z = 0.02$, this layer will not be resolved. It means that the interpolation of the particle density back to the

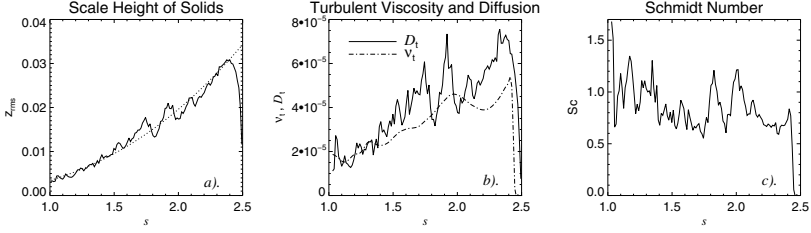


Fig. 16. Time-averages of the dispersion of vertical positions of particles w.r.t. the disk midplane, revealing the scale height of the sedimentary layer that forms due to the equilibrium between sedimentation and turbulent diffusion for model A. The dotted line is a power law fit, yielding an exponent of ≈ 2.5 . This radial profile is a time average between orbits 4 and 20 (see text). The resulting diffusion coefficient resulting from this scale height is shown as solid line in the middle panel. The time averaged gas-phase viscosity is shown in dot-dashed line for comparison. It is seen that these two coefficients have similar strength. The right panel shows the Schmidt number of the flow. It is indeed close to unity through the radial domain.

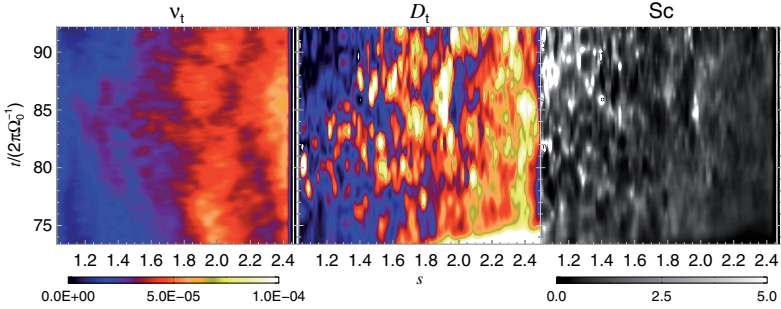


Fig. 17. Azimuthally and vertically averaged turbulent viscosity v_t , turbulent diffusion D_t and the resulting Schmidt number Sc as a function of radial position and time for model A. Time is quoted in orbits at s_0 . Viscosity and diffusion are shown in the same units and color-code. Some localized overdensities in diffusion last for some orbits, while viscosity shows a smoother evolution in time. The quantities have approximately the same strength, as the Schmidt number is overall around unity, and seldom greater than 5.

grid will not allow for a grid-based measurement of the diffusion acting in the turbulent layer as we did for model D.

But as the particles are Lagrangian, we can plot their real positions and trace the scale height of solids in a grid-independent way. The diffusion process operates in much the same way, nearly independent of grid resolution, since the large scale velocities of the gas are well resolved. In order to do this, we define 128 bins in the radial direction and measure the individual vertical positions of the swarm of particles with respect to the midplane of the disk within these bins. The standard deviation z_{rms} of the vertical positions of particles with respect to the midplane in each bin immediately gives the scale height of the sedimentary layer. The result of this process is shown in Fig. 16a, where we average z_{rms} as measured on 17 snapshots, from orbits 4 to 20 at s_0 after the insertion of the particles. The initial time is chosen at 4 orbits because it is the time it takes for the drag force to couple the particles to the gas at s_{ext} , thus making sure that the sedimentary layer is in equilibrium between gravitational settling and turbulent diffusion through the whole radial extent of the disk.

The dashed line in Fig. 16a represents the power law fit $H_p = ar^n$ to the measured scale height. It yields $a = 0.003$ and $n = 2.48$. The rms of the logarithmic fit is 0.09. In Fig. 16b we plot the resulting diffusion coefficient $D_2^{(l)} = \Omega^2 H_p^2 \tau_f$. It can be approximated by a power law of $\approx 9 \times 10^{-6} s^2$. In dimensionless units it corresponds to $\delta^{(l)} = 3.6 \times 10^{-3} s^{-1.5}$, or 0.007 if globally averaged. The uncertainty is 0.001. This behavior of the turbulent

diffusion that acts on solids is quite similar to the one shown by the turbulent viscosity arising from the stresses on the gas phase (dot-dashed line in Fig. 16b). Checking the radial dependency of the Schmidt number (Fig. 16c), we see that it is of the order of unity all over the radial domain. A slight trend is seen towards smaller Schmidt numbers in the outer disk, but it never gets below 0.6.

In Fig. 17 we explore this radial dependency in more detail. The figure shows the vertical and azimuthal average of the turbulent viscosity v_t , turbulent diffusion D_t and their ratio Sc , the Schmidt number, as a function of radial position s . On the time axis we show time in orbits at s_0 since the beginning of the simulations. At 71 orbits the particles are inserted, and quickly fall to the midplane. As seen from the diffusion map, the particles in the innermost radii quickly sediment, settling in a diffusive equilibrium in less than two orbits. After four orbits, $t = 75$, the last radius achieves diffusion equilibrium and the situation becomes statistically unchanged until the end of the simulation.

The gas-phase viscosity and the solid-phase diffusion are similar in average, but the diffusion is seen to fluctuate more. Transient patches of high diffusivity are seen to live for some orbits at a constant radial location before decaying. The turbulent viscosity, in turn, appears much smoother in time. The resulting Schmidt number is shown in greyscale in the right panel of Fig. 17. Due to the high variability of diffusion, some short lived bright areas of $Sc > 5$ are seen, but overall the Schmidt number is around 1 throughout the space-time domain.

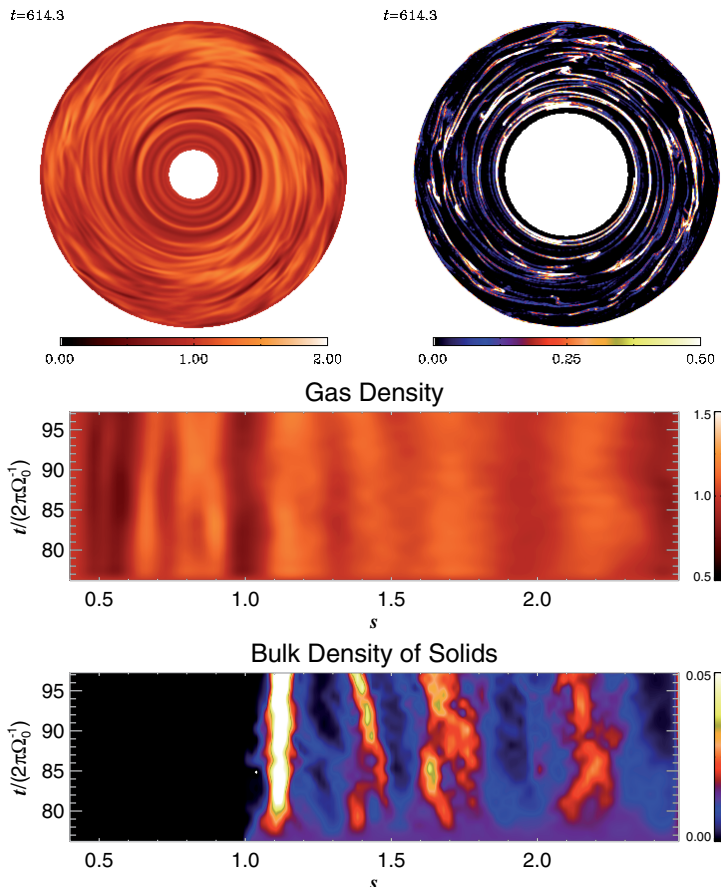


Fig. 18. Density contours at midplane of the gas and solid phases of the disk (*left and right panel*, respectively). The snapshots were taken at 20 orbits at s_0 after the insertion of the particles. The color code for the solid phase is selected to represent 2 sigma (0.25) above the average bulk density of 0.03. The bright areas are saturated as the maximum density reaches as far as 85. A movie of this simulation can be found at <http://www.astro.uu.se/~wlyra/planet.html/>. A correlation with gas density is seen, since the bright clumps of solids correspond to pressure maxima, i.e., areas of high gas density.

In Fig. 18 we show contours of the gas density (left panel) and the bulk density of solids (right panel) in a snapshot taken after 20 orbits after the insertion of the particles. A correlation is seen as the solids show large concentration at areas of high gas density. Initially, the density increases linearly as the particles sediment towards the midplane. As seen before, the sedimentation is complete at the outer radius after ≈ 4 orbits. After that, the growth is only due to the particles being concentrated in transient gas high pressures.

The average bulk density is quite low ($\rho_p = 0.003$, or $6.0 \times 10^{-11} \text{ kg m}^{-3}$ in physical units, see Table 1), and several areas devoid of particles are seen in the disk. However, the overdensities observed as bright clumps in the snapshot are several standard deviations above average. By plotting the maximum solid density (which is roughly the solids-to-gas ratio) throughout the simulation (Fig. 19), we see that its value is usually around 30, but it can reach values as high as 85. Such a behavior was seen in shearing box simulations by Johansen et al. (2006), who report

local enhancements of the solids-to-gas ratio by a factor of 100, also pointing that such concentrations are gravitationally unstable, thus being able to collapse to form km-sized bodies.

As a control, we also simulated the settling for a non-turbulent, purely laminar, unperturbed disk. Without high pressure regions, the particles simply sedimented towards the midplane forming a thin homogeneous layer of solids.

6. Summary and conclusions

We have considered MHD models of global Keplerian disks in Cartesian grids. These disk-in-a-box models are able to develop and sustain MHD turbulence, in good agreement with published results achieved with cylindrical codes and shearing boxes. In this first article of the series, we investigated the dependence of the MRI with disk scale height and the dynamics of solid boulders in the global hydromagnetic turbulence.

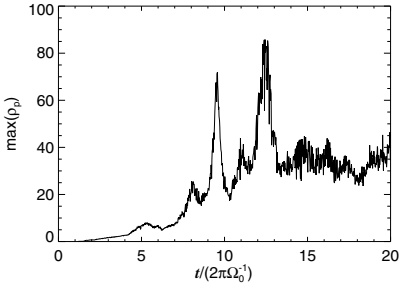


Fig. 19. Maximum bulk density of solids, in units of the mean gas density as a function of time for model A. Time is quoted in orbits at Ω_0 . The maximum density rises as the particles sediment towards the mid-plane. After the sedimentation that lasts for four orbits, the particles are coupled with the gas and trapping in transient gas high pressures raise their maximum density well above average. The maximum density is usually around 30, but between orbits 12 and 13, it reached values as high as 85.

As a numerical solver we have used the PENCIL CODE. This finite-difference code solves the non-conservative form of the dynamical equations using sixth-order spatial derivatives, achieving spatial resolution that approaches that of spectral methods. The numerical scheme is stabilized by using hyperdissipation and shock dissipation terms, which enter as free parameters in the dynamical equations. The effect of hyperdissipation is to quench unstable modes in the small scales of the grid, while affecting the large scale motion as little as possible, whereas shock dissipation is invoked to smear out large divergences in the flow field. We choose these parameters by performing series of 2D gap opening simulations with a Jupiter mass planet and comparing them with a higher resolution calculation without explicit dissipative terms.

We find evidence that the turbulence generated by the magnetorotational instability grows with the thermal pressure. The turbulent stresses depend on thermal pressure obeying a power law of 0.24 ± 0.03 , compatible with the value of 0.25 found in shearing box calculations by Sano et al. (2004). We extend this result to a global disk showing that the rise in pressure increases the turbulent stresses, thus raising the angular momentum transport (and therefore the mass accretion rate) although the alpha viscosity value drops.

We also notice two curious effects. First, the dominance of the radial component of the turbulent kinetic energy increases with temperature. The percentage of the total kinetic energy stored in the radial component is 40% for the cold model A, and 60% for the hotter model C. Second, the ratio of stresses $-M^{s\phi}/R^{s\phi}$ diminished with increasing temperature. It is 5 for model A, and just 1.3 for model C. The same is seen in the model without inner boundary, where the ratio is 6.5 for model A2 and very close to 1 for model C2. This effect is unexpected since it is believed that the shear parameter alone controls the ratio of stresses (Pessah et al. 2006; Ogilvie & Pringle 1996). From the shearing box data of Sano et al. (2004) the stress ratio seems to be constant with temperature.

One explanation could be that, according to Eq. (12), the angular velocity is sub-Keplerian and the increasing effects of pressure from the colder to the hotter models modifies the shear. Quantitatively, however, one sees that the pressure correction is too small to account for the decrease in the stress ratio and, more importantly, would have the opposite effect. According

to the linearized equations for the evolution of the turbulent fluctuations, the Maxwell stress couples with shear $q\Omega$, and the Reynolds stress couples with the large scale vorticity $w = (2 - q)\Omega$ (Balbus & Hawley 1998), where $q = -\partial \ln \Omega / \partial \ln r$ is the shear rate. The pressure-corrected angular velocity of the gas can be approximated from Eq. (12) as

$$\Omega \approx \Omega_K(1 - \eta), \quad (25)$$

where $\eta = (1/2)(\partial \ln P / \partial \ln r)(H/s)^2 > 0$ is a parameter often used to parameterize the strength of the global pressure gradient (see e.g. Nakagawa et al. 1986). Typical values of η lie between 0.001 and 0.1.

The reduction of both the angular frequency and shear rate should reduce the Maxwell stress. Our simulations show the opposite, with the Maxwell stress increasing as the pressure is raised. Regarding the stress ratio, reducing the shear increases this quantity since the Reynolds stress falls faster than the Maxwell stress due to the stabilizing effect of the growing vorticity (Abramowicz et al. 1996). Once again, we see the opposite effect.

As most of the analysis of turbulent thin accretion disks have focused on locally isothermal simulations using $c_s \approx 0.05$, changing the field configuration while keeping the temperature constant, such behavior has been largely overlooked. Although the disk temperatures considered in this case are quite extreme for disks around T-Tauri stars, circumplanetary disks are thought to be rather thick (Klahr & Kley 2006) and therefore the evolution of the MRI in such disks is expected to be more similar to the hotter cases considered in this paper (models CEG) than the colder ones.

We investigated the effect of an inner boundary in the evolution and outcome of the turbulence. By using a Cartesian grid, an inner boundary can be discarded provided we smooth the gravitational potential to avoid a singularity in the flow. Models without an inner boundary do not show the spurious build-up of magnetic pressure and Reynolds stress seen in the models with boundaries, while the global stresses and alpha viscosities are similar in the two cases.

In treating the solids, we make use of a large number of particles, which allows us to effectively map the particles back into the grid as a density field without using fluid approaches. We monitor the settling of the particles toward the midplane and the formation of a sedimentary layer when the solids are subject to gas drag and the gravity from the central object. The effective diffusion provided by the turbulence prevents further settling of solids, in accordance with the results of Johansen & Klahr (2005). By having the global disk perspective, we could measure the radial dependence of the diffusion scale height of the solid component. The measured scale heights imply turbulent vertical diffusion coefficients with globally averaged Schmidt numbers of 1.0 ± 0.2 for model A ($\alpha \approx 10^{-3}$) and 0.78 ± 0.06 for model D ($\alpha \approx 10^{-1}$).

We conclude that the models presented in this first paper of the series are capable of sustaining turbulence and are adequately suited for further studies of planet formation. Future papers will present studies of thermodynamics and radiative transfer in the evolution of the turbulent stresses, planet-planet and planet-disk interaction, the effect of stratification and the dynamics of dead zones.

Acknowledgements. The authors thank the referee, Dr. Ulf Torkelson, for his many constructive comments that helped improve the manuscript. We warmly acknowledge Dr. Paul Barklem for his help on improving the quality of the English. Simulations were performed at the PIA cluster of the Max-Planck-Institut für Astronomie and on the Uppsala Multidisciplinary Center for Advanced Computational Science (UPPMAX).

Appendix A: Anisotropic hyperdissipation

Hyperdiffusion is used to quench unstable modes at the grid scale, therefore being intrinsically resolution-dependent. Because of this, *isotropic* dissipation only gives equal dissipation in all spatial directions if $\Delta x = \Delta y = \Delta z$, i.e., if the cells are cubic. For non-cubic cells, anisotropic dissipation is required as different directions may be better/worse sampled, thus needing less/more numerical smoothing. Such a generalization is straightforward. We notice that hyperdiffusion works as a conservative term in the continuity equation such that

$$f_D(\rho) = \nabla \cdot \mathcal{J}, \quad (\text{A.1})$$

where $\mathcal{J} = D_3 \nabla^5 \rho$ is the mass flux due to hyperdiffusion. For simplicity, we will drop the subscripts “3” from the coefficients hereafter. This formulation reduces to the usual sixth-order hyperdiffusion under the condition that D is constant. Generalizing it to three dimensions simply involves replacing this mass flow by

$$\mathcal{J} = \left(D_x \frac{\partial^5 \rho}{\partial x^5}, D_y \frac{\partial^5 \rho}{\partial y^5}, D_z \frac{\partial^5 \rho}{\partial z^5} \right),$$

so that different diffusion operates in different directions. Since D_x , D_y and D_z are constants, the divergent of this vector is

$$\nabla \cdot \mathcal{J} = D_x \frac{\partial^6 \rho}{\partial x^6} + D_y \frac{\partial^6 \rho}{\partial y^6} + D_z \frac{\partial^6 \rho}{\partial z^6}.$$

The formulation for resistivity is strictly the same. For viscosity it also assumes the same form if we consider a simple n th order rate of strain tensor operator $S_{ij}^{(n)} = \partial_i^n u_j$.

Appendix B: Shocks

Shock viscosity is taken to be proportional to positive flow convergence, maximum over three zones, and smoothed to second order,

$$\zeta_v = \nu_{\text{sh}} \left(\max_3 [(-\nabla \cdot \mathbf{u})_+] \right) \left[\min(\Delta x, \Delta y, \Delta z) \right]^2, \quad (\text{B.1})$$

where ν_{sh} is a constant defining the strength of the shock viscosity, usually around unity. We refer to it as the shock viscosity coefficient (Haugen et al. 2004). In the equation of motion it takes the form of a bulk viscosity so that now the stress tensor contains

$$\tau_{ij} = [\dots] + \rho \zeta_v \delta_{ij} \nabla \cdot \mathbf{u}, \quad (\text{B.2})$$

where [...] refers to the (hyper) viscous terms described in Appendix A. The acceleration due to shock viscosity is therefore

$$f_v(\mathbf{u}, \rho) = \rho^{-1} \nabla \cdot \tau \\ = \zeta_v [\nabla(\nabla \cdot \mathbf{u}) + (\nabla \ln \rho + \nabla \ln \zeta_v) \nabla \cdot \mathbf{u}]. \quad (\text{B.3})$$

Such a viscosity scheme ensures that energy is dissipated in regions of the flow where shocks occur, whereas more quiescent regions are left untouched. The formulations for shock diffusion and shock resistivity are similar, yielding

$$f_D(\rho) = \zeta_D (\nabla^2 \rho + \nabla \ln \zeta_D \nabla \rho), \quad (\text{B.4})$$

and

$$f_\eta(\mathbf{A}) = \zeta_\eta (\nabla^2 \mathbf{A} + \nabla \ln \zeta_\eta \nabla \cdot \mathbf{A}), \quad (\text{B.5})$$

where ζ_D and ζ_η are analogous to ζ_v in Eq. (B.1), containing their respective shock diffusion and shock resistivity coefficients D_{sh} and η_{sh} .

References

- Abramowicz, M. 1996, in *Physics of Accretion Disks*, ed. S. Kato, S. Inagaki, S. Mineshige, & J. Fukue (Amsterdam: Gordon and Breach), 1
- D’Angelo, G., Henning, T., & Kley, W. 2003, *ApJ*, 599, 548
- Armitage, P. J. 1998, *ApJ*, 501, 189
- Armitage, P. J., Reynolds, C. S., & Chiang, J. 2001, *ApJ*, 548, 868
- Balbus, S. A., & Hawley, J. F. 1991, *ApJ*, 376, 214
- Balbus, S. A., & Hawley, J. F. 1992, *ApJ*, 400, 610
- Balbus, S. A., & Hawley, J. F. 1998, *RvMP*, 70, 1
- Barge, P., & Sommeria, J. 1995, *A&A*, 295, 1
- Brandenburg, A., Nordlund, Å., Stein, R. F., & Torkelsson, U. 1995, *ApJ*, 446, 741
- Chandrasekhar, S. 1960, *Proc. Nat. Acad. Sci.*, 46, 253
- Chandrasekhar, S. 1961, *Hydrodynamic and Hydromagnetic Stability* (Oxford: Clarendon), 384
- Dobler, W., private communication
- Dobler, W., Stix, M., & Brandenburg, A. 2006, *ApJ*, 638, 336
- Dubrulle, B., Morfill, G., & Sterzik, M. 1995, 114, 237
- Freytag, B., Steffen, M., & Dorch, B. 2002, *AN*, 323, 213
- Fromang, S., & Nelson, R. P. 2005, *MNRAS*, 364, 81
- Fromang, S., & Nelson, R. P. 2006, *A&A*, 457, 343
- Gammie, C. F. 1996, *ApJ*, 457, 355
- Goldreich, P., & Ward, W. R. 1973, *ApJ*, 183, 1051
- Haugen, N. E. L., & Brandenburg, A. 2004, *PhRvE*, 70, 6405
- Haugen, N. E. L., Brandenburg, A., & Mee, A. J. 2004, *MNRAS*, 353, 947
- Hawley, J. F. 2000, *ApJ*, 528, 462
- Hawley, J. F. 2001, *ApJ*, 554, 534
- Hawley, J. F., & Balbus, S. A. 1991, *ApJ*, 376, 223
- Hawley, J. F., Gammie, C. F., & Balbus, S. A. 1995, *ApJ*, 440, 742
- Johansen, A., & Klahr, H. 2005, *ApJ*, 634, 1353
- Johansen, A., Klahr, H., & Henning, T. 2006, *ApJ*, 636, 1121
- Johansen, A., Oishi, J. S., Mac Low, M.-M., et al. 2007, *Nature*, 448, 1022
- Kant, I. 1755, *Universal Natural History and Theories of the Heaven*
- Klahr, H., & Kley, W. 2006, *A&A*, 445, 747
- Klahr, H., & Lin, D. N. C. 2001, *ApJ*, 554, 1095
- Kwok, S. 1975, *ApJ*, 198, 583
- Laplace, P. S. 1796, *Mécanique Céleste*
- Lin, D. N. C., & Papaloizou, J. 1986, *ApJ*, 309, 846
- Lucas, P. W., & Roche, P. F. 2000, *MNRAS*, 314, 858
- Marcy, G. W., & Butler, R. P. 1996, *ApJ*, 464, 147
- Masset, F., D’Angelo, G., & Kley, W. 2006, *ApJ*, 652, 730
- Mayor, M., & Queloz, D. 1995, *Nature*, 378, 355
- Miller, K. A., & Stone, J. M. 2000, *ApJ*, 534, 398
- Mizuno, H. 1980, *Prog. Theor. Phys.*, 64, 544
- Nakagawa, Y., Sekiya, M., & Hayashi, C. 1986, *Icarus*, 67, 375
- Nelson, R. P. 2005, *A&A*, 443, 1067
- van Noort, M., Hubeny, I., & Lanz, T. 2002, *ApJ*, 568, 1066
- Ogilvie, G. I., & Pringle, J. E. 1996, *MNRAS*, 279, 1520
- Oishi, J. S., Mac Low, M.-M., & Menou, K. 2007 [[arXiv:astro-ph/0702549](https://arxiv.org/abs/0702549)]
- Paardekooper, S.-J. 2007, *A&A*, 462, 355
- Paardekooper, S.-J., & Mellema, G. 2006, *A&A*, 459, 17
- Papaloizou, J. C. B., & Nelson, R. P. 2003, *MNRAS*, 339, 983
- Pessah, M. E., Chan, C.-K., & Psaltis, D. 2006, *MNRAS*, 372, 183
- Pollack, J. B., Hubickyj, O., Bodenheimer, P., et al. 1996, *Icarus*, 124, 62
- Pringle, J. E. 1981, *ARA&A*, 19, 137
- von Rekowski, B., & Piskunov, N. 2006, *AN*, 327, 340
- Rivera, E. J., Lissauer, J. J., Butler, R. P., et al. 2005, *ApJ*, 634, 625
- Safronov, V. S. 1969, *QB*, 981, 26
- Sano, T., Inutsuka, S.-I., Turner, N. J., & Stone, J. M. 2004, *ApJ*, 605, 321
- Shakura, N. I., & Sunyaev, R. A. 1973, *A&A*, 24, 37
- Sicilia-Aguilar, A., Hartmann, L. W., Briceño, C., Muzeroller, J., & Calvet, N. 2004, *AJ*, 128, 805
- de Val-Borro, M., Edgar, R. G., Artymowicz, P., et al. 2006, *MNRAS*
- Velikhov, E. P. 1959, *Soviet Phys. JETP*, 36, 1398
- Ward, W. R. 1981, *Icarus*, 47, 234
- Ward, W. R., & Hourigan, K. 1989, *ApJ*, 347, 490
- Weidenschilling, S. J. 1977, *MNRAS*, 180, 5
- Wolszczan, A., & Frail, D. A. 1992, *Nature*, 355, 145
- Youdin, A., & Johansen, A. 2007, *ApJ*, 662, 613
- Youdin, A. N., & Shu, F. H. 2002, *ApJ*, 580, 494

Paper II



LETTER TO THE EDITOR

Embryos grown in the dead zone

Assembling the first protoplanetary cores in low mass self-gravitating circumstellar disks of gas and solids^{*}

W. Lyra¹, A. Johansen², H. Klahr³, and N. Piskunov¹

¹ Department of Physics and Astronomy, Uppsala Astronomical Observatory, Box 515, 75120 Uppsala, Sweden
e-mail: wlyra@astro.uu.se

² Leiden Observatory, Leiden University, PO Box 9513, 2300 RA Leiden, The Netherlands

³ Max-Planck-Institut für Astronomie, Königstuhl 17, 69117 Heidelberg, Germany

Received 16 July 2008 / Accepted 10 October 2008

ABSTRACT

Context. In the borders of the dead zones of protoplanetary disks, the inflow of gas produces a local density maximum that triggers the Rossby wave instability. The vortices that form are efficient in trapping solids.

Aims. We aim to assess the possibility of gravitational collapse of the solids within the Rossby vortices.

Methods. We perform global simulations of the dynamics of gas and solids in a low mass non-magnetized self-gravitating thin protoplanetary disk with the Pencil Code. We use multiple particle species of radius 1, 10, 30, and 100 cm. The dead zone is modelled as a region of low viscosity.

Results. The Rossby vortices excited in the edges of the dead zone are efficient particle traps. Within 5 orbits after their appearance, the solids achieve critical density and undergo gravitational collapse into Mars sized objects. The velocity dispersions are of the order of 10 m s^{-1} for newly formed embryos, later lowering to less than 1 m s^{-1} by drag force cooling. After 200 orbits, over 300 gravitationally bound embryos were formed, 20 of them being more massive than Mars. Their mass spectrum follows a power law of index -2.3 ± 0.2 .

Key words. accretion, accretion disks – instabilities – stars: planetary systems: formation

1. Introduction

The formation of planets is one of the major unsolved problems in modern astrophysics. In the standard core accretion scenario, sub- μm grains assemble into progressively larger bodies through electrostatic interactions (Natta et al. 2007), eventually growing into centimeter and meter sized boulders. Growth beyond this size, however, is halted since these boulders have very poor sticking properties and are easily destroyed by collisions at the velocities assumed to be prevalent in circumstellar disks (Benz 2000). Furthermore, centimeter and meter sized solids are loosely decoupled from the gas, but remain sufficiently small to be affected by significant gas drag. The resulting headwind from the sub-Keplerian gas reduces their angular momentum and forces them into spiral trajectories onto the star in timescales as short as a few thousand years (Weidenschilling 1977a).

A mechanism for overcoming these barriers was presented by Kretke & Lin (2007). In the presence of sufficient ionization, the gaseous disk couples with the ambient weak magnetic field, which triggers the growth of the magneto-rotational instability (MRI; Balbus & Hawley 1991). In its saturated state, a vigorous turbulence drives accretion onto the star by means of magnetic and kinetic stresses. However, in the water condensation front (snowline) the abundant presence of snowflakes effectively removes free electrons from the gas, lowering the degree of ionization. The turbulence is weakened locally and the accretion flow

is stalled. As the radial inflow proceeds from the outer disk, gas accumulates at the snowline. Since embedded solid bodies move towards gas pressure maxima (Haghighipour & Boss 2003), the snowline environment proposed by Kretke & Lin (2007) is potentially an efficient particle trap. This scenario was further explored by Brauer et al. (2008), who demonstrated that as solids concentrate at this local pressure maximum, rapid growth into kilometer sized planetesimals occurs by coagulation.

Kretke et al. (2008) emphasized that an identical mechanism is supposed to occur elsewhere in the disk. Ionization ought to be present in the very inner disk due to the high temperatures, as well as in the outer regions where the gas is sufficiently thin for cosmic rays to penetrate to the disk midplane and provide ionization throughout. In between, however, temperatures are too low and gas columns too thick to allow sufficient ionization either by collisions or by cosmic rays. In the midplane of this region, the gas is neutral and the turbulence is largely suppressed (Gammie 1996). As in the snowline, the accretion flow from the MRI-active regions halts at the borders of this “dead” zone, where the gas then accumulates.

These models have been tested only by one-dimensional simulations, and these tests have therefore not benefited from an interesting development. As shown by Varnière & Tagger (2006), the density pileup at the border of the dead zone triggers the Rossby wave instability (RWI; Li et al. 2001). The azimuthal symmetry of the problem is broken and long-lived anticyclonic vortices are formed as the waves break and coalesce. Such entities are of significant interest because, by rotating clockwise

^{*} Appendices A–C are only available in electronic form at <http://www.aanda.org>

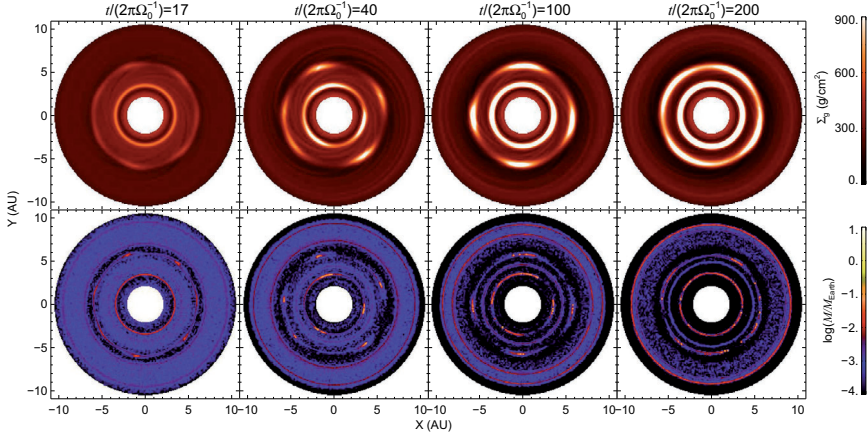


Fig. 1. The appearance of the disk in the gas (*upper panels*) and solid (*lower panels*) phases in selected snapshots. The Rossby vortices first appear at 15 orbits. Collapse of the particles into a gravitationally bound planetary embryo the size of Mars occurs 5 orbits later. The vortices tend to merge and decrease in number, retaining an $m = 4$ dominant mode at the outer edge until the end of the simulation, up to which over 300 embryos were formed.

in the global counterclockwise Keplerian flow, they amplify the local shear and induce a net force on solid particles towards their center (Barge & Sommeria 1995). As shown by Klahr & Bodenheimer (2006), the accumulation of solids under these circumstances is likely to lead to high densities. Inaba & Barge (2006) continued the study of Varnière & Tagger (2006) by including solids and confirming that the Rossby vortices excited in the borders of the dead zone act as powerful traps, enhancing the local solids-to-gas ratio by at least an order of magnitude. Unfortunately, they used a fluid approach – which limited the maximum particle size they could consider – and they did not include the self-gravity of the solids, which is crucial to follow the gravitational collapse. Studies with interacting particles in the literature include a MRI-unstable local box (Johansen et al. 2007) capable of producing dwarf planets out of meter sized boulders, a global massive disk unstable to gas self-gravity (Rice et al. 2006) in which concentrations of $0.5 M_{\oplus}$ are seen in the spiral arms, and a simulation that produces 10–100 km “sandpile” clumps formed out of mm-sized particles (Cuzzi et al. 2008).

In this letter, we build on the studies of Varnière & Tagger (2006) and Inaba & Barge (2006) by including self-gravitating centimeter and meter sized Lagrangian particles to model the solid phase. We show that in the vortices launched by the RWI in the borders of the dead zone, the solids quickly achieve critical densities and undergo gravitational collapse into protoplanetary embryos in the mass range 0.1–0.6 M_{\oplus} .

2. Model

We work in the thin disk approximation, using the vertically averaged equations of hydrodynamics. The gas drag is implemented in the same way as Paardekooper (2007), interpolating between Epstein and Stokes drag (see online supplement). The back reaction of the drag force onto the gas is present. The Poisson solver for the particles is a particle-mesh solver based on multiple Fourier transforms in a Cartesian grid, as used by Johansen et al. (2007).

We follow the Varnière & Tagger (2006) dead zone model, which consists of jumps in the viscosity profile. We artificially

place the inner and outer edges of the dead zone at 0.6 and 1.2 times the semi-major axis of Jupiter (5.2 AU), using Heaviside functions to jump from $\alpha = 10^{-2}$ to zero inside the dead zone. The parameter α is the usual alpha viscosity (Shakura & Sunyaev 1973).

The simulations were performed with the PENCIL CODE¹ in Cartesian geometry. The resolution was 256×256 . The surface density profile followed a power law of $\Sigma(r) \propto r^{-1/2}$, and we chose a disk about twice as massive as the Minimum Mass Solar Nebula, with surface density $\Sigma_0 = 300 \text{ g cm}^{-2}$ at 5.2 AU. The sound speed followed the local isothermal approximation with a radial temperature profile $T(r) \propto r^{-1}$. The disk aspect ratio was $h = 0.05$. For the solids, we used 10^5 Lagrangian superparticles and the interstellar value for the solids-to-gas ratio (10^{-2}). Each superparticle therefore contained $10^{-9} M_{\odot} \approx 2 \times 10^{24} \text{ g}$ of material. We used multiple particles species, of 1, 10, 30, and 100 cm radii, each represented by 1/4 of the total number of particles. We quote time as orbital periods at 5.2 AU.

3. Results

In Fig. 1, we show snapshots of the appearance of the disk for the gas and solids phases. The vortices triggered by the Rossby wave instability are visible as early as 15 orbits. As seen in the solids phase, the particles are trapped by the vortical motion and soon reach extremely high densities. After 17 orbits, seven vortices appear at the outer edge. After 45 orbits have elapsed, the $m = 4$ mode begins to dominate, persisting until the end of the simulation at 200 orbits, their gas surface density peaking at 4.5 times their initial value. In the inner edge of the dead zone, at 40 orbits we see a conspicuous $m = 3$ mode. By the end of the simulation, their surface density has increased by a factor of 8 relative to the initial condition, and a weak $m = 2$ mode is visible, albeit with far less contrast than in the outer disk.

In Fig. 2a, we plot the time evolution of the maximum concentration of solids. The solid line represents the maximum mass of solids contained in a single cell. The red dashed line marks the

¹ See <http://www.nordita.org/software/pencil-code>

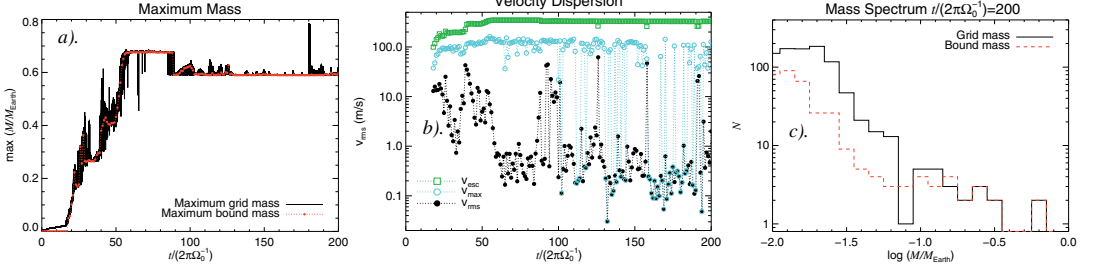


Fig. 2. a) Time evolution of the maximum mass of solids. The black solid line is the maximum mass of solids inside a single cell, and the red dot-dashed line marks the mass that is gravitationally bound. The maximum mass settles at $0.59 M_{\oplus}$ from 90 orbits onwards; b) the internal velocity dispersion v_{rms} of the most massive embryo, compared with its escaped velocity v_{esc} . The embryo is so firmly bound that even the maximum internal speed v_{max} is lower than the escape velocity. Throughout most of the simulation, the velocity dispersion is below 1 m s^{-1} ; c) the mass spectrum by the end of the simulation. The line and color style is the same as in Fig. 2a. Twenty gravitationally bound embryos in the mass range $0.1\text{--}0.6 M_{\oplus}$ were formed in the vortices launched at the edges of the dead zone.

maximum mass that is gravitationally bound. We decide whether boundness is present based on two criteria. First, we consider the mass inside the Hill’s sphere of the clump defined by the black line. Particles inside/outside the Hill’s sphere are added/removed from the total mass, and the Hill’s radius recomputed. The process is iterated until convergence. This positional criterion is followed by a dynamical one. We calculate the velocity dispersion v_{rms} of the particles inside the Hill’s radius, and compare its value with the escape velocity of the enclosed mass. If $v_{\text{rms}} < v_{\text{esc}}$, we consider that the cluster of particles is bound. We plot the velocity dispersion and escape velocity of the most massive clump in Fig. 2b. The first bound clumps appeared at 18 orbits, with masses of 0.050 and $0.036 M_{\oplus}$. At 20 orbits, four clumps of $0.1 M_{\oplus}$ are present. The mass is that of Mars, constituting a protoplanetary embryo. The efficiency of the vortex trapping mechanism can be more clearly appreciated if we consider the time elapsed between the rise of the Rossby vortices and the collapse of the trapped particles into a Mars sized object: only 5 orbits.

Two orbits later, the maximum mass increased to $0.22 M_{\oplus}$. Nine other clumps collapsed into embryos as well, five of them of mass above that of Mars. The maximum bound mass reached $0.67 M_{\oplus}$, but settled at $0.59 M_{\oplus}$ from 89 orbits until the end of the simulation at 200 orbits. We observe evidence that the mass loss episodes are due to tides from the gas, since the vortices concentrate sufficient gas to provide a considerable gravitational pull. In addition to tides, erosion (Cuzzi et al. 2008) also plays a role in disrupting clumps of smaller particles. We discuss this point further in the online supplement.

Figure 2b also indicates that the velocity dispersion remained below 1 m s^{-1} for most of the simulation. This is of extreme importance because it implies that particle encounters are gentle enough for destructive collisions to be avoided. The opposite was reported for the massive disk models of Rice et al. (2006), where particle encounters in the spiral arms occurred at velocities comparable with the sound speed. In Fig. 2b, we plot the maximum speed v_{max} for comparison. It is evident that even v_{max} remains lower than the escape velocity. This indicates that even if destructive collisions occur, the fragments will remain bound, although the strong drag force felt by the fragments might delay any gravitational collapse.

We plot the mass spectrum of the formed embryos in Fig. 2c. The solid black line represents the mass of solids inside a cell of the simulation box, without information on boundness. We overplot the distribution of bound clumps with the red dashed line.

Over 300 bound embryos are formed by the end of the simulation, twenty of these being more massive than Mars. The mass spectrum follows a power law of index -2.3 ± 0.2 in the interval $-2.0 < \log (M/M_{\oplus}) < -1.2$.

The two most massive embryos have 0.59 and $0.57 M_{\oplus}$, and are located in the inner and outer edge, respectively.

A common trait of these embryos is that they consist of an overwhelming majority of particles of a single species. For instance, over 98% of the most massive embryo consists of 30 cm particles. Almost 97% of the second most massive one were 10 cm particles. In one embryo in the Mars mass bin, 94% of the particles were of 1 cm radius. These different particle radii reflect the variations in gas drag strengths experienced by particles of different size. Since particles of a given size drift in a similar way, their spatial convergence becomes easier than the convergence of particles of different sizes. The almost single-phasing of the size spectrum of the bound clumps also contributes to their low velocity dispersions. Since particles of different sizes experience different gas drags, their relative velocities are often far higher than the relative velocities between particles of identical size (Th ebault et al. 2008). We indeed see that clumps with a more non-uniform distribution of particle sizes usually show larger velocity dispersions (≈ 10 instead of $\approx 1 \text{ m s}^{-1}$). It is an observed fact that planetesimals are formed of similarly sized particles (Scott & Krot 2005). Although the constituent particles appear to be sub-mm grains, different nebula parameters could enable smaller grains to be trapped.

At higher resolution (512^2 , and 4×10^5 particles), more bound clumps are formed, which extend to lower masses. More clumps containing similar quantities of particles of different sizes are observed, although the majority of clumps have nearly single phasing. The situation does not alter significantly when the number of particles is increased to 10^6 . In Fig. 3, we follow the collapse of one of these clumps at higher resolution. Although particles of different size are present inside the Hill’s sphere during the first stages of collapse, most are expelled and the collapsed embryo consists primarily of 30 cm particles. A control run without self-gravity achieves higher cell concentration, due to the absence of gas tides. At later times, the clumps also tend to have low rms speeds and small rms radii ($\approx 10^4 \text{ km}$), due to the efficient dynamical cooling provided by the drag force. Size segregation due to aerodynamical sorting is also observed in the control run. Inaba & Barge (2006) reported destruction of the vortices by the drag force backreaction. We see a different

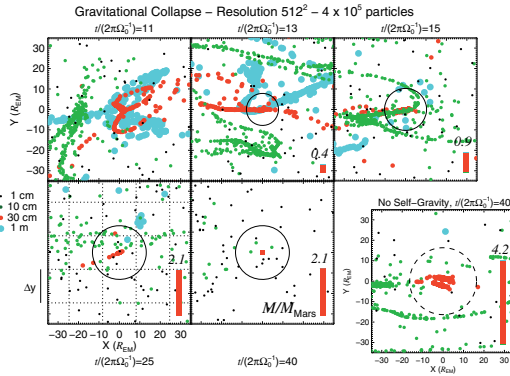


Fig. 3. Gravitational collapse of the particles into an embryo twice the mass of Mars. The unit of length is the Earth-Moon mean separation (R_{EM}). The lower left panel has the grid scale overplotted. The circle marks the Hill's radius. A control run without self-gravity attains higher cell concentration due to the absence of gas tides. The bar shows the mass of the embryo in units of M_{Mars} and the fractional mass of each particle species.

effect, in which the particles alter the evolution of the Rossby vortices and generate a vorticity of their own.

4. Conclusions

In this Letter, we have shown that when modelling the self-gravity of the gas and solids in protoplanetary disks, gravitational collapse of the solids into Mars sized protoplanetary embryos occurs rapidly at the borders of the dead zone, where particles concentrate. We have also found that tides from the dense gaseous vortices may hinder the formation process significantly.

Studies considering the origin of oligarchs usually begin from a collection of 10–20 Mars sized objects (e.g. Kobuko et al. 2006). This Letter presents the first simulation in which a similar number of Mars-sized embryos are formed from centimeter and meter sized building blocks.

It is crucial to the model that particles grow to sufficient size, otherwise the drag force from the gas becomes too strong to allow any concentration. Testi et al. (2003) observed grains of up to cm sizes in the disk surrounding the pre-main-sequence star CQ Tauri, which provides some observational evidence that a sufficient number of particles of the required size may exist in true protoplanetary disks.

We emphasize again that the model used in this Letter is simplistic, and the conditions may differ with a more realistic treatment of the dead zone. Nevertheless, the mechanism presented in this Letter (as proposed originally by Varnière & Tagger 2006) appears robust. It only requires the RWI to be excited in the borders between the active and dead zones, which in turn relies only on the slowdown of the accretion flow at this same border. Future studies should include a coagulation/fragmentation model such as those of Brauer et al. (2008) or Johansen et al. (2008), and focus on the precise state of flow at this transition region in global simulations, to address the question of how the RWI interacts with the MRI and non-ideal MHD in three dimensions.

Acknowledgements. Simulations were performed at the PIA cluster of the Max-Planck-Institut für Astronomie and on the Uppsala Multidisciplinary Center for Advanced Computational Science (UPPMAX). We thank the referee, Dr. Laure Fouchet, for many helpful suggestions for improvement of the paper.

References

- Baines, M. J., Williams, I. P., & Asebiomo, A. S. 1965, *MNRAS*, 130, 63
 Balbus, S. A., & Hawley, J. F. 1991, *ApJ*, 376, 214
 Barge, P., & Sommeria, J. 1995, *A&A*, 295, 1
 Benz, W. 2000, *SSRv*, 92, 279
 Brauer, F., Henning, Th., & Dullemond, C. P. 2008, *A&A*, 487, 1
 Cuzzi, J. N., Hogan, R. C., & Shariff, K. 2008 [arXiv:0804.3526]
 Gammie, C. F. 1996, *ApJ*, 457, 355
 Haghhighipour, N., & Boss, A. P. 2003, *ApJ*, 583, 996
 Inaba, S., & Barge, P. 2006, *ApJ*, 649, 415
 Johansen, A., Oishi, J. S., Mac Low, M.-M., Klahr, H., Henning, Th., & Youdin, A. 2007, *Nature*, 448, 1022
 Johansen, A., Brauer, F., Dullemond, C., Klahr, H., & Henning, T. 2008, *A&A*, 486, 597
 Klahr, H., & Bodenheimer, P. 2006, *ApJ*, 639, 432
 Kokubo, E., Kominami, J., & Ida, S. 2006, *ApJ*, 642, 1131
 Kretke, K. A., & Lin, D. N. C. 2007, *ApJ*, 664, 55
 Kretke, K. A., Lin, D. N. C., Garaud, P., & Turner, N. J. 2008 [arXiv:0806.1521]
 Kwok, S. 1975, *ApJ*, 198, 583
 Li, H., Colgate, S. A., Wendroff, B., & Liska, R. 2001, *ApJ*, 551, 874
 Lyra, W., Johansen, A., Klahr, H., & Piskunov, N. 2008, *A&A*, 479, 883
 Natta, A., Testi, L., Calvet, N., et al. 2007, in *Protostars and Planets V*, ed. B. Reipurth, D. Jewitt, & K. Keil, 767
 Paardekooper, S.-J. 2007, *A&A*, 462, 355
 Rice, W. K. M., Lodato, G., Pringle, J. E., Armitage, P. J., & Bonnell, I. A. 2006, *MNRAS*, 372, 9
 Scott, E. R. D., & Krot A. N. 2005, in *ASP Conf. Ser.*, 341, 15
 Shakura, N. I., & Sunyaev, R. A. 1973, *A&A*, 24, 37
 Testi, L., Natta, A., Shepherd, D. S., & Wilner, D. J. 2003, *A&A*, 403, 323
 Thébaud, P., Marzari, F., & Scholl, H. 2008 [arXiv:0806.0819]
 Varnière, P., & Tagger, M. 2006, *A&A*, 446, L13
 Weidenschilling, S. J. 1977, *MNRAS*, 180, 5
 Woitke, P., & Helling, C. 2003, *A&A*, 399, 297

Appendix A: Dynamical equations

As stated in the main paper, we work in the thin disk approximation, using the vertically integrated equations of hydrodynamics

$$\frac{\partial \Sigma_g}{\partial t} = -(\mathbf{u} \cdot \nabla) \Sigma_g - \Sigma_g \nabla \cdot \mathbf{u} + f_D(\Sigma_g) \quad (\text{A.1})$$

$$\begin{aligned} \frac{\partial \mathbf{u}}{\partial t} = & -(\mathbf{u} \cdot \nabla) \mathbf{u} - \frac{1}{\Sigma_g} \nabla P - \nabla \Phi - \frac{\Sigma_p}{\Sigma_g} f_d \\ & + 2 \Sigma_g^{-1} \nabla \cdot (\nu \Sigma_g \mathbf{S}) + f_v(\mathbf{u}, \Sigma_g) \end{aligned} \quad (\text{A.2})$$

$$\frac{d\mathbf{x}_p}{dt} = \mathbf{v}_p \quad (\text{A.3})$$

$$\frac{d\mathbf{v}_p}{dt} = -\nabla \Phi + f_d \quad (\text{A.4})$$

$$\Phi = \Phi_{\text{sg}} - \frac{GM_{\odot}}{r} \quad (\text{A.5})$$

$$\nabla^2 \Phi_{\text{sg}} = 4\pi G (\Sigma_g + \Sigma_p) \delta(z) \quad (\text{A.6})$$

$$P = \Sigma_g c_s^2 \quad (\text{A.7})$$

$$f_d = - \left(\frac{3\rho_g C_D |\Delta \mathbf{v}|}{8a_* \rho_*} \right) \Delta \mathbf{v}. \quad (\text{A.8})$$

In the above equations, G is the gravitational constant, Σ_g and Σ_p are the vertically integrated gas density and bulk density of solids, respectively, \mathbf{u} represents the velocity of the gas parcels, \mathbf{x}_p is the position and \mathbf{v}_p is the velocity of the solid particles, P is the vertically integrated pressure, c_s is the sound speed, Φ is the gravitational potential, ν is the viscosity, and \mathbf{S} is the rate of strain tensor. The functions $f_D(\Sigma_g)$ and $f_v(\mathbf{u}, \Sigma_g)$ are sixth order hyperdiffusion and hyperviscosity terms that provide extra dissipation close to the grid scale, explained in Lyra et al. (2008). They are required because the high order scheme of the Pencil code has too little overall numerical dissipation.

The function f_d is the drag force by which gas and solids interact. In Eq. (A.8), ρ_* is the internal density of a solid particle, a_* its radius, and $\Delta \mathbf{v} = \mathbf{v}_p - \mathbf{u}$ its velocity relative to the gas. C_D is a dimensionless coefficient that defines the strength of the drag force.

Appendix B: Drag force

The drag regimes are controlled by the mean free path λ of the gas, which can be expressed in terms of the Knudsen number of the flow past the particle $\text{Kn} = \lambda/2a_*$. High Knudsen numbers correspond to free molecular flow, or Epstein regime. Stokes drag is applicable to low Knudsen numbers. We use the formula of Woitke & Helling (2003; see also Paardekooper 2007), which interpolates between Epstein and Stokes regimes

$$C_D = \frac{9\text{Kn}^2 C_D^{\text{Eps}} + C_D^{\text{Stk}}}{(3\text{Kn} + 1)^2}. \quad (\text{B.1})$$

where C_D^{Eps} and C_D^{Stk} are the coefficients of Epstein and Stokes drag, respectively. These coefficients are

$$C_D^{\text{Eps}} \approx 2 \left(1 + \frac{128}{9\pi \text{Ma}^2} \right)^{1/2} \quad (\text{B.2})$$

$$C_D^{\text{Stk}} = \begin{cases} 24 \text{Re}^{-1} + 3.6 \text{Re}^{-0.313} & ; \text{Re} \leq 500; \\ 9.5 \times 10^{-5} \text{Re}^{1.397} & ; 500 < \text{Re} \leq 1500; \\ 2.61 & ; \text{Re} > 1500, \end{cases} \quad (\text{B.3})$$

where $\text{Ma} = |\Delta \mathbf{v}|/c_s$ is the Mach number, $\text{Re} = 2a_* \rho |\Delta \mathbf{v}|/\mu$ is the Reynolds number of the flow past the particle, and $\mu = \sqrt{8}/\pi \rho c_s \lambda/3$ is the kinematic viscosity of the gas.

The approximation for Epstein drag (Kwok 1975) connects regimes of low and high Mach number with a good degree of accuracy, and is more numerically friendly than the general case (Baines et al. 1965). The piecewise function for the Stokes regime are empirical corrections to Stokes law ($C_D = 24 \text{Re}^{-1}$), which only applies for low Reynolds numbers.

Appendix C: Gas tides and mass loss

The most remarkable feature of Fig. 3a of the main paper is the mass loss event at 90 orbits. It consists of the detachment of a $0.8 M_{\text{Mars}}$ object from the original cluster, of $6.7 M_{\text{Mars}}$.

We observe evidence that this puzzling behaviour is due to gravitational tides from the gas. The gas is too pressure-supported to undergo collapse, but the vortices concentrate a sufficient amount of material to exert a considerable gravitational pull. We illustrate this in Fig. C.1, where we show the state of the disk before (at 80 orbits, Figs. C.1a–C.1d) the mass-loss episode and after (at 100 orbits, Figs. C.1e–C.1h). The plots show the surface densities of gas and solids, and the potential associated with them. Even though the clumping of solids yield a considerable gravitational pull (Figs. C.1d and C.1h), these figures indicate that the dominant contribution to the gravitational potential comes from the gas – more specifically from the vortices, where the gas density peaks at a value one order of magnitude higher than that of the initial conditions.

The most massive clump is located in the inner disk at $(X, Y) = (-0.40, -0.53)$ in Fig. C.1b, not clearly identifiable amidst the other particles trapped inside the vortex. However, the embryo is immediately observable as the bright point at $(X, Y) = (-0.65, -0.19)$ in Fig. C.1h (also visible in Fig. C.1f, albeit less prominently). There are two features in this plot that are worth noting. First, by comparing the location of the embryo in these figures with the location of the vortices, we notice that the planet has left its parental vortex. Second, the inner vortices have undergone the transition from the $m = 3$ to the $m = 2$ mode. Due to merging, their gas density has increased, with dramatic consequences for the embryos within them.

We assess how the gravity of the gas influences the motion of the particles in Figs. C.1i–C.1l. In Fig. C.1i, we take a horizontal density slice at the position of the most massive embryo at 80 orbits. Figure C.1j is an enlargement of Fig. C.1i about $X = -0.53$, where the embryo is located. We see that the densities of solids and gas peak at similar values. The subsequent figures show the gravitational potential (Fig. C.1k) and acceleration (Fig. C.1l) about the embryo. The gas produces a deeper gravitational well, albeit smoother than the one displayed by the solids. In the acceleration plot, it is seen that the pull of the gas is more significant than the pull of the embryo at a distance of only 0.26 AU (0.03 in code units, corresponding to two grid cells) away from the center. And even where the pull of the solids is strongest (one grid cell away from the center), the gravity of the gas is still an appreciable fraction of the gravity of the solids. Tides from the gas are unavoidable.

It is beyond the scope of this paper to consider the full mathematical details of the theory of tides, especially because the two bodies (the vortex and the embryo) are extended. Instead, we consider the following toy model. The tidal force F_T experienced by the planet is proportional to the gradient of the acceleration a induced by the gas. It is also proportional to the radius R of the planet: $F_T \propto R \nabla a$. Since $\nabla a = -\nabla^2 \Phi$, according to the Poisson

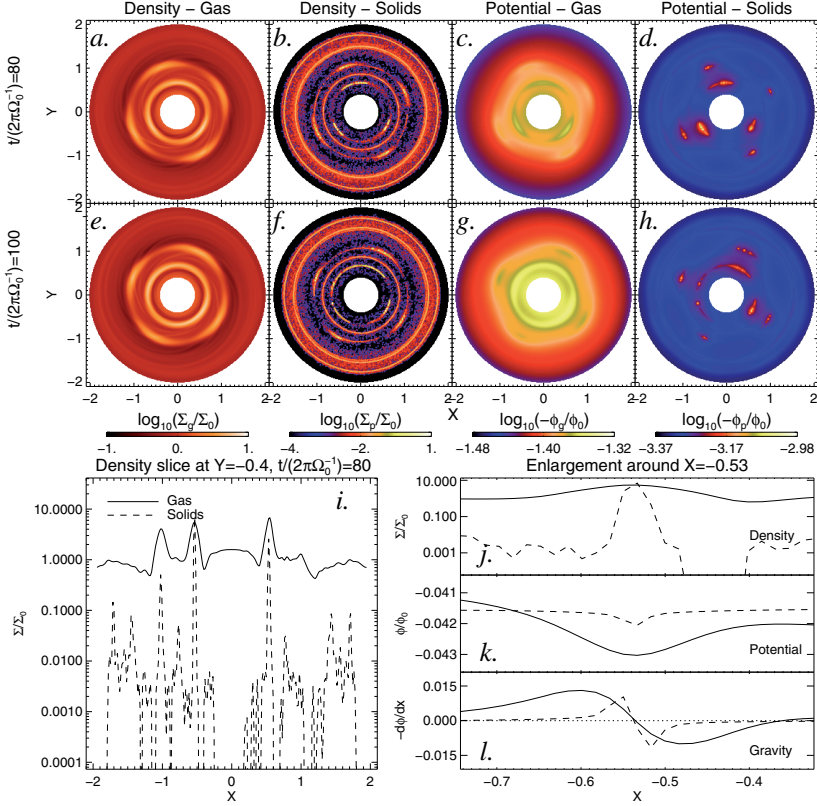


Fig. C.1. The state of the disk before (a)–(d) and after (e)–(h) the mass-loss episode. The conspicuous differences between them are due to the inner vortices passing from the $m = 3$ to the $m = 2$ mode. As a result, the most massive embryo has left its parental vortex between one snapshot and another. It is seen as a bright spot in panels *f* and *h*, at $(X, Y) = (-0.65, -0.19)$. In panel *b* (before the mass loss), the embryo is at $(X, Y) = (-0.40, -0.53)$ but not easily identified among the swarm of solids inside the vortex. Panel *i* shows a horizontal slice through this location, in which we see that the peak in the density of solids is not much higher than the gas density at the location of the embryo (panel *j*). Significant gas tides are expected because the gravitational potential (panel *k*) and acceleration (panel *l*) have similar contributions from gas and solid components.

equation, the tidal force is proportional to the local value of the density

$$F_T \propto R \rho_g. \quad (\text{C.1})$$

We consider the 3D volume density to avoid the requirement of using the Dirac delta in the 2D case. Considering the planet spherical, Newton’s second theorem holds and we can assume that $F_G = -GM/R^2$ for the planet’s (self-)gravitational force at its surface. Substituting $M = 4/3\pi\rho_p R^3$, we have $F_G \propto R\rho_p$, so

$$\zeta = \frac{F_T}{F_G} \propto \frac{\rho_g}{\rho_p}, \quad (\text{C.2})$$

i.e., the ratio of the disrupting tidal stresses to the self-gravitating forces that attempt to keep the planet together is directly proportional to the gas-to-solids ratio. At 80 orbits, as seen in Fig. C.1j, this ratio is around unity. As the vortices undergo the transition from the $m = 3$ to the $m = 2$ mode, their peak density increases (while the planet remains at constant mass). The tides eventually become sufficiently strong for a mass-loss event to occur.

We also witness some of the other, less massive, embryos being completely obliterated by the gas tides. Erosion is also important, since we observe a size dependency in this effect, with embryos consisting of $a_* = 10$ cm particles being more prone to disruption than those consisting of $a_* = 30$ cm particles. We performed tests that indicated that the erosion of bound clumps by ram pressure seen by Cuzzi et al. (2008) only occurs for clumps consisting of particles smaller than cm-size for our initial nebula parameters, larger particles being more stable. However, when the gas density of the vortices reaches a maximum value a factor ten higher than the initial density, the gas drag also strengthens, shifting the onset of erosion towards larger particle radii.

The effect of tides will probably be less dramatic in 3D simulations because, as the particles settle into the midplane, the ratio of the volume gas density to the bulk density of solids ρ_g/ρ_p is expected to be much lower than the ratio of the column gas density to the vertically integrated surface density of solids Σ_g/Σ_p .

Paper III



Planet formation bursts at the borders of the dead zone in 2D numerical simulations of circumstellar disks

W. Lyra¹, A. Johansen², A. Zsom³, H. Klahr³, & N. Piskunov¹

¹ Department of Physics and Astronomy, Uppsala Astronomical Observatory, Box 515, 751 20 Uppsala, Sweden

² Leiden Observatory, Leiden University, PO Box 9513, 2300 RA Leiden, The Netherlands

³ Max-Planck-Institut für Astronomie, Königstuhl 17, 69117 Heidelberg, Germany

Received ; Accepted

ABSTRACT

Context. As accretion in protoplanetary disks is enabled by turbulent viscosity, the border between active and inactive (dead) zones constitutes a location where there is an abrupt change in the accretion flow. The gas accumulation that ensues triggers the Rossby wave instability, that in turn saturates into anticyclonic vortices. It was suggested that the trapping of solids within them leads to a burst of planet formation on very short timescales.

Aims. We study in further detail the formation and evolution of the vortices, focusing on the implications for the dynamics of embedded solid particles and planet formation.

Methods. We perform two-dimensional global simulations of the dynamics of gas and solids in a non-magnetized thin protoplanetary disk with the Pencil Code. We use multiple particle species of radius 1, 10, 30, and 100 μm . We solve for the particles' gravitational interaction by a particle-mesh method, translating the particles' number density into surface density and computing the corresponding self-gravitational potential via fast Fourier transforms. The dead zone is modeled as a region of low viscosity. Adiabatic and locally isothermal equations of state are used.

Results. The Rossby wave instability is triggered under a variety of conditions, thus making vortex formation a robust process. Inside the vortices, fast accumulation of solids occurs and the particles collapse into objects of planetary mass in timescales as short as five orbits. Because the drag force is size-dependent, aerodynamical sorting ensues within the vortical motion, and the first bound structures formed are composed primarily of similarly-sized particles. In addition to erosion due to ram pressure, we identify gas tides from the massive vortices as a disrupting agent of formed protoplanetary embryos. We find evidence that the backreaction of the drag force from the particles onto the gas modifies the evolution of the Rossby wave instability, with vortices being launched only at later times if this term is excluded from the momentum equation. Even though the gas is not initially gravitationally unstable, the vortices can grow to $Q \approx 1$ in locally isothermal runs, which halts the inverse cascade of energy towards smaller wavenumbers. As a result, vortices in models without self-gravity tend to rapidly merge towards a $m=2$ or $m=1$ mode, while models with self-gravity retain dominant higher order modes ($m=4$ or $m=3$) for longer times. Non-selfgravitating disks thus show fewer and stronger vortices. We also estimate the collisional velocity history of the particles that compose the most massive embryo by the end of the simulation, finding that the vast majority of them never experienced a collision with another particle at speeds faster than 1 m s^{-1} . This result lends further support to previous studies showing that vortices provide a favorable environment for planet formation.

Key words. Keywords should be given

1. Introduction

The ill fate of the building blocks of planets in gaseous disks around young stars stands as one of the major unsolved problems in the theory of planet formation. Beginning with micron-sized interstellar dust grains, coagulation models predict growth to centimeter and meter size (Weidenschilling 1980; Dominik et al. 2007) in the denser environments of a circumstellar disk. Such bodies, however, are large enough to have already decoupled slightly from the sub-Keplerian gas, yet still small enough to be subject to a significant gas drag. The resulting headwind drains their angular momentum, leading them into spiral trajectories towards the star, in timescales as short as a hundred years at 1 AU (Weidenschilling 1977a). Another acute problem is that such bodies have poor sticking

properties and a low threshold velocity for fragmentation (Chokshi et al. 1993), such that collisions between them usually lead to destruction rather than growth (Benz 2000; Sirono 2004; Ormel & Cuzzi 2007). Such problems severely hinder growth to km-size by coagulation (Brauer et al. 2008a).

In view of these problems, other routes for breaching the meter size barrier have been pursued. A distinct alternative is gravitational instability of the layer of solids (Safronov 1969; Lyttleton 1972; Goldreich & Ward 1973; Youdin & Shu 2002). When the dust aggregates had grown to centimeter and meter size the gas drag is reduced and the solids are pushed to the midplane of the disk due to the stellar gravity. Although such bodies do not have enough mass to attract each other individually, sedimentation increases the solids-to-gas ratio by orders of magnitude when compared to the interstellar value of 10^{-2} .

It was then hypothesized (Safronov 1969) that due to the high densities of this midplane layer, the solids could collectively achieve critical number density and undergo direct gravitational collapse. Such a scenario has the advantage of occurring on very rapid timescales, thus avoiding the radial drift barrier.

This picture is nonetheless simplistic, in the view that even low levels of turbulence in the disk preclude the midplane layer of solids from achieving densities high enough to trigger the gravitational instability (Weidenschilling & Cuzzi 1993). Even in the absence of self-sustained turbulence such as the one generated by the magneto-rotational instability (MRI; Balbus & Hawley 1991; Balbus & Hawley 1998), the solids themselves can generate turbulence due to the backreaction of the drag force onto the gas. Such turbulence can be brought about by Kelvin-Helmholtz instabilities due to the vertical shear present in the sedimented layer of solids (Weidenschilling 1980; Weidenschilling & Cuzzi 1993; Sekiya 1998; Johansen et al. 2006), or by streaming instabilities induced by the radial migration of solids particles (Youdin & Goodman 2005; Johansen et al. 2006; Paardekooper 2006; Youdin & Johansen 2007; Johansen & Youdin 2007). In the turbulent motion, the solids are stirred up by the gas, forming a vertically extended layer where the stellar gravity is balanced by turbulent diffusion (Dubrulle et al. 1995; Garaud & Lin 2004).

But if turbulence precludes direct gravitational collapse through sedimentation, it was also shown that it allows for it in an indirect way. As solid particles concentrate in high pressure regions (Haghighipour & Boss 2003), the solids-to-gas ratio can be enhanced in the transient turbulent gas pressure maxima, potentially reaching values high enough to achieve gravitational collapse. Numerical calculations by Johansen et al. (2007) show that this is indeed the case, with the particles trapped in the pressure maxima generated by the MRI collapsing into dwarf planets when the gravitational interaction between particles is considered. They also show that the MRI is not necessarily needed, since the weak turbulence brought about by the streaming instability itself can lead to enough clumping under certain conditions. Another way of achieving high enough densities for gravitational collapse of the solid layer was shown by Rice et al. (2004) and Rice et al. (2006), where meter-sized solids concentrate prodigiously in the spiral arms formed in marginally gravitationally unstable circumstellar disks.

Such models, however, ignored the possibility of fragmentation of particles upon collisions. As the turbulence enhances the velocity dispersion of solids, destructive collisions become more likely. Moreover, upon destruction, the smaller fragments are tightly coupled to the gas and therefore dragged away from the midplane (Johansen et al. 2008), reducing the effective amount of solid material available for collapse. Such problem is particularly severe in the high mass disks investigated by Rice et al. (2004) and Rice et al. (2006), where the typical speeds of the boulders upon encounters are comparable to the sound speed.

The fragmentation problem could be avoided if the accumulation of solids happened, for instance, within a protective environment where the collisional speeds are brought down to gentler values. Anticyclonic vortices (Marcus 1990) have been shown to favor planet formation (Barge & Sommeria 1995; Tanga et al. 1996; Bracco et al. 1999; Chavanis 2000; Johansen et al. 2004) since, by ro-

tating clockwise in the global counterclockwise Keplerian flow, they enhance the local shear and induce a net force on solid particles towards their centers. Klahr & Bodenheimer (2006) further argue that anticyclonic vortices would be less turbulent than the ambient gas, which in turn would lead to velocity dispersions that are low enough to prevent fragmentation. Vortices in disks can be the result of the baroclinic instability (Klahr & Bodenheimer 2003; Klahr 2004; Petersen et al. 2007), the Rossby wave instability (Lovelace et al. 1999; Li et al. 2000; Li et al. 2001) or, perhaps, the MRI (Fromang and Nelson 2005).

In this paper, we focus on vortices generated by the Rossby wave instability (RWI), which is a global instability where azimuthal modes experience growth in the presence of local extrema of a quantity interpreted as a combination of entropy and potential vorticity. In the linear phase, the instability launches inertial-acoustic waves. The non-linear saturation is achieved when the Rossby waves break and coalesce into anticyclonic vortices. It was shown by Varnière & Tagger (2006) that a favorable profile of the entropy-modified vorticity naturally arises if the disk has a slow-accretion zone, such as in the layered accretion model of Gammie (1996). In this model, ionization is provided by collisions in the hot inner regions, and by cosmic rays in the outer disk where the column densities are low (a standard value for the penetration depth of cosmic rays is a gas column density of 100 g cm^{-2}). Throughout most of the midplane, however, the temperatures are too cold and the column densities are too thick for ionization to occur either way. The result is that, when threaded by a weak magnetic field, the disk displays MRI-active regions in the ionized layers, and a MRI-dead zone in the neutral parts around the midplane (Gammie 1996, Miller & Stone 2000; Oishi et al. 2007). Matter flows towards the star due to the high turbulent viscosity of the MRI-active layers, but upon hitting the border of the dead zone, it reaches a region of slow accretion and the flow stalls. However, as the flow proceeds unabridgedly from the outer active regions, a surface density maximum forms, which triggers the growth of the RWI.

The implications of this scenario for planet formation were first explored by Inaba & Barge (2006), who use the RWI-unstable dead zone model of Varnière & Tagger (2006) to study the accumulation of solids inside the Rossby vortices. They confirm that the vortices are efficient particle traps, since the solids-to-gas ratio was raised by at least one order of magnitude, modeling the solid phase of the disk as a fluid. Such approximation requires that the size of the solid particles be much smaller than the gas mean free path. Since in the Minimum Mass Solar Nebula (MMSN; Weidenschilling 1977b) at 5.2AU the particles subject to maximum drift have a size comparable to the mean free path, the sizes that a fluid approach can handle correspond to too strong friction, thus ultimately underestimating the trapping performance of the vortical motion. In Lyra et al. (2008b; hereafter LJKP08), we took the works of Varnière & Tagger (2006) and Inaba & Barge (2006) one step further by including gravitationally interacting centimeter and meter size solids treated as Lagrangian particles. In that Letter, we showed that the solids concentrated in the vortices triggered by the RWI rapidly reach critical densities and undergo collapse into rocky planets. The resulting burst lead to the formation of 20 rocky protoplanetary embryos in the mass range 0.1-0.6

M_{\oplus} , along with hundreds of smaller bodies following a mass spectrum of power law -2.3 ± 0.2 .

In this paper we further detail the method used in LJP08, also presenting a number of new results. In the following section we present the dynamical equations, followed by an in-depth analysis of the vortices in Sect. 3. In Sect. 4 we analyze the formation and evolution of the protoplanetary embryos, focusing on stability against erosion (Paraskov et al. 2006; Cuzzi et al. 2008) and tides from the gas, which we identify as an important disrupting agent. In Sect. 6 we investigate the response of the RWI to effects not considered in the original analysis of Lovelace et al. (1999) and Li et al. (2000), and in Sect. 7 we present a discussion of the limitations of the model. A summary and conclusions are presented in Sect. 8.

2. The model

2.1. Dynamical Equations

We work in the thin disk approximation, using the vertically integrated equations of hydrodynamics

$$\frac{\partial \Sigma_g}{\partial t} = -(\mathbf{u} \cdot \nabla) \Sigma_g - \Sigma_g \nabla \cdot \mathbf{u} + f_D(\Sigma_g) \quad (1)$$

$$\frac{\partial \mathbf{u}}{\partial t} = -(\mathbf{u} \cdot \nabla) \mathbf{u} - \frac{1}{\Sigma_g} \nabla P - \nabla \Phi - \frac{\Sigma_p}{\Sigma_g} f_d + 2 \Sigma_g^{-1} \nabla \cdot (\nu \Sigma_g \mathbf{S}) + f_v(\mathbf{u}, \Sigma_g) \quad (2)$$

$$\frac{d\mathbf{x}_p}{dt} = \mathbf{v}_p \quad (3)$$

$$\frac{d\mathbf{v}_p}{dt} = -\nabla \Phi + f_d \quad (4)$$

$$\Phi = \Phi_{sg} - \frac{GM_{\odot}}{r} \quad (5)$$

$$\nabla^2 \Phi_{sg} = 4\pi G (\Sigma_g + \Sigma_p) \delta(z) \quad (6)$$

$$P = \Sigma_g c_s^2 \quad (7)$$

$$f_d = -\left(\frac{3\rho_g C_D |\Delta v|}{8a_{\bullet} \rho_{\bullet}} \right) \Delta v. \quad (8)$$

In the above equations G is the gravitational constant, Σ_g and Σ_p are the vertically integrated gas density and bulk density of solids, respectively; \mathbf{u} stands for the velocity of the gas parcels; \mathbf{x}_p is the position and \mathbf{v}_p is the velocity of the solid particles, P is the vertically integrated pressure, c_s is the sound speed, Φ the gravitational potential, ν the viscosity, and \mathbf{S} the rate-of-strain tensor. The functions $f_D(\Sigma_g)$ and $f_v(\mathbf{u}, \Sigma_g)$ are sixth order hyperdiffusion and hyperviscosity terms that provide extra dissipation near the grid scale, explained in Lyra et al. (2008a). They are needed because the high order scheme of the Pencil Code has too little overall numerical dissipation.

The function f_d is the drag force by which gas and solids interact. In Eq. (8), ρ_{\bullet} is the internal density of a solid particle, a_{\bullet} its radius, and $\Delta v = \mathbf{v}_p - \mathbf{u}$ its velocity relative to the gas. C_D is a dimensionless coefficient that defines the strength of the drag force. We use the formula of Woitke & Helling (2003) that interpolates between Epstein and Stokes drag

$$C_D = \frac{9\text{Kn}^2 C_D^{\text{Eps}} + C_D^{\text{Stk}}}{(3\text{Kn} + 1)^2}. \quad (9)$$

where C_D^{Eps} and C_D^{Stk} are the coefficients of Epstein and Stokes drag, respectively. These are

$$C_D^{\text{Eps}} \approx 2 \left(1 + \frac{128}{9\pi \text{Ma}^2} \right)^{1/2} \quad (10)$$

$$C_D^{\text{Stk}} = \begin{cases} 24 \text{Re}^{-1} + 3.6 \text{Re}^{-0.313} & ; \text{Re} \leq 500; \\ 9.5 \times 10^{-5} \text{Re}^{1.397} & ; 500 < \text{Re} \leq 1500; \\ 2.61 & ; \text{Re} > 1500. \end{cases} \quad (11)$$

where $\text{Ma} = |\Delta v|/c_s$ is the Mach number, $\text{Re} = 2a_{\bullet} \rho_g |\Delta v|/\mu$ is the Reynolds number of the flow past the particle, and $\mu = \sqrt{8/\pi} \rho_g c_s \lambda/3$ is the kinematic viscosity of the gas. We defer the reader to Lyra et al. (2008c) for further details of the drag force. The self-gravity solver is also explained in that paper.

2.2. Initial and boundary conditions

In this paper, we use the Pencil Code¹ in Cartesian and cylindrical geometry. The cylindrical runs do not include the gravity of the particles and were therefore only used for tests or runs without particles, as will become clear in the next sections. A Cartesian box was used for the production runs. The Cartesian box ranges $x, y \in [-2.0, 2.0]r_0$. The resolution is 256×256 , unless stated otherwise. The cylindrical grid ranges $r \in [0.3, 2.0]r_0$, with 2π coverage in azimuth.

The density profile follows the power law $\Sigma_g = \Sigma_0 r^{-0.5}$ and the sound speed is also set as a power law $c_s = c_{s0} r^{-0.5}$. The velocity field is set by the condition of centrifugal equilibrium

$$\dot{\phi}^2 = \Omega_K^2 + \frac{1}{r} \left[\frac{1}{\Sigma_g} \frac{\partial P}{\partial r} + \frac{\partial \Phi_{sg}}{\partial r} \right] \quad (12)$$

We use units such that $r_0 = \Sigma_0 = GM_{\odot} = 1$. We choose $c_{s0} = 0.05$ and a Toomre Q parameter of 30 at r_0 . The gas is throughout stable against gravitational instability. Assuming that $r_0 = 5.2 \text{ AU}$ and that $\Sigma_0 = 300 \text{ g cm}^{-2}$, the disk has $10^{-2} M_{\odot}$ of gas within the modeled range. The dead zone is modeled as static viscosity jumps following arc-tangent profiles

$$\nu = \nu_0 - \frac{\nu_0}{2} \left[\tanh \left(\frac{r - r_1}{\Delta r} \right) - \tanh \left(\frac{r - r_2}{\Delta r} \right) \right] \quad (13)$$

where $r_1 = 0.6$ and $r_2 = 1.2$ are the locations of the jumps and Δr its width. We adopt $\Delta r = 10^{-2}$, which provides a smooth jump over two grid cells only. The jump is thus close to a Heaviside function yet still differentiable. We use $\nu_0 = 2.5 \times 10^{-5}$ in code units, corresponding to an alpha value (Shakura & Sunyaev 1973) of $\alpha \equiv \nu \Omega / c_s^2 \approx 10^{-2}$.

For the solids, we use 10^5 or 4×10^5 Lagrangian numerical particles. For a gas mass of $10^{-2} M_{\odot}$ and the interstellar solids-to-gas ratio of 10^{-2} , each numerical particle

¹ See <http://www.nordita.org/software/pencil-code>

therefore is a super-particle containing (in the lower resolution case) $10^{-9}M_{\odot} \simeq 2.7 \times 10^{-2}M_{\text{Moon}}$ of material. We use particles of radii $a_* = 1, 10, 30,$ and 100 cm, as also used in Lyra et al. (2008c). For our nebula parameters, maximum drift occurs for particles of 30 cm, as detailed in that paper.

The particles are initialized as to yield a surface density following the same power law as the gas density, and their velocities are initialized to the Keplerian value. We use reflective boundaries for the cylindrical grid and frozen boundaries for the Cartesian grid (Lyra et al. 2008a). Both use the buffer zone described in de Val-Borro et al. (2006) to damp waves before they reach the boundary. Particles are removed from the simulation if they cross the inner boundary.

3. Vortices

The trapping mechanism of vortices is not only due to it being a high-pressure region, but mainly due to the vorticity of the flow. In an anticyclonic vortex (cyclonic vortices are destroyed by the Keplerian shear), the motion occurs in the same sense as the local shear, i.e., the gas rotates clockwise. Therefore, at the antistellar point the angular momentum is decreased with respect to a non-vortical flow; and conversely increased at the substellar point. As a result, the gas at the antistellar point is accelerated inwards, while the gas at the substellar point is accelerated outwards. A net centripetal force towards the eye ensues. The streamlines of vortices (or vortex lines) are a set of Keplerian ellipses with the same semimajor axis but different eccentricities, being circular in the center and more eccentric outwards (Barge and Sommeria 1995). We show contours of $|u|$ on the surroundings of one of the giant vortices, in the upper left panel of Fig. 1. As the gas drags the particles, the particles also revolve around the vortex eye. But because the gas-solids coupling is not perfect, the particles lose angular momentum and sink deeply towards the center. In the next subsections we describe some of the properties of the vortices present in our simulations

3.1. Launching Mechanism - the RWI

The vortices in LJKP08 are triggered by the Rossby wave instability (RWI), a case of purely hydrodynamical instability in accretion disks. Considering azimuthal perturbations to the inviscid Euler equations, Lovelace et al. (1999) and Li et al. (2000) find that instabilities exist when the following quantity has a local extremum

$$\mathcal{L}(r) \equiv \mathcal{F}(r) (P\Sigma^{-\gamma})^{2/\gamma} \quad (14)$$

The quantity \mathcal{F} is defined as

$$\mathcal{F} \equiv \frac{\Sigma\Omega}{\kappa^2 - \Delta\omega^2 - c_s^2 / (L_s L_p)} \quad (15)$$

where

$$\kappa \equiv \left[\frac{1}{r^3} \frac{d}{dr} (r^4 \Omega^2) \right]^{1/2} \quad (16)$$

is the epicyclic frequency and

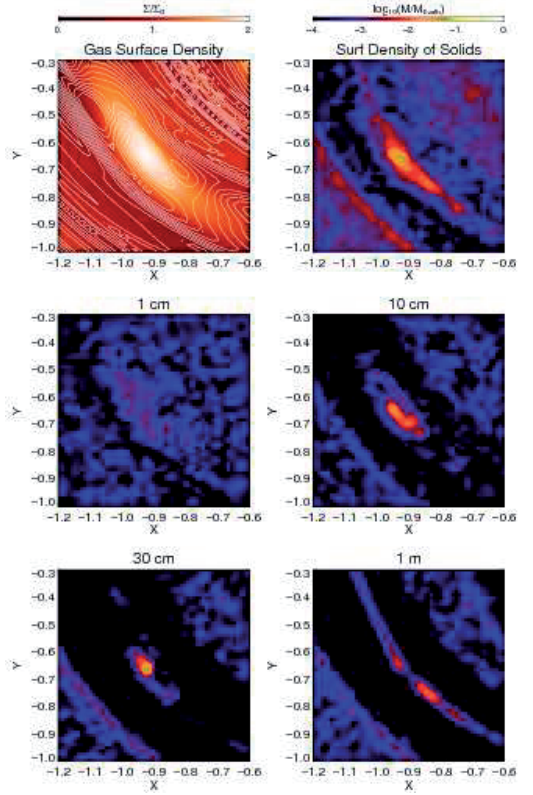


Fig. 1. Enlargement around one of the vortices in a snapshot at 20 orbits. Contours of $|u|$ are superimposed on the gas surface density plot, showing that the density enhancement is associated with intense vorticity. In the upper panel we show the multi-phase (total) surface density of solids, whereas in the middle and lower panels we show the contribution of each particle species. The vortical motion preferentially traps particles of $a_* = 10$ and 30 cm.

$$L_s \equiv \gamma \left/ \left[\frac{d}{dr} \ln (P\Sigma^{-\gamma}) \right] \right. \quad (17)$$

$$L_p \equiv \gamma \left/ \left[\frac{d}{dr} \ln P \right] \right. \quad (18)$$

are the radial length scale of the entropy and density variations, respectively. γ is the adiabatic index. For corrotational modes ($\Delta\omega \equiv \omega - m\Omega \ll \kappa$) in a barotropic ($L_s \rightarrow \infty$) disk, the quantity \mathcal{F} reduces to $\Sigma\Omega\kappa^{-2}$, which is readily identified with (half) the inverse of vortensity ξ

$$\xi = \omega_z / \Sigma \quad (19)$$

$$\omega_z = |\nabla \times \mathbf{u}|_z \quad (20)$$

$$= \frac{1}{r} \frac{\partial}{\partial r} (r^2 \Omega) = \frac{\kappa^2}{2\Omega},$$

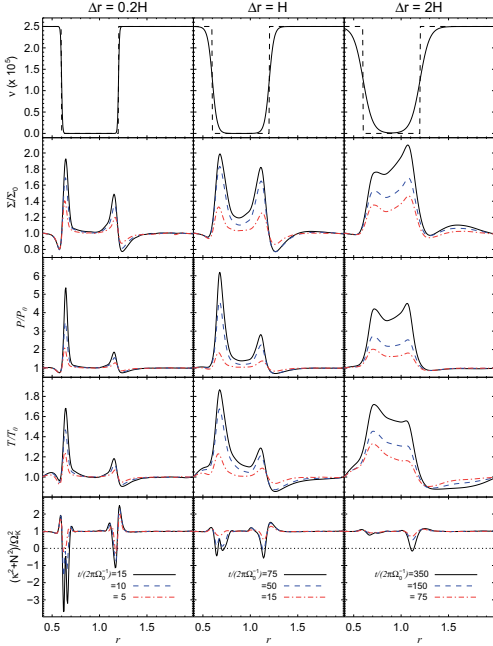


Fig. 2. Evolution of the pressure bump with different widths of the viscosity jump (uppermost panels; the dashed line is the Heaviside jump, for comparison). The violation of the Solberg-Høiland criterion (lowermost panels) is a conservative indication that the threshold of instability of the RWI was reached. As the width of the jump increases, the threshold takes increasingly longer time to be breached. For jumps smoother than two scale lengths, the threshold was not reached (up to 500 orbits).

which in turn led Lovelace et al. (1999) to interpret \mathcal{L} as an entropy-modified version of, or generalized, potential vorticity. An extremum in the profile of \mathcal{L} can be generated, for example, by a pressure bump somewhere in the disk. The dispersion relation of the disturbances is analogous to the dispersion relation of Rossby waves in planetary atmospheres, hence the name of the instability.

3.2. How sharp need the jump be?

Although formally the instability is triggered by a minimum or maximum of \mathcal{L} , ones finds in practice that the amplitude and radial width of the pressure bump present critical values beyond which instability does not occur. Li et al. (2000) find that typically, a pressure variation of 10-20% over a length similar to the scale height of the disk is sufficient to trigger the instability. The threshold, however, is problem dependent, depending - among other things - on the geometry of the pressure variation (step jump or Gaussian, for example; see Li et al. (2000) for details). Due to this, we use a more general criterion to assess the threshold of instability. Li et al. (2000) note that the threshold of instability for the RWI is always reached before the

Solberg-Høiland criterion for stability of axis-symmetric disturbances

$$\kappa^2 + N^2 \geq 0 \quad (21)$$

is violated. Eq. (21), therefore, provides a *conservative* estimate of whether or not the RWI is excited. The Solberg-Høiland criterion is easily understood. In a pressureless disk, the condition $\kappa^2 \geq 0$ suffices to determine stability. The other term

$$N^2 \equiv \frac{1}{\Sigma} \frac{dP}{dr} \left(\frac{1}{\Sigma} \frac{d\Sigma}{dr} - \frac{1}{\gamma P} \frac{dP}{dr} \right) \quad (22)$$

is the square of the Brunt-Väisälä frequency, associated with the oscillations of buoyant structures in the presence of an entropy gradient. Physically, Eq. (21) means that a mode that is unstable/stable to shear can be stabilized/destabilized by pressure gradients and vice-versa.

We measure the epicyclic and Brunt-Väisälä frequencies in a series of 1D simulations where we varied the width Δr of the viscosity jump (Eq. (13)). We find that for locally isothermal simulations, the Solberg-Høiland criterion is violated at the outer edge for $\Delta r \leq 0.04$, which is slightly less than one scale height. In these isothermal simulations, the criterion depends almost solely on the epicyclic frequency because, as the temperature does not rise with compression, the pressure does not change enough for N^2 to go appreciably negative.

To assess the effect of non-barotropic behavior, we replace the locally isothermal flow by an isentropic one with an adiabatic equation of state

$$\frac{\partial S}{\partial t} = -(\mathbf{u} \cdot \nabla) S + f_\chi(S) \quad (23)$$

$$P = \Sigma c_s^2 / \gamma \quad (24)$$

which means that we allow heating and cooling by compression and rarefaction only, excluding viscous heating and radiative cooling. In Eq. (23), $S = \ln P - \gamma \ln \Sigma$ is the vertically integrated specific entropy of the gas. The function $f_\chi(S)$ is a sixth order hyperconductivity term, analogous to hyperdiffusion for density. The adiabatic index is $\gamma=7/5$.

The results are illustrated in Fig. 2, where we plot the viscosity profile (upper panel) for different widths Δr , and the time evolution of the density, pressure and temperature bumps. The lower panels measure if the Solberg-Høiland criterion was violated. We find that the pressure bump sharpens considerably compared to the isothermal case, due to the high temperatures associated with the compression. The consequence is that the Solberg-Høiland criterion is violated by viscosity jumps up to $\Delta r \leq 0.12$, i.e., 3 times broader than in the isothermal simulations. In this non-isothermal case, it is mostly the Brunt-Väisälä frequency that leads $\kappa^2 + N^2$ to negative values. The effect of increasing the width is mainly of slowing the evolution of the quantity $\kappa^2 + N^2$ towards negative values. It only takes five orbits for $\Delta r = 0.01$, but it takes 350 orbits when Δr is increased to 0.1. In Fig. 2 we state Δr in terms of the scale height $H=0.05 r_0$. We present a resolution study of vortex excitation in Appendix A. We also address the issue of vortex survival in a non-static dead zone in Appendix B.

3.3. Steady-state dead zone

If no transport happens in the dead zone, matter can do little more than piling up there as the inflow proceeds from the active layers. However, the accumulation of matter cannot proceed indefinitely since, as matter piles up, the conditions for gravitational instability would eventually be met (Armitage et al. 2001). The gravitational turbulence that ensues (Lodato 2008) would therefore empty the dead zone as the excess matter accretes, thus re-starting the cycle.

However, local simulations show that the dead zone has some level of residual turbulence. This happens because the turbulence on the active layers induce small levels of Reynolds stress in the dead zone (Fleming & Stone 2003). If the inertia of the midplane layer is not too high (Oishi et al. 2007), this forced turbulence can lead to moderate α values with non-negligible transport².

Terquem (2008) shows that steady state solutions in 1D models exist in this case, as the dead zone gets denser and hotter to match the condition of constancy of the mass accretion rate with radius, $\partial_r(\nu\Sigma)=0$. In this case, the steady state will have an ν_T viscosity value in the active layers and a lower ν_D in the dead zone.

Vortex formation by the RWI requires the presence of a pressure maximum. In our model, and that of Varnière & Tagger (2006) and Inaba & Barge (2006), the pressure maximum comes about by stalling the accretion flow in the border of the dead zone. There is no requirement that the dead zone should have zero viscosity, just a viscosity significantly lower than that of the active regions. We tested different values of ν_D/ν_T , and found that changing it from 0 to 0.1 has little effect on the instability. For higher values, the Solberg-Høiland criterion takes increasingly longer to be violated. For $\nu_D/\nu_T = 0.5$, the Solberg-Høiland criterion is violated after 60 orbits. We also notice that the steady-state dead zones of Terquem (2008; see Fig. 3 of that paper) have the surface density varying by more a factor of ~ 10 over a few scale lengths at the inner edge. Such profiles violate the Solberg-Høiland criterion, so the RWI is expected to be excited in those conditions as well.

4. Embryos

4.1. Drag force cooling and compactness

The embryos formed in our simulations present a number of interesting features. We first would like to address the issue regarding their physical size. The embryos consist of a cluster of a large number of particles, held together by their collective gravitational pull. But are they strongly bound like solid objects? Or do they consist of loosely coupled objects in the same potential well? To answer this question we measure the rms spatial dispersion of the particles inside the cluster, defined as

$$r_{\text{rms}} = \sqrt{\sum_{i=1}^n |r_i - r_{\text{CM}}|^2} \quad (25)$$

² Another alternative is local ionization provided by the decay of the short-lived radioactive nuclide ^{26}Al (Umebayashi & Nakano 2009), although Turner & Sano (2008) show that the free electrons given out by this low ionization source would quickly recombine on the surface of μm -sized dust grains.

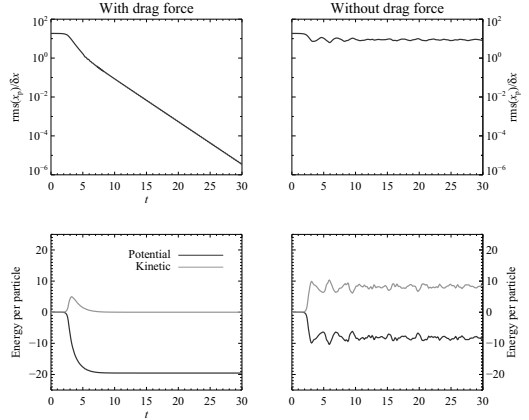


Fig. 3. 1D simulation of collapse of 1000 particles. With drag force the kinetic energy of the particles is efficiently dissipated and the particles collapse at subgrid scale towards infinite density. When the drag force is excluded the system cannot dissipate energy and a halo of particles, 10 grid cells wide, is formed.

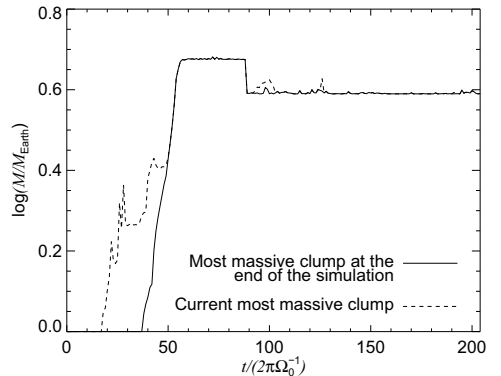


Fig. 4. Evolution of the most massive clump formed (solid line), that we traced back in time from the end of the simulation. It differs from the instantaneous most massive clump (dashed line) because the clumps have different feeding rate and can also experience mass loss, as in the episode that happened at ≈ 90 orbits (see text).

where n is the number of particles within the Hill sphere of the clump, r is the vector radius of each particle and r_{CM} is the vector radius of their center of mass. We take this value as a measurement of the “radius” of the embryo. The most massive embryo has a radius of $1.13 R_{\oplus}$. This compactness corresponds to a tenth of a thousandth of the resolution element.

Such compactness is due to the dynamical cooling provided by the drag force. We illustrate this in Fig. 3. The figure shows the results of 1D simulation with a thousand in-

teracting particles with and without gas drag. Without gas drag the particles have no means to dissipate energy and perform oscillations about the center of mass. The very inner particles show virialization, while the outer particles form a halo extending for a radius of 10 grid cells in average.

When including gas drag, the system gets so dissipative that the kinetic energy is soon lost and the ensemble of particles collapses. The exponential decay of the particles' rms position seen in the upper left panel of Fig. 3 shows no sign of flattening, down to a millionth of a resolution element. This leads us to infer that collapse to zero volume is ongoing. This is of course expected, since no mechanism to provide support against the gravitational pull is present.

In view of this, the question is why our planets, that are subject to drag forces, do not shrink to zero as well but stabilize at a very small but finite radius. We are drawn to the conclusion that this is a numerical issue. The tests of Fig. 3 were done with a fixed time-step. But when the particles cluster together to form a planet in our simulations, they end up dominating the time-step. The position update $x(t) = x_0 + v\Delta t$ therefore occurs with the maximum Δt allowed by the Courant condition, which is that the fastest particle should move by one grid cell. Due to this, the time resolution of the subgrid motion around the center of mass of the cluster is under-resolved. With the overshoot Δt , the particles that are attracted towards the center of mass of the clump will end up in a position *past* it. In the next time step they will be attracted to the center of mass from the other side, but will once again overshoot it. The result of this is that the particles will execute undamped oscillations, leading to a finite rms radius. We performed tests like those of Fig. 3 with a particle-controlled variable timestep, confirming this explanation. We conclude that the fact that the most massive embryo has a stable rms radius compatible with its mass is but a deceptive coincidence.

We stress that this drag force cooling will cease to be efficient as the solids-to-gas ratio grows too large ($\rho_p/\rho_g \gg 1$), because in this case the backreaction would be too strong and the gas would simply be dragged along with the particles. In this case, a Keplerian disk of solids might form, accreting matter onto the planet due to collisions between the orbiting solids. This accretion regime is nevertheless beyond the scope of the current paper.

4.2. Mass loss

In Fig. 2a of LJKP08 we showed the evolution of the most massive clump. However, as the clumps have different feeding rate and some of them experience mass loss, the most massive clump shown there is not always the same clump. In Fig. 4 we contrast this with the evolution of the most massive clump *at the end of the simulation*, which we tracked backwards in time. Such clump started in the inner disk, showing $0.8 M_{\text{Mars}}$ by 40 orbits. By this time, the most massive clump was a $3 M_{\text{Mars}}$ clump in the outer disk.

The most remarkable feature of this plot is the mass loss event at 90 orbits. Fig. 5 shows that it consists of the detachment of a $0.8 M_{\text{Mars}}$ object from the original cluster, of $6.7 M_{\text{Mars}}$. The detachment is already seen at 87 orbits, although the separation is quite small (4 times the Earth-Moon mean separation, R_{EM}). At 89 orbits, the smaller object left the Hill sphere of the more massive embryo. They

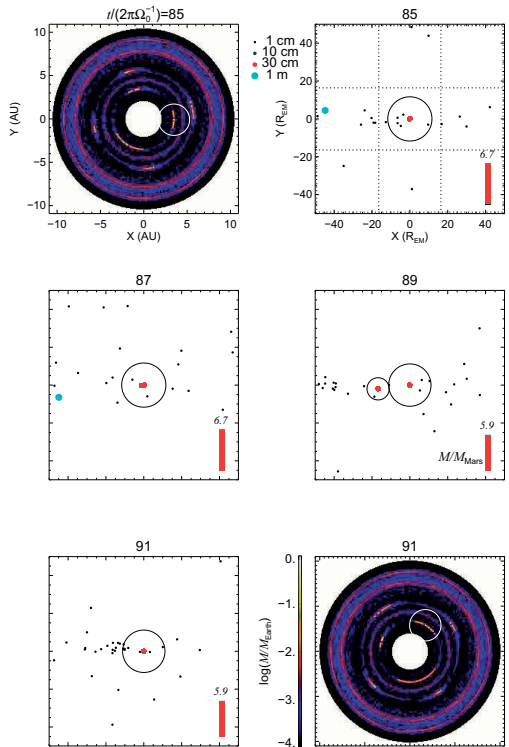


Fig. 5. Time series of the mass loss episode. Due to gravitational tides from the massive vortex whence the embryo formed, a large chunk of particles was detached from the original cluster. At 87 orbits, a separation 4 times the Earth-Moon distance is seen. The separation grows and two orbits later the two bodies do not overlap Hill radii, thus counting as separate objects.

finally appeared as separate objects, and the maximum mass decreased.

We see evidence that this puzzling behavior is due to gravitational tides from the gas. The gas is too pressure-supported to undergo collapse, but the vortices concentrate enough material to yield a considerable gravitational pull. We illustrate this in Fig. 6, where we show the state of the disk before the mass loss episode (at 80 orbits, Fig. 6a-Fig. 6d) and after that (at 100 orbits, Fig. 6e-Fig. 6h). The plots show the surface densities of gas and solids, and the potential associated with them. Even though the clumping of solids yield a considerable gravitational pull (Fig. 6d and Fig. 6h), these figures show that the dominant contribution to the gravitational potential comes from the gas - more specifically from the vortices, where the gas density peaks one order of magnitude denser than the initial condition.

The most massive clump is located in the inner disk at $(X,Y)=(-0.40,-0.53)$ in Fig. 6b, not clearly identifiable amidst

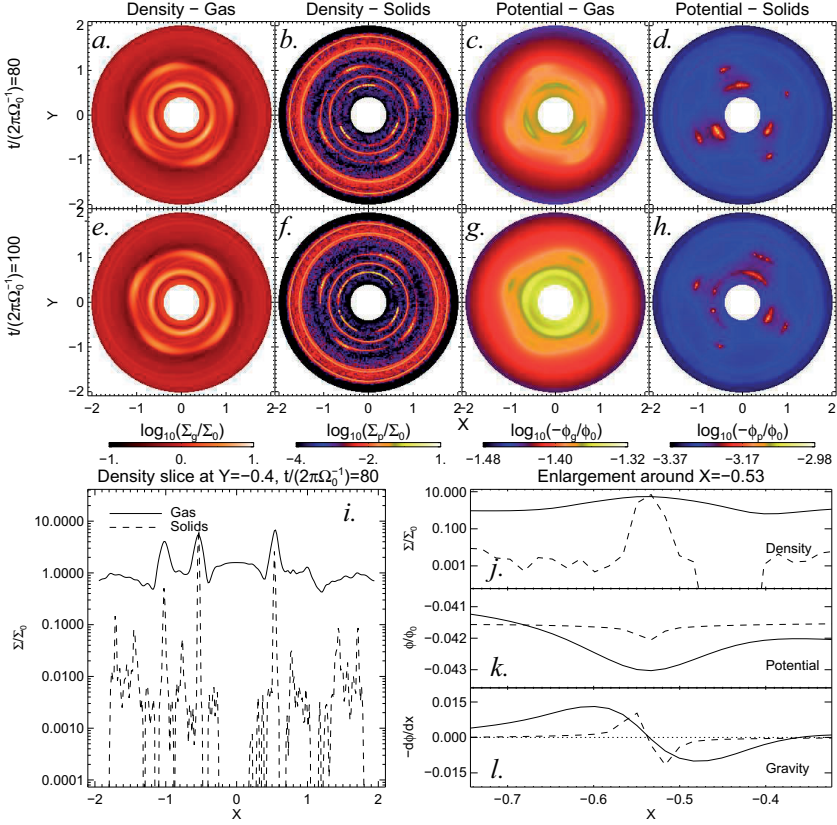


Fig. 6. The state of the disk before (a-d) and after (e-h) the mass loss episode. The conspicuous difference between them is that the embryo has left its parental vortex from one snapshot to the other. It is seen as a bright spot in panels f and h, at $(X,Y)=(-0.65,-0.19)$. In panel b (before the mass loss), the embryo is at $(X,Y)=(-0.40,-0.53)$ but not easily spotted among the swarm of solids inside the vortex. Panel i shows a horizontal slice through this location, in which we see that the density of solids does not peak much higher than the gas density at the location of the embryo (panel j). Significant gas tides are expected as the gravitational potential (panel k) and acceleration (panel l) have similar contributions from the gas and solid components.

the other particles trapped inside the vortex. However, the embryo is immediately observable as the bright point at $(X,Y)=(-0.65,-0.19)$ in Fig. 6h (also visible in Fig. 6f, albeit less prominently). There are two features in this plot that are worth noting. First, by comparing the location of the embryo in these figures with the location of the vortices, we notice that the planet has left its parental vortex. Second, the inner vortices have undergone the transition from the $m=3$ to the $m=2$ mode. Due to merging, their gas density has increased, with dramatic consequences for the embryos within them.

We assess how the gravity of the gas influences the motion of the particles (Fig. 6i-Fig. 6l). In Fig. 6i we take a horizontal density slice at the position of the most massive embryo at 80 orbits. Fig. 6j is an enlargement of Fig. 6i around $X=-0.53$, where the embryo is located. We see that the densities of solids and gas peak at similar values. The

next figures show the gravitational potential (Fig. 6k) and acceleration (Fig. 6l) around the embryo. The gas produces a deeper gravitational well, albeit smoother than the one displayed by the solids. In the acceleration plot it is seen that the pull of the gas is greater than the pull of the embryo already at a distance of just 0.26 AU (0.03 in code units, corresponding to two grid cells) away from the center. And even where the pull of the solids is strongest (one grid cell away from the center), the gravity of the gas still is an appreciable fraction of the gravity of the solids. Tides from the gas are unavoidable.

It is beyond the scope of this paper to consider the full mathematical details of the theory of tides, especially because the two bodies (the vortex and the embryo) are extended. Instead, we consider the following toy model. The tidal force F_T experienced by the planet is proportional to the gradient of the acceleration a induced by the gas. It is

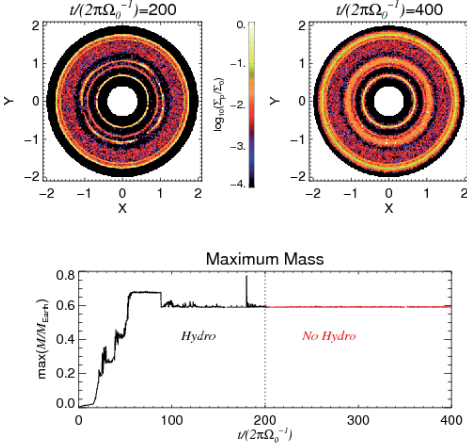


Fig. 7. Can self-gravity alone maintain the formed embryos together? We switch off the hydrodynamics at the last snapshot and run for additional 200 orbits. The most massive embryo, that had already left the parental vortex (at ≈ 90 orbits), does not disperse.

also proportional to the radius R of the planet: $F_T \propto R \nabla a$. Since $\nabla a = -\nabla^2 \Phi$, according to the Poisson equation, the tidal force is proportional to the local value of the density

$$F_T \propto R \rho_g. \quad (26)$$

We consider the 3D volume density to avoid the requirement of using the Dirac delta in the 2D case. Considering the planet spherical, Newton's second theorem holds and we can write $F_G = -GM/R^2$ for the planet's (self-)gravitational force at its surface. Substituting $M = 4/3\pi\rho_p R^3$, we have $F_G \propto R\rho_p$, so

$$\zeta = \frac{F_T}{F_G} \propto \frac{\rho_g}{\rho_p}, \quad (27)$$

i.e., the ratio of the disrupting tidal stresses to the self-gravitating forces that attempt to keep the planet together is directly proportional to the gas-to-solids ratio. At 80 orbits, as seen in Fig. 6j this ratio is around unity. As the vortices undergo the transition from the $m=3$ to the $m=2$ mode, their peak density increases (while the planet remains at a constant mass), the tides eventually become strong enough to cause the mass loss event of Fig. 5. This effect will probably be less dramatic in 3D simulations because, as the particles settle in the midplane, the ratio of the volume gas density to the bulk density of solids ρ_g/ρ_p is expected to be much lower than the ratio of the column gas density to the vertically integrated surface density of solids Σ_g/Σ_p .

4.3. Erosion?

Cuzzi et al. (2008) points that erosion is of prominent importance in the stability of self-gravitating clumps of particles. They put forth a model where self-gravity plays a

role analogous to that of surface tension in liquid drops, preventing disruption against ram pressure forces from the gas. The clumps are held together by self-gravity if the gravitational Weber number (in analogy with the surface tension case) is less than a critical value, close to 1. The gravitational Weber number is defined as the ratio of the drag to self-gravitational accelerations

$$We_G = \frac{|f_d|}{|\nabla\Phi_{sg}|}. \quad (28)$$

Cuzzi et al. (2008) further point that in numerical models, artificial viscosity can largely exaggerate the disrupting effect of the ram pressure. This happens because, as the clumps are small, they are deeply within the viscous range of the grid, whereas in the real solar nebula the dissipation happens at much smaller scales. The Reynolds number of the flow past the particles is therefore much smaller than what a real clump would experience³, and the exaggerated viscous stresses might de-stabilize potentially stable clumps.

It is interesting to assess if this mechanism plays a significant role in our models, or even if it can account for at least some of the mass loss events.

We can estimate how important erosion will be for our clumps the following way. We approximate the clumps as single point masses so that $|\nabla\Phi_{sg}| \approx GM/r^2$, where M is the total mass of the clump. Plugging this in Eq. (30), we write the gravitational Weber number as

$$We_G = \frac{3\rho C_D |\Delta v|^2 r^2}{8GM a_* \rho_*}. \quad (29)$$

For Epstein drag (Eq. (10)), C_D does not depend on a_* . So, for all other quantities being constant, we expect We_G to decrease linearly as a_* increases. In other words, self-gravitating clumps of larger particles should be more stable than clumps composed of smaller particles.

We can simplify the We_G by writing the mass M as $M = \pi r_{rms}^2 \Sigma_p$, and the drag force as $|f_d| = Ma c_s / \tau$. Thus, at $r = r_{rms}$,

$$We_G = \frac{Ma c_s}{\tau \pi G \Sigma_p}. \quad (30)$$

We confirm in Appendix C that Eq. (30) is sufficiently accurate in predicting the onset of erosion. For our choice of parameters,

$$We_G \approx \frac{17 Ma}{(\tau \Omega) \Sigma_p r^2} \quad (31)$$

so for a flow of $Ma \approx 10^{-2}$, a clump of $\Sigma_p = 1$ at $r \approx 1$ will be stable if $\tau \Omega \gtrsim 0.1$. The embryos we consider are formed

³ The Reynolds number of the flow past a clump can be written as $Re = R_{rms} v_{rms} / \nu$. At the grid scale our choice of viscosity is usually $3 \times 10^{17} \text{ cm}^2 \text{ s}^{-1}$ (it decreases very fast as we go to smaller wavenumbers, as k^6). For a clump as the ones of this study, of $R_{rms} = 10^4 \text{ km}$ and $v_{rms} = 1 \text{ m s}^{-1}$, the Reynolds number is $Re \approx 3 \times 10^{-7}$. At such incredibly low Reynolds numbers, inertia plays no role. The self-gravity of the particles, therefore, is not holding the cluster together against drag forces from the gas, but against largely exaggerated viscous stresses. In comparison, in the solar nebula, the molecular viscosity is much lower and the Reynolds number is expected to be $> 10^6$ (Cuzzi et al. 2008).

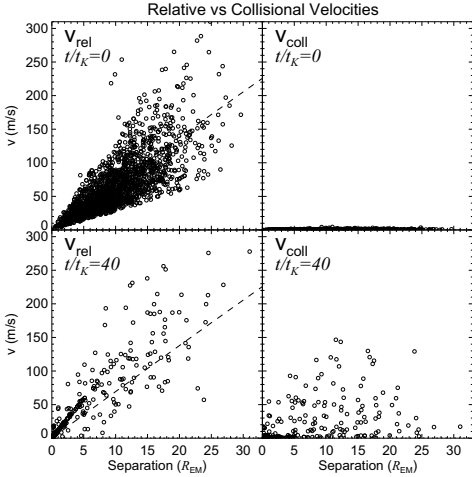


Fig. 8. The relative velocities between particles are contrasted with collisional velocities calculated from Eq. (32). At the initial condition ($t=0$) the relative velocities between particles follow what is expected from the Keplerian shear (dashed line), reaching as far as 300 m s^{-1} inside a grid cell (which is $31 R_{EM}$ wide). In contrast, the true collisional velocities are much lower. The figure shows that estimating fragmentation with the relative velocities would greatly overestimate its likelihood. Time is quoted in orbits ($t_K=2\pi/\Omega_0$).

predominantly of particles of 10 cm ($\tau\Omega \approx 0.1$) and 30 cm ($\tau\Omega \approx 0.3$). We conclude that erosion might play a role in our case. The sharp dependence of We_C on the distance in Eq. (31) also means that embryos at the inner edge of the dead zone are more prone to erosion than the ones at the outer edge. We will develop this further in Sect 5.2.2.

4.4. Can the embryos be held together indefinitely?

To answer the question of how long lived these clumps are, we take the last snapshot of the simulation and switch off the hydrodynamics. The particles now move under the influence of the stellar gravity and their own self-gravity only. We run for additional 200 orbits to assess if self-gravity alone can maintain the cluster of particles together. The result is shown in Fig. 7.

The clustered particles do not disperse, and the most massive embryo maintains the same mass for the additional simulating time. We do not see difference in the degree of compactness of the most massive embryo. As the vortices are shut down, the unbound 1 cm sized particles that were too well coupled to the gas to be dragged into and spread over a wider annulus.

We have no reason to suspect that the situation will change over longer timescales. We conclude that the embryos can be held together indefinitely.

4.5. Collisions

As stated before, one of the problems that solids accumulation inside vortices can potentially solve is the issue of fragmentation of particles upon collisions, a drawback for both coagulation (Brauer et al. 2008a) and gravitational instability models (Rice et al. 2006, Johansen et al. 2007) of planetesimal growth.

To assess if fragmentation poses a significant barrier for the formation of the protoplanetary embryos in this study, we take the most massive embryo by the end of the simulation, flag the particles that constitute it and trace them back in time, calculating their collisional velocity history. The collisional speed for each particle is calculated by taking the closest neighbor to that particle within the range of a grid cell. There is, however, a subtlety concerning the difference between collisional velocities and relative velocities. A collision between particles i and j only happens when the separation r_{ij} between them tends to zero. For our resolution and choice of r_0 , a grid cell is 0.08 AU wide, thus existing plenty of room for subgrid Lagrangian dynamics. In particular, the velocity difference due to the Keplerian shear between the inner and outer radial borders of a grid cell can be significant. At the inner edge of the dead zone of the model presented in this paper (3.12 AU) for instance, this difference amounts to 434 m s^{-1} . As this velocity difference is due to the separation between particles, it vanishes when r_{ij} tends to zero, thus never contributing to the true collisional speed. In Fig. 8 we show these uncorrected relative velocities in the initial condition and in a snapshot at 40 orbits, plotted against separation. The clear correlation follows what is expected from the Keplerian shear (dashed line) in the initial condition.

The gas motion adds another velocity that has to be taken into account. Solid particles are dragged by the gas motion, yet gas streamlines never intersect. The gas motion itself thus introduce velocities that never participate in collisions. We correct for these two by the following procedure. For each particle in the pair involved in a collision, we consider its velocity Δv relative to the gas (the same quantity that appears in the drag force, $\Delta v = v_p - u$). We then define the collisional velocity vector as

$$v_{\text{coll}}^{ij} \equiv \Delta v(x_{p_i}) - \Delta v(x_{p_j}). \quad (32)$$

Equation (32) ensures that tracer particles, that follow the gas streamlines, should never experience collision. Furthermore, as the shear dependence of $\Delta v = \eta v_K$ is much smaller than the shear dependence of $v_p = v_K$ (where $\eta = (1/2)(H/r)^2(\partial \ln P / \partial \ln r) = 3.75 \times 10^{-3}$ is the pressure-correction factor), we can assume that it also corrects for this quantity. Figure 8 also shows the collisional speeds calculated by Eq. (32). The dependence on separation was greatly suppressed.

The results of the collisional velocity history of the particles that constitute the most massive embryo at the end of simulation are plotted in Fig. 9.

Figure 9a shows a cumulative plot of the mass of the embryo, that defines the time t_0 that each flagged particle was accreted. We define the time of accretion as the moment when the particle approached the grid point x_{near} nearest to the maximum of particle number density (also defined by the flagged particles) by less than $d_{\text{diag}} = dx \sqrt{2}$

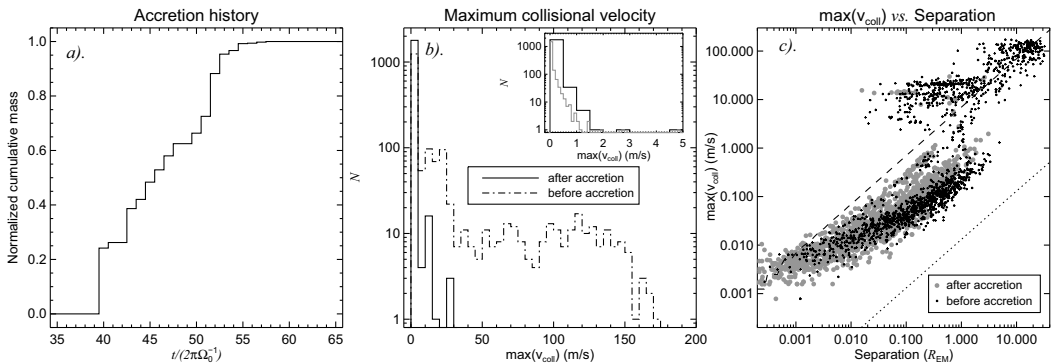


Fig. 9. *a.* Accretion history of the most massive embryo. Collapse happens at 40 orbits, and further accretion of particles happens through the next 18 orbits, after which the maximum mass is attained. This plot defines the time t_0 that each particle is accreted. *b.* Histograms of the maximum collisional velocities experienced by a given particle, before (dot-dashed line) and after (solid line) its accretion time t_0 . The solid line histogram represents the maximum collisional speed from t_0 until the end of the simulation. The dot-dashed line histogram covers a time interval of ten orbits before t_0 . As the vortices form at ≈ 30 orbits, the latter better represents v_{coll} under vortex trapping. The vast majority of the particles are in the bin of $0\text{--}5\text{ m s}^{-1}$. The smaller window zooms into this bin. The black line corresponds to bins of 1 m s^{-1} whereas the grey line to bins of 0.1 m s^{-1} . Both represent v_{coll} after t_0 . It shows that most of the particles never experience collisions more violent than 1 m s^{-1} . *c.* Same as *b.* but plotting the maximum collisional speeds as function of separation between the particle and its nearest neighbor. Before t_0 , three populations are seen, of low speed at short separations, high speeds at short separations, and high speeds at large separations. Only the second group would have experienced destructive collisions. After t_0 , 99% of the particles belong to the first group. The correlation with distance for the first group is not due to the Keplerian shear (dashed line) or the residual shear present in Δv (dotted line).

(the grid cell diagonal) and kept

$$|\mathbf{x}_p - \mathbf{x}_{\text{near}}| \leq d_{\text{diag}} \quad (33)$$

until the end of the simulation. Although this is not as strict as the definition of accretion we have been using before (based on the Hill criterion and escape velocity), this simpler criterion captures what happens before collapse (i.e., before the maximum of particle number density becomes a bound protoplanetary embryo) and serves well our purpose of illustrating the behavior of collisional speeds at close separations. The first episode of accretion takes place at 40 orbits, coinciding with the time that the clump of particles became bound (in accordance with Fig. 4). Further accretion proceeds over the next 18 orbits, with the maximum mass being attained at 58 orbits. No other particle was accreted after this time.

Figure 9b shows histograms of the maximum collisional speed that a particle experienced before (dot-dashed line) and after (solid line) accretion. The latter refers to the maximum of v_{coll} taken between t_0 and the end of the simulation (200 orbits). The former refers to a time interval of 10 orbits before t_0 . As the vortices in the inner disk just fully develop at ≈ 30 orbits, the dot-dashed histogram is more representative of a situation where particles are inserted in a disk with existent vortices. The conclusion is striking: the vast majority of the particles that constitute the embryo never experienced a collision more violent than 1 m s^{-1} .

In Fig. 9c we show the maximum collisional velocities of Fig. 9b as a function of the separation between a given particle and its closest neighbor, also before and after accretion. The distribution before accretion is trimodal,

with particles with low speeds ($<1\text{ m s}^{-1}$) at small separations, particles with high speeds ($<20\text{ m s}^{-1}$) at small separations, and particles with high speeds at large separations ($>10R_{\text{EM}}$). Only the second group of particles would have undergone fragmentation. The first group is below the fragmentation velocity threshold, whereas the large separations of the third group imply they never experienced an encounter close enough to lead to a collision. After accretion, virtually all particles (99%) belong to the first group.

In Fig. 10 we plot the collisional velocities versus separation at selected snapshots instead of historical maxima. In these plots, we only used the particles for which Eq. (33) was satisfied, i.e., considering only the collisions that are participating on the formation process of the embryo. At 30 orbits, a small number of particles is observed (87), 78% of these showing safe collisional speeds ($<10\text{ m s}^{-1}$). 5 orbits later 119 particles are within the grid cell of the forming embryo, 92% of which show gentle collisions. At the time the overdensity gets bound (40 orbits), it is formed by 639 particles, with just 7 of these showing collisional speeds greater than 10 m s^{-1} . At 45 orbits, all 877 particles display safe speeds. The tendency seen in this time series towards an increasing number of encounters at low separations and at low collisional speeds indicates that collapse towards zero volume is ongoing. Indeed, at 70 orbits, we observe that most of the particles occupy the same point in space.

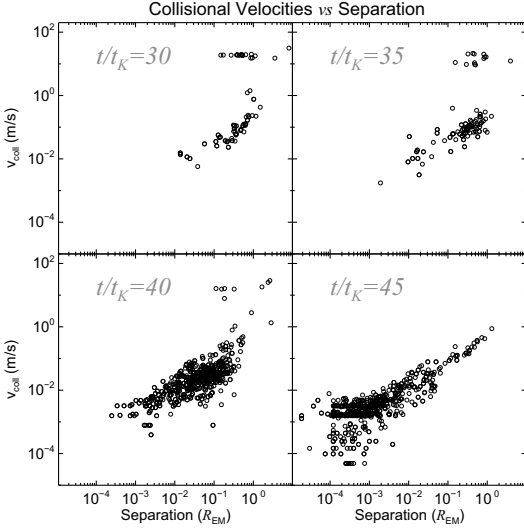


Fig. 10. Collisional speeds as a function of separation at selected snapshots at 30, 35, 40, and 45 orbits ($t/t_K=2\pi/\Omega_0$). The figure only shows particles that are closer than the distance of a grid cell to the clump of maximum number density. The group at low separations and high speeds observed in the upper plots would undergo fragmentation. Nevertheless, they represent only a minority of particles (22% at 30 orbits, 8% at 35). At the time the cluster gets bound (at 40 orbits), the vast majority of particles (99%) is safely at low speeds. The presence of a fourth group at 45 orbits, at very low separations ($<10^{-3} R_{EM}$) and with very low collisional speeds ($<10^{-3} \text{ m s}^{-1}$) indicates that collapse towards zero volume is ongoing.

5. Size distribution

In our simulations, we considered the solid phase of the disk represented by particles of 1, 10, 30, and 100 cm. In this section we discuss a number of issues, relevant to the simulations, related to having a size spectrum instead of single-phasing.

5.1. Aerodynamical sorting

One of the most prominent features of the embryos formed in our models is that they are composed primarily of same-sized particles. This is mostly due to aerodynamical sorting. As particles of different size have different friction times, differential drag occurs inside the vortex, effectively sorting the particles spatially by size. Moreover, the stationary point is determined by a balance between the Coriolis and the drag force, in such a way that the eye of the vortex is the stationary point only for $\tau_s \rightarrow 0$, or perfect coupling. In general, the stationary point is azimuthally shifted with respect to the eye, according to the particle size (Youdin 2008).

The aerodynamical sorting inside the vortex can be seen in Fig. 11, which corresponds to the vortex of Fig. 1. As similar particles drift alike, streams of same-sized particles are clearly seen in the vortical flow.

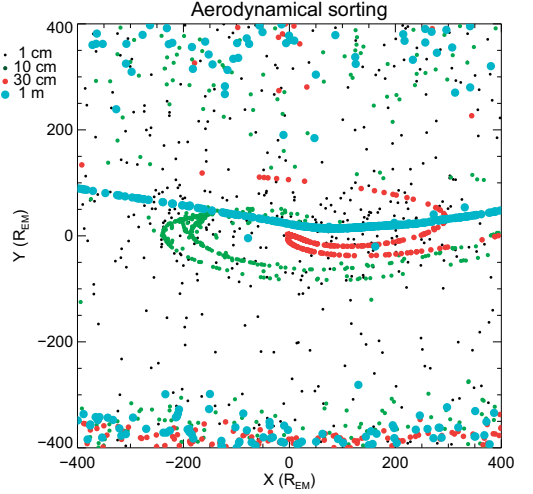


Fig. 11. Aerodynamical sorting for the particles trapped in the vortical motion. The figure is centered at the vortex shown in Fig. 1, at 18 orbits. The unit of length is the Earth-Moon mean distance, and the Y-coordinate points to the star. As particles of different size have different friction times, differential drag occurs inside the vortex, effectively sorting the particles spatially by size.

5.2. Differences between the inner and outer embryos

Another interesting feature of our results is that once the vortices are formed, they easily trap the 10 cm and 30 cm particles both in the inner and in the outer edge of the dead zone. Yet, by the end of the simulation there seems to be a preference for the embryos in the inner disk to be composed of larger particles (30-100 cm), while in the outer disk, more embryos formed of the smaller particles (1-10 cm) are seen. We explain these two features in the following sections.

5.2.1. Preferential sizes in different locations of the nebula

The first feature (inner and outer vortices equally trapping particles of same size) follows from the fact that the general drag coefficient (Eq. (9)) yields a nearly flat profile for the radius of the particle with maximum drift ($\tau\Omega=1$) versus distance. This is seen by calculating the stopping times t_s of the different particles as a function of the dynamical variables

$$\begin{aligned} t_s &= \tau\Omega \\ &= \frac{\sqrt{32\pi} \lambda \rho_\bullet}{\text{Kn}' \text{Ma} \Sigma_g} \frac{(\text{Kn}' + 1)^2}{(\text{Kn}'^2 C_D^{\text{Eps}} + C_D^{\text{Stk}})} \end{aligned} \quad (34)$$

and calculating the radius for a given stopping time t_s . Substituting $C_D^{\text{Eps}}=16/(3\text{Ma})\sqrt{2/\pi}$ (Eq. (10)) at sub-

sonic regime) and Stokes law $C_D^{\text{Stk}}=24/\text{Re}$ (with $\text{Re} = 3\text{Ma}/\text{Kn}\sqrt{\pi/8}$) yields the quadratic equation for a_\bullet

$$2a_\bullet^2 + 3\lambda a_\bullet - \frac{6\lambda\Sigma_g t_s}{\pi\rho_\bullet} = 0 \quad (35)$$

and, as the radius is positive, the solution is unique

$$a_\bullet = \frac{3\lambda}{4} \left(\sqrt{1 + \frac{16\Sigma_g t_s}{3\pi\lambda\rho_\bullet}} - 1 \right) \quad (36)$$

Fig. 12 shows this curve as a function of radius for $t_s=1$ and our initial parameters. The particle radius of $t_s=1$ predicted by both pure Epstein and pure Stokes drag are shown for comparison. The mean free path λ is also shown. The figure shows that the curve is so flat for our choice of parameters, that inner and outer vortices must have similar efficiency on trapping particles of a given size.

5.2.2. Tidal disruption and erosion of the inner embryos of $a_\bullet=10\text{ cm}$

We see evidence that the second feature (the absence of clumps of 10 cm in the inner disk at later times even though they were formed) is due to tidal disruption in the same episode that lead the most massive embryo to lose mass. We illustrate this in Fig. 13, a time series of the gas and the solid phases, the latter split into the 4 different particle sizes. The upper plots, at 75 orbits, show that embryos of 30 cm and 10 cm were formed in both the inner and outer vortices.

The gas plots of the time series of Fig. 13 illustrate the transition from the $m=3$ to the $m=2$ undergone by the inner vortices, as mentioned in Sect. 4.2. This raises their density so the tides get stronger. The plots of the 30 cm phase show that the embryos composed of these particles split into smaller objects, that nevertheless can still keep their physical integrity.

The fate of the clusters composed of particles of 10 cm is different, though. As the gas density increases, so does the gravitational Weber numbers of the embryos. Erosion starts to play a more significant role. As the density increases inside the inner vortices (a factor 5 relative to the initial condition at 75 orbits; 8 at 200 orbits), the embryos of 10 cm particles start to behave more and more like the $\tau\Omega=0.01$ clusters of Fig. C.1. At 85 orbits, one of embryos of 10 cm particles in the inner edge was destroyed. At 95 orbits, a second embryo was disrupted. At 105 orbits, the third embryo was also destroyed by the combined effect of tides and erosion. 25 orbits later, the 10 cm particles have dispersed through the inner edge of the dead zone. The tides from the gas prevent them from assembling once again.

The outer vortices never get as strong as the inner ones. The result is that although the inner embryos of 10 cm particles are destroyed, the outer ones are kept until the end of the simulation.

6. The response of the RWI to the drag backreaction and self-gravity

The evolution of the RWI was studied analytically for the case of a low mass dustless disk only. In Fig. 14 we show

how the effects of gas self-gravity and backreaction from the solids affect the evolution of the instability.

The upper panels of Fig. 14 show a disk without solids and without self-gravity. In the middle panels we included self-gravity, while in the lower panels we included solids. The appearance of the disk in the three simulations is shown in selected snapshots at 5, 10, and 15 orbits.

The self-gravitating and non-selfgravitating dustless cases (upper and middle panels) look similar, with the RWI being excited first in the outer edge of the dead zone. However, there is a crucial difference between them. The snapshot at 15 orbits shows a prominent $m=2$ mode in the outer disk for the non-selfgravitating case, while the run with self-gravity displays a dominant $m=5$ mode at the same time. This puzzling result is made even more interesting by recalling that the gas is gravitationally stable ($Q\approx 30$). That the growth rates of different modes vary that significantly for such a value of Q is indicative that the dispersion relation of the RWI is probably remarkably sensitive to self-gravity.

The simulation with drag backreaction (lower panels) also displays a number of interesting features. First, the RWI was excited in the inner disk as early as 5 orbits. In contrast, the control run without solids (upper panels) has the instability appearing first in the outer disk, and at later times (10 orbits). The conclusion is that the particles induce vorticity on their own. Even though it is clear that this behavior has to do with free energy being transferred from the particle motion to the gas motion, it is not obvious if this result can be linked to the streaming instability (Youdin & Goodman 2005) since the solids-to-gas ratio is not nearly as high as the one needed to excite it ($\rho_p/\rho_g \gtrsim 1$). Instead, it is more likely that the backreaction is modifying the dispersion relation of the RWI.

Another interesting feature of this run is that although the RWI was excited in the inner edge of the dead zone as early as 5 orbits, the outer edge just went unstable as late as 15 orbits. In contrast, the control run (upper panels) shows the outer disk going unstable at 10 orbits. As the backreaction hastens the growth of the RWI in the inner edge, it is unclear why it should stall it in the outer edge. One possibility is that the Rossby waves launched by the edge that first goes unstable interferes destructively with the perturbations fighting to grow in the other edge.

The dominant mode also changed from the dusty to the dustless case. The latter has $m=4$ and $m=5$ modes being dominant in the inner edge. In the dusty case a $m=2$ mode is seen instead. However, since in the dustless case it is the outer edge that displays a $m=2$ mode, another explanation comes to mind. As the models are 2D, we are probably witnessing the inverse cascade phenomenon due to enstrophy conservation. The vortices are simply cascading energy towards the larger scales, so the edge that goes unstable first (outer in the dustless case, inner in the dusty) will also reach a dominant $m=2$ mode first (possibly also $m=1$ at later times).

If this is the case, then self-gravity somehow halts the inverse cascade that took place in the dustless non-selfgravitating case. It is also instructive to compare the dusty non-selfgravitating run (lower panel) with the dusty selfgravitating run of LJKP08 (Fig. 1 of that paper). In that case, the $m=4$ was dominant in the outer edge of the dead zone until the end of the simulation at 200 orbits. We also perform a test (Fig. 15) that consists of switching the self-

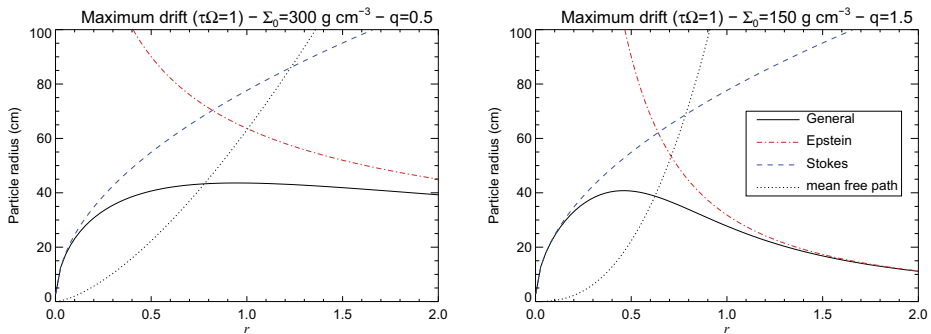


Fig. 12. The radius of the particle subject to maximum drift ($\tau\Omega=1$) for our choice of parameters (left panel) and in the MMSN (right panel). $q = -\partial \ln \Sigma / \partial \ln r$ is the power law of the surface density profile. The profile is very flat compared to the ones predicted by the limiting cases of Epstein and Stokes drag, especially for our choice of parameters. The vortices in the inner and outer edge of the dead zone should have similar efficiency on trapping particles of a given size.

gravity off in the run of LJKP08, and checking the evolution of the vortices. Without self-gravity, the $m=4$ mode turns into a $m=3$ mode in less than 15 orbits. In the inner edge, a $m=2$ mode developed out of the otherwise dominant $m=3$ mode. The inverse cascade indeed resumed.

This result was also very recently reported by Mamatsashvili & Rice (2009). Without self-gravity, the vortex size is limited by the pressure scale height H . Once vortices grow to sizes of a few times H , the vortical flow becomes super-sonic. The vortex then radiates density waves that carry energy away and limit further growth. Mamatsashvili & Rice (2009) point that in the presence of self-gravity, the Jeans length $\lambda_J \sim QH$, where $Q = (\kappa c_s) / (G\pi\Sigma)$ is the Toomre Q parameter, poses another limitation to the maximum size of a vortex. We measure Q at the location of the vortices and confirm that it is close to 1 (in the range 0.5-3). The growth seen when self-gravity is switched off is a result of this constrain being lifted.

7. Limitations of the model

The presented models are admittedly simplified. In this section, we state what we consider the main limitations of our calculations to be.

7.1. Two-dimensionality

The most stringent limitation of the models is the 2D approximation, that leads to a number of features, stated below.

7.1.1. Vortex formation and survival

The question of the excitation and sustainability of vortices in three dimensions is the matter of an old, yet unsettled, debate. Once excited, anticyclonic vortices are easily maintained in 2D simulations where, unless viscosity is present, they cannot decay and will instead merge, growing in size in a cascade of energy towards the largest scale of box (e.g., Johnson & Gammie 2005). However, three-dimensional studies in the context of protoplanetary disks

found that tall vortex columns are destroyed, both in non-stratified (Shen et al. 2006) and in stratified (Barranco & Marcus 2005) local boxes. This phenomenon is understood as a result of the elliptic instability (Crow 1970, Gledzel et al. 1975, Kerswell 2002), by which the stretching term $(\omega \cdot \nabla)u$, absent in 2D, breaks down elliptical streamlines such as vortical flow. For a vortex to grow in 3D, the baroclinic term $\rho^{-2}\nabla\rho \times \nabla p$ has to counter the stretching term.

An indication that vortices can be sustained in three dimensions is present in the study of Edgar & Quillen (2008). These authors simulate a stratified disk in spherical coordinates with an embedded giant planet. In their inviscid run, the RWI is excited, leading to Rossby vortices at the edges of the gap, much like as in the 2D runs of de Val-Borro et al (2007). The vortices launched in three dimensions are long lived and vertically extended, apparently following the same scale height as the surrounding disk. We remark that the MRI-generated vortex of Fromang & Nelson (2005) is also seen to be long-lived in a unstratified global disk. The studies of Edgar & Quillen (2008) and Fromang & Nelson (2005) both use a locally isothermal equation of state, which has large-scale non-zero baroclinity due to the static radial temperature gradient. Furthermore, the existence of the RWI in 3D is demonstrated by the simulations of Méheut et al. (2008).

7.1.2. Strength of the vortices

The first major impact of this is the inverse cascade due to entropy conservation that overpowers the vortices. An in depth study of the formation, development and structure of Rossby vortices in 3D global accretion disks is needed to realistically address the issue of planet formation inside these structures.

7.1.3. Particle sedimentation

Another limitation posed by the two-dimensionality is that the particles and the gas have the same infinitely thin scale height. The result of this is that the back-reaction of the

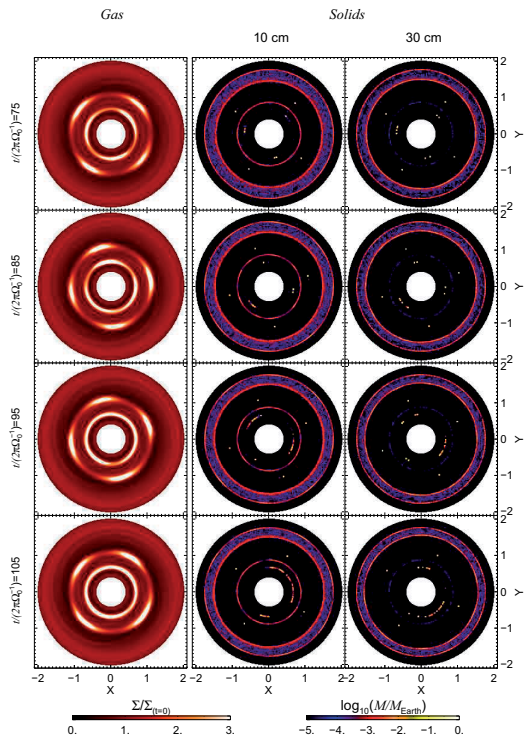


Fig. 13. Time series of the gas and solid density (for each individual particle size), evidencing the destruction of the embryos of 10 cm particles when the inner vortices undergo the transition from the $m=3$ to the $m=2$ mode. At 75 orbits (upper panels), embryos are seen in both the inner and outer vortices, for both 10 cm and 30 cm particles. At 85 orbits one of the embryos in the 10 cm phase was disrupted, followed by a second at 95 orbits, and the last one ten orbits later. The embryos composed of 30 cm particles are smaller, they just undergo splitting, the large fragments being more stable against erosion than the embryos composed of particles of 10 cm.

drag force from the particles onto the gas is largely underestimated in our models. In 3D disks, the midplane particle layer is far denser due to sedimentation, so the ratio ρ_p/ρ_g is far greater than the ratio Σ_p/Σ_g used in Eq. (3). The stronger backreaction that ensues is known to excite the streaming instabilities if $\rho_p/\rho_g \gtrsim 1$ (Youdin & Goodman 2005, Youdin & Johansen 2007, Johansen & Youdin 2007). This instability enhances particle clumping, thus aiding collapse (Johansen et al. 2007). However, the effect of this strong backreaction on the vortices is poorly known.

7.1.4. Different particle scale heights

As the particles sediment, what sets the particle scale height is the equilibrium between turbulent diffusion and

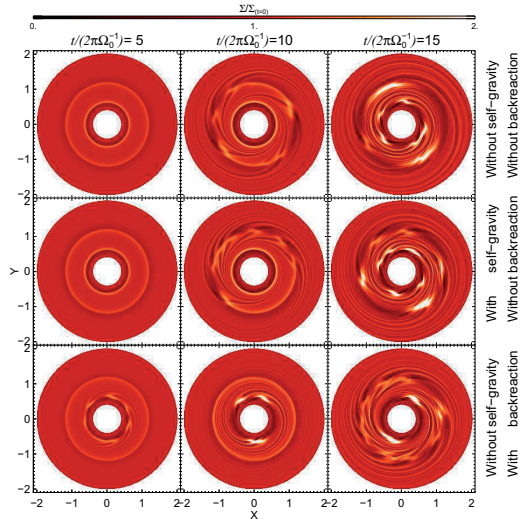


Fig. 14. Upper panels. Evolution of a disk without particles and without self-gravity, that serves as a control run for the next plots. Middle panels. Evolution of a disk without particles but with self-gravity. The difference compared to the upper panels is that the dominant mode in the outer disk changed from $m=2$ to $m=5$. Self-gravity modifies the dispersion relation of the RWI, or it stalls the inverse cascade of power known to occur in 2D turbulence, or both.

Lower panels. Evolution of a disk without self-gravity but with particles. The backreaction leads to an early excitation of the RWI in the inner edge of the dead zone. Conversely, the outer edge goes unstable later when compared to the other two runs. Since the particle density is not high enough to excite the streaming instability, we take it as evidence that the backreaction modifies the dispersion relation of the RWI.

vertical gravity. Controlled by the drag force, the turbulent diffusion depends on the particle radius, and so does the equilibrium scale height of the solids (Dubrulle et al. 1995). Because of this, particles of 1 m radius settle in a thinner layer than those of 1 cm particles. Inside a vortex, turbulent motions are expected to be weaker (Klahr & Bodenheimer 2006), bringing the layer of solids closer to a 2D configuration, but a dependence on radius is still expected. We could not model this effect on our simulations.

7.1.5. Gas tides and mass loss

The strength of the disrupting gas tides is yet another effect related to the difference between 2D and 3D models. As discussed in Sect. 3.2, the tides are proportional to the gas-to-solids ratio ρ_g/ρ_p , thus expected to be much weaker in 3D where sedimentation considerably increases ρ_p in the midplane. As the vorticity is also expected to be weaker in 3D, the peak of ρ_g at the vortex's eye would be weaker than in a 2D calculation, further weakening the effect of tides. We therefore anticipate embryos formed in 3D

simulations to be significantly less prone to mass loss than the ones presented in this study.

7.2. Equation of state

In this study, we used very simple equations of state: isothermal (Eq. (7)) or adiabatic (Eq. (24)). The effect of the equation of state can be appreciated by seeing the evolution of the Solberg-Høiland criterion in isothermal and adiabatic simulations. In the former, it is the epicyclic frequency that brings $\kappa^2 + N^2$ to negative values, while in the latter the criterion is broken mainly by the Brunt-Väisälä frequency. The excitation of the Rossby wave instability is greatly favored in the presence of a strong entropy gradient, and made more difficult (yet not impossible) as the disk approaches isothermality. Therefore, an accurate modeling of the energy budget - solving for radiative cooling and turbulent heating τ , is something to pursue in order to more realistically address the evolution of the RWI and the issue of planet formation inside the vortices that constitute its saturated state.

7.3. Aerodynamics of the embryo

The aerodynamics of a super-particle is controlled by the radius a_\bullet of the individual rocks. This means that even though the ensemble of rocks has the same position and velocity, there is still space between them and therefore they have contact with the gaseous nebula through all their surface area.

However, after gravitational collapse occurs, the solids are not any longer an ensemble of pebbles and boulders with free space between them, but a single massive object of planetary dimensions. This leads to a radical change in the aerodynamical properties. Yet, in our simulations, we still consider the collapsed body as an ensemble of super-particles, with the aerodynamical properties of individual pebbles and boulders. This is certainly a limitation of the model.

For a large planet, the correct treatment would be to consider that, after collapse, we leave the regime of particle-gas Stokes drag and enter planet-disk interaction by gravitational friction (type I migration). In the solar nebula the two drags have similar strength for bodies of 100 km. As we solve for the self-gravity of the gas, the latter is included in our model, albeit limited by the resolution of the grid. The fact that we keep using Epstein-Stokes drag on the super-particles after collapse might make an embryo more stable, especially in view of the very effective dynamical cooling provided by the drag force (Fig. 3). Substituting collapsed clusters by a sink particle that feels the gas gravity but not the gas drag is a possible solution, but also has caveats on its own. The evolution of sink particles depends too much on artificial numerical parameters such as the accretion radius. Furthermore, a sink particle does not suffer tidal effects, which we showed to be non-negligible.

7.4. Coagulation and Fragmentation

As dust particles are drawn together, electromagnetic interactions occur at their surface, causing sticking under favorable conditions. Brauer et al. (2008b) show that den-

sity enhancements like the ones we see - where matter accumulates due to a discontinuity in viscosity τ , dramatically favor coagulation. As particles are drawn together and the relative velocities are reduced, growth by coagulation occurs for a range of mass accretion rate \dot{m} and threshold fragmentation velocity v_{ft} . They find that the meter size barrier can be breached for mass accretion rates up to $\dot{m}=10^{-8}M_\odot/\text{yr}$ (for $v_{ft}=10\text{ m s}^{-1}$) and threshold fragmentation velocities no less than $v_{ft}=5\text{ m s}^{-1}$ (for $\dot{m}=8 \times 10^{-9}M_\odot/\text{yr}$).

This raises the possibility that even before the RWI excites the vortices, coagulation will have depleted the population of centimeter and meter sized objects onto bodies that are too large for our proposed mechanism to occur efficiently. As we see, it is preferentially the 10 and 30 cm sized particles that concentrate into planetary embryos.

The timescale for coagulation, however, is much longer than the time-scale for gravitational collapse. We see growth to Mars size taking place in only five orbits (≈ 60 yr), while growth by coagulation from meter to kilometer size occurs in timescales of a few thousand years according to Brauer et al. (2008b). On the other hand, it could as well be that the favorable environment provided by the vortices act as to speed up coagulation even further. This, of course, is not bad. Growth beyond the preferred size will lead to decoupling from the gas and ejection from the vortex that, in the end, behaves as a planetesimal factory.

Fragmentation is an important piece of reality that we did not include in our model. Nevertheless, we showed in Sect 4.5 that the majority of the particles were never involved in collisions with speeds greater than 1 m s^{-1} . These are of course very good news for planet formation. However, we feel the need to stress that the time interval between snapshots in Fig. 9a is of whole orbits (totaling 200 snapshots). The number of high-speed impacts could be greater had we checked the collision speeds at every time-step instead. Although desirable, this would have made the simulations computationally very expensive since it must be done in runtime. The result of Fig. 9b should therefore be taken only as further evidence for low collisional speeds inside vortices, not as conclusive proof of it. Carballido et al. (2008) further point that the low collisional speeds at low separation may be unrealistic. This is because the particles couple to the smallest eddies, whose size is a function of the mesh Reynolds number. These authors find average collisional speeds of $0.05c_s$ for particles of stopping time $\Omega_K\tau_f=0.2$ ($a_\bullet\approx 15\text{ cm}$ in our models), but notice a sharp decrease of the collisional speeds towards smaller separations. In our simulations, we are considering encounters that happen inside a grid cell, where we do not resolve the velocity field, so this may indeed be the reason behind the low collisional velocities we find. However, we point that there is a difference between the simulations of Carballido et al. (2008) and those presented in this paper. They considered particle concentrations in the transient pressure maxima of the turbulence generated by the MRI, whereas we consider particle concentrations within long lived anticyclonic vortices. As vortex structures tend to merge and grow, there is less power available at the smallest scales when compared to MRI turbulence.

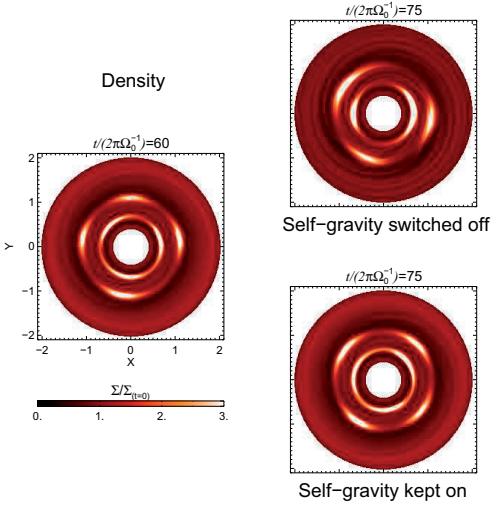


Fig. 15. In the simulation shown in LJKP08, the vortices maintained a $m=4$ mode in the outer edge of the dead zone until the end of the simulation. By switching self-gravity off, we see that in less than 15 orbits the outer vortices merged into a $m=3$ mode, while the $m=3$ mode in the inner disk edge into a $m=2$ mode. This is because as Q decreases, the size of the vortices approaches the Jeans length scale, which effectively halts the inverse cascade of energy.

8. Summary and conclusions

We have undertaken simulations of disks of gas and solids, where the solids are represented by Lagrangian particles of radii 1, 10, 30, and 100 cm. We show that in the borders of the dead zone, where the accretion flow stalls due a difference in turbulent viscosity, rapid gravitational collapse of the particles into protoplanets occurs within the vortices that form due to the excitation of the Rossby wave instability (Lovelace et al. 1999). As shown in LJKP08, over 300 gravitationally bound planetary embryos were formed, 20 of them being more massive than Mars. The mass spectrum follows a power law of index -2.3 ± 0.1 in the interval $-2.0 < \log(M/M_{\oplus}) < -1.2$.

Although for the main results of this study we have used sharp viscosity jumps to model the transition between the active and dead zones, we show that the RWI is excited up to viscosity jumps as smooth as $\Delta r = 2H$ where H is the pressure scale height. For this conclusion, we used the Solberg-Høiland criterion as providing a conservative estimate of whether the RWI is excited. The consequence of increasing the width of the viscosity jumps seems to be that the threshold of instability is reached at increasingly longer times. It only takes five orbits with $\Delta r = 0.2H$ (the usual width used in the models presented in this paper), but takes 350 orbits for $\Delta r = 2H$. We also assessed if the vortices would survive in the more realistic environment of a turbulent disk by making the location of the viscosity shift oscillate with an amplitude typical of the scale length of MRI turbulence over the period of a Keplerian revolution.

We find that this has little effect on the excitation of the RWI and saturation into vortices.

We model the solid phase with Lagrangian superparticles representing physical pebbles and rocks of different size (1, 10, 30, and 100 cm). As these particles are subject to different gas drag, an aerodynamical sorting by size takes place within the vortices. The consequence of this is that the first bound structures are formed of single particles species. This is a very interesting result, since it is an observed fact that planetesimals are formed of similar-sized building blocks (Scott & Krot 2005). These building blocks seem to be sub-mm sized grains, but different nebula parameters could work as to trap smaller particles. Youdin (2008) also points that the stationary point of a particle trapped in vortical motion is shifted azimuthally with respect to the eye, according to its radius a_* . We indeed see that clumps of particles of different size, that collapse into different embryos inside the same vortex, usually retain significant azimuthal displacements between each other for long times instead of forming a single, more massive, embryo at the vortex eye. This may or may not be a result of the size-dependent azimuthally shifted stationary points of Youdin (2008).

A collapsed embryo is observed to be very compact. The compactness is mainly provided by the drag force, which makes the system very dissipative (dynamical cooling by gravity alone works on much longer timescales). Collapse towards “infinite” density is seen to occur in some cases, with most of the particles occupying the same position in space (limited by numerical precision). In the specific case when the particles dominate the time-step, the Courant condition leads a particle to overshoot the center of the mass, so that it executes oscillations about it, which in turn leads to a finite rms radius. We also observe that a clump of particles is susceptible to the disrupting effects of ram pressure erosion and gravitational tides from the gas. Both effects are proportional to the local gas-to-solids density ratio. When the vortices in the inner border of the dead zone undergo the transition from the $m=3$ to the $m=2$ mode, their surface density increases, with drastic consequences for the embryos within them. The most massive embryo by that time, a protoplanet 6.7 times the mass of Mars, mostly formed of $a_* = 30$ cm particles, was split into two smaller objects, of 5.9 and 0.8 M_{Mars} , due to the action of the gas tides. The fate of the embryos formed mostly of 10 cm was more dramatic. As the 10 cm particles experience stronger drag forces, the ram pressure is also stronger. During the mode transition, the combined effects of tides and erosion completely obliterated these embryos, leaving extended arcs of particles that did not reaccumulate until the end of the simulation. We anticipate that this effect will be very reduced in 3D simulations. In 2D simulations, the ratio of the vertically integrated solids density to the gas column density Σ_p/Σ_g never gets much above unity even for the most massive embryo. In contrast, the ratio of the bulk density of solids to the volume gas density ρ_p/ρ_g is greatly increased in the midplane of 3D disks due to sedimentation.

We also observe that the solids modify the evolution of the RWI. We are drawn to this conclusion because a simulation without the backreaction of the drag force from the particles onto the gas developed vortices at later times when compared to the ones that include particle feedback. We stress that this is not due to the streaming instabil-

ity, since the solids-to-gas ratio was much lower than the value needed to excite it ($\rho_p/\rho_g \gtrsim 1$). Instead, it is more likely that the backreaction of the drag force contributes non-negligibly to the dispersion relation of the RWI. Self-gravity is also seen to play a role on modifying the evolution of the turbulence. We observe that in simulations without self-gravity, the disk tends to show less vortices at later times. In a simulation where we switched off the self-gravity after the vortices had developed, the dominant $m=4$ mode in the outer edge of the dead zone rapidly turned into a $m=3$ mode. The vortices in the inner edge also quickly turned from a dominant $m=3$ mode to displaying a $m=2$ mode instead. We measured the Toomre Q parameter and found that the vortices have $Q \approx 1$. This constitutes further evidence that in the presence of self-gravity, vortex growth is not only limited by the pressure scale height but also by the Jeans length (Mamatsashvili & Rice 2009).

An important finding in this paper is that under vortex trapping, the collisional speeds between particles are greatly reduced. We measured the collisional velocity history of every particle that is bound to the most massive embryo at the end of the simulation, and found that the vast majority of them never experienced close encounters at speeds greater than 1 m s^{-1} . This is well below the fragmentation threshold and lends support to the long-held belief that vortices provide a superbly favorable environment for planetary growth. Growth by coagulation beyond the optimal size for planet formation is also avoided because the timescales for coagulation are much longer than the rapid timescale for gravitational collapse witnessed in our models. This does not exclude the possibility that coagulation itself is sped up within a vortex. In this case, the vortex will behave as a planetesimal factory, quickly producing kilometer sized bodies that leave the vortex due to their decoupling from the gas. This, as noted by Klahr & Bodenheimer (2006) is very positive for planet formation, since the formed planetesimals are then scattered through the disk, where they can be used to form planets independently from a vortex. Even though it implies that we are facing the comfortable position of a win-win situation for planet formation, one has to decide which process (planet formation by direct gravitational collapse or planetesimal formation by fast coagulation) is getting the upper hand inside the Rossby vortices. A definite answer to this question can only be drawn from a simulation that includes the processes of coagulation/fragmentation. Unfortunately, inclusion of sophisticated coagulation/fragmentation models such as that of Brauer et al. (2007) would render a hydrodynamical simulation overly expensive. A possible alternative would be a Monte Carlo model of dust coagulation, such as the one recently developed by Ormel et al. (2007). A further development of the Monte Carlo technique is described in Zsom & Dullemond (2008). The main difference between the two models is that while Ormel et al. (2007) simulate coagulation between real dust particles, Zsom & Dullemond (2008) use superparticles to model coagulation and fragmentation. Therefore the latter one is more suitable for hydrodynamical simulations such as ours and simple estimations show that this model could be adapted to a hydro model with no prohibitive overhead.

We reiterate that the models presented suffer from a number of limitations, detailed in Sect 7. Some of them,

like refining the particle mass resolution to the individual pebbles and rocks, are beyond the capabilities of the current generation of computer models. Others, however, such as inclusion of detailed thermal physics, could be tackled with relatively little effort. We urge researchers active on the field to consider these problems. It is our hope that a coherent picture of planet formation in the magnetically dead zones of accretion disks shall emerge as a result of it.

Acknowledgements. Simulations were performed at the PIA cluster of the Max-Planck-Institut für Astronomie and on the Uppsala Multidisciplinary Center for Advanced Computational Science (UPPMAX). This research has been supported in part by the Deutsche Forschungsgemeinschaft DFG through grant DFG Forschergruppe 759 “The Formation of Planets: The Critical First Growth Phase”. A. Zsom acknowledges support by the IMPRS for Astronomy & Cosmic Physics at the University of Heidelberg.

References

- Armitage, P. J., Livio, M., & Pringle, J. E. 2001, *MNRAS*, 324, 705
 Balbus, S.A., & Hawley, J.F. 1998, *RvMP*, 70, 1
 Balbus, S.A., & Hawley, J.F. 1991, *ApJ*, 376, 214
 Barranco, J.A., & Marcus, P.S. 2005, *ApJ*, 623, 1157
 Barge, P., & Sommeria, J. 1995, *A&A*, 295, 1
 Benz, W. 2000, *SSRv*, 92, 279
 Bracco, A., Chavanis, P.-H., Provenzale, A., & Spiegel, E. A. 1999, *Physics of Fluids*, 11, 2280
 Brauer, F., Dullemond, C. P., Johansen, A., Henning, Th., Klahr, H., & Natta, A. 2007, *A&A*, 469, 1169
 Brauer, F., Dullemond, C. P., & Henning, Th. 2008a, *A&A*, 480, 859
 Brauer, F., Henning, Th., & Dullemond, C. P. 2008b, *A&A*, 487, 1
 Carballido, A., Stone, J. M., & Turner, N. J. 2008, *MNRAS*, 386, 145
 Chavanis, P.-H. 2000, *A&A*, 356, 1089
 Chokshi, A., Tielens, A. G. G. M., & Hollenbach, D. 1993, *ApJ*, 407, 806
 Crow, S.C. 1970, *AIAAJ*, 8, 2172
 Cuzzi, J. N., Hogan, R. C., & Shariff, K. 2008, arXiv0804.3526
 Dominik, C., Blum, J., Cuzzi, J.N., & Wurm, G. 2007, *Protostars and Planets V*, p783
 Dubrulle, B., Morfill, G., & Sterzik, M., 1995, *Icarus*, 114, 237
 Edgar, R. G., & Quillen, A. C. 2008, *MNRAS*, 387, 387
 Fleming, T. & Stone, J. M. 2003, *ApJ*, 585, 908
 Fromang, S., & Nelson, R. P. 2005, *MNRAS*, 364, 81
 Gammie, C. F. 1996, *ApJ*, 457, 355
 Garaud, P., & Lin, D. N. C. 2004, *ApJ*, 608, 1050
 Gledzer, E.B., Dolzhanskii, F.V., Obukhov, A. M., & Ponomarev, V. M. 1975, *Isv. Atmos. Ocean. Phys.*, 11, 617
 Goldreich, P., & Ward, W. R. 1973, *ApJ*, 183, 1051
 Haghhighipour, N., & Boss, A. P. 2003, *ApJ*, 583, 996
 Johansen, A., Andersen, A. C., & Brandenburg, A. 2004, *A&A*, 417, 361
 Johansen, A., & Youdin, A. 2007, *ApJ*, 662, 627
 Johansen, A., Oishi, J. S., Mac Low, M.-M., Klahr, H., Henning, Th., & Youdin, A. 2007, *Nature*, 448, 1022
 Johansen, A., Brauer, F., Dullemond, C., Klahr, H., & Henning, T. 2008, *A&A*, 486, 597
 Johansen, A., Henning, Th., & Klahr, H. 2006, *ApJ*, 643, 1219
 Johnson, B.M., & Gammie, C.F. 2005, *ApJ*, 635, 149
 Kerswell, R.R. 2002, *Annu. Rev. Fluid Mech.*, 34, 83
 Klahr, H., & Bodenheimer P., 2006, *ApJ*, 639, 432
 Klahr, H., & Bodenheimer P. 2003, *ApJ*, 582, 869
 Klahr, H. 2004, *ApJ*, 606, 1070
 Li, H., Finn, J. M., Lovelace, R. V. E., & Colgate, S. A. 2000, *ApJ*, 533, 1023
 Li, H., Colgate, S. A., Wendroff, B., & Liska, R. 2001, *ApJ*, 551, 874
 Lodato, G. 2008, *New Astronomy Reviews*, 52, 21
 Lovelace, R. V. E., Li, H., Colgate, S. A., & Nelson, A. F. 1999, *ApJ*, 513, 805
 Lyra, W., Johansen, A., Klahr, H., & Piskunov, N. 2008a, *A&A*, 479, 883
 Lyra, W., Johansen, A., Klahr, H., & Piskunov, N. 2008b, arXiv0807.2622 (LJKP08)
 Lyra, W., Johansen, A., Klahr, H., & Piskunov, N. 2008c, arXiv0810.3192
 Lytleton, R. A. 1972, *MNRAS*, 158, 463
 Mamatsashvili G.R., & Rice, W.K.M. 2009, arXiv:0901.1617
 Marcus, P. 1990, *Journal of Fluid Mechanics*, 215, 393

- Méheut, H., Casse, F., Varnire, P., & Tagger, M. 2008, Proceedings of the Annual meeting of the French Society of Astronomy and Astrophysics, p.417, Eds.: C. Charbonnel, F. Combes and R. Samadi.
- Miller, K.A. & Stone, J.M. 2000, *ApJ*, 534, 398
- Oishi, J. S., Mac Low, M.-M., & Menou, K. 2007, *ApJ*, 670, 805
- Ormel, C.W. & Cuzzi, J.N. 2007, *A&A*, 466, 413
- Ormel, C. W., Spaans, M., & Tielens, A. G. G. M. 2007, *A&A*, 461, 215
- Paardekooper S.-J. 2006, PhD
- Paraskov, G. B., Wurm, G., & Krauss, O. 2006, *ApJ*, 648, 1219
- Petersen, M. R., Julien, K., & Stewart, G. R., 2007, *ApJ*, 658, 1236
- Rice, W. K. M., Lodato, G., Pringle, J. E., Armitage, P. J., & Bonnell, I. A. 2004, *MNRAS*, 355, 543
- Rice, W. K. M., Lodato, G., Pringle, J. E., Armitage, P. J., & Bonnell, I. A. 2006, *MNRAS*, 372, 9
- Safronov, V. S. 1969, *QB*, 981, 26
- Scott, E.R.D., & Krot A.N. 2005, in *A.S.P. Conf. Series* 341, 15
- Sekiya, M. 1998, *Icarus*, 133, 298
- Shakura, N.I., & Sunyaev, R.A. 1973, *A&A*, 24, 337
- Shen, Y., Stone, J.M., & Gardiner, T.A. 2006, *ApJ*, 653, 513
- Sirono S.-I. 2004, *Icarus*, 167, 431
- Tanga, P., Babiano, A., Dubrulle, B., Provenzale, A., 1996, *Icarus*, 121, 158
- Terquem C. 2008, *ApJ*, 689, 532
- Turner, N. J. & Sano, T. 2008, *ApJ*, 679, 131
- Umebayashi, T. & Nakano, T. 2009, *ApJ*, 690, 69
- de Val-Borro, M., Edgar, R.G., Artymowicz, P., Cieliegiel, P., Cresswell, P., D'Angelo, G., Delgado-Donate, E.J., Dirksen, G., Fromang, S., Gawryszczak, A., Klahr, H., Kley, W., Lyra, W., Masset, F., Mellema, G., Nelson, R., Paardekooper, S.-J., Peplinski, A., Pierens, A., Plewa, T., Rice, K., Schäfer, C., & Speith, R. 2006, *MNRAS*, 370, 529
- de Val-Borro, M., Artymowicz, P., D'Angelo, G., & Peplinski, A., 2007, *A&A*, 471, 1043
- Varnière, P., & Tagger, M. 2006, *A&A*, 446, 13
- Weidenschilling, S.J. 1980, *Icarus*, 44, 172
- Weidenschilling, S.J. 1977a, *MNRAS*, 180, 57
- Weidenschilling, S.J. 1977b, *Ap&SS*, 51, 153
- Weidenschilling, S. J., & Cuzzi, J. N. 1993, *Protostars and Planets III*, p1031
- Woitke, P., & Helling, C., 2003, *A&A*, 399, 297
- Youdin, A. N., & Goodman, J. 2005, *ApJ*, 620, 459
- Youdin, A., & Johansen, A., 2007, *ApJ*, 662, 613
- Youdin, A. N., & Shu, F. H. 2002, *ApJ*, 580, 494
- Youdin, A. N. 2008, arXiv0807.1114
- Zsom, A., & Dullemond, C. P. 2008, *A&A*, 489, 931

Online Material

Appendix A: Resolution study

In Fig. A.1 we present a resolution study of our models. The upper panels show Cartesian models, including self-gravity and solids, while the lower panels show cylindrical models with dustless non-selfgravitating gas. Both are shown in selected snapshots at 10, 20, and 30 orbits.

In the Cartesian runs, the vortices in the high-resolution run (512^2) are excited earlier than in the middle resolution run (256^2). At later times, the vortices in the high-resolution run also appear sharper. While in the two runs the vortices in the outer edge of the dead zone look remarkably similar, the inner edge displays very different behavior. Up to 30 orbits the middle resolution run has not shown signs of prominent vortices. In contrast, the high resolution run had the inner edge developing vortices as early as 10 orbits. This is not only due to the high resolution run having a larger inertial range, but also because a flow with cylindrical symmetry is more coarsely resolved near the origin in a Cartesian grid. Because of this, the most unstable modes are under-resolved in the inner disk of the middle resolution run. A Cartesian run with low resolution (128^2 , not shown) did not develop vortices even in the outer disk by the same time. At 30 orbits, the density inside the vortices peak at similar values, $\Sigma/\Sigma_0=3.3$ and 3.7 for the middle and high resolution runs, respectively.

The cylindrical runs also evidence the small amount of differences between the vortices in different runs. With better azimuthal resolution, the vortices are excited even in the 128^2 run, and in both runs they peak with surface density $\Sigma/\Sigma_0=4.6$. In fact, the main effect of resolution appears to be that, as it increases, the RWI is excited increasingly earlier. The high-resolution run displays weaker vortices than the others because in this case we were forced to use shock viscosity.

Appendix B: Emulating turbulent motions

In this study, we considered the dead zone to be represented by a static viscosity profile. In a more realistic scenario, turbulent motions caused by the MRI and variations in the coupling between the magnetic field and the plasma will give rise to a turbulent resistivity. This is expected to cause the border of the dead zone to vary in space and time, with implications for the evolution of the RWI.

To assess the impact of space and time variability of the edges of the dead zone, we model the viscous jumps using $\Delta r=0.01$ but make the jumps shift radially in time by substituting r_1 and r_2 in Eq. (13) by

$$r_1(t) \rightarrow r_1 [1 + h \sin(\Omega_K(r_1)t)] \quad (\text{B.1})$$

$$r_2(t) \rightarrow r_2 [1 + h \sin(\Omega_K(r_2)t)] \quad (\text{B.2})$$

where $h=H/r$ is the aspect ratio. So, the location shifts by two scale heights over a Keplerian revolution. The results are shown in Fig. B.1, where we show the appearance of the disk at 30 orbits and the azimuthal average of $(\kappa^2 + N^2)/\Omega_K^2$ (in the same 2D model, as opposed to 1D as in Sect. 3.2).

In this simulation, the RWI is still excited and vortices are launched. The main difference when compared to simulations with static profiles is that the instability takes more time to violate the Solberg-Høiland criterion,

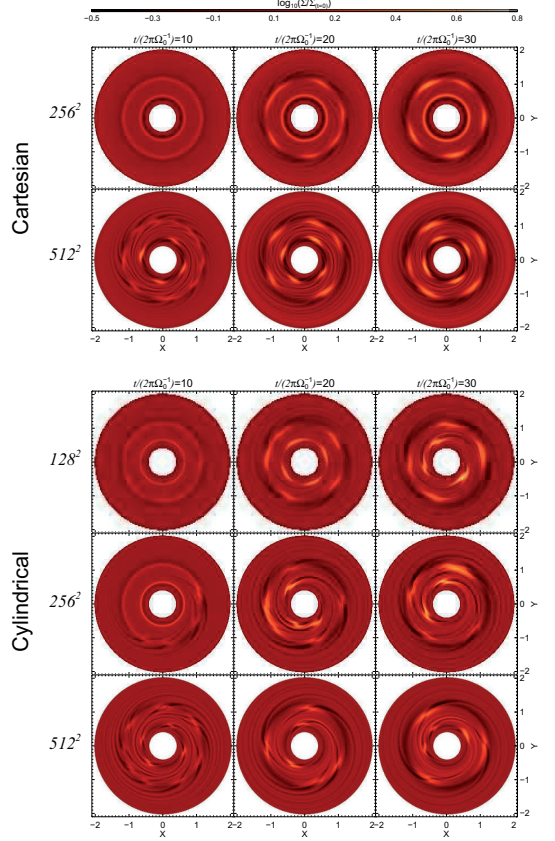


Fig. A.1. The development of the dead zone vortices in different resolution and grid geometry. With increased resolution the RWI is excited increasingly earlier. In general the vortices in cylindrical runs look sharper than in the Cartesian ones, due to the better azimuthal resolution. The Cartesian run of middle resolution (256^2) has too coarse azimuthal resolution in the inner disk, and only developed vortices in the inner edge of the dead zone at later times (≈ 40 orbits). Apart from these differences, the vortices look remarkably similar, having nearly the same peak density and same vorticity.

≈ 10 orbits, compared to 5 in the static case. This is due to the fact that the shifting viscosity jump smears the pressure maximum, so the amplitude of the pressure jump is shorter and the width is larger than in the static case.

Appendix C: Onset of erosion

According to Eq. (30), a tight distribution of particles under Epstein drag should suffer erosion if

$$\text{We}_G = \frac{\text{Mac}_s \Omega}{(\tau \Omega) \pi G \Sigma_p} \geq 1 \quad (\text{C.1})$$

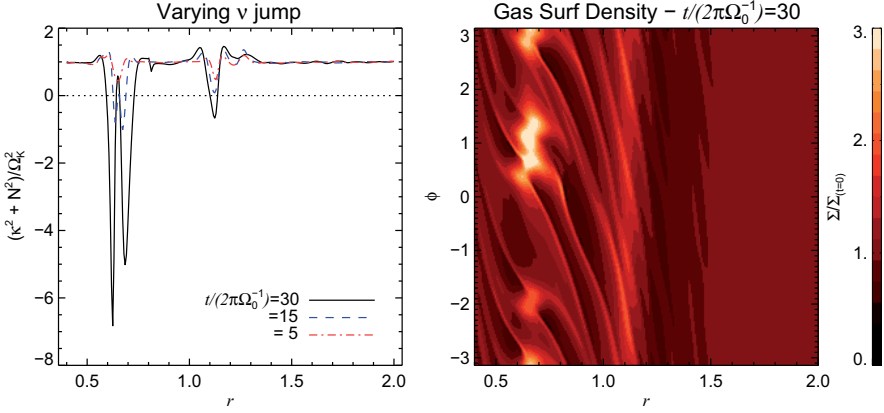


Fig. B.1. Evolution of the RWI with a time-varying viscosity jump as specified by Eq. (13) and Eqs. (B.1)–(B.2). The panel on the left-hand side measures the violation of the Solberg-Høiland criterion. The right-hand side panel shows the appearance of the disk at 30 orbits. Both the inner and outer edge quickly reach the threshold of instability (left panel). At 30 orbits, the inner edge already reached a saturated state and launched vortices (right panel).

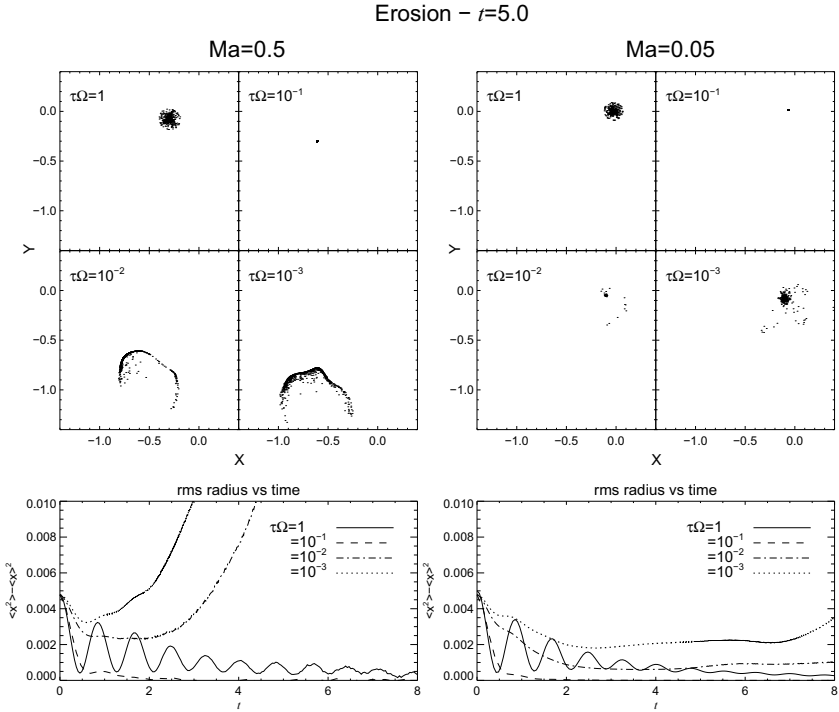


Fig. C.1. A clump of 1000 massive particles moving against headwinds of $Ma=0.5$ and $Ma=0.05$, for different values of the friction time $\tau\Omega$. In the case of $Ma=0.5$, self-gravity cannot hold the clump together for $\tau\Omega \lesssim 10^{-2}$. In our simulations it corresponds to 1 cm sized particles, approximately. Clumps formed of larger particles do not experience erosion. For the more subsonic motion, the effect of ram pressure is lower so the clump of $\tau\Omega=10^{-2}$ is more stable against erosion. The case of $\tau\Omega=1.0$ takes longer to contract because of the weaker drag force, that provides less dynamical cooling than in the case with $\tau\Omega=0.1$. It eventually shrinks, as seen in the time series (bottom plot).

In this appendix, we perform numerical simulations to test the validity of this condition. We model a clump of 10^3 particles suffering a strong headwind from the gas ($\text{Ma}=1/2$). The blob of particles is initially set as a tight Gaussian distribution about the center of the grid, with surface density peak of $\Sigma_p/\Sigma_0 = 2.31$. In units where $G=c_s=\Sigma_0=\Omega_0=1$, the initial gravitational Weber number at the surface of the blob is therefore $\text{We}_G \simeq 7 \times 10^{-2}/(\tau\Omega)$.

We plot in Fig. C.1 the evolution of clumps for four different values of $\tau\Omega$. For $\tau\Omega=1.0$ and $\tau\Omega=0.1$, We_G is less than 1 so the clump is stable against ram pressure and contracts. The other clumps ($\tau\Omega=0.01$ and $\tau\Omega=0.001$) have We_G above unit, and experience intense erosion. We also considered a flow of Mach number $\text{Ma}=0.05$. In this case the initial gravitational Weber number is $\text{We}_G \simeq 7 \times 10^{-3}/(\tau\Omega)$, and the clumps of smaller particles are supposed to be more stable. Indeed, this is what we see in the figure. The clump of particles of $\tau\Omega=0.01$ is now marginally stable and contracts, experiencing much less erosion than in the $\text{Ma}=0.5$ case.

We would like to draw attention to an interesting feature of Fig. C.1. The cases of $\tau\Omega=1$ and $\tau\Omega=0.1$ (upper panels) provide yet another perspective for the action of drag force cooling. Both clumps are stable against erosion but the clump of $\tau\Omega=0.1$ has shrunk considerably more than the clump of $\tau\Omega=1.0$, that looks very extended. What is happening is that the clump with $\tau\Omega=1$ is too weakly coupled to the gas and therefore takes longer to collapse, as seen in the time series of the rms position (Fig. C.1, lower panels).

Paper IV



Standing on the shoulders of giants

Trojan Earths and vortex trapping in low mass self-gravitating protoplanetary disks of gas and solids

W. Lyra¹, A. Johansen², H. Klahr³, & N. Piskunov¹

¹ Department of Physics and Astronomy, Uppsala Astronomical Observatory, Box 515, 751 20 Uppsala, Sweden

² Leiden Observatory, Leiden University, PO Box 9513, 2300 RA Leiden, The Netherlands

³ Max-Planck-Institut für Astronomie, Königstuhl 17, 69117 Heidelberg, Germany

Received ; Accepted

ABSTRACT

Context. Centimeter and meter-sized solid particles in protoplanetary disks are trapped within long-lived, high-pressure regions, creating opportunities for collapse into planetesimals and planetary embryos.

Aims. We aim to study the effect of the high-pressure regions generated in the gaseous disks by a giant planet perturber. These regions consist of gas retained in tadpole orbits around the stable Lagrangian points as a gap is carved, and the Rossby vortices launched at the edges of the gap.

Methods. We performed global simulations of the dynamics of gas and solids in a low mass non-magnetized self-gravitating thin protoplanetary disk. We employed the Pencil code to solve the Eulerian hydro equations, tracing the solids with a large number of Lagrangian particles, usually 100 000. To compute the gravitational potential of the swarm of solids, we solved the Poisson equation using particle-mesh methods with multiple fast Fourier transforms.

Results. Huge particle concentrations are seen in the Lagrangian points of the giant planet, as well as in the vortices they induce at the edges of the carved gaps. For 1 cm to 10 cm radii, gravitational collapse occurs in the Lagrangian points in less than 200 orbits. For 5 cm particles, a $2 M_{\oplus}$ planet is formed. For 10 cm, the final maximum collapsed mass is around $3 M_{\oplus}$. The collapse of the 1 cm particles is indirect, following the timescale of gas depletion from the tadpole orbits. Vortices are excited at the edges of the gap, primarily trapping particles of 30 cm radii. The rocky planet that is formed is as massive as $17 M_{\oplus}$, constituting a Super-Earth. Collapse does not occur for 40 cm onwards. By using multiple particle species, we find that gas drag modifies the streamlines in the tadpole region around the classical L4 and L5 points. As a result, particles of different radii have their stable points shifted to different locations. Collapse therefore takes longer and produces planets of lower mass. Three super-Earths are formed in the vortices, the most massive having $4.5 M_{\oplus}$.

Conclusions. A Jupiter-mass planet can induce the formation of other planetary embryos at the outer edge of its gas gap. Trojan Earth-mass planets are readily formed; although not existing in the solar system, might be common in the exoplanetary zoo.

Key words. Keywords should be given

1. Introduction

Losing angular momentum by friction with the ambient gaseous headwind, centimeter to meter-sized bodies in protoplanetary disks spiral into the star on timescales as short as a hundred years (Weidenschilling 1977). Avoiding this fate is a major unsolved problem in modern astrophysics. The question of the formation of rocky planets is intimately connected with this problem, since the kilometer-sized bodies (planetesimals) whence they are believed to form (Safronov 1969) must be formed faster than the already rapid timescale of radial drift of the rocks (0.1-1 meter-size) and boulders (1-10 meter-size).

As colliding boulders have very poor sticking properties (Benz 2000), a possible scenario for the formation of planetesimals is direct gravitational collapse of the layer of boulders (Goldreich & Ward 1973). This hypothesis has met with criticism because no route for achieving crit-

ical densities could be found (Weidenschilling & Cuzzi 1993), but it has recently gained momentum due to a series of advances in modeling the coupled dynamics of gas and boulders through both analytical calculations and numerical simulations. Youdin & Goodman (2005) showed that when rocks and boulders migrate due to the drag force, they trigger a streaming instability that develops into a traffic jam in their migrating flow, with dramatic effects for the particle concentrations (Johansen et al. 2006b, Paardekooper 2006, Johansen & Youdin 2007, Balsara et al. 2008). Fromang & Nelson (2005) modeled the dynamics of particles in magnetized global disks and showed that trapping occurs in the pressure maxima of the turbulence generated by the magneto-rotational instability (MRI). The number of particles, however, was too low (≤ 3000) to say anything about possible gravitational collapse. Johansen et al. (2006a) simulated the flow in an MRI-active local box using a statistically significant number of particles (10^6),

and showed that the particle concentration is high enough to achieve critical densities.

Studies with self gravity to follow the collapse are restricted to local boxes (Johansen et al. 2007) and the massive disk case (Rice et al. 2004, Rice et al. 2006). The former couples the effects of particle concentrations due to the streaming instabilities with those due to the turbulence generated by the MRI to show that the turbulent layer of boulders locally collapse into dwarf planets on very short timescales. The latter is a global disk calculation of marginally gravitationally unstable gaseous disks, where boulders are shown to concentrate in the spiral arms that develop, where they also achieve critical density.

A broad conclusion that can be drawn from these studies is that any region with higher pressure than its surroundings tends to concentrate solids (Haghighipour & Boss 2003). Therefore, in order to trigger collapse of the solids, one has to create long-lived, high-pressure regions in the gas phase. A perturber, then, is expected to have major consequences in the dynamics of embedded rocks and boulders. Paardekooper & Mellema (2004) studied the dynamics of dust in a gaseous disk, finding that even low mass planets carve a deep dust gap. An update by Paardekooper (2007) showed an interesting feature. As early as 20 orbits, meter-sized particles tend to concentrate at the gap edges and at co-rotation in tadpole orbits. However, as Lagrangian trapping was not the main scope of their study, they did not further assess the consequences of particle concentration in 1:1 resonance, focusing instead on the other mean motion resonances brought about by the planet.

Fouchet et al. (2007) also explored the same problem, in 3D SPH simulations, considering not only different particle radii, but also different masses for the perturber. The results are very similar to those of Paardekooper (2007), but they argue against the accumulation they see being the result of resonance trapping. They come to this conclusion because the signatures of resonance trapping, easily identifiable in an eccentricity vs. semi-major axis plot for decoupled particles, disappears when one considers gas drag. Instead, they claim that it occurs more likely due to the dust concentrating at the gas pressure maxima at the edges of the gap. Fouchet et al. (2007) also notice that the 1 m sized boulders are found in 1:1 resonance at later times. They speculate that the same occurs for other particle sizes they considered (10 cm and 1 cm sized pebbles), but as the dust gap in this case was too narrow compared to the extended disk they considered (20 AU), they could not spot the rocks trapped in the co-orbital region.

One possibility that was unexplored in these works is whether a direct collapse can occur at the enhanced particle concentrations. There are significant gas overdensities in co-rotation, especially at the Lagrangian points, for at least 200 orbits (de Val-Borro et al. 2006). In these regions, the solids are subject to drag forces for a period long enough to allow concentration and eventual collapse into kilometer-sized bodies in 1:1 resonance. In this paper, we show that the trapping provided in the Lagrangian points is so efficient that the final mass of the collapsed body is that of terrestrial planets.

The collapse of the solids that get trapped at the edges of the gas gap is also an interesting issue. As shown by de Val-Borro et al. (2007), the gap that the planet carves has a density gradient propitious to the excitation of the

Rossby wave instability (RWI; Li et al. 2001). The anti-cyclonic vortices that form are entities of great interest, since they induce a net force on solid particles toward their centers, raising the local solids-to-gas ratio and favoring gravitational collapse (e.g. Barge & Sommeria 1995, Bracco et al. 1999, Chavanis 2000). We show in this paper that the combination of the particle concentration seen by Paardekooper (2007) and Fouchet et al. (2007), together with the vortices predicted by de Val-Borro et al. (2007) lead to a powerful particle trap, raising the density of solids by three to four orders of magnitude. The collapse leads not to a kilometer-sized body or to a dwarf planet, but to masses comparable to that of the terrestrial planets and in some cases, super-Earths.

An initial step towards modeling this scenario was put forth by Beaugé et al. (2007). In this recent study, these authors perform pure N -body calculations of a few number (usually 500) of dwarf planets of $0.3 M_{\text{Moon}}$ around the L4 point of Jupiter. They find that a reasonable fraction of the bodies escape the tadpole orbit by close encounters with the giant. The rest of the particles successfully concentrate into a single Trojan planet, but no more massive than $0.6 M_{\oplus}$. They do not solve concurrently for the dynamics of gas and solids, but they assess how the formation process would work in a gas rich scenario by performing planet-disk simulations and verifying the gas conditions around the Lagrangian points. The densities and velocities are then used to quantify coefficients for the drag laws. This *ad hoc* drag force is then added in the pure N -body calculations.

In this paper we model gas and dust self-consistently, using 10^5 particles to represent the solids phase. Unlike Beaugé et al. (2007), we do not assume the particles to be as massive as dwarf planets. Instead, we treat them as meter-sized bodies, their gravitational potential computed by solving the continuous Poisson equation. Although the formation of Trojans is our primary interest, we model a radially extended region of the disk, and are able to explore the gap edge as well, where the anti-cyclonic vortices form.

In the next sections we describe the model equations, the Poisson solver and drag law used. The results are presented in Sections 3-6, followed by a concluding discussion in Sect. 7.

2. Dynamical equations

We work in the thin disk approximation, using the vertically averaged equations of hydrodynamics

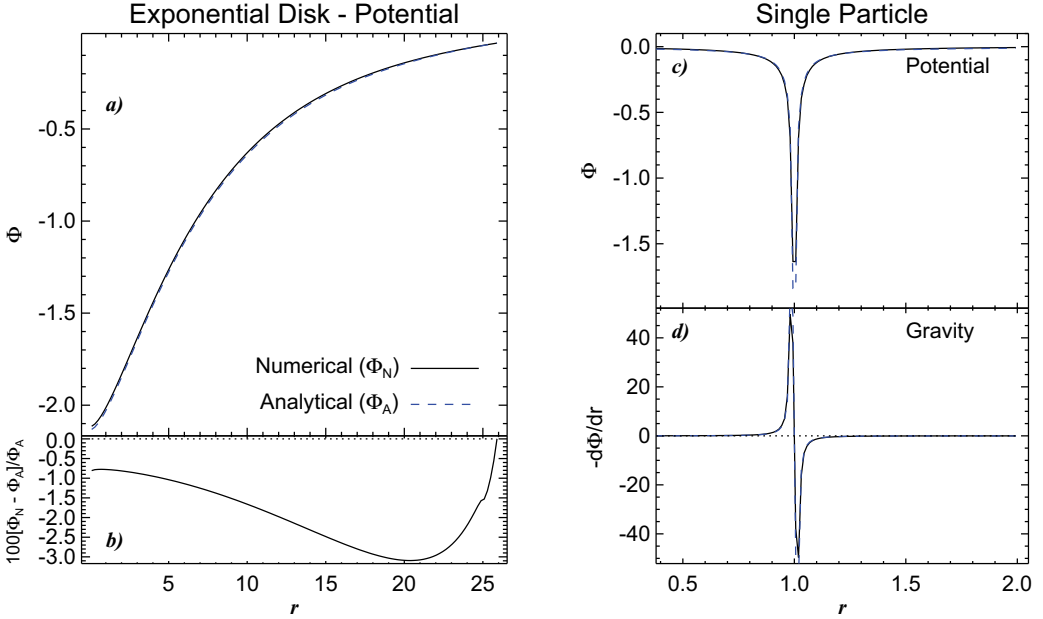


Fig. 1. *a.* The potential generated by an exponential disk computed by Eq. (11) is compared with the analytical expression. The accuracy (*b.*) is at the percent level. *c.* The potential generated by a single particle agrees very well with its Newtonian prediction. In particular, the scheme ensures that the gravity (*d.*) is smooth and the particle does not suffer self-acceleration.

$$\frac{D\Sigma_g}{Dt} = -\Sigma_g \nabla \cdot \mathbf{u} + f_D(\Sigma_g) \quad (1)$$

$$\frac{D\mathbf{u}}{Dt} = -\frac{1}{\Sigma_g} \nabla P - \nabla \Phi - \frac{\Sigma_p}{\Sigma_g} f_d + f_v(\mathbf{u}, \Sigma_g) \quad (2)$$

$$\frac{dv_p}{dt} = -\nabla \Phi + f_d \quad (3)$$

$$\frac{dx_p}{dt} = v_p \quad (4)$$

$$\Phi = \Phi_{sg} - \sum_i^n \frac{GM_i}{\sqrt{\mathcal{R}_i^2 + b_i^2}} \quad (5)$$

$$\nabla^2 \Phi_{sg} = 4\pi G \Sigma \delta(z) \quad (6)$$

$$P = \Sigma_g c_s^2 \quad (7)$$

$$f_d = -\left(\frac{3\rho_g C_D |\Delta v|}{8a_\bullet \rho_\bullet} \right) \Delta v. \quad (8)$$

In the above equations, Σ_g and Σ_p are the vertically integrated gas density and bulk density of solids, respectively. In Eq. (6), Σ is their sum. \mathbf{u} stands for the velocity of the gas parcels; v_p is the velocity of the solid particles, and x_p is their position; P is the vertically integrated pressure, c_s is the sound speed, Φ the gravitational potential and f_d is the drag force by which gas and solids interact. In Eq. (8), ρ_\bullet is the internal density of a solid particle,

a_\bullet its radius, and $\Delta v = v_p - \mathbf{u}$ its velocity relative to the gas. The nature of the drag is concealed in the dimensionless coefficient C_D , discussed in section 2.2. The operator $D/Dt = \partial/\partial t + \mathbf{u} \cdot \nabla$ represents the advective derivative.

The gravitational potential Φ has contributions from the star, the giant planets, and the disk's self-gravity. The star and the planets are treated as massive particles with a simple N -body code. In Eq. (5), G is the gravitational constant, M_i is the mass of particle i and $\mathcal{R}_i = |\mathbf{r} - \mathbf{r}_{p_i}|$ is the distance relative to particle i . The quantity b_i is the distance over which the gravity field of particle i is softened to prevent singularities.

The function $f_D(\Sigma_g) = D_3 \nabla^6 \Sigma_g$ is a third order hyper-diffusion term. In Fourier space, it is proportional to k^6 , where k is the wavenumber. Being so, it behaves as a high-frequency filter, and is very effective in providing numerical stabilization near the grid scale while having little effect in the more quiescent larger scales. The function $f_v(\mathbf{u}, \Sigma_g)$ has both a hyperviscosity and a shock viscosity term

$$f_v(\mathbf{u}, \Sigma_g) = \Sigma_g^{-1} \nabla \cdot \left(2\Sigma_g \nu_3 S^{(3)} \right) + \zeta_\nu \left[\nabla (\nabla \cdot \mathbf{u}) + (\nabla \ln \Sigma_g + \nabla \ln \zeta_\nu) \nabla \cdot \mathbf{u} \right] \quad (9)$$

where $S_{ij}^{(3)} = \partial_j^3 u_i$ is a simplified (third-order) rate-of-strain tensor and the shock term ζ_ν follows the formulation of

Haugen et al. (2004), being proportional to the smoothed (over three grid cells in each direction) maximum (also over three grid cells) of the positive part of the negative divergence of the velocity, i.e.

$$\zeta_v = v_{\text{shock}} \left\langle \max_3 [(-\nabla \cdot \mathbf{u})_+] \right\rangle (\Delta x)^2. \quad (10)$$

The shock viscosity coefficient v_{shock} is a parameter of order unity. We use $v_{\text{shock}}=1$ and $v_3=D_3=5 \times 10^{-12}$. This hyperviscosity relates to the usual Laplacian viscosity by $v_3=\nu k^4$. Therefore, it corresponds to $\nu \simeq 3 \times 10^{-3}$ (or $\alpha \simeq 1$) at the grid scale $k=\pi/\Delta x$, and $\nu \simeq 10^{-11}$ ($\alpha \simeq 4 \times 10^{-9}$) at the largest scale of the box. Here $\alpha=\nu\Omega_K c_s^{-2}$ is the usual Shakura-Sunyaev viscosity parameter (Shakura & Sunyaev 1973) and Ω_K the Keplerian frequency.

The simulations were done with the Pencil Code¹ in Cartesian and cylindrical geometry. We write Cartesian coordinates as (x,y) and cylindrical coordinates as (r,ϕ) .

2.1. Self-gravity

We solve the Poisson equation Eq. (6) using the traditional rapid elliptic solvers with multiple Fast Fourier Transforms. For a single Fourier component $\hat{\Sigma}$ the solution to Eq. (6) is

$$\hat{\Phi} = -\frac{2\pi G \hat{\Sigma}}{|k|}, \quad (11)$$

where $\mathbf{k} = (k_x, k_y)$ is the in-plane wavenumber and the hat denotes Fourier transformed quantities. The potential is then found by taking the inverse transform to real space.

As the Fourier transform assumes periodic boundaries, the potential derived is as if the disk was accompanied by mirror images of itself, the gravity of these images influencing the motion of the fluid. To reduce this problem, we expand the grid by a factor 2 prior to solving the Poisson equation. In this expanded grid, the mirrors are still present, but they are now located so far away from the regions of interest that no spurious behavior is introduced by the periodic boundaries. We show in Fig. 1a the potential of an exponential disk, typical of galaxies, in which case the analytical solution is well known (Freeman 1970). The deviations are at the percent level, as seen in Fig. 1b.

The gravitational potential of the swarm of particles is found by the same method outlined above. The surface density of particles is assigned to the mesh using the Triangular Shaped Cloud (TSC) scheme (Hockney & Eastwood 1981, Youdin & Johansen 2007), whereby the influence of a particle is assigned to three grid points in each direction. After finding the potential, the acceleration is interpolated back to the position of the particles, using the same TSC scheme, to avoid self-acceleration (Johansen et al. 2007).

Analytical prediction and numerical solution for the potential of a single particle are compared in Fig. 1c. Deviations occur only near the particle position, as expected for a particle-mesh method. Fig. 1d shows the gravitational acceleration generated by this potential. The agreement is excellent and the particle does not experience any self-acceleration.

2.2. Drag force

Solid particles and gas exchange momentum due to interactions that happen at the surface of the solid body. The many processes that can occur are generally described by the collective name of “drag” or “friction”. The drag regimes are controlled by the mean free path λ of the gas, which can be expressed in terms of the Knudsen number of the flow past the particle $\text{Kn} = \lambda/(2a_\bullet)$. High Knudsen numbers correspond to free molecular flow, or Epstein regime. Stokes drag applies at low Knudsen numbers. In this section we describe our numerical implementation of drag forces in the Pencil Code for general values of Kn. We use the formula of Woitke & Helling (2003; see also Paardekooper 2007), which interpolates between Epstein and Stokes regimes

$$C_D = \frac{9\text{Kn}^2 C_D^{\text{Eps}} + C_D^{\text{Stk}}}{(3\text{Kn} + 1)^2}. \quad (12)$$

where C_D^{Eps} and C_D^{Stk} are the coefficients of Epstein and Stokes drag, respectively. They read

$$C_D^{\text{Eps}} \approx 2 \left(1 + \frac{128}{9\pi \text{Ma}^2} \right)^{1/2} \quad (13)$$

$$C_D^{\text{Stk}} = \begin{cases} 24 \text{Re}^{-1} + 3.6 \text{Re}^{-0.313} & ; \text{Re} \leq 500; \\ 9.5 \times 10^{-5} \text{Re}^{1.397} & ; 500 < \text{Re} \leq 1500; \\ 2.61 & ; \text{Re} > 1500. \end{cases} \quad (14)$$

where $\text{Ma} = |\Delta v|/c_s$ is the Mach number, $\text{Re} = 2a_\bullet \rho_g |\Delta v|/\mu$ is the Reynolds number of the flow past the particle, and $\mu = \sqrt{8/\pi} \rho_g c_s \lambda/3$ is the kinematic viscosity of the gas.

The approximation for Epstein drag (Kwok 1975) connects regimes of low and high Mach number ($\text{Ma} = |\Delta v|/c_s$) to good accuracy, and is more numerically friendly than the general case (Baines et al. 1965). The piece-wise function for the Stokes regime are empirical corrections to Stokes law ($C_D = 24\text{Re}^{-1}$), which only applies for low Reynolds numbers.

Fig. 2a shows the value of this coefficient in the plane of Mach and Knudsen numbers. As stressed by Woitke & Helling (2003), at intermediate Knudsen numbers, the true friction force yields smaller values than in both limiting cases, which is illustrated in Fig. 2b. Another measurement of the strength of the drag force is the friction time τ_f , defined as the inverse of the quantity in parentheses in Eq. (8)

$$\tau_f = \frac{4\lambda\rho_\bullet}{3\rho_g C_D c_s} \frac{1}{\text{MaKn}}. \quad (15)$$

The drag acceleration can then be cast in the compact form

$$f_d = -\frac{1}{\tau_f} \Delta v_p. \quad (16)$$

2.3. Initial conditions

We use a Cartesian box ranging $x, y \in [-2.0, 2.0]r_0$, with resolution 256×256 . The small extent in radius is justified because we want to understand what is happening at the vicinity of the planet’s orbit at r_0 and the gap it opens. The

¹ See <http://www.nordita.org/software/pencil-code>

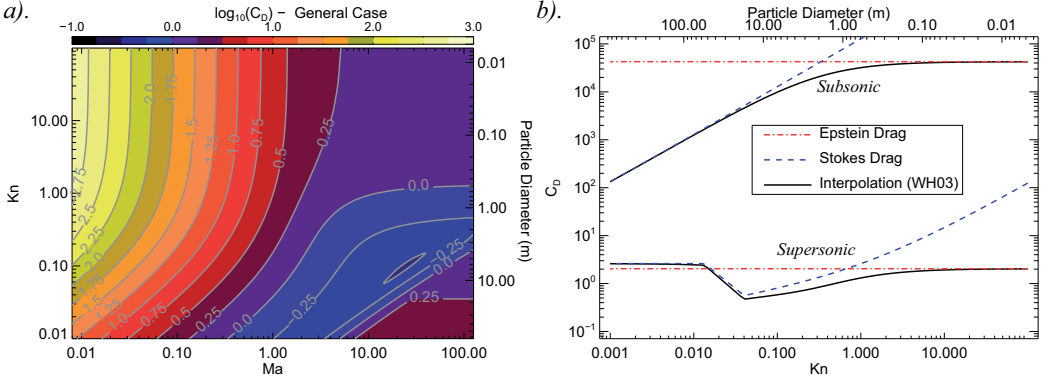


Fig. 2. The interpolated general drag coefficients in *a*). the plane of Knudsen and Mach numbers. In *b*). we show two slices at subsonic and supersonic motion, comparing to the respective predictions of Epstein and Stokes drag. For particles up to 10 centimeters, Epstein drag does not deviate much from the general (interpolated) coefficient. Pure Stokes drag starts to apply only beyond 10 meters.

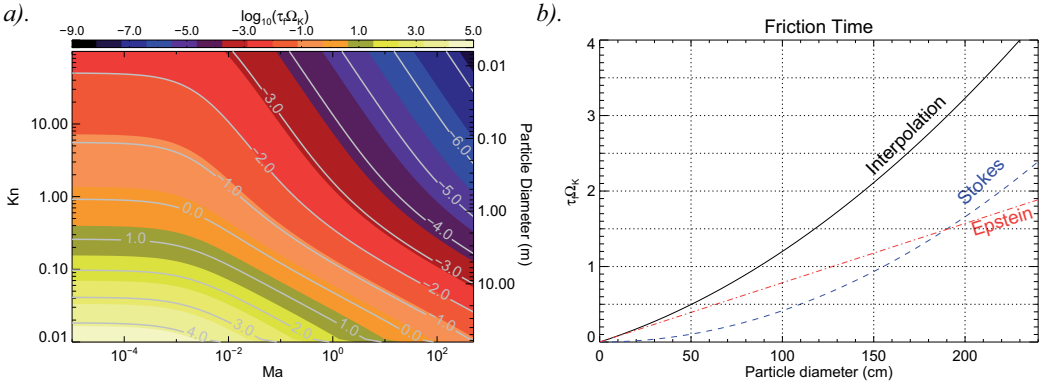


Fig. 3. *a*). The drag coefficient translated to friction times for our choice of numerical parameters at Jupiter’s orbital position. In *b*). we show a slice of *a*). at subsonic regime, where the predictions of Epstein and Stokes law are shown for comparison. The general drag yields more loose coupling than both limiting cases.

density profile follows the power law $\Sigma_g = \Sigma_0 r^{-0.5}$ and the sound speed is also set as a power law $c_s = c_{s0} r^{-0.5}$.

The gravitational potential is then computed via the Poisson solver and the initial velocity profile is set to match the condition of centrifugal equilibrium

$$\phi^2 = \Omega_K^2 + \frac{1}{r} \left[\frac{1}{\Sigma_g} \frac{\partial P}{\partial r} + \frac{\partial \Phi_{sg}}{\partial r} \right] \quad (17)$$

The planet is placed initially at $(r, \phi) = (r_0, 0)$, and the star at $(r, \phi) = (0, \pi)$. To avoid giving the gas and the particles too much impulse when the planet is introduced in the unperturbed disk, we ramp its mass up from 0 to its final mass in five orbits, in the way described in de Val-Borro et al. (2006). We computed simulations with companion mass ratios $q=10^{-3}$ (Jupiter) and $q=10^{-4}$ (“Neptune”). The quotation marks are used because calling this mass ratio “Neptune” is a jargon, since the actual mass of the planet

is the equivalent to $q=5 \times 10^{-5}$. The Earth has a mass ratio of $q=3 \times 10^{-6}$.

We use units such that $r_0 = \Sigma_0 = GM_\odot = 1$. We choose $c_{s0} = 0.05$ and a Toomre Q parameter of 30 at the position of the planet, so the gas there is stable against gravitational instability. Assuming that r_0 is the position of Jupiter (5.2 AU) and that $\Sigma_0 = 300 \text{ g cm}^{-2}$, the disk has $10^{-2} M_\odot$ of gas within the modeled range.

For the solids, we use 10^5 Lagrangian numerical particles, and the interstellar solids-to-gas ratio of 10^{-2} . Each numerical particle therefore is a super-particle containing $10^{-9} M_\odot \simeq 3 \times 10^{-2} M_{\text{Moon}}$ of material. The super-particle formalism considers that each numerical particle is an ensemble of a large number of individual smaller physical particles of radius a_\bullet . These particles share the same position and velocity, interacting gravitationally by their collective mass (the mass of the super-particle). The aerodynamics, however, is controlled by the radius a_\bullet , which in

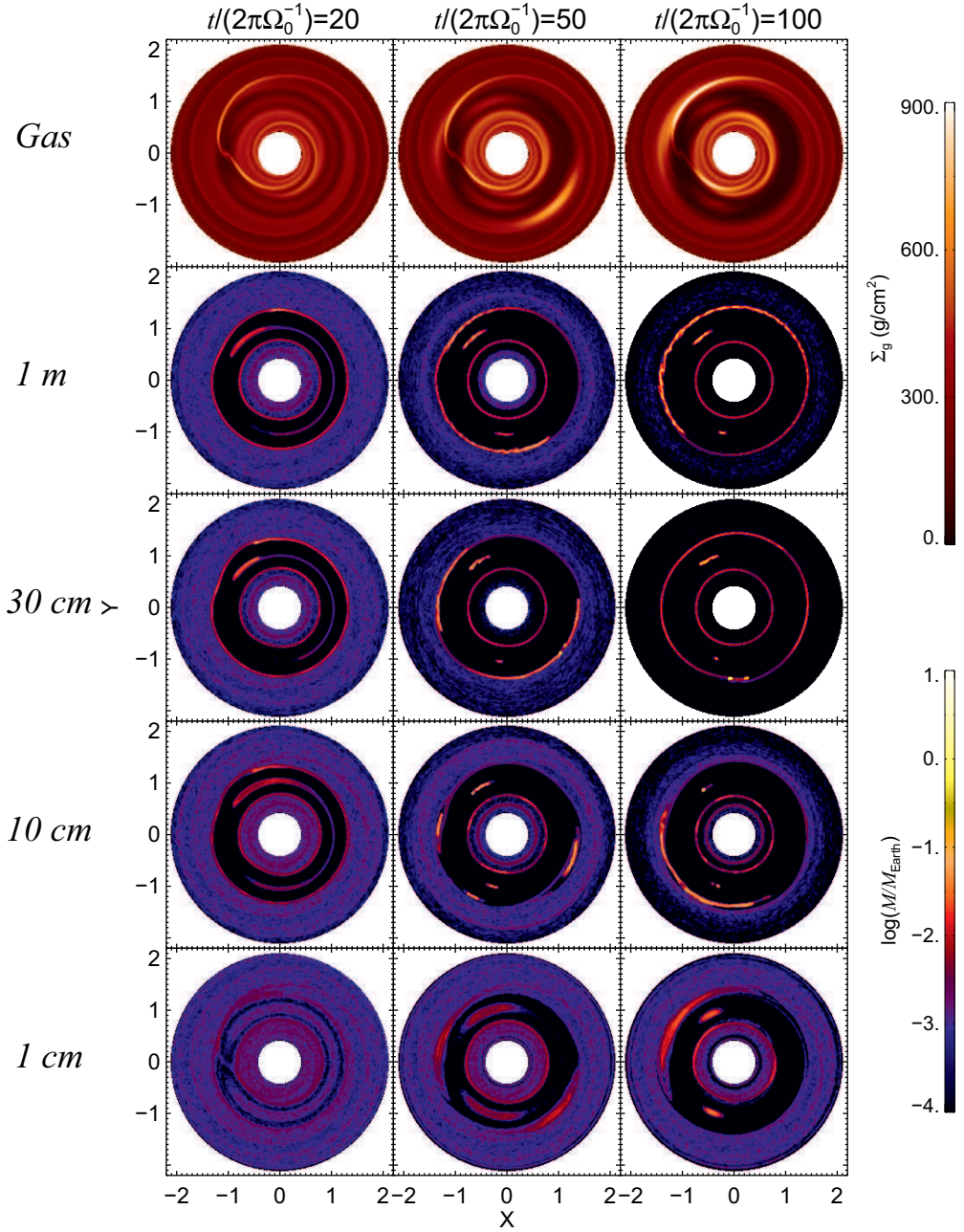


Fig. 4. Snapshots of the gas and solid phase of the disk for several single particle species runs, for a perturber of Jupiter’s mass. At the end of the simulations at 100 orbits, the swarms of particles in the L4 and L5 points of the $a_*=1$ m run remain unbound. The 10 cm and 30 cm particles underwent collapse at the Lagrangian points, with the fragmentation being more efficient for the 10 cm particles than for the 30 cm ones. In the $a_*=10$ cm case, the particles underwent collapse in both Lagrangian points, L5 harboring a $2.6 M_{\oplus}$ planet, L4 a $0.6 M_{\oplus}$. At the edges of the gap, even $a_*=1$ cm particles are trapped within the vortices. In the $a_*=10$ cm run, the effect of the anti-cyclonic motion lead to a final collapsed mass of $0.3 M_{\oplus}$. When the vortices merge into a single giant vortex, the $a_*=30$ cm particles are seen to have undergone runaway growth of solids, reaching $17 M_{\oplus}$.

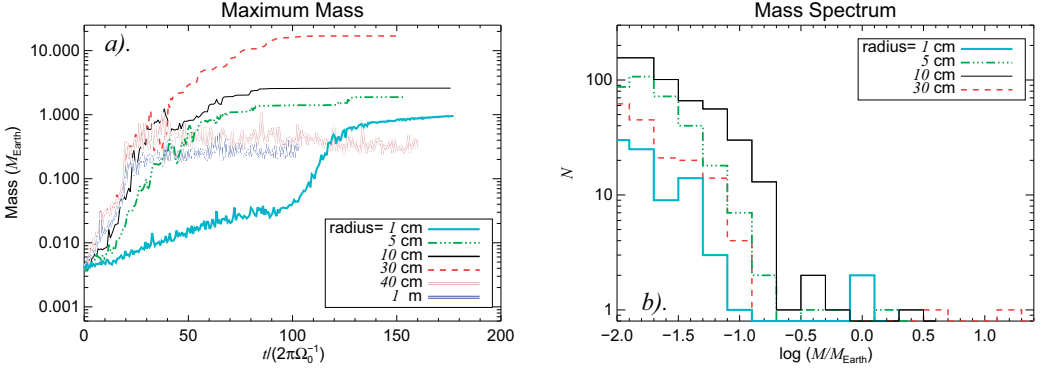


Fig. 5. *a).* Time evolution of the maximum concentration of mass for different particle radii. From 40 cm onwards, the drag force is too weak to provide enough damping for collapse. For 1 cm to 30 cm radii, gravitational collapse occurs forming Earth-mass planets. For 5 cm, a $2 M_{\oplus}$ planet is formed. For 10 cm, the final maximum collapsed mass is around $3 M_{\oplus}$. The particles of 30 cm radius collapse in a planet as massive as 17 Earths. The $a_{\bullet}=1$ cm are subject to strong coupling and undergo growth on the timescale of depletion of gas in the Lagrangian points. This leads to a delay in the collapse, taking twice the time it took in the 5-30 cm case. The final mass is $1 M_{\oplus}$.

b). The mass spectrum in the end of the simulations. Along with the super-Earths formed with the 30 cm, 10 cm and 5 cm particles, dozens of Mars sized and hundreds of Moon sized objects were also formed. The two symmetric Trojan Earths in the 1 cm case are apparent. The runs with particles of $a_{\bullet}=40$ cm and $a_{\bullet}=1$ m were excluded for clarity.

turn means that there is free space between the physical particles, so that each of them exposes its whole surface area to the nebular gas.

We stress that the mass resolution of solids in the models presented in this paper is not much greater than that used by Beaugé et al. (2007). The main difference between this study and theirs lies in the global character of our study; the greater number of numerical particles; and the radius a_{\bullet} of the individual pebbles and boulders, which translates into a much stronger drag force.

We survey several particle radii. The dimensionless friction time as a function of particle size is found by plugging Eq. (12) into Eq. (15), which yields

$$T_f = \tau_f \Omega_K = \frac{\sqrt{32\pi} \lambda \rho_{\bullet}}{\text{Kn}' \text{Ma} \Sigma_g} \frac{(\text{Kn}' + 1)^2}{(\text{Kn}'^2 C_D^{\text{Eps}} + C_D^{\text{Stk}})} \quad (18)$$

where we already substituted $\rho_g = \Sigma_g / (\sqrt{2\pi} H)$. Here, $H = c_s / \Omega_K$ is the pressure scale height. We consider that the particles have an internal density $\rho_{\bullet} = 3 \text{ g cm}^{-3}$. The mean free path λ is

$$\lambda = \frac{\mu_{\text{mol}}}{\rho_g \sigma_{\text{mol}}} \quad (19)$$

where $\mu_{\text{mol}} = 3.9 \times 10^{-24} \text{ g}$ is the mean molecular weight of a 5:1 H_2 -He mixture, and $\sigma_{\text{mol}} = 2 \times 10^{-15} \text{ cm}^2$ is the cross section of molecular hydrogen. For our densities and sound speed, it corresponds to 20 cm at the inner radius $r=0.3$, and to 1.3 m at the outer radius $r=2.0$.

The result of Eq. (18) for our choice of parameters (at the position of Jupiter's orbit) is shown in Fig. 3a for the grid of Knudsen and Mach numbers. Fig. 3b shows a slice of the grid at the subsonic regime. For particle of 1m di-

ameter, the coupling due to Eq. (18) is 50% looser than predicted by Epstein law. A factor 2 in the friction time is seen at 2m diameter between Eq. (18) and the Stokes law.

The particles are initialized as to yield a surface density following the same power law as the gas density, and their velocities are initialized to the Keplerian value.

We use reflective boundaries and damp waves in the way described in de Val-Borro et al. (2006). Particles are removed from the simulation if they cross the inner boundary or if they approach the giant planet by less than $1/5$ of its Hill's radius.

3. Simulations with single particle species

In Fig. 4 we show the time evolution of the disk under the influence of a $q=10^{-3}$ companion, for different particle radii. Each run has only one particle size, but as the gas density does not change significantly between the runs, we just show the gas for the $a_{\bullet}=1$ cm case.

3.1. Collapse in the Lagrangian points L4 and L5

As the planet opens a gap in the gas, the particles also move out of the co-rotational region, in the same manner seen in Paardekooper (2007) and Fouchet et al. (2007). The solids at the border of the gap are expelled and those in the immediate vicinity of the planet are accreted. The particles inside the co-rotational region librate in horseshoe orbits. The stable leading (L4) and trailing (L5) Lagrangian points retain high gas densities even after the planet has carved a deeper gas gap in its orbit, which has a beneficial effect for the particle concentration. Due to the presence of high gas densities, the Lagrangian islands are not only a region of convergence of streamlines, but also a region with higher pressure than its surroundings. The drag force

therefore forces the particles into them, also damping the motion caused by eventual perturbations that could otherwise make a particle drift away from it. These effects combined make L4 and L5 highly stable points in the motion of a solid particle.

At 20 orbits, an asymmetry is seen in the particle concentration between L4 and L5, as the trailing Lagrangian point is more efficient in trapping than the leading one. The 10 cm, 30 cm and 1 m particles achieve high concentrations in the vicinity of L5, while experiencing depletion in L4. The 1 cm particles are too coupled to the gas to be affected by particle-gas drift.

At 50 orbits, the concentration in the Lagrangian points has increased by two orders of magnitude relative to the initial condition in the 10 cm, 30 cm and 1 m runs. The particles of 10 cm and 1 m still present an azimuthally extended cloud of material in L4 and L5, but the particles of 30 cm radii have already concentrated into a small swarm spanning but a few grid cells. Inspection of the snapshot reveals that the maximum mass in this swarm is of $0.03 M_{\oplus}$. The L4 concentration is more extended, but the maximum density is greater, achieving $0.25 M_{\oplus}$, already exceeding the mass of planet Mars ($0.1 M_{\oplus}$).

At the end of the simulation at 100 orbits, the swarms of particles in the L4 and L5 points of the $a_{\bullet}=1$ m run remain unbound. We ran for additional 50 orbits, but no progress in the maximum mass was seen. If collapse happens, it requires timescales longer than 150 orbits. The total mass in L4 is $0.29 M_{\oplus}$, peaking at 0.05. The L5 point has $1.9 M_{\oplus}$ in total, with maximum mass concentration of $0.3 M_{\oplus}$. The 10 cm and 30 cm particles underwent collapse at the Lagrangian points, with the gravitational fragmentation being more efficient for the 10 cm particles than for the 30 cm ones. For the $a_{\bullet}=30$ cm case, what appears in Fig. 4 as a single clump at L4 has a mass of $0.18 M_{\oplus}$. The L5 point is still azimuthally extended, with a total mass of $2.5 M_{\oplus}$ but maximum concentration of only $0.27 M_{\oplus}$ by the end of the simulation.

The $a_{\bullet}=10$ cm particles underwent collapse in both Lagrangian points, L5 harboring a $2.6 M_{\oplus}$ planet, L4 a $0.6 M_{\oplus}$. In Fig. 5a we plot the time evolution of the maximum mass of solids for different runs. In addition to the runs showed in Fig. 4 we add runs with particles of 5 cm and 40 cm radii. Collapse in the Lagrangian points occurs for the 5 cm case as well, forming a planet of $2 M_{\oplus}$. In this figure, the difference between a run where collapse occurred and a run where collapse did not occur is readily apparent by the behavior of the time-series. The non-collapsed ones are very noisy at late times, as the number of particles in a cell fluctuates up and down. When collapse is achieved, the maximum mass stays constant unless more mass is accreted. This gives the time series a ladder-like appearance, as seen in the figure for the 5, 10, and 30 cm cases. Collapse is hindered for $a_{\bullet}=40$ cm onwards.

The 1 cm particles present an interesting behavior. They are so strongly coupled to the gas that their collapse does not occur at the same time-scale, as seen from Fig. 5a. Instead, as Fig. 4 evidences, it occurs on the timescale of depletion of gas in the tadpole orbits. As the gap is cleared and its depth increases, the gas clouds in the Lagrangian islands shrink in size. As the particle are strongly coupled, they are forced to concentrate as the cloud shrinks, eventually achieving high densities. As the time series of Fig. 5

shows, after 100 orbits the steady increase due to gas clearing gives place to a runaway growth that lasts for about 20 orbits. In the end, one gravitationally bound planet encircling one Earth mass of solids - purely out of 1 cm sized pebbles -, is formed in each stable Lagrangian point.

3.2. Collapse at the gap edge vortices

Concurrently, at the edges of the gap, the considerable density gradient resulting from the gap opening process excites the RWI, leading to a large generation of potential vorticity. At fifty orbits, two vortices are seen to have been excited by the planet at the outer edge of the gap, seen in Fig. 4 at 5 and 10 o'clock. The effect of these vortices in the motion of the solids can be readily seen in the $a_{\bullet}=1$ cm run, as even for these tightly coupled particles, the concentration reaches an order of magnitude higher than in the immediate surroundings.

In the $a_{\bullet}=10$ cm run, as the particles are more loosely coupled to the gas, the effect of the anti-cyclonic motion is better appreciated. The particles are forced in spiral trajectories towards the center of the vortices, raising the density of solids by another order of magnitude when compared to the $a_{\bullet}=1$ cm particles.

In the $a_{\bullet}=30$ cm and $a_{\bullet}=1$ m runs, the coupling is too loose to form the extended structure seen for the $a_{\bullet}=1$ cm and 10 cm particles. However, the looseness is a benefit as long as the goal is to increase the concentration of solids. As the coupling weakens, the particles are not forced away from the center, and concentrate more efficiently. A massive clump of particles is seen in the 4 o'clock vortex in the $a_{\bullet}=30$ cm run, that already concentrates $2 M_{\oplus}$ of solid material. High particle concentration is also seen for the $a_{\bullet}=1$ m particles, but they do not seem to get dense enough to achieve gravitational collapse. Instead, they form a very azimuthally extended belt of particles at the outer and inner edge. No collapse is seen at the inner edge of the gap in any of the runs. At 100 orbits, the vortices have merged into a single giant vortex. Inside it, in the 30 cm run, the collapsed mass underwent runaway growth of solids, reaching $17 M_{\oplus}$. The 10 cm particles have a maximum mass in the vortex of $0.3 M_{\oplus}$. The 1 m particles show a similar maximum mass, of $0.25 M_{\oplus}$. The high mass achieved in the 30 cm run is quite likely overestimated, since it is seen that the efficient and unimpeded particle drift had the effect of feeding this radial region with virtually all particles present in the simulation. Such a situation may be made quite different in a more realistic case, where particle drift is stalled by turbulence, for instance.

In Fig. 5b, we show the mass spectrum at the end of the different simulations. In addition to the super-Earths, two planets in the $0.5-0.8 M_{\oplus}$ range were formed out of 5 cm particles, and other two in the $0.3-0.5$ range with the 30 cm particles. Dozens of Mars-sized planets in the $0.08-0.3 M_{\oplus}$ range, along with hundreds of smaller Moon-sized objects, were also formed in all simulations.

4. A spectrum of particle sizes - segregation and the counter-intuitive role of self-gravity

To understand the effect of self-gravity in the runs, we perform a control run with only gas drag. To diminish the computational time, we include in this run a spec-

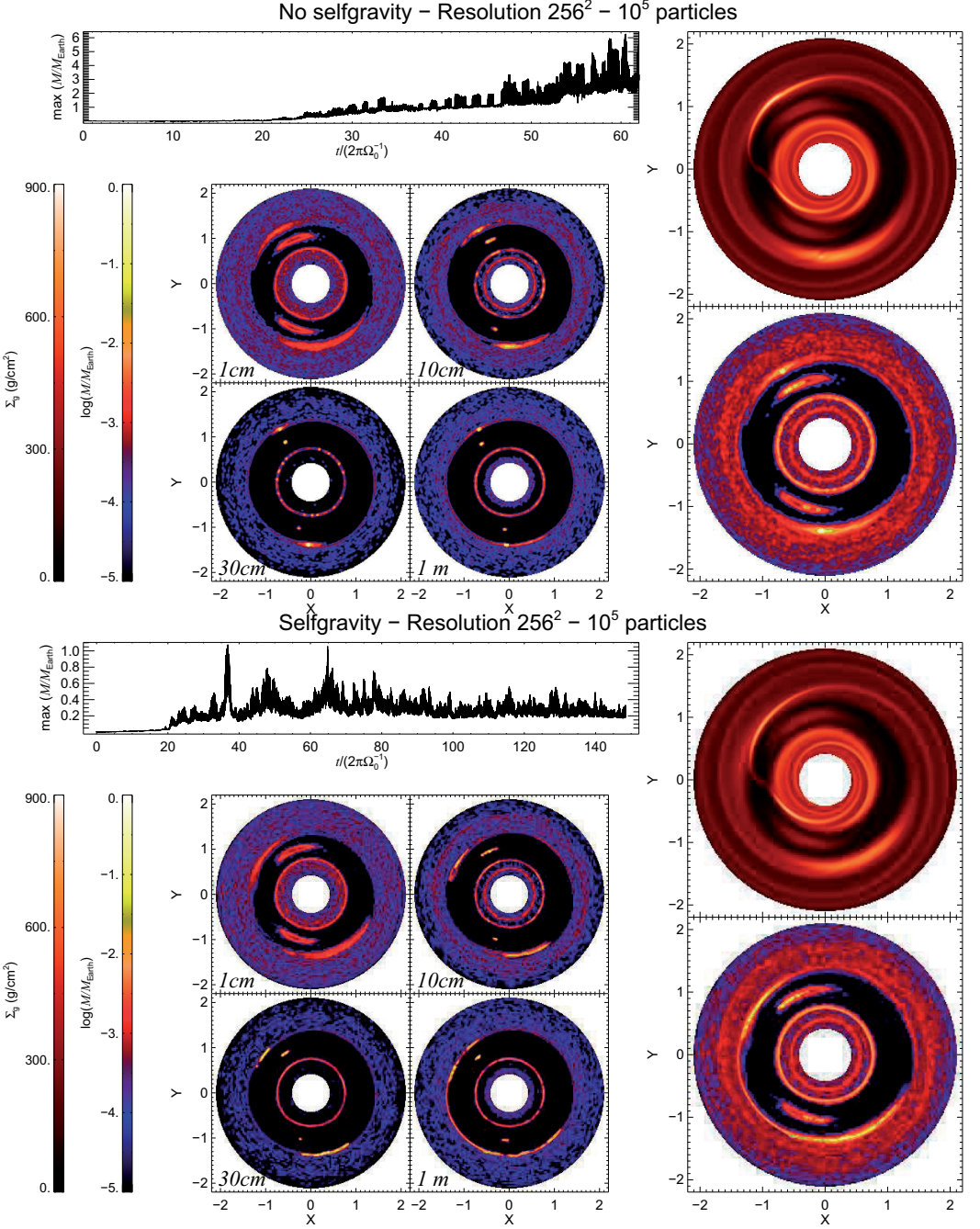


Fig. 6. Comparison between the runs with resolution 256^2 , 10^5 particles and multiple particle species, with and without self-gravity (upper and lower panels, respectively). Counter-intuitively, self-gravity is seen to work against collapse as in the second run the maximum mass is never high enough to allow it. In the presence of self-gravity, the tadpole orbits are modified, and gas tides from the massive vortices can be disruptive for planets forming within them. The motion of the particles inside the vortices are also modified in the presence of self-gravity. Notice in particular how the 30 cm and 1 m particles are spatially split in the vortex at 10 o'clock, near L5. Collapse proceeds only if the grid resolution is refined (see text and Fig. 7.)

trum of particles radii, including four species: 5, 10, 30, and 100 cm. Each particle species is represented by 1/4 of the total number of particles. To compare with this non-selfgravitating run, we also compute a self-gravitating run with a size spectrum. These runs not only shed light onto the role of self-gravity, but can also discern the possible artificial effects introduced by the single-species approximation used by us so far.

4.1. Excluding self-gravity: gas drag alone assembles super-Earths

In Fig. 6a we show the time evolution of the maximum mass in the non-selfgravitating run, along with the disk disappearance in the gas phase as well as the contribution of each particle species in the solids phase. As stated before, the drag provides a very efficient damping, so that the particles of all species except 1 cm concentrate in the L4 and L5 as well as in vortices as early as 50 orbits. The 30 cm and 1 m particles successfully concentrate all its remaining particles that lie in the co-orbital region in a single cell in each of the stable Lagrangian points. The 30 cm particles concentrate with $0.66 M_{\oplus}$ in L5 and 0.04 in L4; the 1 m particles with $0.54 M_{\oplus}$ in L5 and 0.1 in L4. The concentration of 10 cm particles is less efficient, with a maximum concentration of only 25% of the particles in L5 (which nonetheless means $0.13 M_{\oplus}$). Of the 2.1 Earth masses of material in L5, the representation is $0.25 M_{\oplus}$ in 1 cm particles, equal shares of $0.66 M_{\oplus}$ of 10 and 30 cm, and $0.54 M_{\oplus}$ of 1 m particles. The L4 point has $0.55 M_{\oplus}$, distributed 0.23 , 0.17 , 0.04 , and $0.1 M_{\oplus}$ for 1, 10, 30, and 100 cm, respectively.

At the outer edge of the gap, as more material is available, the concentration achieves higher masses. Without self-gravity, the clumps cannot collapse, quickly dispersing and regrouping instead. The maximum mass then is highly fluctuating. After 60 orbits, it has grown to 2 Earth masses, but sporadically reaching as high as $6 M_{\oplus}$, due to gas drag alone. The vortex closest to L5 seen in Fig. 6, a snapshot at 62 orbits, concentrates $2.9 M_{\oplus}$ in the densest cell. The 1 m particles have a maximum concentration of $2.75 M_{\oplus}$, similarly to the 30 cm ones, which peak at $2.3 M_{\oplus}$. It shows that the different particle species preferentially concentrate in different cells, a result of the different drag they feel. The same was seen in the Lagrangian points. The 10 cm is more extended, peaking at $0.1 M_{\oplus}$, a relatively low mass. The leading vortex presents the same qualitative behavior, with a peaking mass of $1.64 M_{\oplus}$, 10, 30, and 100 cm particles showing highest concentration of 0.3, 1.3 and $1.25 M_{\oplus}$, respectively.

4.2. Including self-gravity: collapse hampered

When self-gravity is considered (Fig. 6b), the accretion is seen to be stalled. Sparse episodes of high particle concentration happen at ~ 38 and 65 orbits, reaching maximum masses of $1 M_{\oplus}$, but the collapse of this mass did not occur and the clump quickly dispersed. After a hundred orbits, the maximum mass was still at the $0.2 M_{\oplus}$ level. The L4 point was cleared of particles compared to the non-selfgravitating run, displaying $0.7 M_{\oplus}$ of solid material, more than half of it in 1 cm particles. The highest concentration is of $0.19 M_{\oplus}$, which is mostly represented by 10 cm particles, contributing $0.17 M_{\oplus}$, 100% of the 10 cm particles

remaining in the L4 vicinity. The totality of 30 cm particles in the region are also concentrated in a single cell, but its mass is of only $0.04 M_{\oplus}$, and although spatially close to the $0.17 M_{\oplus}$ clump of $a_{*} = 10$ cm, they are not at the same cell. The 1 m particles still show a slightly extended cloud, with total mass $0.1 M_{\oplus}$, some degrees away from both 10 cm and 30 cm concentrations. The tadpole of particles around L5 is still highly extended spatially. We ran the simulation for additional 50 orbits, but the conditions remained unchanged. In particular, the 3 nearby clumps of different particle species did not collapse into a single body.

There are four reasons as to why collapse did not proceed as in the single species runs. First, the mass of solids was equally split in particles of different size. The 1 cm particles retain 1/4 of the mass, and they concentrate very poorly due to their short friction time. This mass is thus effectively removed from the mass of potentially collapsible bodies. Running for longer times to allow the shrinking Lagrangian gas clouds to squeeze the 1 cm particles into a collapsed body (as occurred in the single species $a_{*} = 1$ cm run after 150 orbits) did not produce the same results, as seen in the time series in the lower panels of Fig. 6.

Second, the gravitational potential of the massive particles acts to de-stabilize the Trojan orbits. As the mass in the Lagrangian points grow, the massless approximation ceases to apply, and the body starts to librate around the otherwise stable point. As the mass increases, the librations increase in amplitude and lead the other particles into close encounters with the giant, that are thence accreted or ejected from the system. In the limiting case that the mass of the Trojan body becomes comparable to the mass of the planet itself, the amplitude of libration would become so high that an encounter between the two would occur. Beaugé et al. (2007) find that a $0.15 M_{\oplus}$ object is enough to de-stabilize the orbits of other bodies in the vicinity of L4.

The effect of this libration in our simulations is evident when comparing Fig. 6a and Fig. 6b. Instead of concentrating at L4 and L5 as the massless particles do, the massive particles display an azimuthally extended structure, evidence of the enhanced librating motion.

Third, the inclusion of gas gravity leads to tides that can be disruptive for a prospective planet (Lyra et al. 2008b). In a simple yet informative approximation, the tides can be taken as proportional to the radius R of the clump and to the gradient of the gravitational acceleration which, by the Poisson equation, is proportional to the local value of the density, $F_T \propto R \rho_g$. For a spherical clump of constant density $\rho_p = 3M_p / (4\pi R^3)$, the self-gravitational pull it exerts on its own surface is $F_G = GM_p / R^2 \propto R \rho_p$. The ratio F_T / F_G is therefore proportional to the gas-to-solids ratio. For a protoplanet forming inside high-pressure regions such as vortices or the Lagrangian clouds, the gas tides can lead to destruction or significant erosion of the forming planets (Lyra et al. 2008b).

Fourth, a common feature of all simulations is that the particles of different radii tend to concentrate in different locations within the tadpole region. This is somewhat similar to the effect of self-gravity. Gas drag taps energy from the Keplerian motion, so the stability conditions on the Lagrangian points are modified. As gas drag depends on radius, the location of the stable points of the 3-body problem with gas drag also depend on particle size. In other

words, the L4 and L5 points of the restricted 3-body problem are defined as points where there is a balance between the gravitational attraction between the 2 massive bodies and the centrifugal force. When including gas drag, a third force comes into play in the particle motion, and the stable points will be displaced accordingly. In general, a particle of a given size will librate about its own particular stationary point. Numerical and analytical investigations by Peale (1993) and Murray (1994) confirm that the location of the stable points is a function of particle radius. Asymmetries between L4 and L5 are also expected from the analytical treatment, which are seen in our simulations as well, with L4 shifting further away than 60° ahead of the planet, while L5 is displaced closer behind it. In some extreme cases, the stable points can vanish altogether. As the drag force increases and L5 approaches the planet, it can merge with the shifted L2 point. L4 experiences the same as it moves further out and merges with the shifted L3 point. Both Murray (1994) and Peale (1993) find a limiting location of 108° ahead of the planet for L4. At this maximum angular separation, the merging with L3 takes place and the leading stationary point disappears. For a $13 M_{\oplus}$ proto-Jupiter, Peale (1993) finds that L4 does not exist for objects smaller than $a_* = 15$ m. L5 is seen to be more stable, but the stable point of a $a_* = 50$ cm particle is expected to lie only a few degrees behind the proto-Jupiter. In this location, they speculate, the wake of the planet (not taken into account in their model) might effectively eliminate L5.

Increasing the mass of the perturber to that of Jupiter's present mass tends to increase stability and to bring L4 and L5 closer to the "classical" locations predicted by the restricted 3-body problem. In a gap homogeneously depleted by 1 order of magnitude relatively to the initial density, the shift for the 10 m particles is less than 2° . However, the analysis of Peale (1993) and Murray (1994) did not consider the presence of higher gas densities in the (classical) Lagrangian points as the gap is cleared. As we see, it has an effect similar to a potential well, keeping the particles around the classical tadpole. As the 1 cm particles have shorter friction time, the gas trap is more efficient, and the prediction of their particular L5 getting too close to the planet, or L4 merging with L3 is avoided as long as a local pressure maximum is present at the classical L4 and L5. The more loosely coupled 1 m particles had their L4 shifted to 90° ahead of the planet, and L5 to 50° behind it.

5. Resolution study

Motivated by the failure of the run just presented above to assemble massive gravitationally bound structures, we explore the effects of particle and grid resolution in our simulations. We first raise the total number of particles to $N_p = 400\,000$, to verify the effect of particle resolution. The mass of the disk is the same, so the mass of an individual super-particle decreases, being now $2.5 \times 10^{-10} M_{\odot} \simeq 7 \times 10^{-3} M_{\text{Moon}}$. This first run has the same grid resolution as used before, 256^2 . The second is twice as fine, 512^2 .

The $N_x \times N_y = 256^2$ and $N_p = 4 \times 10^5$ run does not show major differences when compared to the simulation with same resolution but only 10^5 particles. The same behavior of sparse episodes of high concentrations but never achieving critical densities is seen. At the end of the simu-

lation, the maximum mass is still around only $0.2 M_{\oplus}$. We conclude from this that changing the particle resolution by at least a factor 4 does not change the results significantly.

On the other hand, the situation changes considerably when changing the grid resolution. In the run with $N_x \times N_y = 512^2$ and $N_p = 4 \times 10^5$ (Fig. 7), the maximum mass steadily increases towards $1 M_{\oplus}$ in 30 orbits. Inspection of the snapshots reveals that this high concentration occurs inside the vortices excited in the outer gap. At fifty orbits, the leading vortex shows two planets, one of $1.43 M_{\oplus}$, and a smaller one of $0.38 M_{\oplus}$. Unlike the 256^2 run, the mass peaks of different particles species occur at the same cell, attesting to the boundness of the structures. The first planet is 57.6% composed of 30 cm particles, 35.0% of 10 cm, 6.5% of 1 m and 0.9% of 1 cm particles. The second is 87% composed of 30 cm particles, about equal shares (6.5%) of 10 cm and 1 m particles, with only trace amounts of 1 cm particles.

The trailing vortex also shows two gravitationally bound planets, both of high mass. The most massive one has $3.1 M_{\oplus}$, its composition of 1, 10, 30, and 100 cm particles being 0.2%, 17.9%, 63.0%, and 18.9%, respectively. The other planet is of $1.9 M_{\oplus}$, being constituted by 0.2%, 27.8%, 48.9%, and 23.1% of 1, 10, 30, and 100 cm, respectively.

A common trait of these planets is, therefore, that they are formed by a majority of 30 cm particles, with approximately equal shares of 10 cm and 1 m particles. This is expected, since for our choice of parameters, the 30 cm particles are those for which the drift due to gas drag is maximum. The 1 cm are too well coupled to the gas to contribute significantly to the growth of terrestrial planets inside the vortices. For reasons of load imbalance, we terminated the simulation at 83 orbits, when a large fraction of the computational time was idle and one orbit took 6 hours in 64 processors. The most massive planet had grown to $4.5 M_{\oplus}$ by then. The other planets formed at the outer edge of the gap show masses of 4.36, 4.14, and 0.80 Earth masses.

In Fig. 8a we show the time evolution of the mass of this massive planet. The black solid line represents the maximum mass of solids contained in a single grid cell. The red dashed line marks the maximum mass that is gravitationally bound. We decide for boundness based on two criteria. First we consider the clump defined by the black line, and calculate the center of mass of its particles. The Hill's sphere associated with this mass is drawn, centered on the center of mass. As the Hill's sphere encompasses more/less than a grid cell, particles inside/outside are added/removed from the total mass, and the center of mass and Hill's radius recomputed. The process is iterated until convergence. After the clumps' mass and Hill's radius are defined, we compare the internal velocity dispersion v_{rms} of its constituent particles with the escape velocity of the enclosed mass, defined at the Hill's radius. If $v_{\text{rms}} < v_{\text{esc}}$, we consider that the cluster of particles is gravitationally bound. As seen in Fig. 8b, the internal velocities are usually lower than 10 m s^{-1} . We also plot the maximum speed and escape velocity of the planet (defined at the Hill's radius). The maximum speed is usually greater than the escape velocity, which means that not all particles present in the cluster are actually bound, and the planet (as we define it) can lose mass during the accretion pro-

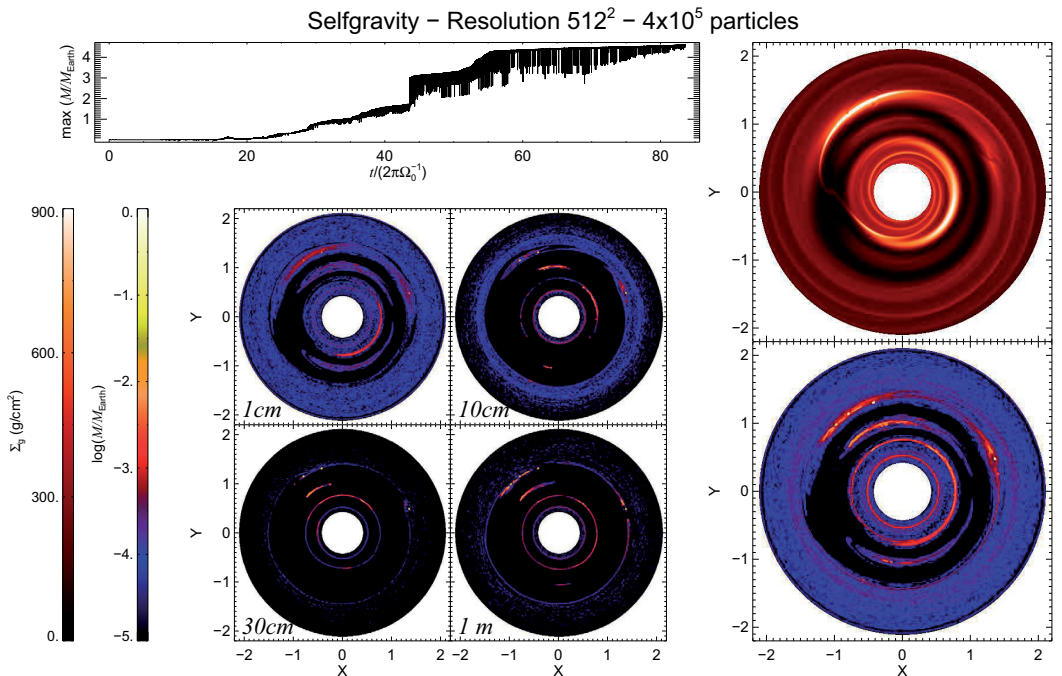


Fig. 7. Results of the high-resolution run (512^2 grid points and 4×10^5 particles) with multiple particle species. Four rocky planets form at the outer edge of the gap, the most massive one with $4.5 M_{\oplus}$. They are easily spotted in the solids plot as very bright small dots. A movie of this simulation can be found at <http://www.astro.uu.se/~wlyra/planet.html>

cess. However, the low v_{rms} compared to v_{esc} attests that the vast majority of the particles is gravitationally bound.

At the end of the simulation, the gas in co-rotation is still spread over the whole horseshoe region, so a massive loss of particle from L4 is observed. The same process was seen in the other runs, with single and/or multiple species. But in this case, the effect is more severe as the L4 point of the 30 cm particles disappeared. At the end of the simulation, a small cloud of $2 M_{\text{Mars}}$ of 10 cm particles is observed in the tadpole region around L4, peaking at a maximum mass of $3.5 M_{\text{Moon}}$. L5 presents $3.3 M_{\oplus}$ of solid material, but still in extended clouds. The boundness analysis shows that these clouds are fragmented into ≈ 20 sub-Mars sized bodies of mass between 1-5 lunar masses.

6. Neptune-mass perturber

In this section, we consider the case of a giant planet perturber of mass ratio $q=10^{-4}$, dubbed “Neptune”. This case is important to assess since, according to our current understanding, a forming gas giant is expected to spend a long time (of the order of millions of years) with a mass similar to this value - corresponding to the phase II of the model of Pollack et al. (1996). Even models that predict a faster transition from Neptune to Jupiter mass (Klahr & Bodenheimer, 2006) still predict timescales of ($\sim 10^5$ years). Therefore, when the perturber has achieved Jupiter’s mass, the state of the solids subdisk should be

more similar to the state left by a Neptune-mass perturber than to the unperturbed disk of particles we have used so far.

We observe that when the perturber has a smaller mass, a more pronounced asymmetry between the L4 and L5 point is observed, as expected from the analysis of Peale (1993) and Murray (1994). The 1 m and 30 cm sized particles experience more depletion, with their L4 point having vanished altogether and the L5 shifted to but a few degrees behind the planet (Fig. 9). The 10 cm particles also experience depletion but not as severe as the larger particles. The 1 cm particles are well coupled and remain in co-rotation as no deep gas gap is carved.

The shifted L5 points of the 30 cm and 1 m particles concentrate about only $0.01 M_{\oplus}$ of solids, each. Nevertheless, a Trojan planet of $0.16 M_{\oplus}$ was formed at the vicinity of L5, its bulk consisting of 99.4% of particles of 10 cm radii. A second bound clump of $0.09 M_{\oplus}$, also consists of a large majority of 10 cm particles, is observed at the vicinity of L5, 0.39 AU away from the former.

We conclude that a Neptune Trojan can only be formed with a very narrow range of particle species around 10 cm, at least for our choice of parameters. A simulation at high-resolution (with 512^2 grid points and 4×10^5 particles) showed the same behavior for the first 100 orbits.

A distinct difference from the Neptune runs when compared to the Jupiter runs is that there are no visible vortices formed at the edge of the gas gap, even when run-

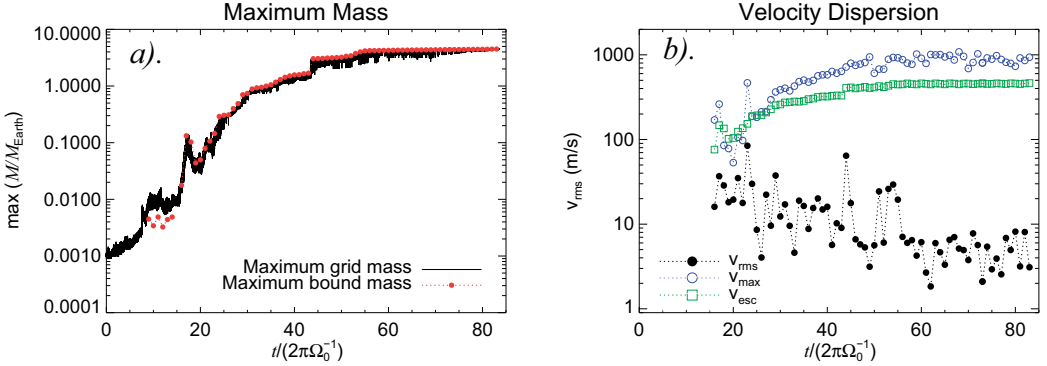


Fig. 8. Time-series of the most massive clump present in Fig. 7. *a).* The maximum mass in a grid cell and the maximum bound mass. Even though the Hill’s radius exceeds the dimension of a grid cell, the planet has most (or all) of its mass within a single cell. This is evidence of subgrid compactness.

b). The internal velocity dispersion v_{rms} of the planet, compared with its escape velocity v_{esc} defined at the Hill’s radius. Throughout most of the simulation, v_{rms} is below 10 m s^{-1} . The maximum internal speed is plotted for comparison. It usually exceeds the escape velocity, so some particles are not bound to the planet.

ning as long as 200 orbits. This was unexpected, since the gap is shallow when compared to the one carved by the Jovian tides, but deep enough to excite the RWI. Therefore, there is no clear reason as to why vortices do not form. The solution was hinted by de Val-Borro et al. (2007), who notice the same feature. They identify it as being due to the Cartesian grid, as vortices are seen in a cylindrical run. Furthermore, in de Val-Borro et al. (2006), where several codes were compared in the specific problem of a planet opening a gas gap, vortices are seen in some of the inviscid runs with cylindrical codes. Indeed, we ran simulations with the cylindrical version of Pencil, and some weak vortices were excited after 100 orbits. This is readily understandable in view of the fact that for a flow with cylindrical symmetry, a Cartesian grid has exaggerated numerical dissipation for the same resolution ($r\Delta\phi = \Delta y$). To make matters worse, the azimuthal modes responsible for the RWI, are more coarsely resolved in a Cartesian grid. We are drawn to the conclusion that the combination of both drawbacks quenched the growth of the unstable modes of the RWI in the case of the shallow Neptune gap.

In the cylindrical run at two hundred orbits, the vortices had trapped large amounts of particles, with a few cells achieving masses above $0.1 M_{\oplus}$. However, the cylindrical Poisson solver - which relies on discretization of the analytical potential based on continuous Hankel transforms (Toomre 1963, Binney & Tremaine, 1987) - does not ensure that a particle is free of self-acceleration. Therefore we do not trust its accuracy to draw definitive conclusions on the possibility or impossibility of gravitational collapse in the cylindrical runs.

We stress that the expulsion of particle of radii $>10 \text{ cm}$ from the co-rotational region during the Neptune-phase does not imply that these particles will not be present when the giant planet achieves Jupiter’s mass. As the planet grows in mass, the width of the gas gap increases. This has the positive effect of feeding the co-rotational region with fresh larger particles from the outer and inner

edge of the narrow and shallow gap carved during phase II. Moreover, it is reasonable to suspect that growth by coagulation should be continuously replenishing the population of these particles, as the pebbles sweep up dust grains that remain in the co-rotational region.

We show in Fig. 10 the mass spectrum at the end of the Neptune simulation, comparing it with the one from the Jupiter case (Sect. 5). In addition to the two Trojans, the Neptune run also shows a smaller planet, of mass 4.6 times that of the Moon, which was formed at the outer edge of the gap. The outer edge also displays hundreds of other Moon-sized objects. In the Jupiter case the three super-Earths are conspicuous in the plot. The smaller $0.80 M_{\oplus}$ planet is also visible. Of the seven lunar-sized bodies in the bin centered at $\log(M/M_{\oplus}) = -1.4$ ($M \approx 4M_{\text{Moon}}$), three are in the co-rotational region. Their masses are 4.8, 4.3, and $4.2 M_{\text{Moon}}$. Other sixteen lunar-sized bodies in the mass range $1-4M_{\text{Moon}}$ are also observed in the co-rotational region. As more mass is trapped in the bigger planets, the Jupiter run shows a smaller number of Moon-mass gravitationally bound clumps when compared to the Neptune case.

7. Summary and conclusions

We have undertaken simulations of low mass self-gravitating disks with gas and solids. While the gas is gravitationally stable ($Q \approx 30$), the solid phase undergoes rapid collapse in the Lagrangian points of a giant planet. A companion with the mass of Jupiter (mass ratio $q=10^{-3}$) produces Earth-mass Trojan planets for particle radii up to $a_* = 30 \text{ cm}$. The particles of $a_* = 40 \text{ cm}$ and 1 m remained unbound. The 10 cm and 30 cm particles underwent collapse at the Lagrangian points, with the gravitational fragmentation being more efficient for the 10 cm particles than for the 30 cm ones. In the $a_* = 10 \text{ cm}$ case, the particles underwent collapse in both Lagrangian points, L5 harboring a $2.6 M_{\oplus}$ planet, L4 a $0.6 M_{\oplus}$. The 30 cm particles show only

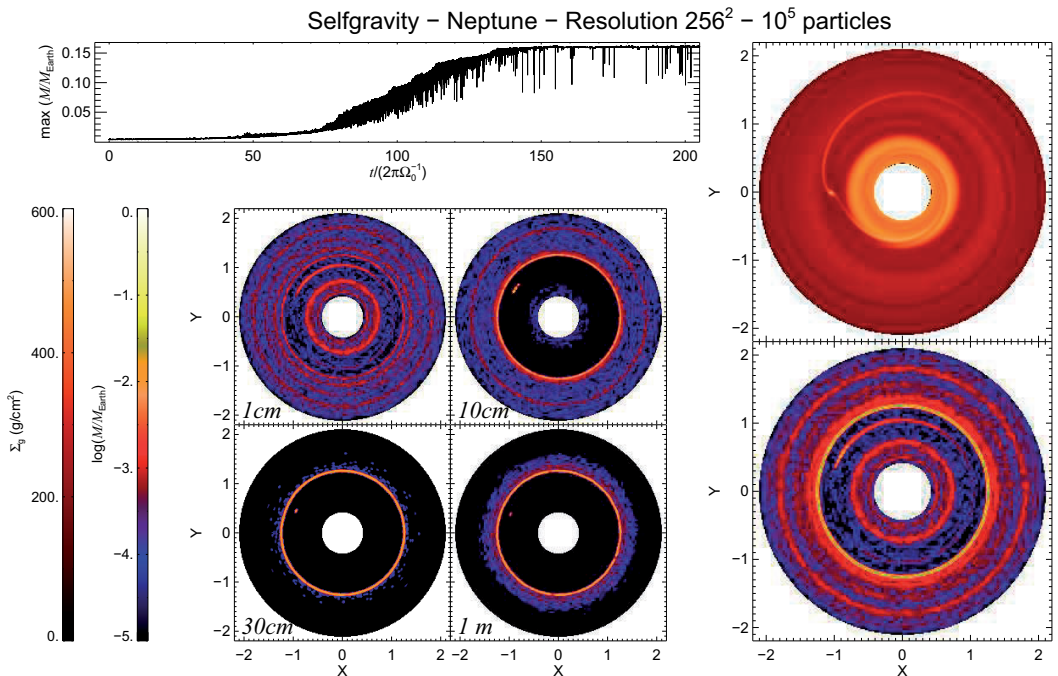


Fig. 9. Same as Fig. 7 but for a Neptune-mass perturber. The Lagrangian point L4 has vanished and the L5 shifted to a position much nearer to the planet than in the Jupiter case. The wake of the planet does not destroy the stability of the shifted L5, and a Trojan of $1.6 M_{\text{Mars}}$ was formed.

a low mass $0.1 M_{\oplus}$ at L4, and an extended unbound swarm at L5. Particles of 5 cm radius assembled in Trojans of $1.8 M_{\oplus}$, 0.8 and $0.5 M_{\oplus}$. The 1 cm particles present an interesting behavior. As they are too well coupled to the gas, their density increase primarily not due to their mutual attraction, but due to the shrinking of the gas cloud retained in the tadpole region. Their collapse therefore occurs on the timescale of gas depletion in the L4 and L5 points. Two symmetric Trojans of $1 M_{\oplus}$ are formed out of particles of $a_{\bullet}=1$ cm after 150 orbits. The boundness of the formed planets is confirmed as the internal velocities are much lower than the escape velocity.

Fast rocky planet formation also occurs in the vortices the giant planets induce at the edges of the gas gaps they open. In this case, the 30 cm particles set the record of highest concentration, by collapsing into a super-Earth encircling as much as 17 Earth masses. The mass is likely to be overestimated, since the vortex captured virtually all of the influx of particles from the outer disk, but this result nonetheless illustrates that the efficiency of vortex trapping for particles this size is superb. For other particle radii, the mass spectrum shows that dozens of Mars-sized planets were formed, along with hundreds of Moon-sized objects.

We compare runs with single and multiple particle species, finding that gas drag modifies the streamlines in the tadpole region around the classical L4 and L5 points. As a result, particles of different species have their stable

points shifted to different locations. This brings down the mass of the Trojan planets, as now the clumps are segregated spatially by size, each of them having less mass available for assemblage. As a result, collapse is hindered in a low-resolution run with 256^2 grid points and 10^5 particles equally distributed in mass and number among four species (1, 10, 30, and 100 cm). Counter-intuitively, a run with the same parameters but without self-gravity achieved higher mass concentrations (up to $6 M_{\oplus}$). We conclude that the gravity of the solids modifies the stability of the tadpole orbits. Inside the massive vortices, the tidal forces from the gas also stall the gravitational growth of the solids into planets. The same negative results are observed when the number of numerical super-particles is raised by a factor 4.

Collapse resumed when the grid resolution was refined by a factor 2, producing 3 super-Earth mass planets at the outer edge of the gap. The most massive one has $4.5 M_{\oplus}$ by the end of the simulation. The other super-Earths are of 4.36 and $4.14 M_{\oplus}$. In addition, a fourth, smaller, planet of $8.0 M_{\text{Mars}}$ was also formed within the gap edge vortices. These planets are composed primarily of 30 cm particles ($\approx 50\%$), with smaller and almost equal shares of 10 cm and 1 m, and only trace amounts of 1 cm particles. Judging by their mass and location, these objects may be the embryos that gave rise to planet Saturn. Although the distance of formation of Saturn in this model seems too close to Jupiter, it is not at all unlikely that

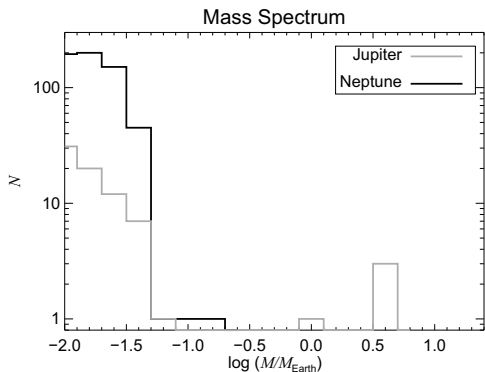


Fig. 10. Mass spectrum at the end of the Jupiter (Sect. 5) and Neptune (Sect. 6) simulations. The most massive planet in the Neptune case is the Trojan of $0.16 M_{\oplus}$. It is followed by another Trojan of $0.09 M_{\oplus}$. In the Jupiter case the most massive planets are formed within the vortices at the outer edge of the gas gap. It includes the three super-Earths and a $8 M_{\text{Mars}}$ planet. The Jupiter simulation was terminated at 83 orbits. At that time, the mass in the tadpole orbits was split into 19 lunar-sized objects in the mass range $1.5 M_{\text{Moon}}$. Other 26 gravitationally bound objects of mass between 0.5 and $1 M_{\text{Moon}}$ are also observed in the co-rotational region.

Saturn was indeed formed in this orbital position. The ice giants Uranus and Neptune are presently located in regions of the solar system where the dynamical timescales are too large and the densities are too low to account for their current masses (Thommes et al. 2002, and references therein). This is an indication that they were formed further in and, therefore, that the giant planets displayed a much more compact spacing in the early Solar system than they present today. Our results seem to corroborate this scenario

When the mass of the perturber is reduced to that of Neptune, the asymmetry between L4 and L5 is accentuated. The L5 point of the particles of $a_{\bullet}=10\text{cm}$ moves to $\approx 35^{\circ}$ behind Neptune, and the $a_{\bullet}=1\text{m}$ to $\approx 25^{\circ}$. The L4 point was shifted too far ahead of the planet and eventually lost all particles, a behavior attributed to its merging with the shifted unstable L3 point (Peale 1993, Murray 1994). Of the particles retained at L5, the ones of 10cm concentrated into a $1.6 M_{\text{Mars}}$ Trojan planet.

One question to ask is if the formation of Trojan bodies as massive as terrestrial planets is so easily achievable, why we do not see it in the Solar System. The answer might lie in the fact that, according to recent models by Morbidelli et al. (2005), all Trojan orbits of the Jovian system were de-stabilized when Jupiter and Saturn crossed the 2:1 mean motion resonance. The initial Trojan population of Jupiter was lost and a new one was captured. Without the gas to damp their motions and increase the number density, the new Trojan population could not assemble into rocky planets. This scenario raises the possibility that in extrasolar planetary systems with only one giant or with giants that did not undergo the destructive resonance crossing that Jupiter and Saturn underwent, Trojan

Earth-mass companions to the giant planets are common. This includes the giants in Earth-like orbits in a list of potentially habitable stellar systems.

Of course, it might as well be that the formation scenario we present is overly simplistic and that some important piece of physics that prohibits the process is missing. We did not include, for instance, the possibility of destructive collisions between boulders. Checking the velocity dispersion at the bound clumps, we find that they are typically lower than 10m s^{-1} for a formed planet. As the initial stages of collapse, however, the speeds are greater, $10\text{-}30\text{m s}^{-1}$, eventually reaching as fast as 80m s^{-1} . These speeds are comparable to or larger than the break-up collisional speeds ($\sim 10\text{m s}^{-1}$, Benz 2000). These high collision speeds indicate that collisional fragmentation will play an important role during the gravitational collapse in a more realistic coagulation-fragmentation model (Brauer et al. 2008a). On the other hand, the fact that collapse occurs for particles of 1-10cm radius is particularly relevant since they are too small to be easily destroyed by collisions. Moreover, the escape velocities of the formed clumps are high enough so that most debris of catastrophic collisions might remain bound. Johansen et al. (2008) find that cm-sized fragments of such collisions are easily swept up away from the midplane by turbulent motions. This leaking is anticipated to not occur in the cases presented in this paper, where planets are formed inside vortices. As vortices do not have vertical shear and revolve at the Keplerian orbital rate (Klahr & Bodenheimer 2006) the sedimentation of the solids layer does not trigger the Kelvin-Helmholtz instability (Johansen et al. 2006b) when this sedimentation happens inside a vortex. The sedimentation is therefore more efficient, which helps collapse.

Our neglecting of coagulation is also an issue that causes pause. Solid bodies grow by sweeping up smaller dust grains, so coagulation raises the possibility that the trapped rocks and boulders might breach the meter-size barrier inside the gap edge vortices and Lagrangian gas clouds. If so, they would produce km-sized bodies that are too loosely coupled to undergo gravitational collapse in the way presented in this paper. Brauer et al. (2008b) has indeed showed that growth to kilometer-size is highly favored within gas pressure maxima. However, the timescale for coagulation seems to be slow ($\sim 1000\text{yr}$) compared to the timescales we observe for gravitational collapse in all cases except for the formation of Trojan planets with the $a_{\bullet}=1\text{cm}$ particles. In this case, the timescales are comparable and we can expect coagulation to influence the growth. In particular, coagulation onto the 1cm particles can aid on replenishing the population of 10cm and 30cm particles lost during the Neptune phase.

Once a cluster of particles collapses to form a single object, aerodynamical drag ceases to be the most important driver of particle dynamics. Instead the planet enters the regime of gravitational drag in which it interacts with its own gravitational wakes. Since we solve for both the particle gravity (that causes the wakes) and gas gravity (that makes the wakes backreact on the particles), our simulations in principle resolve this stage as well, although limited by the grid resolution. However, the drag influence of the planet on the gas is strongly exaggerated, since the influence of particles is always spread over the nearest three grid points in each direction. The friction time is also

still that of the individual rocks, where as a solidified body of a few thousand kilometers in size should have a much longer friction time. A better treatment would thus be to replace the ensemble of particles by a single particle representing the planet. This would also allow a much longer integration time, and we plan to go this way to model the long term evolution of the planet system in a future project.

An immediate question to ask is how (or if) the collapse would occur in three dimensions. Johansen & Klahr (2005), Fromang & Papaloizou (2006) and Lyra et al. (2008a) show that the particles are stirred up by the hydromagnetic turbulence to form a layer of finite vertical thickness, maintained by turbulent diffusion. We performed a 3D simulation of planet-disk interaction in spherical coordinates, similar to those of Bate et al. (2003), Kley et al. (2005) and Edgar & Quillen (2008), but inviscid instead of viscous. The Lagrangian points of the planet do not change much in 3D, with the scale height being about the same as in the unperturbed disk case. Fromang et al. (2004) and Lodato (2008) calculate the effects of self-gravity in the vertical extent of the disk, showing that the thickness is reduced by the disk's self-gravity. This flattening of the scale height in self-gravitating disks bring it closer to the 2D configuration.

Of course, we are only assessing this by simple estimates based on isolated bits of physics done by individual works. A definite answer to this question has to be addressed by a 3D simulation that combines these effects.

The collapse of the solids is triggered by the gravitational influence of a perturber, but more fundamentally due to the presence of long-lived, high-pressure regions: the vortices and the accumulation of gas in the Lagrangian points. As such, a giant is not necessary for the rapid formation of rocky planets. Paardekooper et al. (2008) show that passing binaries can stir the material in the disk. Such encounters usually last for long times, and therefore gravitational collapse of the boulders might happen in such case. Vortices similar to the ones presented in this paper, excited by a giant planet, are also expected at the border of the dead zone (Varnière & Tagger, 2006; Lyra et al. 2008b). Therefore, the accumulation into rocky planets shown to occur inside the vortices induced by a giant planet should also happen inside these dead zone vortices. If so, this paper provides not only a plausible mechanism for the formation of Trojan planets and Saturn, but also of the very first planetary embryos that - in the core accretion scenario - gave rise to Jupiter.

Acknowledgements. Simulations were performed at the PIA cluster of the Max-Planck-Institut für Astronomie and on the Uppsala Multidisciplinary Center for Advanced Computational Science (UPPMAX). This research has been supported in part by the Deutsche Forschungsgemeinschaft DFG through grant DFG Forschergruppe 759 "The Formation of Planets: The Critical First Growth Phase".

References

Baines, M. J., Williams, I. P., Asebiomo, A. S. 1965, *MNRAS*, 130, 63
 Balsara, D. S., Tilley, D. A., Rettig, T., & Brittain, S. A. 2008, arXiv0810.0246
 Barge, P., Sommeria, J. 1995, *A&A*, 295, 1
 Bate, M. R., Lubow, S. H., Ogilvie, G. I., Miller, K. A. 2003, *MNRAS*, 341, 213
 Beaugé, C., Sándor, Zs., Érdi, B., Süli, Á. 2007, *A&A*, 463, 359
 Benz, W. 2000, *SSRv*, 92, 279
 Binney, J. & Tremaine, S. 1987, *Galactic Dynamics*, Princeton Univ. Press, Princeton, NJ

Bracco, A., Chavanis, P.-H., Provenzale, A., & Spiegel, E. A. 1999, *Physics of Fluids*, 11, 2280
 Brauer, F., Dullemond, C.P., & Henning, Th. 2008a, *A&A*, 480, 859
 Brauer, F., Henning, Th., & Dullemond, C.P. 2008b, *A&A*, 487, L1
 Chavanis, P.-H. 2000, *A&A*, 356, 1089
 Edgar, R. G., Quillen, A. C. 2008, *MNRAS*, 387, 387
 Fouchet, L., Maddison, S. T., Gonzalez, J.-F., Murray, J. R. 2007, *A&A*, 474, 1037
 Freeman, K. C. 1970, *ApJ*, 160, 811
 Fromang, S., Balbus, S. A., Terquem, C., De Villiers, J.-P. 2004, *ApJ*, 616, 364
 Fromang, S., Nelson, R. P. 2005, *MNRAS*, 364, 81
 Fromang, S., Papaloizou, J. 2006, *A&A*, 452, 751
 Goldreich, P., Ward, W. R. 1973, *ApJ*, 183, 1051
 Haghhighipour, N. & Boss, A. P. 2003, *ApJ*, 583, 996
 Haugen, N.E.L., Brandenburg, A., & Mee, A.J. 2004, *MNRAS*, 353, 947
 Hockney, R. W., Eastwood, J. W. 1981, *Computer Simulation Using Particles*, McGraw-Hill, New York
 Johansen, A., & Klahr, H. 2005, *ApJ*, 634, 1353
 Johansen, A., Klahr, H., Henning, Th. 2006a, *ApJ*, 636, 1121
 Johansen, A., Henning, Th., Klahr, H. 2006b, *ApJ*, 643, 1219
 Johansen, A., Oishi, J. S., Mac Low, M.-M., Klahr, H., Henning, Th., & Youdin, A. 2007, *Nature*, 448, 1022
 Johansen, A., Brauer, F., Dullemond, C., Klahr, H., & Henning, Th. 2008, *A&A*, 486, 597
 Johansen, A., Youdin, A. 2007, *ApJ*, 662, 627
 Klahr, H., Bodenheimer, P. 2006, *ApJ*, 639, 432
 Kley, W., D'Angelo, G., Henning, Th. 2001, *ApJ*, 547, 457
 Kwok, S. 1975, *ApJ*, 198, 583
 Li, H., Colgate, S. A., Wendroff, B., Liska, R. 2001, *ApJ*, 551, 874
 Lodato, G. 2008, arXiv0801.3848
 Lyra, W., Johansen, A., Klahr, H., & Piskunov, N. 2008a, *A&A*, 479, 883
 Lyra, W., Johansen, A., Klahr, H., & Piskunov, N. 2008b, arXiv0807.2622
 Morbidelli, A., Levison, H. F., Tsiganis, K., Gomes 2005, *Nature*, 435, 462
 Murray, C. D. 1994, *Icarus*, 112, 465
 Paardekooper, S.-J. 2007, *A&A*, 462, 355
 Paardekooper 2006, PhDT
 Paardekooper, S.-J., Mellema, G. 2004, *A&A*, 425, 9
 Paardekooper, S.-J., Thébaud, P., Mellema, G. 2008, *MNRAS*, tmp, 370
 Peale, S. J. 1993, *Icarus*, 106, 308
 Pollack, J. B., Hubickyj, O., Bodenheimer, P., Lissauer, J. J., Podolak, M., Greenzweig, Y. 1996, *Icarus*, 124, 62
 Rice, W. K. M., Lodato, G., Pringle, J. E., Armitage, P. J., & Bonnell, I. A. 2004, *MNRAS*, 355, 543
 Rice, W. K. M., Lodato, G., Pringle, J. E., Armitage, P. J., Bonnell, I. A. 2006, *MNRAS*, 372, 9
 Safronov, V.S. 1969, *QB*, 981, 26
 Shakura, N.I., & Sunyaev, R.A. 1973, *A&A*, 24, 37
 Skorov, Y. V. & Rickman, H., 1999, *Planet. Space. Sci.*, 935, 949
 Toomre, A. 1963, *ApJ*, 138, 385
 Thommes, E. W., Duncan, M. J., & Levison, H. F. 2002, *AJ*, 123, 2862
 de Val-Borro, M., Artymowicz, P., D'Angelo, G., Peplinski, A. 2007, *A&A*, 471, 1043
 de Val-Borro, M., Edgar, R.G., Artymowicz, P., Cieliegiel, P., Cresswell, P., D'Angelo, G., Delgado-Donate, E.J., Dirksen, G., Fromang, S., Gawryszczak, A., Klahr, H., Kley, W., Lyra, W., Masset, F., Mellema, G., Nelson, R., Paardekooper, S.-J., Peplinski, A., Pierens, A., Plewa, T., Rice, K., Schäfer, C., & Speith, R. 2006, *MNRAS*
 Varnière, P., & Tagger, M. 2006, *A&A*, 446, L13
 Weidenschilling, S. J. 1977, *MNRAS*, 180, 5
 Weidenschilling, S. J., Cuzzi, J. N. 1993, *Protostars and Planets III*, p1031
 Woitke, P. & Helling, C., 2003, *A&A*, 399, 297
 Youdin, A. N., Goodman, J. 2005, *ApJ*, 620, 459
 Youdin, A. N., Johansen, A. 2007, *ApJ*, 662, 613